Heinrich Heine
Universität
Düsseldorf

NMR spectroscopic and biophysical characterisation of functional DNA

Inaugural-Dissertation

zur Erlangung des Doktorgrades
der Mathematisch-Naturwissenschaftlichen Fakultät
der Heinrich-Heine-Universität Düsseldorf

vorgelegt von

Jessica Felice Schmuck
aus Dortmund

Düsseldorf, Dezember 2025

aus dem Institut für Physikalische Biologie
der Heinrich-Heine-Universität Düsseldorf

Gedruckt mit der Genehmigung der
Mathematisch-Naturwissenschaftlichen Fakultät der
Heinrich-Heine-Universität Düsseldorf

Berichterstatter:

1. Dr. Manuel Etzkorn

2. Prof. Dr. Henrike Heise

Tag der mündlichen Prüfung: 30.04.2026

Eidesstattliche Versicherung

Ich versichere an Eides Statt, dass die Dissertation von mir selbständig und ohne unzulässige fremde Hilfe unter Beachtung der „Grundsätze zur Sicherung guter wissenschaftlicher Praxis an der Heinrich-Heine-Universität Düsseldorf“ erstellt worden ist.

Düsseldorf, 11.12.2025

Jessica Felice Schmuck

für meine Eltern
&
Opa Walter

Abstract

Since the first discovery of nucleic acids in 1869, our understanding has diversified, and their importance has expanded from being solely a building block of life to becoming an essential tool in biology, biochemistry, medicine, and biotechnology. However, this functional diversity is not reflected in the building blocks provided by nature, making it crucial to understand how sequences, metal ions, biophysical factors (e.g., temperature or pH), and cellular, cellular-like, or synthetic environments determine function and applications.

Overall, this thesis aims to elucidate how the structure, folding, and dynamics of nucleic acids relate to their function, to improve or apply functional nucleic acids. This thesis focuses on three classes of functional DNA: a self-cleaving DNAzyme (1), two RNA-cleaving DNAzymes (Dz46-like (2) and DNAzyme 8-17 (3)), and a G-quadruplex (4), whose diversity is reflected in their functions and applications as therapeutics, biosensors, and target in diseases. In detail, this thesis addresses using NMR spectroscopy and biophysical approaches (1) how a completely new and innovative self-cleaving DNAzyme system is functionally, structurally and mechanistically characterised, (2) how nucleic acid modifications influence the structure and folding of an RNA-cleaving Dz46-like DNAzyme, (3) how the choice of target nucleic acids for the RNA-cleaving DNAzyme 8-17 influences its structure and catalytic activity, and (4) how and if a chemotherapeutic is interacting with a cancer-driving G-quadruplex.

This thesis reveals a paradigm shift in the understanding of DNA catalysts, as the pin system (1) does not rely on a stable structural framework to catalyse its cleavage reaction. Our studies reveal that pin acts in a dynamic interplay between conformational plasticity and the cadmium cofactor. For the Dz46-like DNAzyme (2), this thesis reveals: changing the cleavage site pattern leads to increased overall system dynamics; a shortage of three nucleotides in target binding arms abolishes the formation of a DNAzyme-RNA complex; the G14 MOE modification in the catalytic loop improves the catalytic activity and folding, leading to intermediate exchange of the system, which prevented further assessment. Results for the RNA-cleaving DNAzyme 8-17 (3) highlight that a chimeric DNA target, compared to the usual RNA target, enhances the catalytic cleavage activity and alters the folding of the DNAzyme-target complex. Moreover, the results of the interaction study with the cancer-driving G-quadruplex (4) and the chemotherapeutic doxorubicin strongly indicate a specific binding through stabilisation of G-quadruplex, strongly supporting recent *in vivo* studies. In summary, this thesis demonstrates that the studied function of functional nucleic acids is defined by their conformation and dynamics, which are directly connected by factors such as sequence, temperature, metal ions, and the environment. Additionally, NMR spectroscopy and biophysical methods are demonstrating their potential as versatile tools for comprehensive scientific analysis of an increasing diversity of nucleic acids.

Zusammenfassung

Seit der ersten Entdeckung von Nukleinsäuren im Jahr 1869 hat sich unser Verständnis erweitert, und ihre Bedeutung hat sich von einem reinen Baustein des Lebens zu einem unverzichtbaren Werkzeug in der Biologie, Biochemie, Medizin und Biotechnologie gewandelt. Diese funktionale Vielfalt spiegelt sich jedoch nicht in den von der Natur bereitgestellten Bausteinen wider, weshalb es von entscheidender Bedeutung ist, zu verstehen, wie Sequenzen, Metallionen, biophysikalische Faktoren (z. B. Temperatur oder pH-Wert) sowie zelluläre, zellähnliche oder synthetische Umgebungen die Funktion und Anwendungen bestimmen.

Insgesamt zielt diese Arbeit darauf ab, aufzuklären, wie die Struktur, Faltung und Dynamik von Nukleinsäuren mit deren Funktion zusammenhängen, um funktionelle Nukleinsäuren zu verbessern oder anzuwenden. Diese Arbeit konzentriert sich auf drei Klassen funktioneller DNA: ein selbstspaltendes DNAzym(1), zwei RNA-spaltende DNAzyme (Dz46-ähnliche (2) und DNAzyme 8-17 (3)), und ein G-Quadruplex (4), deren Vielfalt sich in ihren Funktionen und Anwendungen als Therapeutika, Biosensoren und Zielmoleküle bei Krankheiten widerspiegelt. Im Einzelnen befasst sich diese Arbeit unter Verwendung von NMR-Spektroskopie und biophysikalischen Ansätzen mit (1) der funktionellen, strukturellen und mechanistischen Charakterisierung eines völlig neuen und innovativen selbstspaltenden DNAzym-Systems, (2) dem Einfluss von Nukleinsäuremodifikationen auf die Struktur und Faltung eines RNA-spaltenden Dz46-ähnlichen DNAzyms, (3) wie die Wahl der Zielnukleinsäuren für das RNA-spaltende DNAzym 8-17, dessen Struktur und katalytische Aktivität beeinflusst und (4) wie und ob ein Chemotherapeutikum interagiert. Diese Arbeit offenbart einen Paradigmenwechsel im Verständnis von DNA-Katalysatoren, da das Pin-System (1) zur Katalyse seiner Spaltungsreaktion nicht auf ein stabiles, strukturelles Gerüst angewiesen ist. Unsere Studien zeigen, dass Pin in einem dynamischen Wechselspiel zwischen Konformationsplastizität und dem Cadmium-Cofaktor wirkt. Für das Dz46-ähnliche DNAzym (2) zeigt diese Arbeit: Eine Veränderung der Schnittstelle führt zu einer erhöhten Gesamtdynamik des Systems; das Fehlen von drei Nukleotiden in den Zielerkennungsarmen verhindert die Bildung eines DNAzym-RNA-Komplexes; die G14-MOE-Modifikation in der katalytischen Kernsequenz verbessert die katalytische Aktivität und Faltung, was zu einem *intermediate exchange* des Systems führt, der eine weitere Auswertung verhindert. Die Ergebnisse für das RNA-spaltende DNAzym 8-17 (3) zeigen, dass ein chimäres DNA-Zielmolekül im Vergleich zum üblichen RNA-Zielmolekül die katalytische Spaltaktivität verstärkt und die Faltung des DNAzym-Zielkomplexes verändert. Darüber hinaus deuten die Ergebnisse der Interaktionsstudie mit dem krebsauslösenden G-Quadruplex (4) und dem Chemotherapeutikum Doxorubicin stark auf eine spezifische Bindung durch Stabilisierung des G-Quadruplex hin, was die jüngsten *in-*

vivo-Studien deutlich untermauert. Zusammenfassend zeigt diese Arbeit, dass die untersuchte Wirkungsweise funktioneller Nukleinsäuren durch ihre Konformation und Dynamik definiert ist, die direkt mit Faktoren wie Sequenz, Temperatur, Metallionen und der Umgebung zusammenhängen. NMR-Spektroskopie und biophysikalische Methoden zeigen ihr Potenzial als vielseitige Werkzeuge.

Contents

List of Figures

List of Tables

List of Abbreviations

Abbreviations	Description	Abbreviations	Description
2'F	2'-Fluorine	MD	Molecular Dynamic
2'FU	2'-desoxy-2'-fluoro-uridine	mdeg	Millidegree
2'-OMe	2'-O-methyl	ME	Molar ellipticity
2'-MOE	2'-O-methylethyl	mRNA	Messenger RNA
5-FU	5-fluorouracil	NMR	Nuclear magnetic resonance
A	Adenine	NOESY	Nuclear Overhauser Spectroscopy
APS	Ammonium persulfate	nt	nucleotide
ASO	Antisense Oligonucleotides	PCR	Polymerase chain reaction
BHQ	Black hole quencher	PrP	Proin protein
C	Cytosine	PS	Phosphothimates
CD	Circular Dichroism	RFU	Relative Fluorescence Units
CEST	Chemical Exchange Saturation Transfer	rNTP	ribonucleoside-5'-triphosphates
CPMG	Carr-Purcell-Meiboom-Gill	RT-NMR	real-time NMR
CSP	Chemical shift perturbation	SELEX	Systematic Evolution of Ligands by Exponential Enrichment
DDLPS	Dedifferentiated Liposarcoma	SELOPE	SELective Optimized Proton Experiment
DNAzyme	DNA Enzyme	siRNA	Small interfering RNA
dNTP	Desoxynucleoside-5'-triphosphates	SL	Spinlock
DOX	Doxorubicin	SPR	Surface plasmon resonance
Dz	8-17 DNAzyme (only commentary)	ss	Single stranded
EDTA	Ethylenediaminetetraacetic acid	T	Thymine
EM	Electron Microscopy	TEMED	Tetramethylethylendiamin
FANA	2'-Fluoro-arabinonucleotide	TOCSY	Total Correlation Spectroscopy
FRET	Förster Resonance Energy Transfer	Tris Base	Tris(hydroxymethyl)aminomethan
G	Guanine	U	Uracil
GQ	G-Quadruplex	WDLPS	Well-Differentiated Liposarcoma
G-tetrads	Guanine tetrads	XNA	Xeno nucleic acid
HSQC	Heteronuclear single quantum coherence	Ψ	Pseudouridine
ITC	Isothermal Titration Calorimetry		
LNA	Locked nucleic acid		
M5C	5-methylcytidine		
M6A	N6-methyladenosine		
M7G	N7-methylgaunosine		

1 Background

Nucleic acids are the building blocks of life, storing and expressing genetic information. Nucleic acids **(Figure 1A)** consist of three components: a phosphate group, deoxyribose in the case of DNA or ribose in the case of RNA and a base. The base can be thymine (T), guanine (G), adenine (A) and cytosine (C). In RNA, thymine is replaced by uracil (U). Adenine and guanine are classified as purines, whereas cytosine, thymine, and uracil belong to the pyrimidine class. The nucleotides (nt) are connected through phosphodiester bonds in the phosphate backbone, forming long chains of nucleic acids (polymer). DNA forms a two-stranded helical structure, where one strand is running in the 5' to 3' direction, whereas the other strand is running 3' to 5'. Both DNA chains interact with each other by forming Watson-Crick base pairing through hydrogen bonds. DNA forms A, B, and Z-form helical structures. Chemically, RNA is similar to DNA, but the chain typically forms a monomer (Minchin and Lodge, 2019, Moccia et al., 2024). In every living organism, nucleic acids are essential for all cellular functions, including protein synthesis and heredity (Moccia et al., 2024). Since its first discovery in 1869, the importance of DNA has grown from being solely a carrier of genetic material to becoming an essential tool in biology, biochemistry, medicine and biotechnology. Nucleic acids appear to be limited by the low diversity of bases, but diversity is enormous through secondary and tertiary structures, base, sugar and backbone modification. The versatility and programmability of nucleic acids dramatically expand their potential applications. The possible applications **(Figure 1B)** of nucleic acids are diverse and have multiplied in recent years, primarily encompassing the following categories: therapeutics (both as independent therapeutic agents and as targets in diseases), biosensor technology, nanotechnology, and delivery systems (Moccia et al., 2024, Du and Dong, 2017, Afonin et al., 2022, Bian et al., 2025). To understand function and improve, or apply nucleic acids, whether in the form of oligonucleotides (therapeutics, biosensors, etc.) or at the cellular level (G-quadruplexes, DNA enzymes, etc.), their structure and dynamics must be resolved. Biophysical approaches such as spectroscopy (e.g., Nuclear magnetic resonance (NMR), Circular dichroism (CD, UV/Vis)), X-ray crystallography, Cryo-Electron microscopy (EM) and Molecular Dynamics (MD) simulation are powerful tools for characterising the structure and dynamics of nucleic acids.

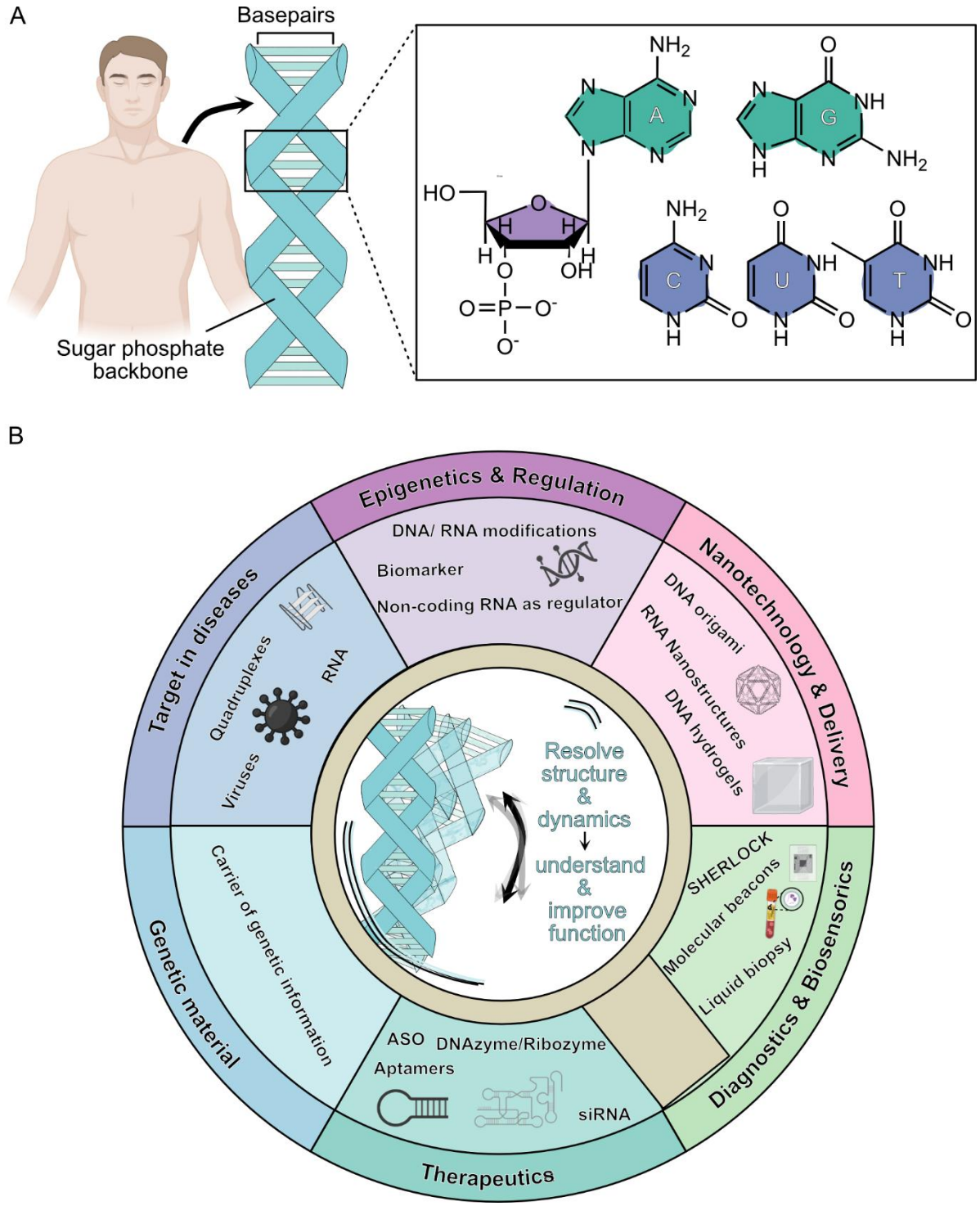

Figure 1: Structure and therapeutic, biotechnological, and general applications of nucleic acids in life and life sciences. A: A nucleic acid is composed of three components: a base (blue: pyrimidines, green: purines), a pentose sugar (purple) and a phosphorus group. The pentose sugar differs in the C2' positions by either being a deoxyribose (DNA) with an OH or a ribose (RNA) with an H. At the C1' of ribose, the base and at the C5', the phosphorus group is attached to the ribose. The nucleotides are connected through the 5' phosphorus and the 3' hydroxyl group. **B:** Nucleic acids are the carriers of genetic information, but also serve as a versatile tool in biological, biotechnological and therapeutic applications. Applications of nucleic acids were categorised in Therapeutics, Diagnostics & Biosensorics, Nanotechnology & Delivery, Epigenetics & Regulation, targeting diseases and Genetic material and are mentioned with common examples of their field. To understand function and improve, or apply nucleic acids, whether in the form of oligonucleotides (therapeutics, biosensors, etc.) or at the cellular level (G-quadruplexes, DNA Enzymes, etc.), their structure and dynamics must be resolved. The figure was partly created using BioRender.

1.1 Modified nucleic acids—enhance the functionality and diversity

The number of approved nucleic acid therapeutics has risen significantly over the last four decades (Kulkarni et al., 2021, Duffy et al., 2020). Nucleic acid therapeutics such as antisense oligonucleotides (ASOs), small interfering RNAs (siRNAs), aptamers, and microRNAs provide a new approach to treating diseases that small-molecule therapeutics fail to target. Conventional therapeutics often fail to target the underlying causes of diseases and rather induce transient effects. Nucleic acid therapeutics can directly target diseases where they arise by inhibition, addition, or editing of genes (Kulkarni et al., 2021). However, poor chemical and biological stability, and chemical diversity remained challenging and led to nucleic acids therapeutics lagged behind by other therapeutics (Duffy et al., 2020). Improving the chemical diversity of nucleic acid therapeutics, chemically modified nucleic acids were introduced. Modifications to the backbone, sugar, and base of nucleic acids, as well as the development of completely new unnatural base pairs, increased the repertoire of nucleic acids (Pradeep et al., 2023).

In general, ribose modifications **(Figure 2A)** are attributed to increasing nuclease tolerance, prolonging the half-life of nucleic acids, altering and modulating the sugar pucker conformation, and affecting the strength and specificity of base pairing (Dhara et al., 2025, Sun et al., 2024). Especially first-generation modifications at the 2'-position of the ribose, like 2'-fluorine (2'F), 2'-O-methoxyethyl (2'-MOE), and 2'-O-methyl (2'-OMe), can affect the duplex binding ability and stability and are widely used in nucleic acid therapeutics like ASO (Yoshida et al., 2024) or siRNA (Dhara et al., 2025, Malek-Adamian et al., 2019). In locked nucleic acid (LNA), C4' and O2' atoms are connected by a methylene bridge, forming a C3'endo conformation of the ribose ring. Duplex formation between nucleic acids and LNA increases the thermal stability and activates RNase H degradation (Sun et al., 2024, Nielsen et al., 2004). In 2′-deoxy-2′-fluoroarabinonucleic acid (2′F-ANA (FANA)), the 2'-H group of the ribose is substituted by a fluorine atom. FANA modifications induce RNAase H-mediated cleavage (Liang et al., 2017), increase the resistance to degradation (Watts et al., 2009), and enhance binding to target messenger RNA (mRNA) (Sandoval-Mojica et al., 2021). Both FANA- and LNA-modifications are used for *in vivo* and *in vitro* applications in siRNA (Dowler et al., 2006), aptamers (Alves Ferreira-Bravo et al., 2015), ASO (Sandoval-Mojica et al., 2021) and DNA enzymes (DNAzymes) (Taylor et al., 2022, Nguyen et al., 2023).

The range of nucleobase modifications is vast. Most commonly used modifications include 5-methylcytidine (m5C), 5-fluorouracil (5-FU), N7-methylguanosine (m7G), pseudouridine (Ψ), N6-methyladenosine (m6A), and 2'-deoxy-2'-fluoro-uridine (2'-FU) and are mainly used to stabilise the duplex and modulate immunogenicity (Sun et al., 2024). Modifications such as 7-deaza-guanine, 6-O-methyl-guanine, and 6-thio-guanine are used less frequently but still cover

important functions **(Figure 2B)**. 7-deaza-guanine suppresses metal ion binding and increases chemical stability (Kowal et al., 2011), whereas 6-O-methyl-guanine favours non-canonical base pairing of thymines over cytosines (Kleibl, 2002), and 6-thio-guanine alters Mg^{2+} binding properties (Borggräfe et al., 2022).

Backbone modifications relied mostly on non-bridging oxygen atoms, such as phosphorothioate (PS) **(Figure 2C)**, methyl phosphate, and baranophosphate (Sun et al., 2024). Backbone modifications are attributed to enhance degradation stability to nucleases, *in vivo* lifetime (renal clearance, blood stream stability) and improve binding to plasma proteins (Herkt and Thum, 2021, Sun et al., 2024). However, positive effects do not come alone; backbone modifications also increase inflammatory responses and hepatotoxic side effects (Herkt and Thum, 2021, 2002).

The combination of base, sugar, and backbone modifications to improve a plethora of functions of siRNA (Kenski et al., 2012), ASO (Benson et al., 2018), and DNAzymes (Nguyen et al., 2023) will likely constitute the next step in next-generation nucleic acid therapeutics.

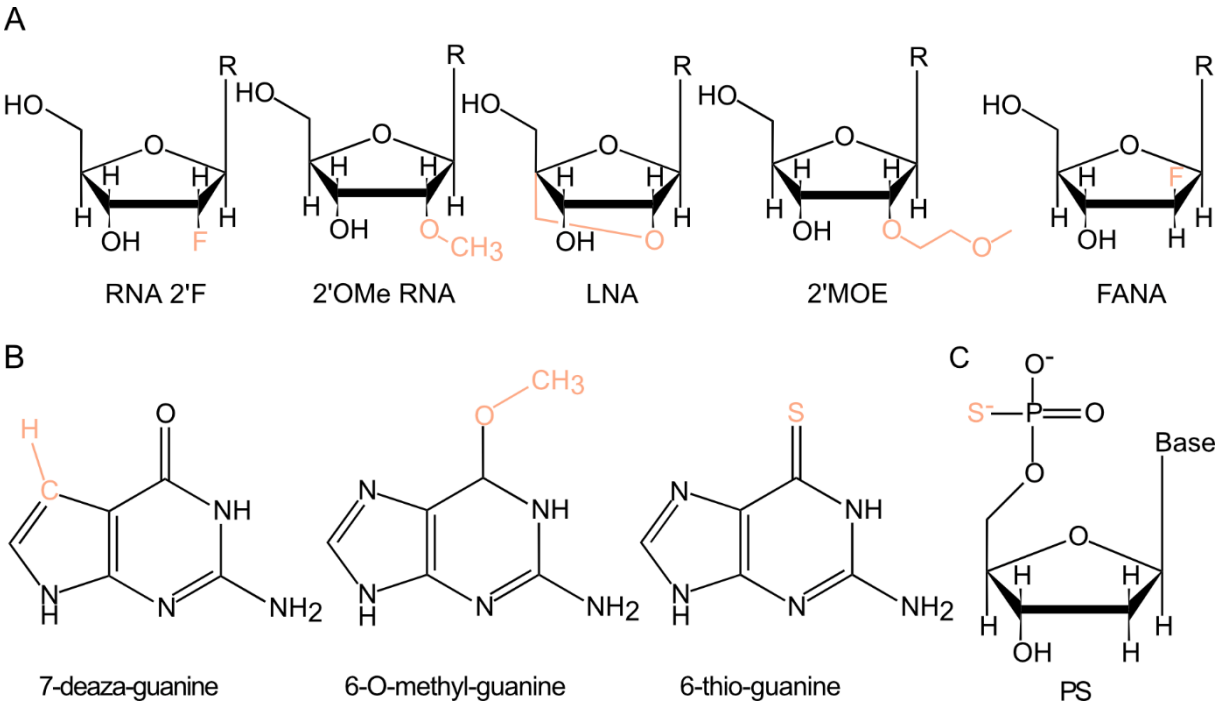

Figure 2: Selection of chemical modifications on nucleic acids relevant for this work. A: Sugar modifications. **B:** Base modifications**. C:** Backbone modifications.

1.2 DNAzymes

For a long time, nucleic acids were solely considered the “building blocks of life”, storing and expressing genetic information. In the last decades, the applications of nucleic acids have diversified. The applications of Systematic Evolution of Ligands by Exponential enrichment

(SELEX) and *in vitro* selection have boosted the development of nucleic acid applications, like DNA-based catalysts. So far, two variants of catalytic DNA are known: (1) complexes of double-helical DNA molecules and metal ions and (2) DNAzymes, short, single-stranded oligonucleotides. Originally, DNAzymes were developed as gene-silencing tools due to their ability to bind and cleave RNA targets in a sequence-specific manner. Nowadays, a toolbox of DNAzymes with various chemical functions is available, and their role as biocatalysts is expanding. DNAzymes are capable of cleaving RNA and DNA, forming carbon-carbon bonds, ligating peptides, and cleaving other bonds, such as DNAzyme-imitating photolyases (Hollenstein, 2015). The following chapters focus on RNA-cleaving DNAzymes (Chapter 1.2.1) and their growing role as therapeutic agents, as well as the latest developments and scientific findings, and also discuss recent developments in DNA-hydrolysing DNAzymes (Chapter 1.2.2).

1.2.1 RNA-Cleaving DNAzymes

In 1994, Joyce and Breaker were the first to discover Pb^{2+}-dependent, RNA-cleaving DNAzymes using *in vitro* selection (Breaker and Joyce, 1994). The naturally occurring background cleavage rate of RNA in mammalian cells is estimated to be $k_{obs}/ min^{-1} \sim 10^{-7}$ (Carmi et al., 1996). The first discovered DNAzymes were cis-catalysts, and cleaved RNA with a rate constant ~ 10^7-fold (k_{obs}/ min^{-1}: 1.4) faster than the background cleavage rate (Breaker and Joyce, 1994, Hollenstein, 2015). The most famous DNAzymes 8-17 and 10-23 were discovered shortly after, in 1997, by Santoro and Joyce (Santoro and Joyce, 1997).

The DNAzymes 10-23 and 8-17 share general features: two target-recognition arms flanking the catalytic loop, cleaving RNA in a sequence-specific manner under physiological, multiple-turnover conditions. DNAzyme 10-23 cleaves after all purine-pyrimidine junctions, whereas DNAzyme 8-17 can cleave after all 16 dinucleotide junctions with highly fluctuating k_{obs} values over five orders of magnitude. DNAzyme 10-23 possesses a 15-nucleotide-long catalytic loop, and DNAzyme 8-17 possesses a 14-nucleotide-long catalytic loop, with a GT wobble base pair, a three-nucleotide-long Watson-Crick base-paired stem, AGC-loop, and four unpaired residues (Hollenstein, 2015, Santoro and Joyce, 1997). The metal-ion dependence of both variants differs strongly. The 17e variant of the DNAzyme 8-17 for single-turnover rates, followed the order of $Pb^{2+} \gg Zn^{2+} \gg Mn^{2+} \approx Co^{2+} > Ni^{2+} > Mg^{2+} \approx Ca^{2+} > Sr^{2+} \approx Ba^2$ (Brown et al., 2003). Whereas the DNAzyme 10-23 for single-turnover rates, followed the order of $Mn^{2+} > Mg^{2+} > Ca^{2+} >> Ba^{2+}$ (Sugimoto et al., 1999). A recent study showed that for the DNAzyme 10-23, high monovalent cation (Na^+ and K^+) concentrations inhibit the activity of the DNAzyme in the presence of Mg^{2+}, while high monovalent cation concentrations in the presence of Mn^{2+} increase the catalytic activity. In the presence of solely monovalent cations, there is no catalytic

activity (Rosenbach et al., 2020a). The proposed catalytic mechanism of both DNAzymes is linked to the cleavage mechanism of the hammerhead ribozyme (He et al., 2002). In the presence of divalent metal ions, the 2'-hydroxyl (nucleophile) residue at the scissile bond is activated either by protonation or deprotonation. A nucleophilic attack facilitates the breakdown of the phosphorus backbone into a 2',3'-cylic phosphate and a 5'OH product (Hollenstein, 2015, Brown et al., 2003).

Since the first discovery, DNAzymes have been studied intensively; however, structural conformation, mechanistic understanding, and recognition of the target substrate remained elusive. Liu and colleagues were the first to report three precatalytic crystal structures of the 8-17 DNAzyme. Crystallisation was facilitated with an all-DNA target, with a 2'-OMe-guanine (RNA) at the cleavage site, in the presence and absence of Pb^{2+}, and in the presence of the African swine fever virus DNA polymerase X. The DNAzyme 8-17 forms a V-like shape with Pb^{2+} bound in a preorganised pocket, intrinsic tertiary interaction and a molecular kink at the cleavage site (Liu et al., 2017). In 2024, Wieruszewska and colleagues reported the solution structure of the 8-17 DNAzyme with Zn^{2+} as a cofactor (Wieruszewska et al., 2024). Further insights into this study will be discussed in a review/commentary in Chapter 3.2.2.

In 2021, for the first time, insights into the DNAzyme 10-23 via high-resolution and time-resolved NMR spectroscopy were provided. The study unravelled the mode of action using time-resolved NMR and complementary techniques. In the precatalytic complex, the catalytic loop winds around the 2'F-stabilised RNA substrate. Using Mg^{2+}, Mn^{2+} and $[Co(NH_3)_6]^{3+}$, three binding sites for divalent metal ions were identified and characterised. Mechanistic insights into the cleavage reaction were gathered by real-time NMR, following the cleavage reaction in combination with MD simulation and dynamic NMR experiments. Multiple rate-limiting transient intermediate states during the cleavage reaction were revealed. The revealed structure and dynamics of DNAzyme 10-23 opened up new possibilities for enhancing the activity of the DNAzyme through nucleic acid modification. A 6-thio-guanine modification was introduced at G14 of the loop in combination with an A5C mutation, strongly increasing the activity of the DNAzyme (Borggräfe et al., 2022).

In the following years, DNAzyme development focused particularly on the modification of DNAzyme 10-23 (Dz46 and FANAzym) to build DNAzymes suitable for cellular applications and enhance their activity (Wang et al., 2021, Nguyen et al., 2023, Taylor et al., 2022). Recent modifications and developments of the Dz46 will be further discussed in Chapter 3.1.

RNA-cleaving DNAzymes are promising new nucleic acid therapeutics for gene silencing and provide advantages such as low synthesis costs, independence from RNase H, and multiple turnovers over other small molecule therapeutics (Larcher et al., 2023). Insights into the most

recent developments, therapeutic applications and therapeutic potential of the DNAzyme 10-23 will be further discussed in Chapter 3.

1.2.2 DNA hydrolysing DNAzymes

The Breaker Lab was the first to attempt generating hydrolysing DNAzymes through directed evolution. At that time, ribozymes capable of cutting single-stranded DNA were already well established (Robertson and Joyce, 1990). The challenging development of self-cleaving DNAzymes was driven by the need to expand the toolbox for new artificial nucleases (Hollenstein, 2015). The complexity of the task is related to the half-life of the phosphodiester bond in DNA. Under physiological buffer conditions, the half-life is considered to be several million years. Therefore, DNAzymes must achieve a rate enhancement greater than 10^6-fold to promote the useful hydrolysis of a DNA-phosphodiester bond (Gu et al., 2013). In contrast, the half-life of RNA is estimated between four and ten years (Hollenstein, 2015, Wolfenden and Snider, 2001, Li and Breaker, 1999). From a chemical perspective, DNA is considered more resistant to degradation due to the missing ribose 2'-hydroxyl. In the presence of cationic metals, the hydroxyl of the RNAs' ribose forms a 2'-oxyanion, which acts as a nucleophile in a transesterification reaction and results in the cleavage of the RNA phosphodiester bond (Carmi et al., 1996). Since DNA is the only vehicle carrying and storing genetic information, a high degree of stability seems feasible for long-term, precise conservation of genetic information (Buko et al., 2023).

In 1996, Breaker and colleagues succeeded in isolating DNA-cleaving DNAzymes, two classes, both requiring Cu^{2+} as a cofactor, using *in vitro* selection. Class I of self-cleaving DNAzymes requires Cu^{2+} and ascorbate, whereas class II exclusively requires Cu^{2+}. Both discovered DNAzyme classes use oxidation as a self-cleavage mechanism (Carmi et al., 1996). However, single-stranded DNA that can be oxidatively cleaved using Cu^{2+} and ascorbate was nothing new at the time. Ten years earlier, single-stranded DNA strands that could cleave themselves site-specifically by means of a redox reaction had already been identified (Kazakov et al., 1988). Unexpected was the finding that DNA can cleave itself exclusively using Cu^{2+} without any additional reductant (Carmi et al., 1996). The discovered Cu^{2+} DNAzyme was systematically shortened to further generate the smallest possible active construct with 46 nucleotides. The DNAzyme has a duplex and a triplex substructure that flank a highly conserved catalytic core. However, the cleavage site and cleavage products were described as rather nonspecific. Especially, other groups describe that by oxidative destruction, "diffusible intermediates" are formed (Chandra et al., 2009). The discovery of DNA that can hydrolyse DNA in the same DNA strand at a specific cleavage site, on the other hand, happened rather by chance during an attempt to identify DNAzymes that can cleave peptide

bonds. The discovered 40-nucleotide-long DNAzyme (10MD5) requires both Mn^{2+} and Zn^{2+} as cofactors to catalyse, and uses ATGT as a pattern for the cleavage site. The DNAzyme substrate can be present as both chimeric and all-DNA without significantly affecting activity (Chandra et al., 2009). From 2010 to 2012, Silverman and colleagues did extensive studies on DNA-hydrolysing DNAzymes, especially on the 10MD5. The DNAzyme 10MD5 is working at a very sharp pH optimum. To increase the activity of the DNAzyme at a broader pH range, *in vitro* evolution experiments were conducted and yielded 9NL27. When attempting to overcome unfavourable features, the pH range could be expanded (7.2–7.7), but specificity also decreased (Xiao et al., 2010). A bunch of DNA-hydrolysing DNAzymes was discovered in an attempt to understand the required length of unpaired nucleotides in the substrate, while trying to increase the sequence tolerability of the DNAzyme. (Xiao et al., 2011c). Two nucleotide mutations in 10MD5 resulted in a monometallic, Zn^{2+} only DNAzyme (Xiao et al., 2011a). By *in vitro* selection, DNA-hydrolysing DNAzymes were selected, using the lanthanides Ce^{3+}, Eu^{3+}, and Yb^{3+} as monovalent or bivalent cofactors, along with Zn^{2+}. The DNAzymes discovered have specific metal-ion requirements; for example, some can only function with Yb^{3+} in the absence of Zn^{2+} (Dokukin and Silverman, 2012).

All of the previously described DNAzymes share the common feature of a catalytic core, which is embedded by two target recognition arms. The structure, composition, and mode of action can be linked to the known RNA-cleaving DNAzymes 10-23 and 8-17 (Santoro and Joyce, 1997). In previous work, the DNA-hydrolysing DNAzymes and targets were already connected by a linker. This results in a DNAzyme that “virtually” cuts itself (Xiao et al., 2011c). However, they would not be considered as actual self-cleaving DNAzymes.

In 2013, a completely new approach by the Breaker lab was used to discover and select novel Zn^{2+}-dependent DNA-hydrolysing DNAzymes and revealed the first real self-cleaving DNAzymes. Therefore, a randomised circular DNA library was generated using the ATP-dependent CircLigase. The DNA constructs were incubated with Zn^{2+} as a cofactor to promote DNA hydrolysis. For ligation, CircLigase requires a 3′-OH and a 5′-phosphate on the same single-stranded DNA to form a phosphodiester bond. CircLigase thus works simultaneously as a bottleneck, directly excluding other cleavage mechanisms such as oxidation. The hydrolysed products were then transferred to a second ligation reaction. This was followed by PCR amplification, which allowed the determination of the distinct sequence identity. Using the previously described method, two new classes of DNA-hydrolysing DNAzymes were identified. Class I is a Zn^{2+}-dependent DNAzyme, active at nearly neutral pH, with a rate constant of k_{obs} 1 min^{-1}. The catalytic core of the DNAzyme is composed of 15 conserved nucleotides forming a bulge or loop and carrying a distinct cleavage site between A-A nucleotides. Interestingly, it was once again found that class I DNAzymes can only be catalytically active within a very

narrow pH range (Gu et al., 2013, Xiao et al., 2010). Cofactor concentrations that deviate both above and below 1 mM Zn^{2+} also dramatically reduce activity. Temperatures of up to 45°C are also tolerated without any significant loss of activity. Class II DNAzymes share similar characteristics with class I, but are significantly larger. They have a 32-nucleotide unpaired bulge with a base-paired stem at both ends. Their activity at 45°C is 50-fold higher than at 23°C (Gu et al., 2013). This selection strategy was extended by the programming of a terminal hybridisation stem into the DNA library. Thus, class III and IV of Zn^{2+}-dependent self-cleaving DNAzyme, with a conserved catalytic core length of approximately 20 nucleotides, were identified. Benefits of the terminal hybridisation were suggested as: a stem provides a pre-existing structure which, as previously shown, improves the library's functional potential. The addition of already pre-existing structures is also considered a critical structural element to support the catalysis (Zhang et al., 2021). In recent years, research into self-cleaving and hydrolysing DNAzymes has focused more on optimising existing motifs (Liu and Gu, 2021, Etheridge et al., 2023), developing applications in the field of biotechnology and medicine (Wang et al., 2019, Praetorius et al., 2017, Li et al., 2023), and developing more robust selection methods (Dantu et al., 2024) than on developing and designing novel classes of DNAzymes.

1.3 G-Quadruplexes

G-quadruplexes are guanine-rich nucleic acid sequences that form stacked guanine tetrads (G-tetrads) (Meier-Stephenson, 2022). Usually, G-tetrads consist of four guanine residues forming a square-planar platform **(Figure 3A)**, which is stabilised by Hoogsteen base pairing, and pile up in 2–4 stacks on each other (Guiset Miserachs et al., 2016). G-quadruplexes require monovalent or divalent cations, in particular K^+, which coordinates to the O6 of the guanine in each planar square. Nucleic acid sequences prone to build G-quadruplexes are usually described as $(G_x N_y)_4$, where $x \geq 2$ guanosine residues and y is 1–7 non-guanine residues (Meier-Stephenson, 2022, Davis, 2004). Both RNA and DNA can form parallel, antiparallel or hybrid G-quadruplexes **(Figure 3B)**, whereas RNA mostly forms parallel G-quadruplexes. In parallel G-quadruplexes, all planar tetrads show in the same direction; in an antiparallel G-quadruplex, all neighbouring G-tetrads are located antiparallel to each other, hybrid quadruplexes possess both parallel and antiparallel tetrads. Conformations of quadruplexes are determined by the orientation of the glycosidic bonds of the guanines in the tetrads, as well as the length and sequences of the connecting loops (Maizels, 2015). Quadruplexes are either monomeric or multimeric and can therefore be formed out of more than one nucleic acid molecule (Yang, 2019, Chen and Yang, 2012). Multimeric quadruplexes

are connected by diverse loop conformations like propellers, lateral or diagonal structures and can fold dynamically into different conformations (Yang, 2019).

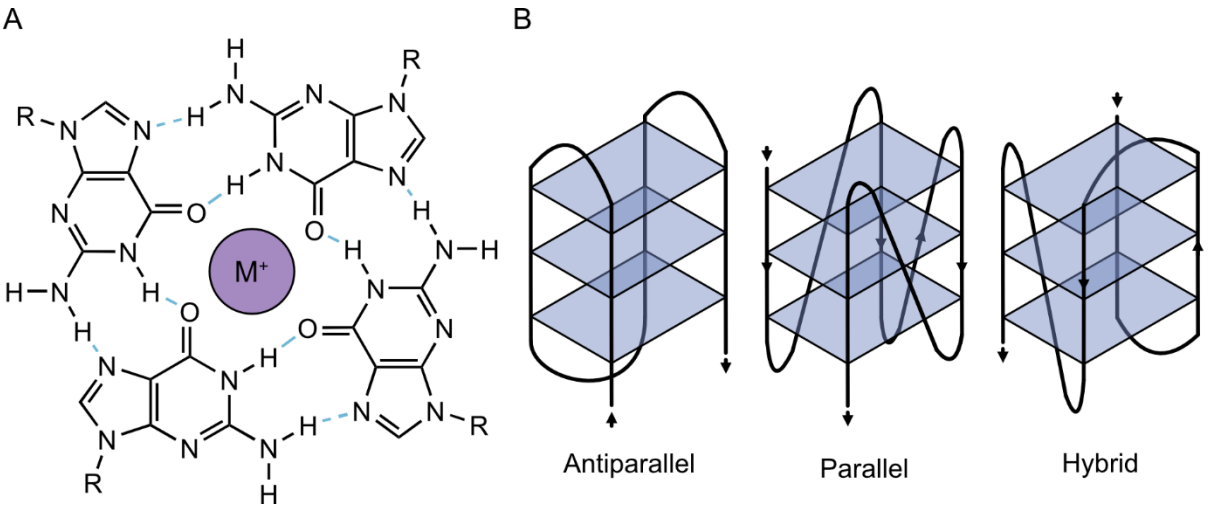

Figure 3:Structure and topologies of G-quadruplexes. A: structure of a G-tetrad. Four guanines are stabilised by Hoogsteen base pairing (dashed blue line) and a metal ion. **B:** Topologies of monomeric G-quadruplexes.

It took fifty years from the first observation of G-tetrads in telomeres in 1910 to the determination of the structure. Until now, more than 700,000 putative G4-quadruplex structures in the human genome have been identified (Hänsel-Hertsch et al., 2017). As quadruplex structures are located in highly regulatory regions like promoter regions or telomeres, they are linked to diverse cellular processes. The function of G-quadruplexes varies depending on their localisation and is associated with telomere maintenance, DNA replication, transcriptional regulation and many more cellular processes. G4-quadruplexes are also associated with an increasing number of diseases, such as cancer, neurological, or viral diseases, and their structures are interesting targets for drug design (Xu et al., 2021, Adrian et al., 2012). Biophysical methods, such as CD-, NMR-spectroscopy, surface plasmon resonance (SPR) or isothermal titration calorimetry (ITC), are used to study stability, ligand binding, interaction and structure of G-quadruplexes (Yang, 2019).

1.4 NMR spectroscopy of nucleic acids

NMR spectroscopy is a versatile tool to study nucleic acids with single-atom-level resolution. Studying RNA and DNA oligonucleotides using NMR spectroscopy to gain knowledge of structure and dynamics is important for understanding the underlying biological mechanisms and the development of novel therapeutics. Using NMR spectroscopy, insights into the structure, base-pairing patterns, conformational equilibria, metal-ion binding, local structures and dynamics, interaction with proteins, nucleic acids or ligands and solvent molecules can be given. Like every technique, NMR spectroscopy comes with advantages, disadvantages and

benefits from other complementary techniques, spectroscopic and biophysical methods for structure characterisation, such as X-ray crystallography or cryo-electron microscopy (Fürtig et al., 2003).

1.4.1 1D ^{1}H experiments

In the 13 to 15 ppm region of a 1D ^{1}H NMR spectrum **(Figure 4A and B)** with efficient water suppression, imino proton peaks of the four nucleobases can be observed. Imino protons occur due to the involvement of the amine group (NH) of the four bases in Watson-Crick base pairing. These groups are protected from fast exchange with bulk water. In a G:C Watson-Crick base pair, the proton of the NH1 of guanine binds to the N3 of a cytosine, and appears between 12–14 ppm. In a T:A Watson-Crick base pair, the proton of the NH3 of the thymine binds to the N1 of adenine and appears between 13–14 ppm. Irregular base pairs usually appear between 10 and 16 ppm. Imino peaks are broader and weaker than the usual proton peaks (Fürtig et al., 2003, Plavec, 2023). In G-quadruplexes, special imino peaks of the H1 of the guanine appear between 10–12 ppm. These imino peaks also exchange with the bulk water, but slowlier than their counterparts in a Watson-Crick duplex (Adrian et al., 2012). Aromatic protons H2 (adenine), H8 in purines and H6 in pyrimidines resonate between 7–9 ppm. These peaks are usually narrow and sharp due to slow solvent exchange. H1’ of the ribose and H5 of pyrimidines resonate between 5–6 ppm, in RNA, between 3–4.5 ppm. Remaining sugar protons (H3’, H4’, H5’, H5’’ and H2’) resonate, whereas in DNA, remaining sugars resonate between 2–5 ppm (H3’, H4’, H5’, H5’’, H2’, H2’’ and H7). In DNA, due to the absence of the 2’OH group, H2’ and H2’’ resonate at lower ppm values compared to RNA (Plavec, 2023).

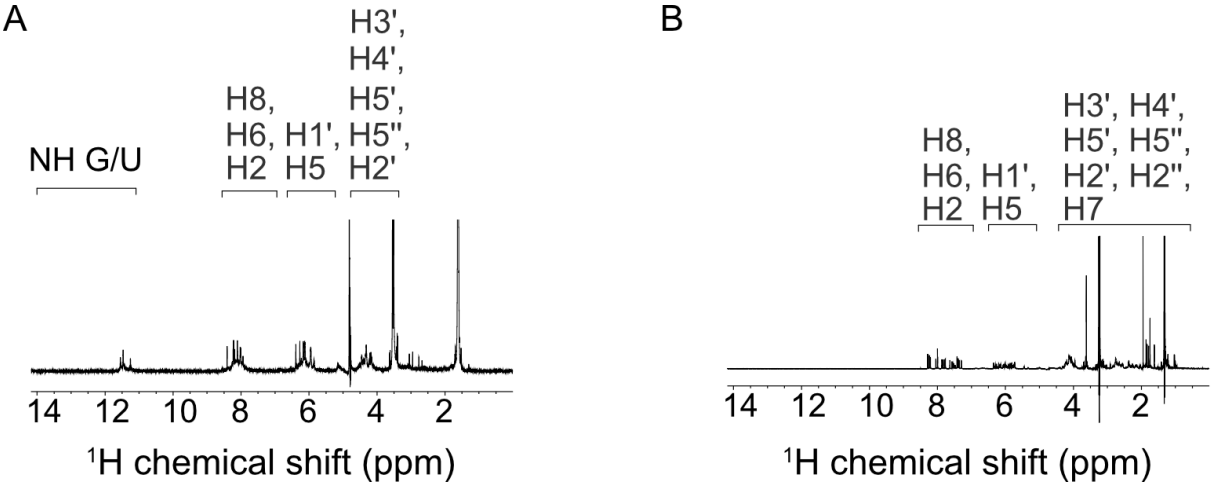

Figure 4: 1D ^{1}H spectra of nucleic acids. **A:** Spectrum of RNA G-quadruplex with imino G4-quadruplex peaks between 10–12 ppm. **B:** Spectrum of DNA.

1.4.2 2D ^{1}H-^{1}H NOESY/ TOCSY and ^{1}H-^{13}C HSQC experiments

2D NMR experiments, such as ^{1}H-^{1}H NOESY/ TOCSY and ^{1}H-^{13}C HSQC, are frequently used since they do not rely on isotope labelling. The ^{1}H-^{1}H Nuclear Overhauser Effect Spectroscopy (NOESY) makes use of the nuclear Overhauser effect (NOE), which facilitates magnetisation transfer by cross-relaxation of two different nuclei. The effect depends on the distance and typically has a maximum of 6 Å between the two different nucleic acids and is not dependent on covalent bonds, but goes through space (Binas, 2020). Experimentally, the chosen mixing time depends on the oligonucleotide size and cross-peaks of interest and ranges between 30 to 300 ms. In ^{1}H-^{1}H Total Correlation Spectroscopy (TOCSY), spin-spin coupling through-bonds between H5 and H6 protons of cytosine and uracil, and the H7 methyl group of thymine are correlated. The chosen mixing times vary between 80 and 120 ms. TOCSY cross-peaks can serve as a fingerprint for nucleic acids. In a ^{1}H-^{13}C experiment, C8H8 of purines, C6H6 and C5H5 of pyrimidines, C1'H1 of all residues, C2H2 of adenines and all of the sugar CH resonances can typically be visualised (Thompson et al., 2019).

1.4.3 Isotope labelling of nucleic acids

Since RNA and DNA are limited to four bases, a pentose sugar and a phosphorus group, chemical shift dispersion of occurring nuclei ^{1}H (natural occurring isotope propensity: 99.98%), ^{13}C (natural occurring isotope propensity: 1.06%), ^{15}N (natural occurring isotope propensity: 0.38%), and ^{31}P (natural occurring isotope propensity: 100%) is limited (Lu et al., 2010). In non-isotopically labelled samples, solution-NMR spectroscopy faces limitations for samples comprising greater than 30 nucleotides due to increased linewidth and overlapping signals. Overlapping signals arise from a lack of dispersion in the chemical structures of nucleic acids. R_2 relaxation rates increase depending on the molecular weight of a biomolecule and result in broad signals (Hilber et al., 2025). NMR spectroscopic experiments with natural abundance of ^{13}C and ^{15}N nuclei can be recorded, but they do rely on high sample concentrations and a large number of scans. Correlation experiments between natural abundance ^{13}C and ^{15}N nuclei are nearly impossible. Nowadays, three different strategies are applied in isotope-labelled oligonucleotide synthesis. *In vitro* transcription using T7 RNA polymerase for RNA synthesis is a well-established protocol. Uniformly labelled samples are achieved by using isotope-labelled ribonucleoside-5'-triphosphates (rNTPs) in the transcription process (Becette et al., 2019, Hilber et al., 2025). Enzymatic methods for isotope-labelled DNA exist, but are uncommon due to the difficulty of splitting the double-helical strand into two single-stranded DNA-oligonucleotides. Isotopically labelled DNA is produced using ^{13}C/^{15}N-labelled phosphoramidites or ^{13}C/^{15}N-labelled building blocks for solid-phase synthesis (Hilber et al., 2025). With this technique, it is even possible to label specific residues in the oligonucleotide.

The last, most common technique is polymerase chain reaction (PCR) for DNA oligonucleotide synthesis by incorporating desoxynucleoside-5'-triphosphates (dNTPs) (Louis et al., 1998).

For NMR spectroscopic studies using oligonucleotides larger than 30 nucleotides or for experiments aiming to correlate ^{13}C and ^{15}N nuclei, isotopic labelling of the oligonucleotide is inevitable. All of the above-explained methods have their advantages and disadvantages, and careful consideration should always be given to which method is particularly well-suited to the oligonucleotide in question. Especially for RNA, but also for all nucleic acids, commercially available isotope-labelled building blocks are very costly. It should always be considered whether isotope labelling is appropriate for a particular construct, as various experiments can be performed without labelling (Hilber et al., 2025).

1.4.4 Resonance Assignment/ Assignment Strategy without labelling

Sequential resonance assignment of ^{1}H in unlabelled oligonucleotides is possible mostly through NOE connectivities and through-bond homonuclear correlations. Some of the unlabelled carbon and nitrogen atoms can be assigned through heteronuclear NMR experiments, involving ^{13}C or ^{15}N at natural abundance (Wijmenga and van Buuren, 1998). If the oligonucleotide possesses stable base pairing, assignment of imino peaks in a ^{1}H-^{1}H-NOESY spectrum can be the start of the assignment. Assignment of the imino peaks is followed by the partial assignment of the non-exchangeable base and sugar protons. Cytosine and Uracil H6/H5 proton cross peaks **(Figure 5A)** are identified using ^{1}H-^{1}H-TOCSY (which identifies cross peaks of their own spin system). Thymine is identified using the same approach, through the methyl group of H7 (1.5–3 ppm). The sequential assignment is done by following the sequential NOE connectivities. If two residues/spin systems are in proximity to each other, NOESY cross peaks of their own spin system will also be visible, but with weaker cross peaks, as in the cross peaks of the nearby residue. Therefore, sequential walk from the H8/H1' cross peak (n) horizontally forward to H1' (n)–H8/H1' (n+1) or backwards from H'(n)–H8/H1' (n-1) to H1'(n-1) (H8 can equally be replaced by H6) can be used for usual assignments (Binas, 2020). This sequential assignment walk can be repeated with H8/H3' (n) to H8 (n)–H8/H3' (n+1) or for the H2' and H2'' residues. For sequential assignment, π-π-stacking is also considered. Assignment of carbon residues of the bases and sugars can easily be done by using ^{1}H-^{13}C- heteronuclear single quantum coherence (HSQC) **(Figure 5B)** by correlating the already assigned chemical shifts of the protons with the chemical shifts of the carbon. Two main problems occur in the sequential assignment of protons in non-labelled oligonucleotides: signal-overlap and dependency on NOE contacts. NOE contact can be ambiguous, and assignment requires assumptions of the structural conformation of the oligonucleotide (Wijmenga and van Buuren, 1998).

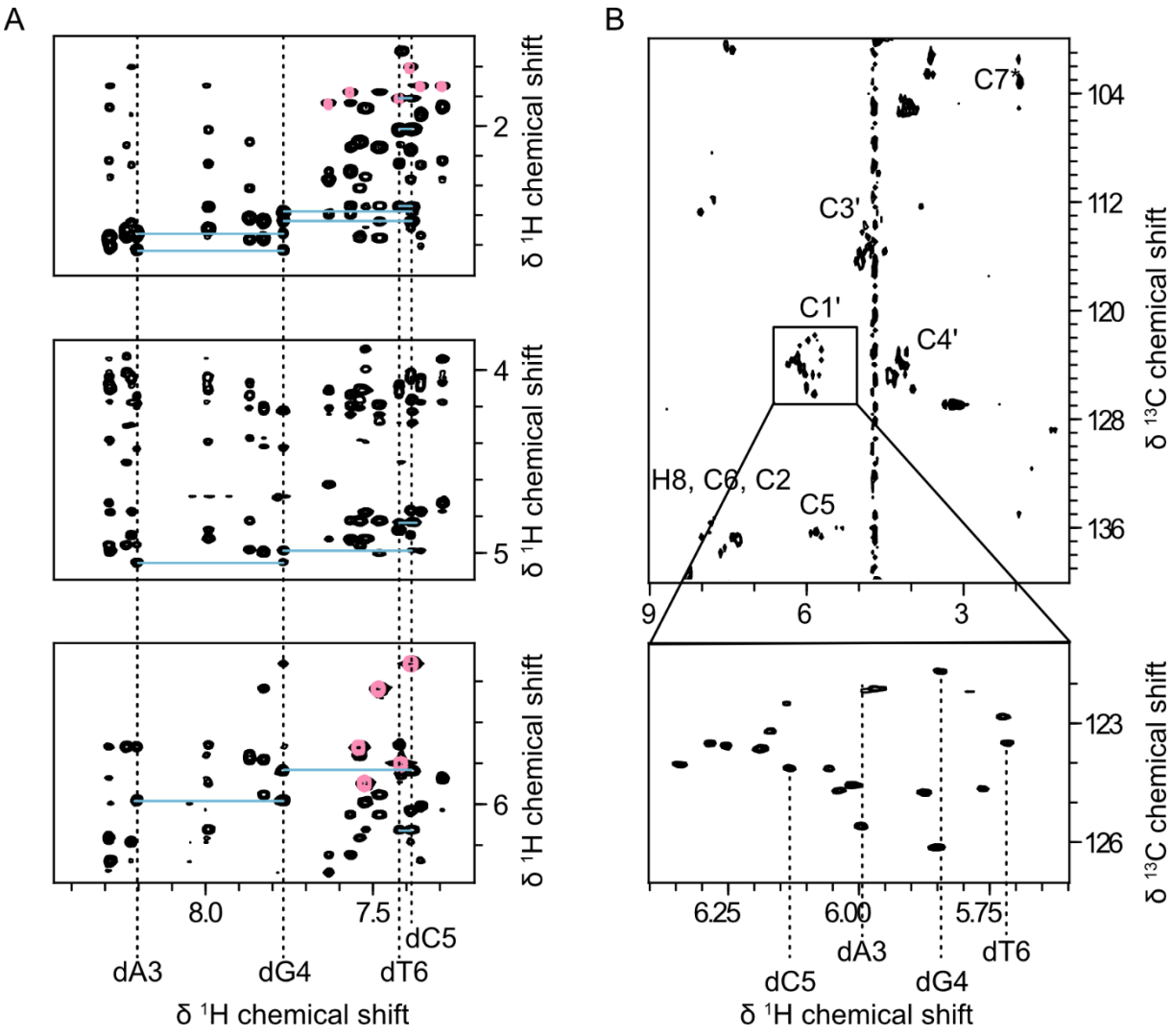

Figure 5: Sequential resonance assignment of Pin20 (DNA) using ^{1}H-^{1}H -NOESY, ^{1}H-^{1}H -TOCSY and natural abundance ^{1}H-^{13}C-HSQC. A: Overlay of ^{1}H-^{1}H-NOESY (black), ^{1}H-^{1}H-TOCSY (pink). In the direct dimension, the ^{1}H chemical shift of H8 and H8 are correlated with the indirect dimension chemical shift of H1' (approx. 5–6.5 ppm), H3', H4' and H5' (approx. 4–5 ppm) and H2', H2'' and H7 of thymine (approx. 1.2–3 ppm). The vertical dashed line identifies a spin system with all NOE cross-correlation (residues in proximity to the H1' of each spin system). Blue horizontal lines illustrate a sequential walk from dA3–dG4–dC5–dT6. **B:** ^{1}H-^{13}C-HSQC (natural abundance). ^{1}H protons in the direct dimension are correlated with indirect dimension ^{13}C chemical shift of H8, H6 and H2 (approx. 136 ppm), C5 (approx. 135–136 ppm), C1' (approx. 122–126 ppm), C4' (approx. 122–126 ppm), C3' (approx. 113–116 ppm) and C7 of thymine (approx. 103 ppm). A close-up of the C1' region with the assigned residues dA3, dG4, dC5 and dT6.

1.4.5 Dynamics of nucleic acids

Conformational flexibility and changeability in the structure of biological molecules are essential for biological function. More than a decade ago, the importance of the flexibility of nucleic acids in biological processes, such as replication, expression, and regulation, was unravelled (Rangadurai et al., 2019). Nucleic acids undergo dynamic processes on a timescale from picoseconds to hours (Rangadurai et al., 2019). These dynamic processes can be, for example, conformational (e.g., Watson-Crick to Hoogsteen base pairing) or chemical exchange (e.g., keto-enol tautomer). Frequently, the ground state of biomolecules is observed,

often using classical structural analysis methods such as NMR, X-ray or Cryo-EM. Using classical structural analysis methods, the excited states remain invisible due to low population. In contrast to other structural analysis methods, dedicated NMR experiments offer a comprehensive toolbox **(Figure 6)** for investigating ongoing, low-populated dynamical processes in nucleic acids (Marušič et al., 2019).

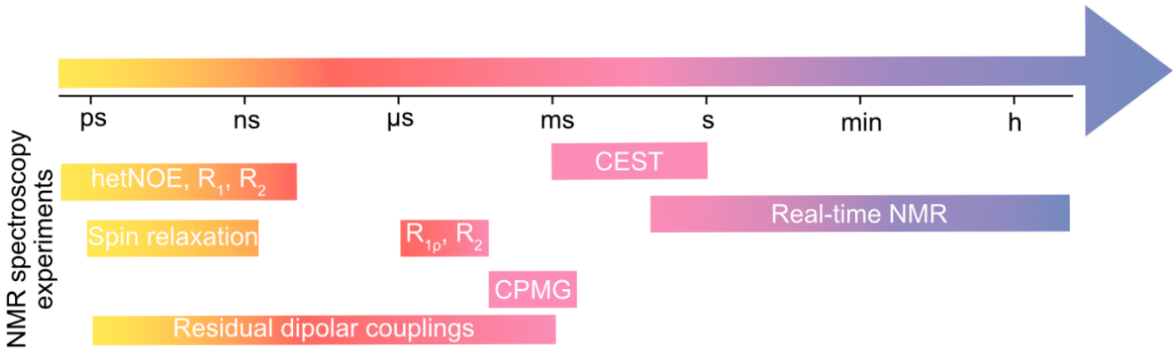

Figure 6: NMR spectroscopic methods to study dynamic processes in nucleic acids within the time scale of ps to hours. Detached from (Kawale and Burmann, 2021, Bothe et al., 2011, Bibow, 2019).

1.4.5.1 Chemical exchange saturation transfer (CEST)

Chemical exchange saturation transfer is used to measure intermediate exchange in the ms–s timescale. The exchange between a visible and an invisible state is unravelled, especially if one of the two states is low-populated and cannot be observed directly. Minor states are usually not visible in regular NMR experiments due to very weak signals (compared to the major state) and line broadening. CEST experiments can unravel the distribution of populations and the exchange rate constants (Marušič et al., 2019). CEST experiments with nucleic acids have been used to study the closing and opening of Watson-Crick base pairing (Manghrani et al., 2024) or hidden conformational states (Zhao et al., 2020).

A low-power spinlock (SL) is used to saturate the resonance frequency of a nucleus of interest. Saturation is a process where the Boltzmann distribution of nuclear spins is altered by applying a low-power SL to the resonance frequency of a nucleus. The nuclear spins can be either aligned parallel or antiparallel to the outer magnetic field **(Figure 7A)**. Saturation balances the number of spins aligned antiparallel and parallel to the magnetic field, thereby increasing the number of spins aligned antiparallel to the magnetic field. The resulting net magnetisation is zero ($M_z \approx 0$), and no signal can be observed (Sherry and Woods, 2008). During CEST experiments, the SL is applied to different ^1H frequencies. If the applied SL frequency is on resonance with the minor state, saturation of the spin population will be transferred from the minor state to the major state. The exchange of magnetisation will happen within the timescale of SL (Marušič et al., 2019). Exchange from the minor state to the major state transfers spins

aligned antiparallel to the magnetic field. Spins aligned parallel to the magnetic field are exchanged from the major state to the minor state. The net result is the transfer of saturation from the minor state to the major state and a decrease in the amplitude of the observed major state **(Figure 7B)**. If the SL offset does not match another invisible state, no saturation and exchange effects will be visible – signal intensity stays in the original amplitude signal (Marušič et al., 2019, Sherry and Woods, 2008).

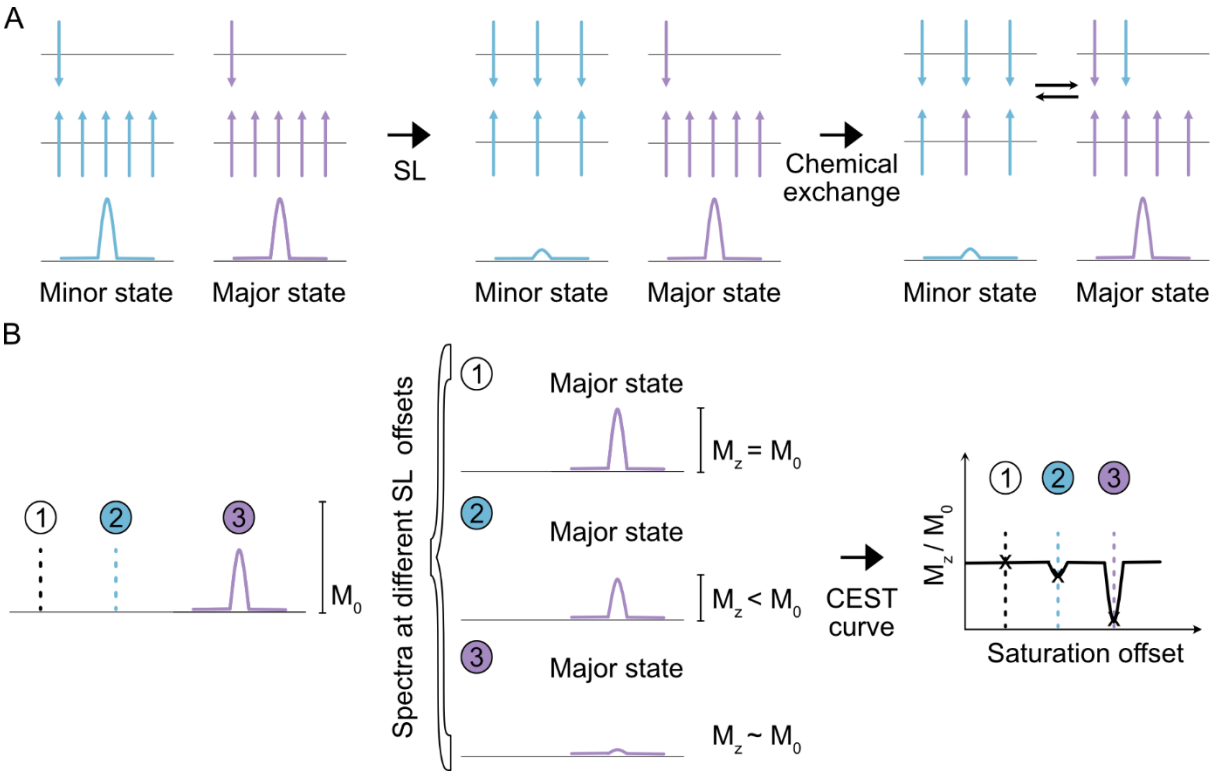

Figure 7: Schematic illustration of CEST experiments. A: Illustration of spin distribution aligned parallel or antiparallel to the magnetic field. In the middle: spins after saturation through SL. On the right: System ongoing chemical exchange after saturation of the minor state. **B:** On the left side, 1D spectrum of three different populated states (1: not populated, 2: Minor state, 3: Major state) of one nucleus. In the middle: Spectra with SL and different offsets (1: offset at a not populated state does not affect the amplitude of the signal, 2: offset at a minor state affects the amplitude of the major state, 3: offset at a major state, net magnetisation is zero). On the right side: Resulting CEST curve. Illustration created based on the template of (Sherry and Woods, 2008, Marušič et al., 2019).

1.4.5.2 SELective Optimized Proton Experiment (SELOPE)

SELective Optimized Proton Experiment (SELOPE) is a measurement technique to avoid expensive isotope labelling (^{13}C, ^{15}N) for dynamic NMR experiments. Especially since ^{1}H, due to its high natural abundance and high sensitivity, is easily detected and can be used for selective excitations. The main features of SELOPE **(Figure 8)** are the selective excitation of a specific proton group and spectral editing to reduce crowding in the overlying resonances. Reduced crowding is managed by a selective excitation of a specific nucleic acid region (e.g., H8/H6) in combination with coherence transfer, using homonuclear *J*-couplings (8–10 Hz). The transverse magnetisation is transferred from H6 to H5, whereas the magnetisation of H8

remains, resulting in a depletion of signal on the diagonal. This technique can be used to study exchange processes in the µs to ms timescale (Schlagnitweit et al., 2018b).

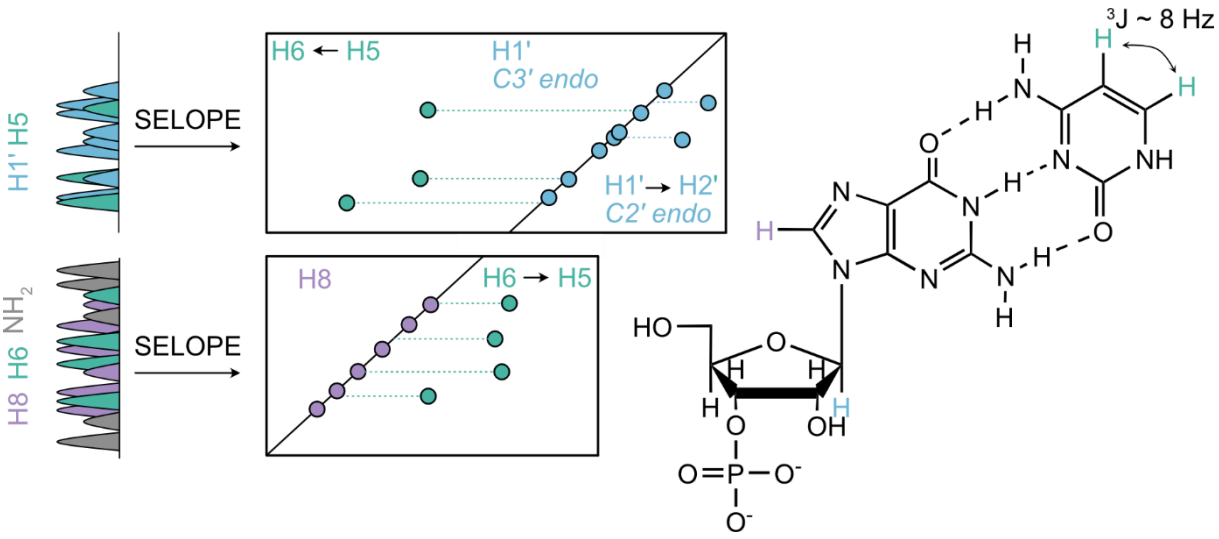

Figure 8: Schematic figure of how 2D spectra of nucleic acids are decrowded using the SELOPE approach. The figure was adapted from (Schlagnitweit et al., 2018b).

1.4.5.3 Real-time NMR

1D or 2D real-time (RT) NMR can be used to measure slow dynamic processes in the minutes to hours/days timescale. Time resolution is achieved by either recording 1D or 2D spectra consecutively. RT-NMR provides time-resolved, atomic-resolution insights into biological processes such as protein folding, cleavage or chemical reactions (Smith et al., 2015). In general, changes in the chemical shifts and linewidth of resonance over time can be used to analyse populated states during dynamic processes (Zeeb and Balbach, 2004).

1.4.6 NMR spectroscopy combined with complementary biophysical approaches

NMR spectroscopy is a versatile tool for studying structures (secondary and tertiary structural elements, etc.), dynamics, diffusion, interaction with ligands, effects of pH, ionic strength or metal ions on nucleic acids. Results of NMR spectroscopy can be extended and complemented with various biophysical assays and approaches like the Förster resonance energy transfer (FRET), CD-Spectroscopy, qPCR, MD- Simulation or ITC (Steffen et al., 2024, Borggräfe et al., 2022). Spectroscopic methods (UV/Vis, FRET, CD, or quantitative PCR (qPCR)) highlight secondary structural features such as the stability of duplexes, the influence of mismatches, or changes in conformations. Especially, CD-spectroscopy helps to reveal first insights into structure and conformation and can complement assignment strategies for NMR (Vorlíčková et al., 2012). MD-Simulations in combination with NMR spectroscopy may help improve the accuracy of dynamic ensembles (Liu et al., 2021, Al-Hashimi, 2013).

1.5 Aim of this Thesis

This thesis aims to study different kinds of DNA catalysts (RNA-cleaving and self-hydrolysing DNAzymes) and G-quadruplexes using biophysical approaches, especially NMR spectroscopy, to characterise and resolve structural features and dynamics, thereby understanding and connecting structure to function.

For **self-hydrolysing DNAzymes,** the central aims are,

based on the recently developed new class of autohydrolytic DNAzyme (Gu lab), to:

- generate first structural insights into self-hydrolysing DNAzymes
- characterise temperature-induced effects, metal ion-induced effects, and the general cleavage mechanism
- obtain insights into the conformational plasticity of the system

For **RNA-cleaving DNAzymes,** the central aims are:

- Characterisation of recent developments and target-DNA/RNA effects on activity and structure of RNA-cleaving DNAzymes 8-17, for which the crystal and NMR structure has already been unravelled using a chimeric DNA target.
- First structural insights into Dz46-like DNAzymes, which have been developed by Chaput and colleagues via chemical evolution. In the catalytic loop of the DNAzyme, a G14 MOE modification was introduced, which significantly improves its catalytic activity. In this regard. Particular attention should be given to these chemical modifications and their reported dependency on an altered cleavage site. Another key interest is the characterisation of construct stability and the effect of an A5C modification in relation to the cleavage activity.

For the **quadruplex MDM2-119**, an oncogene associated with dedifferentiated liposarcoma and a potential new target for cancer treatment, the central aim is to:

- investigate and characterise the potential interaction between the G-quadruplex-forming MDM2 (MDM2-119) and doxorubicin, a cancer therapeutic, using biophysical methods (NMR, CD and UV-Spectroscopy)

2 NMR spectroscopic characterisation of the self-cleaving DNAzyme pin

This part of the thesis contains the NMR spectroscopic characterisation of the pin system. The content of this chapter 2 reflects the content of the following manuscript (submitted):

Structural (d)evolution of a minimalistic DNA enzyme

By

Canyu Zhang*, Jessica Schmuck*, Mingdi Wang*, Robert Hesse, Christoph Gertzen, Mo Zhou, Chunhai Fan, Gerhard Steger, Holger Gohlke, Manuel Etzkorn, and Hongzhou Gu

* Authors contribute equally to this manuscript

This (so far unpublished) manuscript summarises all performed experiments and evaluations of data. It also contains results and experiments not performed by the author of this thesis. All described NMR spectroscopic experiments, analysis and evaluation were performed by the author of this thesis.

2.1 Structural (d)evolution of a minimalistic DNA enzyme

DNA is formed through the polymerisation of deoxyribonucleotides via phosphodiester bonds, a linkage exceedingly resistant to uncatalyzed hydrolysis. In nature, numerous protein and RNA enzymes have evolved specifically to cleave these bonds, enabling the reorganisation of genetic information within DNA. Studying these enzymes, such as CRISPR-Cas (Jinek et al., 2012) and HYER (Liu et al., 2024), has significantly advanced our understanding of biochemical processes and provided a robust toolbox for DNA manipulation both *in vitro* and *in vivo*.

Interestingly, DNA per se can also catalyse its hydrolysis under laboratory conditions. Since the debut in 2009, a total of four classes of autohydrolytic DNAs and ~30 additional individual sequences have been identified through *in vitro* selection (Chandra et al., 2009, Xiao et al., 2011b, Dokukin and Silverman, 2012, Velez et al., 2012, Xiao et al., 2012, Gu et al., 2013, Zhang et al., 2021). These catalytic DNAs (deoxyribozymes or DNAzymes) typically rely on specific structural motifs and cofactors such as Zn^{2+}, Mn^{2+}, or lanthanides for their function. However, despite their ability to achieve rapid cleavage rates, their structural and mechanistic details remain poorly understood. The inherent flexibility and relatively large size of these deoxyribozymes (~40–80 nucleotides, nt) have posed challenges for high-resolution structural

analyses using techniques like crystallography and NMR (Wijmenga and van Buuren, 1998, Schnieders et al., 2020, Borggräfe and Etzkorn, 2022, Borggräfe et al., 2022).

In principle, autohydrolytic deoxyribozymes offer exciting opportunities to (i) expand the current DNA-processing toolbox beyond protein and RNA enzymes, (ii) uncover new insights into the molecular architecture of DNA catalysts, and (iii) reimagine DNA's functional role in biology beyond its capacity as a genetic information carrier. However, their rarity and the limited understanding of their molecular structures have hindered further advances in the field.

Upon re-examining previously identified autohydrolytic DNAs (Chandra et al., 2009, Xiao et al., 2011b, Dokukin and Silverman, 2012, Velez et al., 2012, Xiao et al., 2012, Gu et al., 2013, Zhang et al., 2021), we observed a consistent preference for reaction conditions near the critical point of hydroxide precipitation formed by cofactor metal ions, such as Zn^{2+}, Mn^{2+}, or lanthanides. Although the mechanism underlying this phenomenon remains misty, we hypothesised that novel autohydrolytic deoxyribozyme classes might exhibit similar reaction preferences when other metal ions are used as cofactors. Based on this hypothesis, we devised a corresponding selection strategy to uncover new classes.

In this study, we report a novel class of autohydrolytic deoxyribozymes, termed "pin", discovered under conditions near the critical precipitation point. These catalysts are notable for their minimal size (19–24 nt) and exceptional thermophilicity, achieving half-lives as short as 4 seconds at 90°C while requiring Cd^{2+} ions as essential cofactors. Their low molecular weight enables high-resolution NMR characterisation, offering atomistic and time-resolved insights into the autohydrolysis process. Structural analyses and molecular dynamics simulations reveal that pin deoxyribozymes leverage conformational plasticity to catalyse efficiently in the absence of a conventional structural scaffold. Furthermore, specific structural elements appear to guide catalysis thermodynamically by preorganising the DNA into unproductive states, thereby facilitating transitions to active conformations. These findings not only deepen our mechanistic understanding of DNA catalysis but also open new avenues for dynamic DNA nanotechnology and programmable DNA editing.

2.2 Results and Discussion

2.2.1 Directed evolution identifies a novel class of autohydrolytic DNAs

Previously, we have developed a powerful method (Gu et al., 2013, Zhang et al., 2021) that permits the selection of individuals in a DNA sequence library that autohydrolyse at any linkage, leading to the discovery of four classes of Zn^{2+}-dependent autohydrolytic DNAs. Here, we further optimised the strategy and applied it to select for deoxyribozymes that use Cd^{2+} as

a cofactor. We chose cadmium because it, on the one hand, shares similarities with the previously successfully used Zn^{2+}, and, on the other hand, may help identify a novel class of deoxyribozymes.

A library of ~10^{14} linear DNAs of 149 nt in length that contain a total of 100 random-sequence positions was circularised, autohydrolytic activity was evaluated, and respective constructs were selected via denaturing polyacrylamide gel electrophoresis (dPAGE). After 16 rounds of selective amplification, the DNA library (G16) displayed 33% linearization during 5-min. incubation, and extension to 1 h did not increase cleavage, suggesting that the population was enriched for deoxyribozymes undergoing rapid autohydrolysis. High-throughput sequencing analysis of the G16 library uncovered the existence of a major class of deoxyribozymes termed Cd-I **(Figure 9A).**

2.2.2 A surprisingly short sequence maintains activity, displaying a high degree of conformational plasticity.

A full-length (150 nt) representative (R1) of Cd-I confirmed that the identified sequence possesses autohydrolytic activity that will precisely cleave the DNA into two defined fragments **(Supplement Figure 25)**. To identify the functional unit responsible for the catalytic activity, we set out to identify a minimal active DNA sequence. Evaluation of the expected secondary structure of the R1 construct identifies different structural elements. Interestingly, truncation of nearly all of these elements **(T1–T5, Figure 9A and B, Supplement Figure 25)** did not reduce cleavage activity, converging on a 37 nt fragment (ΔT1–5) carrying the functional unit. Further systematic truncation identifies a minimal sequence of 21 nt, from hereon named pin21, that even shows slightly elevated activity as compared to the original 150 nt R1 construct **(Figure 9A, Supplement Figure 25)**.

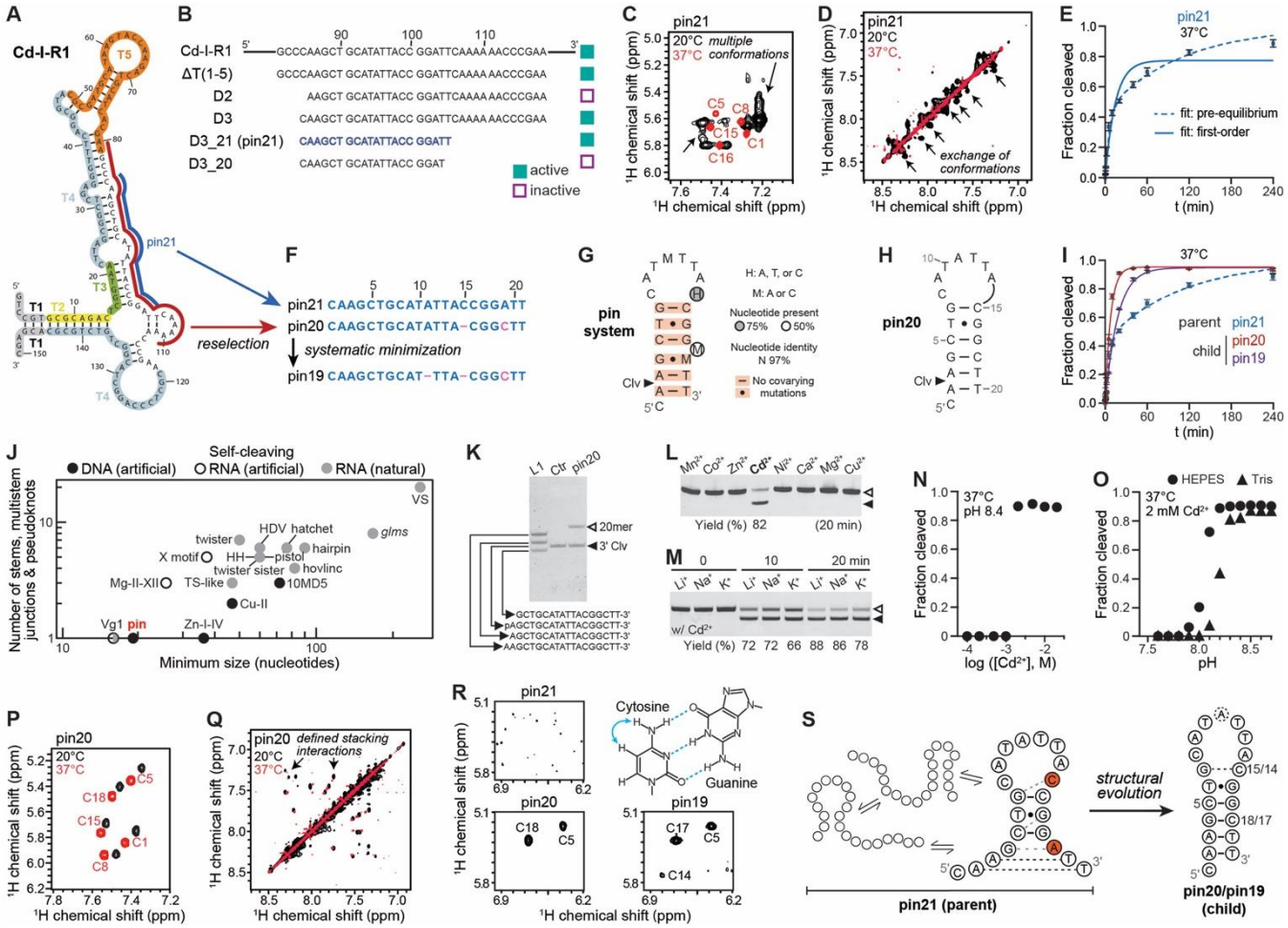

Figure 9: *In vitro* selection, systematic truncation, and rational reselection identify three pin deoxyribozymes with different structural features. A: Schematic of Cd-I-R1 identified through *in vitro* selection. **B:** Central constructs used in systematic truncation, including elements labelled in A **(Supplement 25). C, D:** Fingerprint NMR spectra of pin21 (C/D: TOCSY/NOESY spectra, respectively) showing the presence of exchanging conformations at 20°C (black) and lack of structural elements at 37°C (red). **E:** Cleavage activity of pin21 deviating from first-order kinetics. **F**: Comparison of pin constructs obtained before (pin21) and after rational reselection (pin20), and subsequent minimisation (pin19). **G, H:** Central elements of the pin system (G) and pin20 (H) (arrowheads point to cleavage (clv) site). **I:** Activity of different pin constructs at 37°C. **J:** Size and structural complexity of pin and other self-cleaving nucleic acids. HDV: hepatitis delta virus. HH: hammerhead. VS: Varkud satellite. **K:** All pin variants cleave the 3' phosphorester bond between the 2nd and 3rd nucleotides. L1: a 17-19mer DNA ladder. Ctr: an 18mer DNA with 5' phosphate (p) modification. Hollow and filled arrowheads point to the full length and 3' cleavage product of pin20, respectively. L: Cd^{2+} is required and the only identified potent metal ion cofactor (2 mM of each metal ion was used). **M:** The tested monovalent metal ions (100 mM) have negligible effects on pin20 activity. **N, O:** Dependence of cleavage activity on Cd^{2+} concentration (N) and pH (O). **P, Q:** Fingerprint NMR spectra of pin20 (P/Q: TOCSY/NOESY spectra, respectively) showing homogenous conformation at 20 °C (black) and defined structural elements at 37°C (red). **R:** NMR peaks recorded at 20°C, indicative of stable Watson-Crick base pairing (as shown in the schematic), are detected for pin20 and pin19 but not pin21. **S:** Schematic model of structural features of different pin variants. Central sequence differences linked with potential differential base pairing patterns between pin21 and pin20 are highlighted in red. While pin21 displays a high level of structural heterogeneity, structural evolution favoured a better-defined hairpin arrangement of pin20 and pin19.

Excitingly, the largely reduced size of the identified autohydrolytic 21nt DNA sequence renders pin21 an ideal target for structural characterisation via high-resolution NMR. Indeed, our data confirm decent NMR-spectral features that allow resonance assignments and enable first atomistic insights into pin21's molecular architecture **(Figure 9C and D)**. Surprisingly, the central structural features appear to be the presence of multiple conformations in slow

exchange at 20°C and a low amount of defined structural elements, including the absence of stable H-bonds and/or detectable Pi-Pi stacking at 37°C, which is in accordance with structure prediction by common algorithms (Zuker, 2003, Markham and Zuker, 2005) **(Supplement Figure 25,** Figure **26).** More detailed analysis of the pin21's reaction kinetics reveals strong deviation from expected first-order kinetics and suggests the presence of a pre-equilibrium reaction **(Figure 9E),** which is consistent with the conformational heterogeneity and exchange processes observed via NMR. We hypothesise that the observed conformational plasticity may limit pin21's activity due to extensive sampling of inactive states and that a sequence with better-defined structural features may exist that could possess superior catalytic activity. This motivated us to perform a rationally designed reselection to further optimise the system.

2.2.3 Systematic construct optimisation identifies more active and smallest known self-cleaving deoxyribozymes

Following a similar methodology as in the first selection process, we performed reselection using a DNA library focusing on degenerate sequences of the minimal functional unit around pin21 **(Figure 9A, red)**. This second selection process revealed the existence of 18 highly conserved nucleotides and the absence of covariations along possible base pairing **(Figure 9F, G and H)**. In silico analyses via *mfold* and *unafold* (Zuker, 2003, Markham and Zuker, 2005) predict the presence of a 6 bp stem for most sequences in the reselected pool (G4), resulting in a hairpin model of pin **(Figure 9G)**. The reselection particularly identifies a 20 nt variant (pin20) as a prototypical representative of the predicted hairpin conformation **(Figure 9F–H)**.

In contrast to the parent (pin21), the child generation (pin20) largely follows first-order kinetics and shows increased cleavage activity **(Figure 9I)**, implying a success in reselection of better-defined and more active variants. Subsequent comprehensive mutagenesis and deletion screens suggest that further deletions in the sequence are only possible with considerable drops in activity **(Supplement Figure 28).** While no active 18 nt sequence was found, the deletion of A11 in pin20 had the least effect on activity; this sequence was named pin19 **(Figure 9F)**. Under the standard conditions used, pin19 still follows first-order kinetics but hydrolyses 1.9-fold slower than pin20 **(Figure 9I).**

The minimum length of 19 nt and the presence of a maximum of one stem make the pin constructs the smallest and simplest of all known self-cleaving deoxyribozymes (Carmi et al., 1998, Chandra et al., 2009, Xiao et al., 2011b, Dokukin and Silverman, 2012, Velez et al., 2012, Xiao et al., 2012, Gu et al., 2013, Zhang et al., 2021). It is also smaller and simpler than all known self-cleaving ribozymes in nature (Fedor, 2009, Roth et al., 2014, Weinberg et al., 2015, Chen et al., 2021, Zhang et al., 2024), and only a few nucleotides longer than the

smallest lab-designed self-cleaving ribozyme, the minimal Vg1 (Kazakov and Altman, 1992) **(Figure 9J)**. However, at a comparably small size, pin deoxyribozymes are 3–4 orders of magnitude more active than Vg1 ribozymes (Bombard et al., 1998, Kuo and Herrin, 2000).

2.2.4 Pin constructs share a common cleavage mechanism

All three pin constructs have identical cleavage sites and produce the same cleavage products, pointing to hydrolysis of the 3′ phosphoester bond between the 2nd and 3rd nucleotides (ApA) as a common cleavage mechanism **(Figure 9K, Supplement Figure 29)**. Focusing on the pin20 variant as a prototypical pin sequence **(Figure 9G, H)**, subsequent biophysical and biochemical characterisations showed that the deoxyribozyme has a strong preference for Cd^{2+} as cofactor **(Figure 9L)**. Inhibiting or auxiliary roles of other metal ions were not observed under the tested conditions **(Figure 9M).** At pH 8.4, pin20 displayed full activity with (or above) 2 mM Cd^{2+} and no activity with (or below) 1 mM Cd^{2+}; at 2 mM Cd^{2+}, the pH activity profile further identifies a narrow transition range with abolished activity below pH 7.9 and full activity above pH 8.2 **(Figure 9O)**. Collectively, pin20 has sharp requirements regarding minimal Cd^{2+} concentration and pH, which coincide well with reaction conditions near the critical point of $Cd(OH)_2$ precipitation.

2.2.5 Reselection guides the structural evolution of hairpin conformation

The child generation of the pin system (pin19/20) evolved from the pin21 precursor during reselection, exhibiting enhanced cleavage activity and an apparent shift in reaction kinetics from pre-equilibrium to first-order behaviour **(Figure 9I)**. This observation is well in line with our hypothesis that pin21's activity is restricted by conformational heterogeneity and excessive sampling of inactive states. In order to see what effect the reselection had on the pin's molecular architecture, we carried out a comparative NMR characterisation of the respective variants. Our data identify a general increase in structural elements for all members of the 'child' generation (pin20, pin19) **(Figure 9P, R, Supplement Figure 30, Figure 31).** In comparison to pin21, pin20 shows highly deviating spectral features, which are largely conserved in its related pin19 variant (**Supplement Figure 30, Figure 31).** For both variants, a strongly increased level of Pi-Pi stacking interactions between neighbouring nucleotides is observed at 37°C **(Figure 9Q)**. Interestingly, a homogenous conformation and stable hydrogen-bond formation are also detected at lower temperatures (20°C) **(Figure 9P and R)**. Except for the absence of a stable base pairing between pin20's G7-C15 (present for pin19's G7-C14), the observed hydrogen-bond formations are consistent with the predicted hairpin conformation **(Figure 9H)**. Thus, it appears that structural heterogeneity is reduced in all

members of the child generation and that pin20 and pin19 have evolved to a better-defined hairpin conformation **(Figure 9S)**.

2.2.6 The hairpin structure is not the active conformation

To obtain more detailed mechanistic insights into the catalysis reaction at the atomistic scale and in real-time, we acquired a series of NMR spectra after the addition of 2 mM Cd^{2+}. Making use of the structural similarities but NMR-favourable slower reaction rates, pin19 was selected for the real-time NMR experiments. The time-resolved data reveal that Cd^{2+} binding is fast and predominantly involves the four guanine nucleotides in the sequence **(Figure 10A and B)**. The cleavage reaction itself occurs from the Cd^{2+} equilibrated state at a much slower rate than the detected Cd^{2+} binding **(Figure 10A, vertical arrows)**. The observed Cd^{2+} binding pattern **(Figure 10B and C)** does not correlate well with the hairpin structure, which is consistent with the general lack of features required for catalysis in the hairpin arrangement. More detailed analysis of the real-time NMR data further suggests that, in addition to the expected effects on the direct proximity of the cleavage site (A2 and A3), predominantly G16 and G17 are affected by the autohydrolysis reaction, shadowing the time-dependent changes at the cleavage site **(Figure 10D and E)**. All other resolved nucleotides show only subtle or no changes during the reaction **(Figure 10D and E; Supplement Figure 32),** suggesting that the post-catalytic state shares the overall structural features with the uncleaved Cd^{2+} equilibrated state **(Figure 10C and E)**. Again, this observed behaviour is not compatible with the hairpin structure (that would, e.g., also affect the base-pairing partners T19 and T20). Our data hence show that the reselection process essentially favoured an increased population of an inactive conformation.

2.2.7 The pin system is highly thermophilic and operates without a classical structural framework

The pin's activity appears to be limited by conformational 'oversampling' at higher temperatures and an 'enthalpic trap' that favours a distinct yet inactive hairpin conformation at lower temperatures. Intriguingly, elevated temperatures should help to overcome the enthalpic trap and accelerate conformational sampling, thereby, in theory, fostering increased activity.

Excitingly, we indeed observe a strong increase in cleavage activity at very high temperatures **(Figure 10F)** with k_{obs} values of 10.1 and 6.0 min^{-1} or half-lives of 4 and 7 s at 90°C for pin20 and pin21, respectively. NMR analysis shows that no tested pin construct maintains detectable structural elements at 60°C **(Supplement Figure 33),** suggesting that the pin systems catalyse autohydrolysis in the absence of a classical structural framework. This is very atypical for enzymatic processes that generally rely on structural scaffolds, which is, e.g., also seen for a previous class of autohydrolytic deoxyribozymes (Zn-I) (Gu et al., 2013, Zhang et al., 2021),

which loses its activity at 90°C likely due to thermal unfolding of the active conformation **(Figure 10G)**.

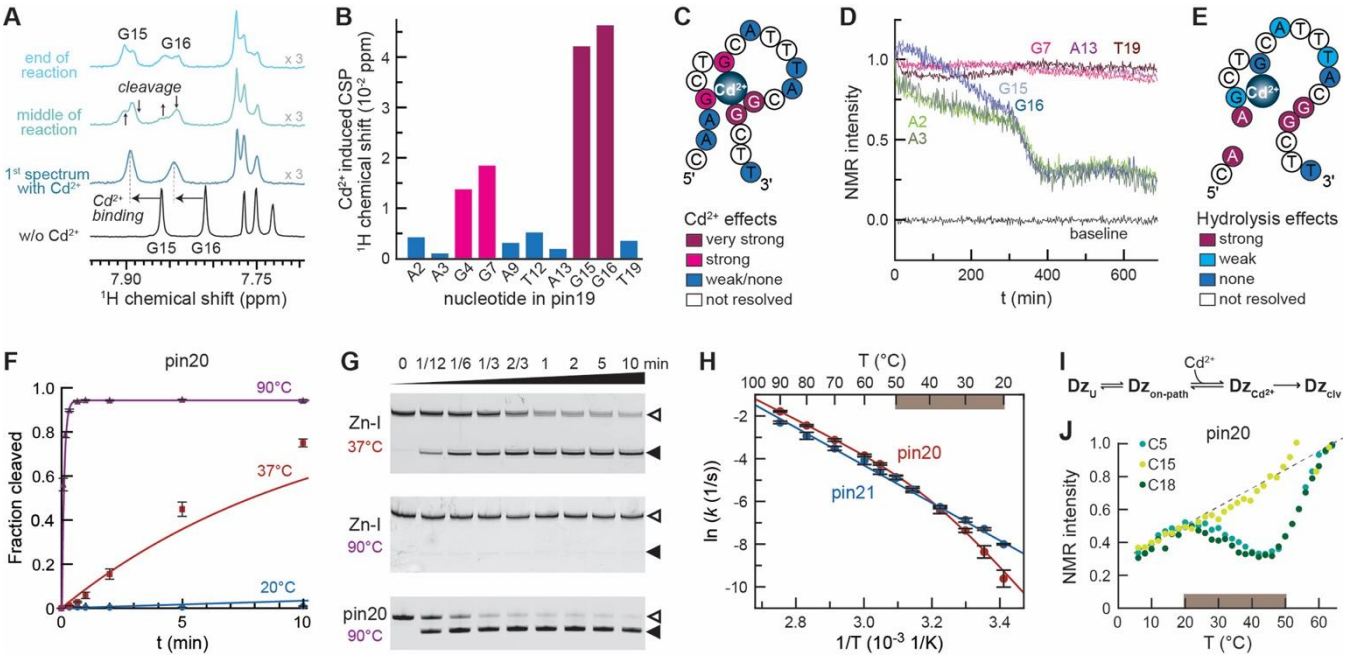

Figure 10: The pin system involves all four guanines in cofactor binding and operates without a classical structural framework, rendering it highly thermophilic. (A-E) Real-time NMR experiments into the cleavage mechanism. **A:** ^{1}H NMR spectra of pin19 before addition of Cd^{2+} (black), directly (4 min) after addition of 2 mM Cd^{2+} (blue), and at two additional time points (green=middle of reaction; light blue=end of reaction). **B:** Chemical shift perturbations (CSP) induced by Cd^{2+} binding along the pin19 sequence (only resolved nt are shown). **C:** Mapping of Cd^{2+} CSPs on a matching schematic model of pin19. **D:** Time course of normalised NMR signal intensities for indicated nucleotides after addition of Cd^{2+}. Nucleotides that are strongly affected as well as not-affected nucleotides were selected **(see Supplement Figure 32, for all resolved signals; baseline=noise level signal)**. **E:** Mapping of nucleotides affected by the cleavage reaction. **F:** Temperature-dependent activity of pin20. **G:** Unlike the Zn-I class of deoxyribozymes, pin20 is highly thermophilic. **H:** Arrhenius plot of temperature-dependent cleavage activity (k) of pin20 (red) and pin21 (blue). Curved Arrhenius characteristics for pin20 are found predominantly in the temperature range of 20–50 °C (brown rectangle). **I:** Kinetic model of different states involved in pin20 catalysis (DzU=unproductive state, $DzCd^{2+}$=Cadmium-bound precatalytic state). The respective model was used to fit the Arrhenius plots (see supplementary information for more details). **J:** NMR-based site-resolved thermal unfolding analysis of pin20 reveals dissociation of base-pairing involving C5 and C18 in the temperature regime exhibiting curved Arrhenius behaviour (brown rectangle). In contrast, and consistent with the hairpin model of pin20, C15 does not exhibit any detectable temperature-induced structural changes.

Given that a classical structural scaffold is not required for pin activity, it appears counterintuitive that structural evolution in general, and selection of a better-defined unproductive state in particular, is associated with increased activity. To resolve this dilemma, we carried out a more detailed analysis of the temperature-dependent activity in the form of an Arrhenius plot. The data confirm that pin20 and pin21 are both highly thermophilic with continuously increasing activity at elevated temperatures **(Figure 10H).**

A striking feature of the Arrhenius plot is a pronounced curvature in the case of pin20, which is not observed for pin21 **(Figure 10H)**. Notably, curved Arrhenius plots have also been observed for ribozymes and have been attributed to the occurrence of an unproductive state (Dz_U), not capable of substrate cleavage (Peracchi, 1999). Indeed, this model can be

transferred to the pin system and allows proper fitting of the experimental data **(Figure 10H)**. It appears plausible, that the inactive hairpin conformation identified for pin20 at lower temperatures represents Dz_U. While inactive on its own, we speculate that the hairpin conformation may facilitate transition to a conformation, which, in combination with Cd^{2+}-binding, adopts a cleavage-competent conformation. In this picture, Dz_U serves as an optional pre-scaffolding step towards the on-pathway conformation $Dz_{on\text{-}path}$ **(Figure 10I)**. Site-resolved NMR thermal denaturation experiments (Borggräfe et al., 2022) are well in line with this picture **(Figure 10J, C5, C18)** and, e.g., show that the base pairing found in the hairpin conformation undergoes conformational exchange in a temperature regime that matches the curved area of the Arrhenius plot **(Figure 10H and J brown box)**. In this regard, it is important that the hairpin structure is not too stable and the structural evolution would be guided by favourable transitions to an 'on-pathway' conformation close to the selection temperature (37°C). This could also explain the small size of the pin system that will generally only allow for a limited number of base-pairing contacts associated with dynamic equilibria between the occurring states over a wide temperature range, while preventing too high energy barriers between Dz_U and $Dz_{on\text{-}path}$ at lower temperatures. Specific modification interfering with the base pairing features of the pin system supports this model **(Supplement Figure 32, M5–6, M13–15)**. The additionally observed GC-pairing in pin19 may thus also be the origin of the lower activity as compared to the less restrained pin20.

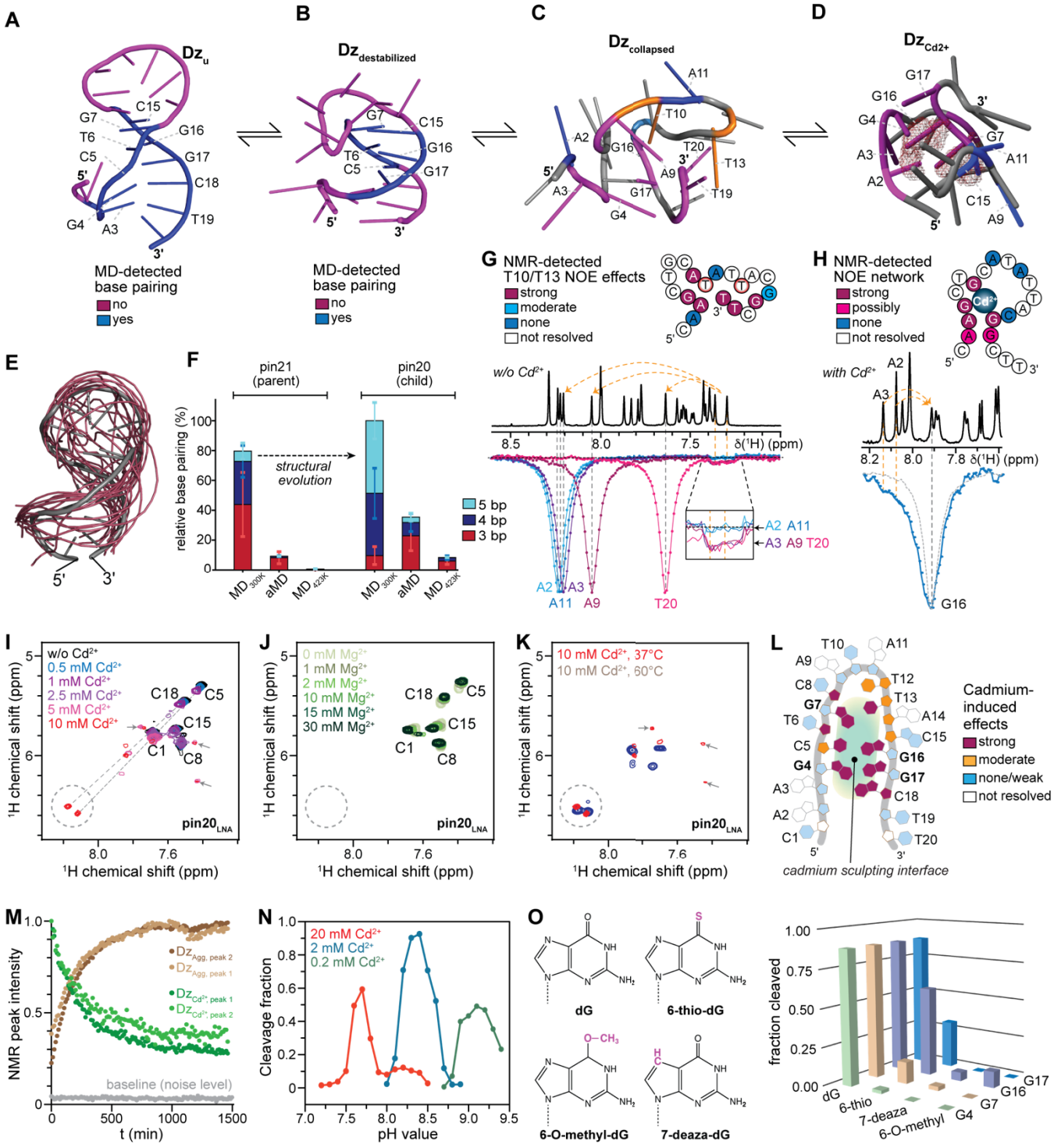

Figure 11: Pin's mode of action is based on conformational plasticity and activation by Cd^{2+}. (A-D) Representatives of MD cluster analysis. **A:** Hairpin conformation comprising a stem with at least four base pairs. **B:** Destabilised hairpin conformation forming a stem with three or fewer base pairs. **C:** Collapsed conformation comprising a compact architecture. **D:** Putative Cd^{2+}-activated conformation, showing a compact core with distinct Cd^{2+} interactions indicated as red mesh. The DNA colour code in C+D refers to NMR results shown in G and H, respectively. **E:** Ensemble representation of the hairpin cluster. **F:** Base-pairings as seen in the indicated MD simulations. **G:** CEST NMR profiles for selected nucleotides recorded on pin20 in the absence of Cd^{2+}. Characteristic signal drops for distinct nucleotides, associated with T10/T13 signals, are highlighted. Orange arrows indicate respective NOE contacts consistent with the observed signals. Affected nucleotides are mapped on the shown schematic model as well as on the MD conformer shown in (C). **H:** Selected CEST profiles for pin20LNA in the presence of Cd^{2+} **(see Supplement Figure 34 for more data and discussion).** Affected nucleotides are mapped on the shown schematic model as well as on the MD conformer shown in (D). **I:** Effects of increasing levels of Cd^{2+} as seen by 2D $^{1}H,^{1}H$ TOCSY NMR (fingerprinting region) recorded on pin20LNA at 37°C and indicated concentrations of Cd^{2+}. **J:** Same as in (I) but using Mg^{2+} at the indicated concentrations. **K:** NMR comparison of

high cadmium conformation at 37°C and 60°C. **L:** Mapping of cadmium-induced CSPs. Note that each nucleotide is separated in effects related to spins in the nucleobase or the sugar region; the drawn schematic depicts only one possible arrangement consistent with the data. **M:** Real-time NMR data following cadmium-induced DNA co-precipitation at 10 mM $CdCl_2$, pH 8.8, T=60°C. N: Analysis of pH-dependent cleavage activity of pin20 at different $CdCl_2$ concentrations. **O:** Activity screen of pin20 containing a single substitution of all four guanine positions with indicated chemical modification

2.2.8 The pin's conformational ensemble comprises distinct states susceptible to structural evolution

The developed kinetic model **(Figure 10I)** contains four distinct states, i.e. Dz_U, $Dz_{on\text{-}path}$, Dz_{Cd2+}, and Dz_{clv}. While Dz_U could be associated with the pin's hairpin conformation, we set out to confirm occurrences and structural features of the postulated states via a combination of molecular dynamics (MD) simulations and chemical exchange saturation transfer (CEST) NMR. To assess the conformational plasticity and thermophilic properties of the pin system, all-atom unbiased MD simulations at high (MD_{432K}) and low (MD_{300K}) temperatures as well as enhanced sampling accelerated MD (aMD) simulations were used Cluster confirms the presence of the hairpin structure as a dominant conformation of pin20 **(Figure 11A)**. Furthermore, guided by the NMR data (vide infra), additional cluster are identified that resemble different conformational states including (i) a destabilized hairpin conformation ($Dz_{destabilized}$) characterized by reduced base paring interactions at the ends of the stem region **(Figure 11B)**, (ii) a collapsed conformation ($Dz_{collapsed}$) characterized by inward-oriented ends and a compact arrangement without classical base pairing **(Figure 11C)**, and (iii) a putative (pre-)activated conformation (Dz_{Cd2+}) characterized by a compact core stabilized via Cd^{2+} interactions in proximity to the cleavage site involving nucleotides A2, G7 and A11-G16 **(Figure 11D)**. In general, the MD data confirm the high molecular plasticity of the pin system and allow to better define the expected conformational space of the respective states. In this regard, even the ensemble representation of the putatively best-defined hairpin conformation reveals a high level of structural heterogeneity under the applied conditions **(Figure 11E)** that is further amplified in the other, less restricted, states.

The MD data also allow more quantitative insights into the pin's base pairing interactions **(Figure 11F)**. Comparison between pin20 (child generation) and the pin21 parent identifies effects associated with the reselection process. The data reveal a child generation with an increased population of the stabilised hairpin structure, accompanied by a reduction of other states at lower temperatures. This is well in line with the observed curved Arrhenius plot present for pin20 and not pin21 **(Figure 11H)**, suggesting that the occurrence of five base paring interactions is particularly detrimental to. Interestingly, data from broader sampling with aMD and MD at higher temperatures further suggest that the structural evolution essentially favoured a destabilised hairpin conformation, such as depicted in **Figure 11B**.

2.2.9 Structural plasticity guided by cadmium-induced scaffolding determines the catalytic capabilities of the pin system

The involved states and associated structural plasticity were further characterised via CEST NMR. Selective optimised proton experiments (SELOPE) (Schlagnitweit et al., 2018a) focusing on the H5 and H6 nucleobase region were used to reduce relaxation effects and resolve spectral overlap in the not-isotope-enriched samples. First, pin20 was investigated in the absence of Cd^{2+} to obtain insights into the starting structure of the on-pathway cleavage reaction ($Dz_{on\text{-}path}$). The resulting CEST profiles do not show classical frequency exchange contributions under the applied conditions, but reveal distinct signal drops for selected nucleotides **(Figure 11G)**. The observed signal attenuations are indicative of nuclear Overhauser effects (NOEs) between the affected nucleotides and T10 and T13 (H6) that would require their close spatial proximity. **(Figure 11D, Supplement Figure 34 for control experiments).** Mapping the affected nucleotides is well consistent with a collapsed conformation **(Figure 11G)** sharing central features with the respective MD cluster **(Figure 11C).** Thus, in the absence of Cd^{2+}, the unproductive hairpin conformation of pin20 appears to be in exchange with this collapsed conformation (representing $Dz_{on\text{-}path}$ in **Figure 10I**).

To be able to record a set of experiments in the presence of Cd^{2+} requires stabilisation of the cleavage site. Screening different chemical modifications reveals that a locked nucleic acid substitution (LNA) at position A2 effectively prevents Cd^{2+} induced cleavage **($pin20_{LNA}$, fig. Supplement Figure 35A and B)**. Notably, a phosphorothioate (PS) modification at the cleavage site, which prevents Zn^{2+}-mediated cleavage of Zn-I deoxyribozymes **(Supplement Figure 35C)** (Gu et al., 2013, Zhang et al., 2021), does not prevent cleavage of pin20, in line with the thiophilic character of Cd^{2+}.

SELOPE-CEST data on $pin20_{LNA}$ in the presence of 1 mM Cd^{2+} do not show the T10/T13 signal drops associated with the collapsed conformation **(Figure 11G and H, Supplement Figure 34)**, indicating that Cd^{2+} indeed stabilises a different conformation **(i.e. Dz_{Cd2+} in Figure 10I)**. More detailed analysis reveals distinct NOE interactions between G17 and A3 **(Figure 11H)**, which is well consistent with the real-time NMR data showing a synchronised transition of both nucleotides **(Figure 10A, B, C and D) (Figure 11D, Dz_{Cd2+})**. The data confirm the central role of cadmium in reshaping the structural features of the pin system.

To better understand these effects, NMR-titration experiments using LNA-stabilised pin variants were carried out. The data reveal that at low Cd^{2+} concentrations ($\leq$ 1 mM), transient binding with fast exchange kinetics induces moderate chemical shift perturbations (CSPs) **(Figure 11I)**. Increasing the Cd^{2+} concentration above 1 mM leads to substantial peak disappearances, indicative of stronger interactions and intermediate exchange processes that coincide with the required Cd^{2+} concentration for autohydrolysis **(Figure 11N)**. Further

increased Cd^{2+} level (5 mM or higher) leads to the appearance of a new set of peaks at very unusual frequencies, indicative of strong interactions and/or Cd^{2+} induced effects **(Figure 11I, grey circle)**. Noteworthy, Mg^{2+} is not able to reproduce the conformational scaffolding carried out by Cd^{2+} **(Figure 11J)**. At elevated temperatures (60°C, 10 mM Cd^{2+}), the characteristic Cd^{2+}-scaffolding remains present (**Figure 11K**, grey circle**,** presumably the on-pathway conformation), while peaks indicative of heterogeneous conformations disappear (**Figure 11K**, grey arrows, presumably off-pathway conformations). The data provide strong evidence that, even in the absence of classical structural features, the cadmium binding and its associated effects on the DNA are highly thermostable.

The unusual CSPs indicate strong interactions of Cd^{2+} affecting the electronic structure of the respective nucleobase regions. More detailed analysis reveals an elongated interface comprising nucleobase and sugar moieties that experience the strongest Cd^{2+} induced effects **(Figure 11L, Supplement Figure 37)**. Our data show similar behaviour between all tested pin constructs, indicating that the Cd^{2+} affinity and binding mode are similar in the different variants **(Supplement Figure 36)**.

Overall, the high number of strictly conserved nucleotides paired with the high number and distribution of atoms that experience strong Cd^{2+} induced CSPs indicate that more than one cadmium atom may provide the scaffold to align a specific, but presumably collapsed and disordered, DNA sequence in a catalytically competent conformation **(Figure 11L, Supplement Figure 37)**.

2.2.10 Pin activity correlates with the formation of polynuclear cadmium complexes and cadmium interaction with all four guanines

Noteworthy and in line with previous reports on other systems (Ma et al., 2016, Moon et al., 2021), we observe precipitation in all samples crossing the conditions inducing formation of polynuclear cadmium hydroxide ($Cd_n(OH)_m$) complexes (defined by the pH and $CdCl_2$ concentration). A DNA co-precipitation under these conditions can be clearly seen in real-time NMR experiments **(Figure 11H)** and obstructs detailed NMR characterisations of the high-cadmium state. Still, 2D NOESY data recorded at 10 mM $CdCl_2$ reveal two key features of the Cd-sculpted on-pathway conformation, i.e., (i) a small subset of NOE correlations is present, suggesting that only a part of the pin sequence is ordered, and (ii) the respective NOE network involves the above-described unusually strong affected spins **(Figure 11K, grey circle)** that are likely associated with the base region of C5 and C18.

Based on our observations and our initial assumption that the pin and similar systems operate near the precipitation condition of their metal ion cofactor, it is tempting to speculate that a

polynuclear cadmium complex, rather than a single or multiple isolated Cd^{2+} ions, acts as the cofactor of catalysis. Measuring pH-dependent activity profiles at three different $CdCl_2$ concentrations supports this view **(Figure 11B, Supplement** Figure **39)**. The data suggest that formation of a polynuclear cadmium complex (that is, depending on the pH and $CdCl_2$ concentration) and not the pKa of a functional base (that is independent of $CdCl_2$ concentration) is the origin of the strong pH dependency. In this regard, an initial $Cd_n(OH)_m$ nucleation step could also explain the often observed sigmoidal contributions observed in respective reaction kinetics **(e.g., Figure 10D or Figure 12G)**.

While deprotonation of a functional guanine appears unlikely as the sole catalytic element, the four guanines still seem to be the central elements in cadmium interaction **(Figure 10B and C, Figure 11L)**. Indeed, individual chemical modifications of either N7 or O6 at each of the four guanines can reduce pin activity. In particular, modifications that prevent Cd^{2+} coordination to the guanine's functional groups (as in 7-deaza-dG or 6-O-methyl-dG) show very strong effects, while 6-thio-dG modifications that still support Cd^{2+} interactions have only moderate effects. The data strongly suggest that the nucleobase region of all four guanines is involved in direct Cd^{2+} interactions, which in turn is essential for catalysis. For the latter, all guanines are important, but G4 and G17 appear to be essential **(Figure 11I, Supplement** Figure **39)**.

Combining this data with the structural insights obtained above, we propose that pin operates via cadmium-induced structural alignment of a disordered but specific DNA sequence. The driving force of this alignment is most likely a distinct polynuclear cadmium complex that is recruited by all four guanines. The high nucleotide conservation among the pin sequences, paired with the CSPs identified for a larger number of nucleobase and sugar moieties, further highlights the involvement of an extended but specific set of functional groups provided by the DNA. We further propose that the pin system is the first (DNA) enzyme that, on its own, does not form an active site via a classical structural framework. Instead, the initial (on-pathway) state largely resembles an intrinsically disordered DNA sequence that is aligned by its essential cadmium cofactor in a very selective and sequence-specific manner. The absence of a classical structural framework in combination with pronounced structural plasticity and the potential role of polynuclear metal-hydroxide cofactors may broaden our view of the fundamental aspects orchestrating DNA-mediated catalysis.

2.2.11 Rational selection identifies pin variants with increased activity

Our mechanistic insights suggest that the reselected pin child generation (pin19/20) has evolved from pin21 by reducing the number of off-pathway conformations, favouring one single unproductive hairpin conformation. Based on this data, we speculate that the reselection pool may contain sequences that underwent structural evolution but are less confined by the

formation of the hairpin conformation. Indeed, rational evaluation of the reselection pool identifies a small number of variants comprising sequence modifications in their 3' end that are associated with weakening of the hairpin conformation **(Figure 12A)**. These variants cover about 1–2% in the G4 pool used to build the consensus model in **Figure 9** and thus would normally stay hidden. NMR characterisation of three representatives (pin22, pin23, and pin24) and MD simulations of pin23 **(Figure 12B, Supplement Figure 40)** corroborate a destabilisation of the hairpin structure and a general reduction of conformational heterogeneity. Excitingly, all rationally selected pin sequences also display first-order kinetics, suggesting that structural evolution also reduced the oversampling of inactive states **(Figure 12C)**. Furthermore, all variants showed a considerably increased activity as compared to pin20 (k(37°C, pin22/pin23/pin24)=0.40/0.29/0.24 min^{-1}, respectively; k(37°C,pin20)=0.10 min^{-1}), which indeed corroborates our speculation that destabilising of the hairpin can increase activity of the system.

Overall, we conclude that, guided by our structural and mechanistic insights, we could optimise the pin system by structural evolution that reduced excessive oversampling of off-pathway conformations, and rational selection of variants that are not confined by an unproductive hairpin conformation.

2.2.12 The pin system provides useful additions to the DNA toolbox

Motivated by its inherent features, we finally explored potential applications that should particularly profit from the unique design and mechanism of the pin class of deoxyribozymes. Unlike all previously discovered self-cleaving deoxyribozymes (for example, the class I Zn^{2+}-dependent (Zn-I) DNA) (Gu et al., 2013, Zhang et al., 2021), the pin class does not rely on a stable globular structure for activity, and additionally, it hydrolyses near the 5′ end of the construct rather than deeply inside, which in principle enables efficient autoseparation of the cleavage fragments at a wide temperature regime **(Figure 12E)**. Comparative analysis confirmed that under the tested reaction conditions (37°C), pin class deoxyribozymes displayed high yields in both cleavage and fragment dissociation, while in Zn-I class, a strong stem was a prerequisite for complete activity, but then the stem became an obstacle to efficient separation of the cleavage fragments **(Figure 12E, F and G)**. This distinctive feature of the pin class makes it a powerful dismantling tool that can be switched on by specific ions and can be of potential use in dynamic DNA nanotechnology and biotechnology (Praetorius et al., 2017, Wang et al., 2017, Jia et al., 2021, Li et al., 2021). As a proof of concept, we inserted a pair of pin deoxyribozyme sequences into a long single-stranded circular DNA scaffold such that two DNA origami shapes (a rectangle and a trapezoid) were assembled from the scaffold and interleaved with pin deoxyribozymes **(Figure 12H)**. Atomic force microscopy (AFM) clearly

showed these two shapes connected together, and upon the addition of Cd^{2+} at 30°C, they separated from each other due to the cleavage of both deoxyribozymes **(Figure 12H).** A yield of >75% in shape separation was observed by AFM, suggesting the robustness of pin deoxyribozymes.

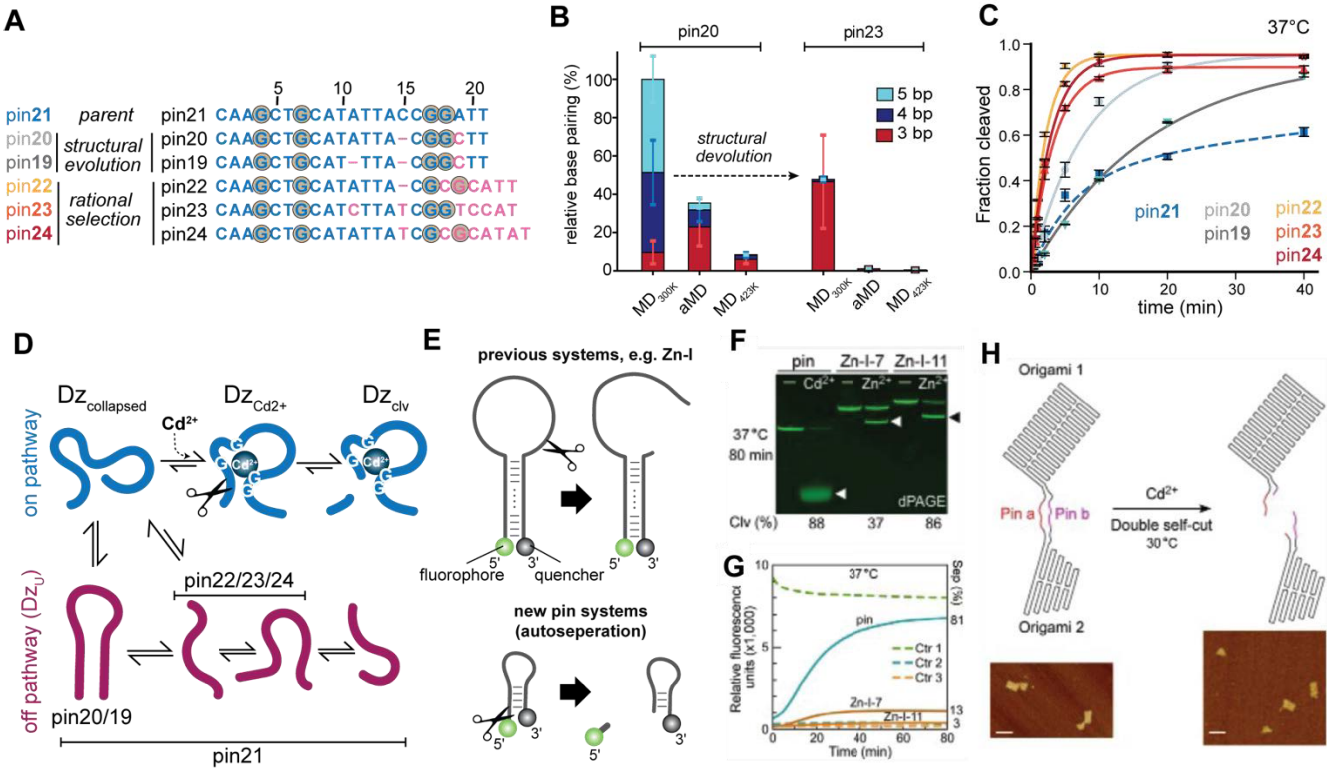

Figure 12: Rational reselection identifies the most active variants, and self-cutting of pin deoxyribozymes leads to efficient autoseparation of the cleavage products. A: Sequence comparison of rational reselected pin variants pin22, pin23, and pin24. **B:** Base-pairings in pin20 and pin23 as seen in the indicated MD simulations. **C:** Cleavage activity of respective pin variants. **D:** Proposed model of the central states sampled by the pin system. While the different variants share common on-pathway states, they differ in the population of their off-pathway (unproductive) states. **E:** Schematics highlighting the central molecular differences between the previously known DNA self-cutters (here Zn^{2+}-I(8)) and the pin deoxyribozymes. Scissors symbols point to the cleavage sites. **F:** Analysis of the self-cleavage of pin and Zn-I deoxyribozymes by dPAGE. Samples were incubated without (—) or with the corresponding metal ions (Cd^{2+} or Zn^{2+}) at 37°C for 80 min. Two Zn-I constructs were tested, one with seven base-pairs in the stem (Zn-I-7) and the other with eleven (Zn-I-11). Cleavage (Clv) yields are listed at the bottom. **G:** Monitoring the separation (Sep) of the cleavage products of pin and Zn-I deoxyribozymes in the reaction buffer. Fluorescent signals of the DNA samples were recorded over 80 minutes of incubation at 37°C. The used controls are: Zn-I-11 DNA without quencher (Ctr 1), pin20 in the absence of Cd^{2+} (Ctr 2) and Zn-I-11 in the absence of Zn^{2+} (Ctr 3). **H:** Reconfiguration of DNA nanostructures controlled by a pin-based switch. A pair of pin DNAs (pin a&b) was inserted into a circular ssDNA scaffold such that the two DNA nanostructures (origami 1&2) were assembled from the scaffold and interleaved with pin deoxyribozymes. Upon the addition of Cd^{2+}, the relative position change (separation) of the two origami structures due to pin DNA self-cleavage was confirmed by AFM. Scale bar: 100 nm.

2.3 Conclusion

Our discovery of the minimalistic pin deoxyribozyme class represents a paradigm shift in the understanding of DNA catalysis. Unlike conventional DNA catalysts, pin deoxyribozymes achieve efficient self-cleavage without relying on a stable inherent structural framework. Instead, they depend on the dynamic interplay between the pin's conformational plasticity and the cadmium cofactor. This interplay enables the cadmium-induced transition of a largely disordered DNA sequence to a catalytically active conformation that forms around the cofactor. We show that reduction of excessive sampling of off-pathway conformations via structural evolution, as well as rational selection of destabilised states, can facilitate the transition to catalytically competent states. Consequently, the remarkable robustness of pin deoxyribozymes at high temperatures becomes understandable.

The minimal size and high catalytic activity of pin deoxyribozymes address longstanding challenges in the structural and mechanistic studies of DNA catalysts. Furthermore, they hold significant potential for practical applications. As demonstrated in this study, their ability to efficiently dissociate cleavage products underscores their utility in dynamic DNA nanotechnology. Additionally, their capacity to operate across a wide temperature range, up to 90°C, highlights their promise for innovative DNA editing applications, such as programmable self-cleavage of double-stranded DNA. Future research exploring alternative cofactors, sequence variations, and reaction conditions adapted to physiological environments will further enhance the versatility and utility of these catalysts, solidifying their position in the expanding toolkit of nucleic acid-based technologies.

2.4 Materials and Methods

2.4.1 NMR data acquisition, processing and analysis

All DNA oligos, including LNA modifications, were purchased from Sigma (HPLC-purified) and are listed in **Table 1**. DNA samples were resuspended in pure water. Samples were measured at DNA concentrations between 90–200 µM in 50 mM deuterated Tris-HCl buffer (Tris-d11, Merck), pH 8.74, 50 mM NaCl and 5 mM $MgCl_2$, 10% (v/v) D_2O. All NMR experiments were recorded with a 200 µl sample volume in a 3 mm NMR sample tube. Experiments were carried out at 20°C, 37°C, and 60°C, using a Bruker spectrometer (Avance III HD+ or NEO), equipped with inverse detection triple-resonance z-gradient cryogenic probes, operating at ^1H frequencies of 700 MHz, 750 MHz, 900 MHz and 1.2 GHz. TOCSY experiments were recorded with an 80-ms mixing time and NOESY experiments with a 300-ms mixing time. NMR data were processed using Topspin 3.6.5 or 4.4.0. Spectra were analysed and plotted using Cara 1.9.1.7, Topspin 3.6.5 or 4.4.0. Data was analysed and plotted using MATLAB R2021a (MathWorks) and matNMR 3.9.94.

Table 1: Used pin sequences.

Oligomer	Sequence 5'-3'
Pin19	CAAGCTGCATTTACGGCTT
Pin20	CAAGCTGCATATTACGGCTT
Pin21	CAAGCTGCATATTACCGGATT
Pin22	CAAGCTGCATATTACGCGCATT
Pin23	CAAGCTGCATCTTATCGGTCCAT

2.4.2 NMR sequential resonance assignment

Resonance assignment of nucleic acid resonances was performed using a combination of ^1H 1D and 2D ^1H-^1H NOESY (Nuclear Overhauser Effect Spectroscopy) and 2D ^1H-^1H TOCSY experiments. The 2D NOESY experiments were used to identify spatially close protons, while the 2D TOCSY provided through-bond correlations within the same residue. Sequential assignment was carried out by identifying matching NOESY cross-peaks between base protons (H6 or H8) and sugar protons (H1', H2', H2'', and H3') within their own and adjacent sugar moieties. TOCSY cross-peaks were used to distinguish between adjacent and own spin systems and to specifically identify cytosine (C) and thymine (T) residues.

2.4.3 NMR titration experiments

Cd^{2+}-titration experiments were performed using 200 µM LNA-stabilised-DNA oligos in 50 mM Tris-HCl buffer pH 8.74, 50 mM NaCl and 5 mM $MgCl_2$, 10% (v/v) D_2O. For the titration experiments, five titration steps (0.5, 1, 2.5, 5 and 10 mM $CdCl_2$) were used by adding 2 µl

aliquots of matching stock solutions. Mg^{2+}-titration experiments were performed analogously with the exception that the initial step did not contain any divalent metal ions.

2.4.4 NMR CEST experiments

SELOPE-CEST experiments were measured at 37°C using the setup and parameters as described. A 25 Hz spinlock was applied for 400 ms; additional sets using a 400 Hz spinlock at 100 Ms were recorded but did not show any additional information (not shown). To obtain the required high spectral resolution and signal-to-noise ratio, each CEST profile was recorded as pseudo-2D with 1024 scans and 227 frequency increments covering the frequency range between 8.92 and 6.68 ppm, leading to a total acquisition time of each pseudo-2D of about 7 days. Data was evaluated with ChemEx and matNMR. The applicable peaks were normalised to their highest peak intensity.

2.4.5 NMR temperature-dependent experiment

TOCSY spectra were recorded at temperatures between 6 and 64°C with increasing temperature in 2°C steps using a Topspin macro. Between each temperature increment, a waiting period of 300 s was applied to allow temperature equilibration. The peak intensity of TOCSY peaks was measured for each temperature step and normalised to the respective maximum peak intensity.

2.4.6 Real-time NMR experiments

Real-time NMR experiments were carried out with 200 µM DNA oligos in 50 mM Tris-HCl, pH 8.74, 50 mM NaCl and 5 mM $MgCl_2$, 10% (v/v) D_2O. The reaction was started by adding either 1, 2, or 10 mM of $CdCl_2$. Before the addition and directly after the addition of $CdCl_2$ ^1H 1D experiment was recorded. Subsequently, a series of 400 ^1H 1D experiments was recorded covering a time period of 12/24h for cleavage/precipitation, respectively.

2.4.7 Oligonucleotides

DNA libraries were purchased from Integrated DNA Technologies, Inc. (IDT, USA), and all other DNA oligonucleotides were synthesised by Generay Biotech Co., Ltd. (Shanghai, China) and Sangon Biotech Co., Ltd. (Shanghai, China). All DNA oligos were purified by 8%–20% denaturing polyacrylamide gel electrophoresis (dPAGE; 8 M urea; acrylamide/bis-acrylamide, 29:1 (w:w), 37.0% (w/v)) and recovered with crush-soak buffer (10 mM Tris-HCl, pH 7.5, 200 mM NaCl, 1 mM EDTA).

2.4.8 Directed evolution and isolation of self-hydrolysing DNAs

To select for novel autohydrolytic DNAs, we chose Cd as a potential cofactor because it is readily attainable and is located in the same IIB group as Zn (a known deoxyribozyme cofactor) in the periodic table. We used a buffer that consisted of 50 mM HEPES, 100 mM LiCl, 5 mM

$MgCl_2$, and 2 mM $CdCl_2$ for selection. The supplementation of Li^+ and Mg^{2+} was expected to provide additional ionic strength to assist the folding of potential deoxyribozymes. According to a solubility-based calculation, we further adjusted the buffer's pH to 8.4 at 23°C so as to approach the critical point of $Cd(OH)_2$ precipitation. To dissolve 2 mM Cd^{2+} in the solution, assume the maximum pH value to be *X*,

$$K_{sp} = [Cd^{2+}] * [OH^-]^2 = (2 * 10^{-3}) * (10^{-(14-X)})^2$$

For $Cd(OH)_2$, at 25°C, $K_{sp} = 2 * 10^{-14}$

$$2 * 10^{-14} = (2 * 10^{-3}) * (10^{-(14-X)})^2$$

$$X = 8.5$$

The selection started with the construction of the 149-nt full-length linear ssDNA pool through primer extension of two half-libraries (~80 nt in length for each library), followed by alkaline (NaOH)-mediated cleavage of the ribonucleotide-containing strand and purification by 8% dPAGE (8 M urea). An 11-base-pair (bp) hybridisation module was also inserted between the 5' and 3' ends of the ssDNA library to ensure high (>75%) circularisation yields and to enhance the library's functional potential as well. CircLigase, an ATP-dependent enzyme, was then used to circularise ~100 pmol linear 149-nt ssDNA library that contains a total of 100 random-sequence positions. The reaction was conducted in a buffer containing 50 mM MOPS, 10 mM KCl, 2.5 mM $MgCl_2$, 2.5 mM $MnCl_2$, 0.05 mM ATP, and 1 mM DTT at 60°C for 4 h. After purification by 8% dPAGE, circular DNA products were incubated with our Cd^{2+}-containing buffer (50 mM HEPES (pH 8.4 at 23°C), 100 mM LiCl, 5 mM $MgCl_2$, and 2 mM $CdCl_2$) at 37°C for 1 h for *in vitro* selection. Hydrolytic scission at any location generated linear DNAs of identical length when separated by 8% dPAGE. These linear DNAs were ligated back to circles by using CircLigase (60°C, 2.5 h), and the recircularised products were recovered again by 8% dPAGE followed by PCR amplification to build the dsDNA library. After alkaline-mediated cleavage (0.25 M NaOH at 90°C for 5 min) of the anti-sense strand that carries a ribonucleotide from the modified primer, the linear ssDNA library was purified out of the dsDNA library by 8% dPAGE for the next round of selection. This iteration was carried on until the library exhibited apparent cleavage signals upon incubation with the selection buffer.

As the selection went on, the incubation time was gradually shortened from 1 h (G1-G9) to 30 min (G10-G12) and then to 5 min (G12-G16) to select for the most active deoxyribozymes. Mutagenic PCR was introduced to the G10 and G11 selection to rapidly bring in more sequence diversity. The G16 DNA population was chosen for high-throughput sequencing. From the G13 population, ~50 clones (pMDTM18-T Vector Cloning Kit, Takara) were also individually sequenced for further analysis.

2.4.9 *In vitro* reselection

In vitro

reselection was performed using a similar strategy as described in *'directed evolution'* above. A 40-nt region slightly expanding over the pin21 sequence of Cd-I-R1 DNA was chosen for sequence degeneration (with a degeneracy of 0.18 for each nucleotide). After supplementation with an adapter sequence, a DNA sequence pool was eventually generated by chemical synthesis, which was then subjected to a 5-step selection protocol similar to that. For the first round of reselection, about 100 pmol of ssDNA pool was utilised for circularisation by CircLigase (60°C, 4 h). The products were separated by 10% dPAGE, and the recovered circular ssDNA pool was incubated in the selection buffer (50 mM HEPES (pH 8.4 at 23°C), 100 mM LiCl, 5 mM $MgCl_2$, and 2 mM $CdCl_2$) at 37°C for 30 min. The cleaved DNAs were then separated by 10% dPAGE and re-ligated by CircLigase (60°C, 2 h) to generate circular DNA templates for PCR amplification to build a dsDNA library. Heating the dsDNA pool in 0.25 M NaOH at 90°C for 5 min rendered the breakup of the anti-sense strand that carries a ribonucleotide from the modified primer, allowing for the efficient purification of the ssDNA library (sense-strand) out of the dsDNA library by 10% dPAGE for the next round of selection.

After 4 rounds of reselection under low stringency (that is, regular PCR and adequate incubation time, the G4 population was subjected to high-throughput sequencing. Under high stringency (that is, mutagenic PCR and harsh incubation time), the reselection continued for 5 rounds. Clones (pMDTM18-T Vector Cloning Kit, Takara) from the G9 population were individually sequenced.

2.4.10 Checking the activity of candidate DNAs

About 5 pmol of the DNA of interest were dissolved in 40 µl of the selection buffer containing 50 mM HEPES (pH 8.4 at 23°C), 100 mM LiCl, 5 mM $MgCl_2$, and 2 mM $CdCl_2$. The samples were then incubated at 37°C for a certain time (a few minutes to 4 hours). The reaction was stopped by adding 40 µl of the loading buffer (90% formamide, 30 mM EDTA, 0.025% bromophenol blue, 0.025% xylene cyanol), and the products were analysed by 8%–20% dPAGE gels.

2.4.11 Mapping the cleavage site of self-hydrolysing DNAs by dPAGE

Approximately 16 pmol of candidate DNA were dissolved in a total volume of 300 µl of the selection buffer to perform the cleavage reaction at 37°C for a certain time (a few minutes to 4 hours). Then the samples were precipitated with ethanol (buffer:ethanol=1:3, v/v) and re-dissolved in 30 µl of deionised H_2O along with 30 µl of loading buffer (90% formamide, 30 mM EDTA, 0.025% bromophenol blue, 0.025% xylene cyanol). Synthetic ssDNAs used as size

markers and controls **(Figure 9K)** were also dissolved in the same loading buffer. About 10 µl of the candidate DNA samples and 1 pmol of synthetic ssDNA markers were separately loaded onto a 20% dPAGE gel for band-migration comparison.

2.4.12 Sample preparation for exact mass spectrometry

A 400 µl sample containing 40 pmol of DNA was incubated in the buffer containing 50 mM HEPES (pH 8.4 at 23°C), 100 mM LiCl, 5 mM $MgCl_2$, and 2 mM $CdCl_2$ at 37°C for 20 min. The products were precipitated with ethanol (buffer:ethanol=1:3, v/v), dried at 37°C for 20 min, and resuspended in 10 µl of deionised H_2O prior to mass-spec characterisation (Novatia, USA).

2.4.13 Kinetic characterisation of self-hydrolysing DNAs

About 25 pmol of the 3'-FAM labelled candidate ssDNA were incubated in 300 µl of the selection buffer (50 mM HEPES (pH 8.4 at 23°C), 100 mM LiCl, 5 mM $MgCl_2$, and 2 mM $CdCl_2$) at a certain temperature (10–90°C). At different time points (0 s, 5 s, 10 s, 20 s, 40 s, 1 min, 2 min, 5 min, 10 min, 20 min, 40 min, 1 h, 2 h, and 4 h for most assays), 10 µl of the sample was pipetted out and mixed with 10 µl of the loading buffer (90% formamide, 30 mM EDTA, 0.025% bromophenol blue, 0.025% xylene cyanol) to stop the reaction. The collected samples were then loaded onto a 20% dPAGE gel for band separation. The fluorescence signal of ssDNA was captured using a Typhoon FLA9500 scanner. Data of the fraction cleaved versus time were extracted from the gels to plot the kinetic curve and calculate the observed rate constants according to a certain reaction model (see below) for each deoxyribozyme.

2.4.14 Fluorescence resonance energy transfer (FRET) assay

The FRET assay was designed to track the separation of the cleavage fragments of the self-hydrolysing deoxyribozymes. Each deoxyribozyme (Zn-I-7, Zn-I-11, or pin20) was labelled with a 6-carboxy fluorescein (FAM) group at its 5' terminus and a Dabcyl group at its 3' terminus, resulting in a quenched fluorescent signal due to the 5'-3' proximity from stem formation **(Figure 12D)**. Upon the cofactor (Zn^{2+} or Cd^{2+}) induced DNA autohydrolysis, the 5' and 3' cleavage fragments have chances to separate from each other depending on the hybridisation strength in the stem, leading to the possible generation of fluorescence signals. To initiate the cleavage reaction, 40 pmol of Zn-I-7 or Zn-I-11 DNA were suspended in 100 µl of the buffer (50 mM HEPES, pH 7.0 at 23°C, 100 mM LiCl, 10 mM $MgCl_2$ and 2 mM $ZnCl_2$), and 40 pmol of pin20 DNA were suspended in 100 µl of the buffer (50 mM HEPES, pH 8.4 at 23°C, 100 mM LiCl, 10 mM $MgCl_2$ and 2 mM $CdCl_2$). The samples were incubated at 37°C for 90 min. The fluorescence intensity was measured at 518 nm using a microplate reader throughout the reaction.

2.4.15 Design, preparation, and self-cutting of DNA origami

The origami nanostructure used in this research was designed following the methodology proposed by Rothemund in 2006. This DNA nanostructure is comprised of origami 1 and origami 2 (a rectangle and a trapezoid) linked by two self-cleaving DNA sequences (pin a and pin b, **Figure 9G)**. A 4130-nt scaffold ssDNA strand was derived from the single-stranded genome of the modified p3024 phagemid, a pBluescript variant, for origami assembly. The DNA origami nanostructure was assembled in a buffer containing 40 mM Tris, 20 mM acetic acid, 2.5 mM EDTA, and 12.5 mM $MgCl_2$. Scaffold DNA (8 nM) and ~3-fold excess of staple DNA was mixed and annealed from 90°C to 22°C in less than 4 h. 4 µl of the assembled origami were pipetted out and added to the selection buffer (50 mM HEPES, pH 8.4 at 23°C, 100 mM LiCl, 10 mM $MgCl_2$ and 2 mM $CdCl_2$) to a final volume of 80 µl. The sample was then incubated at 30°C for 2 h to allow the deoxyribozyme (pin a and pin b) to autohydrolyse. The rectangle and trapezoid origami shapes would be separated from each other when both pin a and pin b underwent self-cleavage.

2.4.16 AFM imaging

Samples were imaged in ScanAsyst mode in an aqueous buffer using ScanAsyst Fluid + tips (Bruker Corporation, Multimode Nanoscope VIII). After annealing, 8 µl of each sample were deposited on the surface of the freshly peeled mica (Ted Pella, Inc.) and allowed to adsorb for 8 min. 25 µl of 1×TAE/Mg buffer (40 mM Tris-HCl, pH 7.5 at 23°C, 20 mM acetic acid, 2.5 mM EDTA, and 12.5 mM $MgCl_2$) were then added onto the mica, and 25 µl of 1×TAE/Mg buffer was deposited onto the microscope tip to expel the air between the cantilever and the holder. The samples were then scanned with a peak force setpoint of ~0.01 N, peak force amplitude of 50 nm, and peak force frequency of 2 kHz.

3 NMR spectroscopy of RNA-cleaving DNAzymes

In the following, the two subchapters 3.1 and 3.2 discuss the NMR spectroscopic characterisation of two RNA-cleaving DNAzymes. Chapter 3.1 addresses Dz46-like DNAzyme with its nucleic acid modification, a DNAzyme of the type 10-23. Chapter 3.2 addresses DNAzyme 8-17 and its recent developments.

3.1 NMR spectroscopic characterisation of Dz46-like DNAzymes

Since their first discovery in 1994, the maturation of RNA-cleaving DNAzymes as therapeutic agents has been underway. DNAzymes have a wide range of applications (e.g., as antivirals, cancer therapeutics or in cardiovascular diseases) in gene silencing through their highly specific, fully customisable target-recognition arms. RNA-cleaving DNAzymes possess numerous advantages over other small-molecule therapeutics, namely, high selectivity, multi-turnover cleavage, and cheap production costs. Between 2009 and 2014, the development of RNA-cleaving DNAzymes as therapeutics gained considerable momentum. Clinical trials reviewing DNAzymes as therapeutics for cancer, asthma, or antiviral applications indicate high safety, but none of the candidates have advanced to clinical trials at level III. (Yan et al., 2023, Hesse et al., 2025). Nevertheless, DNAzymes still face various obstacles – overcoming these appears to be the next step in successfully bringing DNAzymes from the bench to the patient's bedside. Considerable obstacles are the low *in vivo* activity, stability and the need for high intracellular metal ion concentrations. Until recently, deeper insights into the conformation, mode of action, and coordination of metal ions in the DNAzyme-RNA precatalytic complex revealed factors affecting the catalytic activity and opened up the possibility of performing targeted optimisations on DNAzymes (Borggräfe et al., 2022, Borggräfe et al., 2023). The latest developments aimed to improve the target recognition arms and the catalytic core using chemically modified nucleic acids (backbone, sugar and base modifications), especially xeno-nucleic acids (XNAs).

In 2021, Chaput and colleagues introduced an XNA and FANA-modified DNAzyme 10-23, possessing improved stability and metal-ion coordination. The XNAzyme carries enhanced features compared to the unmodified variant for multiple turnover activity under cellular conditions and resistance to nuclease digestion (Yan et al., 2023, Wang et al., 2021). In 2022, Holliger and colleagues followed up on an RNA endonuclease XNAzyme (Fr6_1) developed by *in vitro* evolution and chemical engineering. The XNAzyme can cleave full-length mRNA at physiological cellular conditions and teams up, through phosphorothioate-FANA nucleic acid modifications, with increased biostability *in vivo* (Taylor et al., 2022). Recent publications dealing with modified nucleic acids in DNAzyme 10-23 show that the diversity and the resulting

knowledge gained are far from exhausted (Muñoz-González et al., 2025). Implementation of computational approaches might help to overcome time-consuming and costly large-scale screens (Pine et al., 2023).

In 2023, Chaput and colleagues published a successful chemical evolution of the DNAzyme 10-23 by overcoming one of the major obstacles in DNAzyme activity: low or no intracellular activity. The DNAzyme Dz46 comprises a variety of modified nucleic acids to increase *in vivo* stability and catalytic activity at low Mg^{2+} concentrations. Modifications were designed and developed, taking into account the recently published structural insights into the DNAzyme 10-23 (Borggräfe et al., 2022, Nguyen et al., 2023). To improve catalytic activity, a low frequency of the in-line conformation should be overcome by shifting the conformational equilibrium towards the catalytically active conformation through an MOE modification of the dG14 nucleotide. Moreover, OMe modifications were introduced to C7 and T8 of the catalytic loop. These modifications provide a reduced dependency on Mg^{2+} and a turnover rate of 65 in 30 minutes. The cleavage site pattern was optimised to a 5'-UGUU-3' motif, and it was recognised that the optimised cleavage site pattern does not increase multiple turnover cleavage rates in non-modified DNAzyme 10-23. Therefore, the optimised cleavage site pattern was directly associated with the uniquely introduced modification pattern of the Dz46. Multiple turnover was maximised through binding arm modification (OMe, LNA and PS) and by shifting the equilibrium from the pre- to the post-catalytic state and reducing the recruitment of RNAse H. Construct design and modifications introduced a DNAzyme targeting an undruggable KRAS short nucleotide polymorphism (G12V) through clever cleavage site design (Nguyen et al., 2023).

Here, we aimed to unravel how the introduced nucleic acid modifications influence the structure of Dz46-like DNAzymes, with special regard to the dG14 modification and its influence on the structure and folding of the catalytic loop using NMR spectroscopy. Since structural analysis is preceded by an assignment process, and to simplify this process, the Chaput Lab synthesised a DNAzyme matching the previously assigned sequence of DNAzyme 10-23 prion protein (PrP, Dz839 (Victor et al., 2018, Borggräfe et al., 2022)), but also including modifications and shortening of the target recognition arms of Dz46.

3.1.1 Results and Discussion

Chemical modifications in nucleic acid therapeutics have become increasingly important in the last decades. The effect of chemical modifications can often be determined directly by characterising the cleavage activity, thermodynamic stability or *in vivo* stability. The influence of chemical modifications on structure, folding, active site, or metal-ion binding sites can often

only be determined or assumed indirectly. Therefore, NMR spectroscopy provides a versatile toolbox to study the influence of chemical nucleic acid modifications directly on the structure.

All variants of Dz46nmr2-like and Dz46-like DNAzymes are described in detail in the Materials and Methods section, and their respective names and modifications can be depicted in **Figure 13**. Dz46 does characterise a special sequence targeting the KRAS G12V mutation, in combination with a nucleic acid modification pattern. In the following, the Dz46 variant of the DNAzyme wildtype (wt) 10-23 with PrP sequence is called Dz46-like or Dz46nmr2-like DNAzyme (changed cleavage site pattern from 5'-CGUU-3' to 5'-UGUU-3'). Var1 will also be referred to as the parent DNAzyme, as all subsequent modifications are added to it. All DNAzyme wt 10-23 PrP spectra were measured and evaluated by Jan Borggräfe and served as a reference.

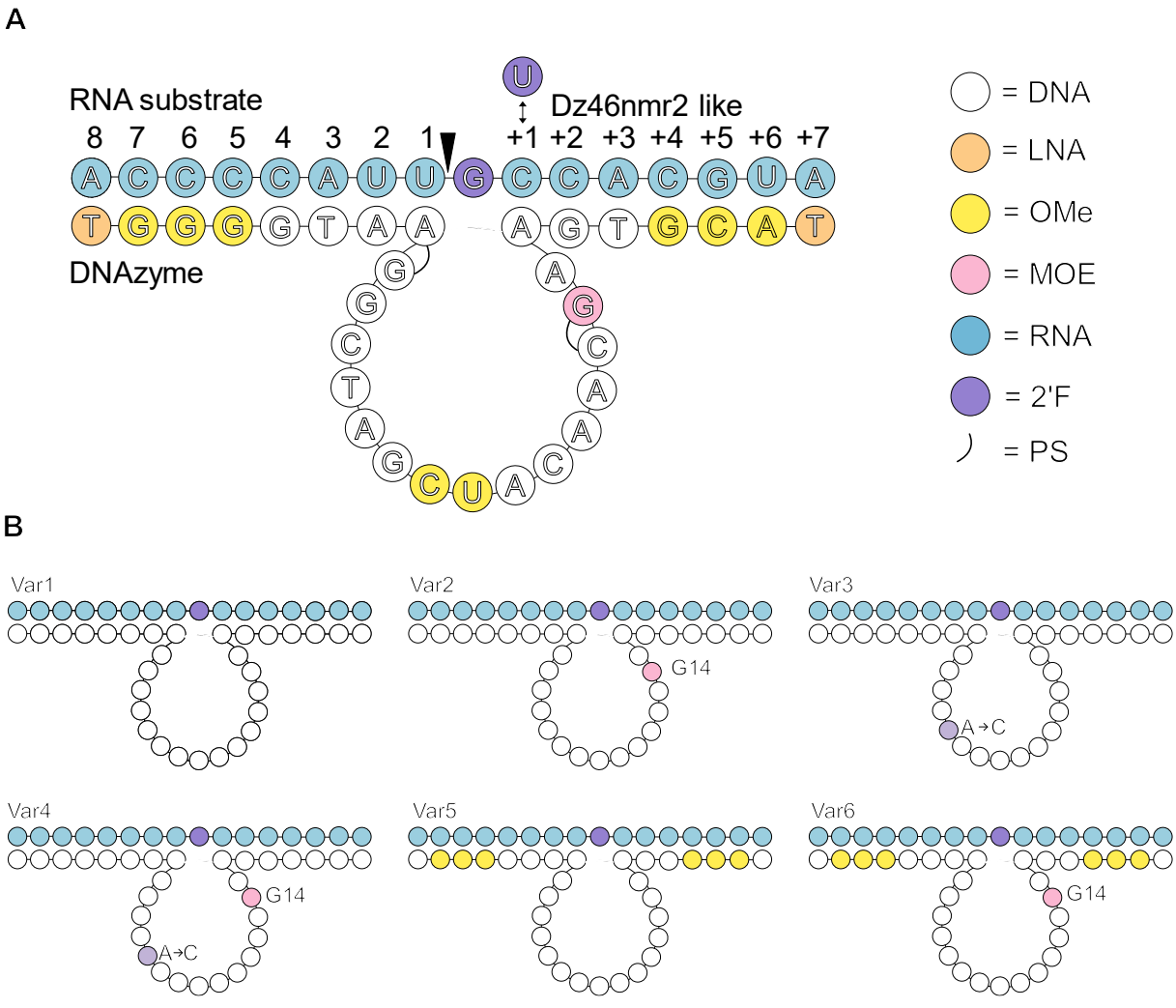

Figure 13: Schematic overview of all constructs used. A: Dz46-like DNAzyme with PrP sequence of the DNAzyme 10-23 of Chaput Lab (University of California, Irvine, CA, USA), both cleavage sites visualised by a two-sided arrow. Sugar, base or backbone modifications are highlighted by a distinct colour: DNA is white, LNA is orange, OMe is yellow, MOE is rose, RNA is blue, 2'F is purple. **B:** Differences between the constructs and their clear designation are presented.

3.1.1.1 Comparison between the fully modified Dz46-like DNAzyme (PrP, newly designed), and Dz46nmr2-like DNAzyme (5'-UGUU-3 cleavage site) to DNAzyme 10-23 wt (PrP)

It was aimed to characterise the alteration of the structure introduced through nucleic acid modifications of the Dz46-like DNAzyme (PrP sequence) to the non-modified wildtype version, with special interest in the dG14 MOE modification in the catalytic loop **(Figure 14A)**. In this regard, understanding how changes in the cleavage site pattern affect the structure was also aimed at. Chaput and colleagues were able to identify that the alteration of the cleavage site pattern to increase the catalytic activity was only "necessary" in the fully modified DNAzyme but not in the non-modified variant. They suspected that the introduction of nucleic acid modification led to increased rigidity in the overall structure of the DNAzyme (Nguyen et al., 2023). To simplify the assignment, the Dz46 modifications were transferred to the DNAzyme Dz839, i.e. a 10-23 wt variant targeting the PrP mRNA sequence (Victor et al., 2018), which had already been successfully assigned and structurally characterised (Borggräfe et al., 2022). To determine the effect of the modified cleavage site more precisely, another variant, Dz46nmr2-like DNAzyme (with a 5'-UGUU-3' cleavage site), was synthesised with an otherwise unchanged PrP target sequence. As a first step, an attempt was made to transfer the assignment from DNAzyme 10-23 wt (PrP sequence) to Dz46-like DNAzyme. It could already be assumed that the chemical modifications would have an influence on the structure and that a modified cleavage site would only reinforce this effect.

Therefore, the first step was to understand and evaluate whether the assignment of DNAzyme 10-23 wt (PrP sequence) can be transferred to the Dz46-like DNAzyme and how nucleic acid modifications may alter the structure of the DNAzyme. The fingerprint region of Dz46-like DNAzyme illustrates a homogenous peak distribution **(Figure 14B)**, indicating proper folding of the DNAzyme and Watson-Crick base pairing is featured in the ^{1}H-^{1}H NOESY data set **(Supplement Figure 41A)**, implying proper duplex formation between the DNAzyme and RNA target. However, several peaks in the fingerprint region are not well-resolved and display increased line broadening, which may indicate a possible conformational exchange. Compared to the non-modified parent DNAzyme, ^{1}H-^{1}H NOESY and TOCSY spectra exhibit a lower signal-to-noise ratio. Spectral peak rU_{+8} is missing in Dz46-like spectra due to a shortened sequence. Peaks for rC_{-7} and rC_{-1} shifted strongly and could not be clearly identified without proper sequential backbone assignment. However, missing spectral peaks for rU_{+6} and dU_{+5} indicate that the shifted peak probably belongs to C_{-1}. The missing resonances suggest that base pairing at the 3′ and 5′ ends of the duplex is destabilised, resulting in increased flexibility and dynamics. The absence of terminal peaks is also referred to as 'fraying' and describes the process in which terminal base pairs wholly or partially rotate out of the helical conformation (Andreatta et al., 2006). It has already been determined that various nucleic acid modifications in the backbone can intensify the process of fraying (Jaroszewski et al., 1996, Moe et al.,

1994). However, LNA modifications are usually utilised to stabilise base pairing and melting temperatures of duplexes (Grünweller and Hartmann, 2007). In this case, it can be assumed that the shortening in the target binding arms lead to a decrease in the melting temperature and the use of LNA and OMe modifications to stabilise the duplex only partially compensates for this aspect. Interestingly, in the catalytic loop, peaks of dC3 and dC7 are either missing or are very broad and not well resolved; peaks adjacent to the dG14 MOE modification, dC13 and dC10, are present. In summary, RNA nucleotides appear to be largely unaffected by the nucleic acid modifications in the DNA duplex arms. However, it should also be noted that the analyses performed are limited exclusively to the pyrimidines in the sequence, and Dz46-like DNAzyme contains few pyrimidines. This makes it rather difficult to assess the whole influence of the applied modification on the arms of the DNAzyme. Compared to the wt, the loop of the Dz46-like DNAzyme appears to exhibit increased conformational heterogeneity, and peaks either disappear or broaden. Overall, the assignment cannot be completely transferred from the unmodified parent DNAzyme to the Dz46-like DNAzyme.

Secondly, we aimed to understand how the altered cleavage site influences the structure of the DNAzyme-RNA complex and if the assignment can be transferred from the unmodified DNAzyme 839. The fingerprint region of Dz46nmr2-like DNAzyme illustrates a homogenous peak distribution **(Figure 14C)**, indicating proper folding of the DNAzyme and Watson-Crick base pairing is featured in the ^{1}H-^{1}H NOESY **(Supplement Figure 41B)**, implying proper duplex formation between the DNAzyme and RNA target. However, several peaks in the fingerprint region are not well-resolved through increased line broadening and elevated background noise. Poor spectral resolution is also more pronounced compared to the Dz46-like DNAzyme without a modified cleavage site **(Figure 14D)**. While most of the peaks of the Dz46nmr2-like DNAzyme appear to be different, dC10 seems to be similar in the catalytic loop, as well as in the arm region rC_{-5}, rC_{-6}, rU_{-2} and rC_{+2}. Due to comparatively broader and poorly resolved peaks, the attempt to transfer the assignment failed. Nevertheless, two interesting features can be observed: firstly, the residues close to the G14 MOE modification continue to show little to no chemical shift perturbation, as already observed for the Dz46 variant; secondly, the alteration of the cleavage site seems to have a general influence on the overall dynamics of the structure rather than just a local effect on neighbouring bases. Bases neighbouring the altered cleavage site appear to be largely unaffected by the change in the cleavage site pattern.

The alteration of the cleavage site appears to have a major influence on the overall structure. Chaput and colleagues suggested that the new cleavage site possibility supports a more rigid structure, introduced through the diverse chemical modifications throughout the catalytic loop and binding arms (Nguyen et al., 2023). NMR spectroscopy reveals that the spectra of

Dz46nmr2-like DNAzyme have significantly broader peaks, a lower signal-to-noise ratio, and inferior spectral resolution, suggesting altered dynamics and possible conformational exchange.

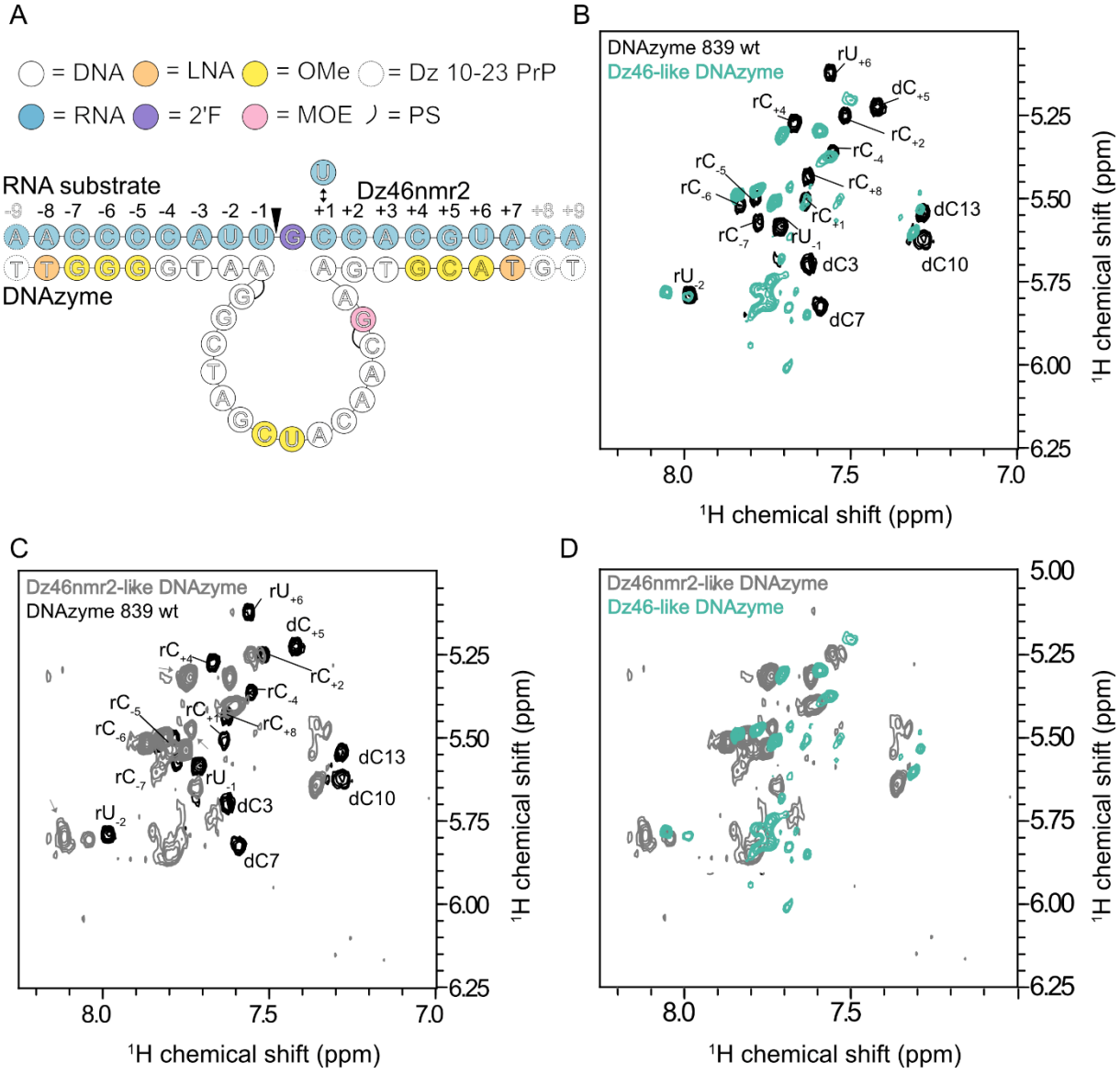

Figure 14: Introduction of chemical nucleic acid modifications on Dz46-like DNAzyme (PrP sequence) and Dz46nmr2-like DNAzyme, and structural comparison between both modified DNAzymes and the non-modified DNAzyme 10-23 (PrP sequence). A: Schematic figure of Dz46-like DNAzyme and Dz46nmr2-like DNAzyme modifications. Dashed lines indicate shortened target recognition arms of Dz46/Dz46nmr2-like DNAzyme compared to the mother sequence of the DNAzyme wt 10-23 (PrP sequence). Dz46nmr2-like DNAzyme possesses an altered cleavage site pattern from 5'-CGUU-3' to 5'-UGUU-3', which is indicated by a two-sided arrow. **B:** Finger print region comparison between 2D ^{1}H-^{1}H TOCSY of DNAzyme wt 10-23 (PrP sequence) in black with suitable assignment and 2D ^{1}H-^{1}H TOCSY of Dz46-like DNAzyme (shortened PrP sequence) in green. Samples were both measured at 37°C (50 mM dTris, pH 7.5, 100 mM NaCl and 10% D_2O). **C:** Finger print region comparison between 2D ^{1}H-^{1}H TOCSY of DNAzyme wt 10-23 (PrP sequence) in black with suitable assignment and 2D ^{1}H-^{1}H TOCSY of Dz46nmr2-like DNAzyme (shortened PrP sequence, altered cleavage site pattern) in grey. Samples were both measured at 37°C (50 mM dTris, pH 7.5, 100 mM NaCl and 10% D_2O). **D:** Finger print region comparison between 2D ^{1}H-^{1}H TOCSY of Dz46-like DNAzyme (PrP sequence) in green and 2D ^{1}H-^{1}H TOCSY of Dz46nmr2-like DNAzyme (shortened PrP sequence, altered cleavage site pattern) in grey. Samples were both measured at 37°C (50 mM dTris, pH 7.5, 100 mM NaCl and 10% D_2O).

3.1.1.2 Identification of dG14 MOE in ^{1}H-^{1}H NOESY

Chaput and colleagues introduced the G14 MOE modification to improve the catalytic activity of Dz46, as it shifts the equilibrium toward a catalytically active conformation (Nguyen et al., 2023). Taking into account that G14 MOE modification of the Dz46 had the greatest effect on activity, it seems highly interesting to understand how the modification affects the structure (Nguyen et al., 2023, Borggräfe et al., 2022). Initial findings have already shown that the local influence on the structure appears to be rather small (the low chemical shift perturbation of spatially close bases was used as an indicator here). To understand the effects of modifications, especially the G14 modification, on the structure of the DNAzyme in detail, the approach must be changed.

As described above, a strategy was developed to identify modifications and their effects on the structure. Until now, there have been very few publications that have investigated and characterised chemical nucleic acid modifications (especially MOE and OMe) using two-dimensional solution-state NMR spectroscopy. These publications can be a helpful tool in the assignment process. Additional peaks of nucleic acid modification, mainly methyl and ethyl groups, need to be unambiguously identified and located in the ^{1}H-^{1}H NOESY with the help of spectral tables. Here, we aimed to (1) compare an unmodified DNAzyme Var1 with a modified DNAzyme Var2 to identify and characterise the G14 MOE modification and its additional peaks and (2) link our insights to the possible effects of the modification on the structure.

^{1}H-^{1}H NOESY/TOCSY spectra of Var2 **(Figure 15 A and B)** display a combination of well-resolved and defined peaks, but also weak, broad and not well-resolved peaks and a general lack of signals. Magnified region I displays peak heterogeneity for the pyrimidines, and magnified region II highlights the appearance of hydrogen bonds classically found in Watson-Crick base pairing. The results indicate that the system undergoes intermediate exchange and high heterogeneity through structural dynamics. Interestingly, similar structural features can also be found in the unmodified Var1 **(Figure 15C, Supplement Figure 42)**. The spectra of Var1 and Var2 have spectral similarities, but are, as already mentioned, very poorly resolved. It appears likely that the better-resolved peaks can be assigned to the RNA target. Peaks of interest, in the catalytic loop, are particularly affected by poor spectral resolution. The aim to identify the G14 MOE modification and its influence on the structure can therefore not be fulfilled, as the signals of the used samples are too poorly resolved to compare Var1 to Var2.

To improve spectral resolution and/or reduce heterogeneity, different sample conditions were subsequently tested. The catalytic loop of the DNAzyme 10-23 wt is known to have disappearing peaks in the presence of Mg^{2+}-induced conformational exchange processes (Borggräfe et al., 2022). Therefore, Var2 was measured in the absence of Mg^{2+} **(Figure 15D, green spectrum)** to study whether spectral resolution is improving. A slight improvement in

spectral resolution is observable–an increase in peak intensity and the 'reappearance' of peaks that had previously disappeared. As described above, this indicates that the absence of Mg^{2+}-induced conformational exchange shifts the exchange from intermediate to faster.

All subsequent measurements and optimisations were therefore performed without $MgCl_2$ in the buffer. Since the spectral resolution of the so far measured samples was still too poor to conduct further analyses of the G14 MOE modification, the idea was to convert the Dz46 wildtype into an A5C variant to further improve spectral quality. It has been shown previously that replacing adenine at position 5 of the catalytic site with cytosine improves NMR spectral quality by increasing exchange processes (Borggräfe et al., 2022).

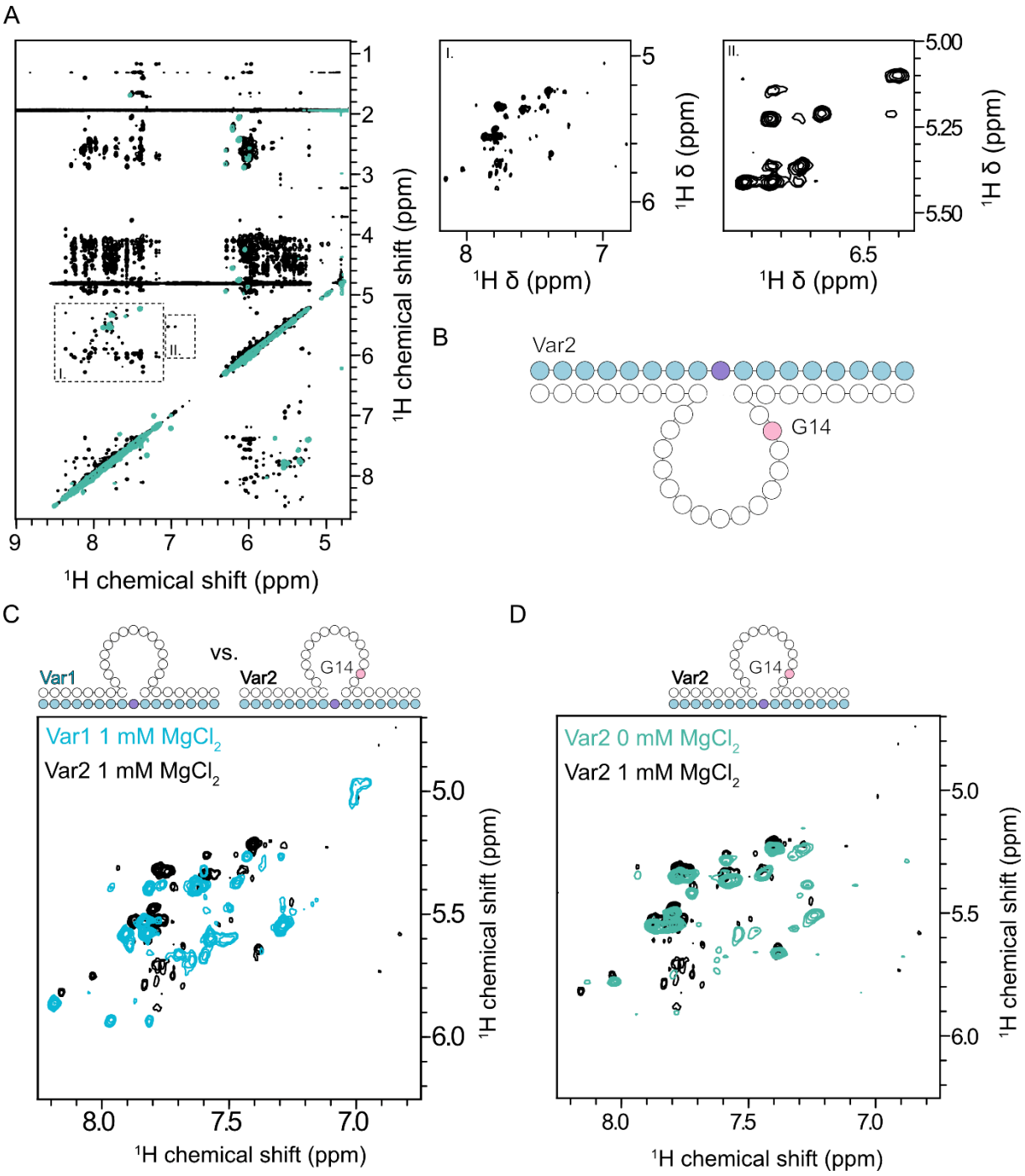

Figure 15: NMR spectroscopic characterisation and measurement optimisation of Var2. A: Overlay of 2D ^{1}H-^{1}H NOESY in black and 2D ^{1}H-^{1}H TOCSY in green (37°C, 50 mM dTris, pH 7.5, 100 mM NaCl, 1 mM $MgCl_2$ and 10% D_2O). Characteristic regions are highlighted and magnified next to the overlay. Region I (^{1}H-^{1}H TOCSY) show the fingerprint region of Var2, and region II (^{1}H-^{1}H NOESY) highlights the appearance of classical hydrogen bonds found in Watson-Crick base pairing. **B:** Schematic figures of modifications featured in Var2. **C:** ^{1}H-^{1}H TOCSY fingerprint overlay of Var1 (blue) and Var2 (black), both with 1 mM of $MgCl_2$. Differences in nucleic acid modifications between the two constructs are shown in colour above the fingerprint spectrum. **D:** ^{1}H-^{1}H TOCSY fingerprint overlay of Var1 (black) and Var2 (green, 25°C, 50 mM dTris, pH 7.5, 100 mM NaCl, and 10% D_2O). Differences in nucleic acid modifications between the two constructs are shown in colour above the fingerprint spectrum.

3.1.1.3 Shortened target recognition arms in combination with the A5C variant destabilise the RNA-DNAzyme complex

As prior attempts to improve spectral resolution yielded only minor improvements, further optimisations were made to visualise the resonances of the catalytic loop. In Var3 and Var4, the adenine at position five in the catalytic loop is replaced by a cytosine. This exchange may be helpful, as the exchange from adenine to cytosine at position 5 of the catalytic loop decreases the rigidity of the catalytic loop and therefore shifts the exchange from intermediate to a faster exchange, which helps visualise the resonances of the catalytic loop (Borggräfe et al., 2022).

As the A5C variant had already been assigned and characterised, a comparison of the fingerprint region of the ^{1}H-^{1}H TOCSY spectrum of DNAzyme 839 A5C and Var3 was possible (Borggräfe et al., 2022) **(Figure 16A, Supplement Figure 43A)**. Compared to the DNAzyme 839 A5C, which has three additional nucleotides in the target recognition arms, Var3 displays broad peaks and a poor signal-to-noise ratio, resulting in diffuse peak shapes and a reduced overall peak count. Reducing the number of nucleotides in the target recognition arms on the 5’ side by one and on the 3’ side by two strongly destabilises the whole DNAzyme-RNA duplex. As a result, the melting temperatures of each target recognition arm dropped below 37 °C, leading to disrupted or incomplete base pairing of the whole complex. These results also agree with the literature: short RNA-DNA hybrids are sensitive to small changes in nucleotide count, leading to significant changes in their melting temperatures (Lesnik and Freier, 1995). However, comparing the fingerprint region of the ^{1}H-^{1}H TOCSY spectrum of Var4 to Var2 **(Figure 16B, Supplement Figure 43B)**, it is noticeable that, in addition to the nucleotide number in the target-recognition arms of the DNAzyme, the introduction of the A5C seems to influence the complex stability. For Var2, the ^{1}H-^{1}H TOCSY displays narrower peaks and improved spectral resolution, but the overall peak count is reduced. It seems like the combination of the nucleotide exchange from adenine to cytosine (A5C) in the catalytic loop and the reduced arm length is mutually negative. Interestingly, the combination of the G14 MOE modification in the catalytic loop and the A5C variant does not appear to significantly affect the spectral resolution of the fingerprint region of the ^{1}H-^{1}H TOCSY spectrum of Var4 **(Figure 16C)**. Comparing the fingerprint region of the ^{1}H-^{1}H TOCSY spectrum of the assigned

Var2 without target RNA and Var4 **(Figure 16D)**, as already suspected in this section, it becomes clear that the DNAzyme Var4 is not base-paired. The peaks of the DNAzyme without target RNA are also found in the other spectra and are highlighted with small arrows.

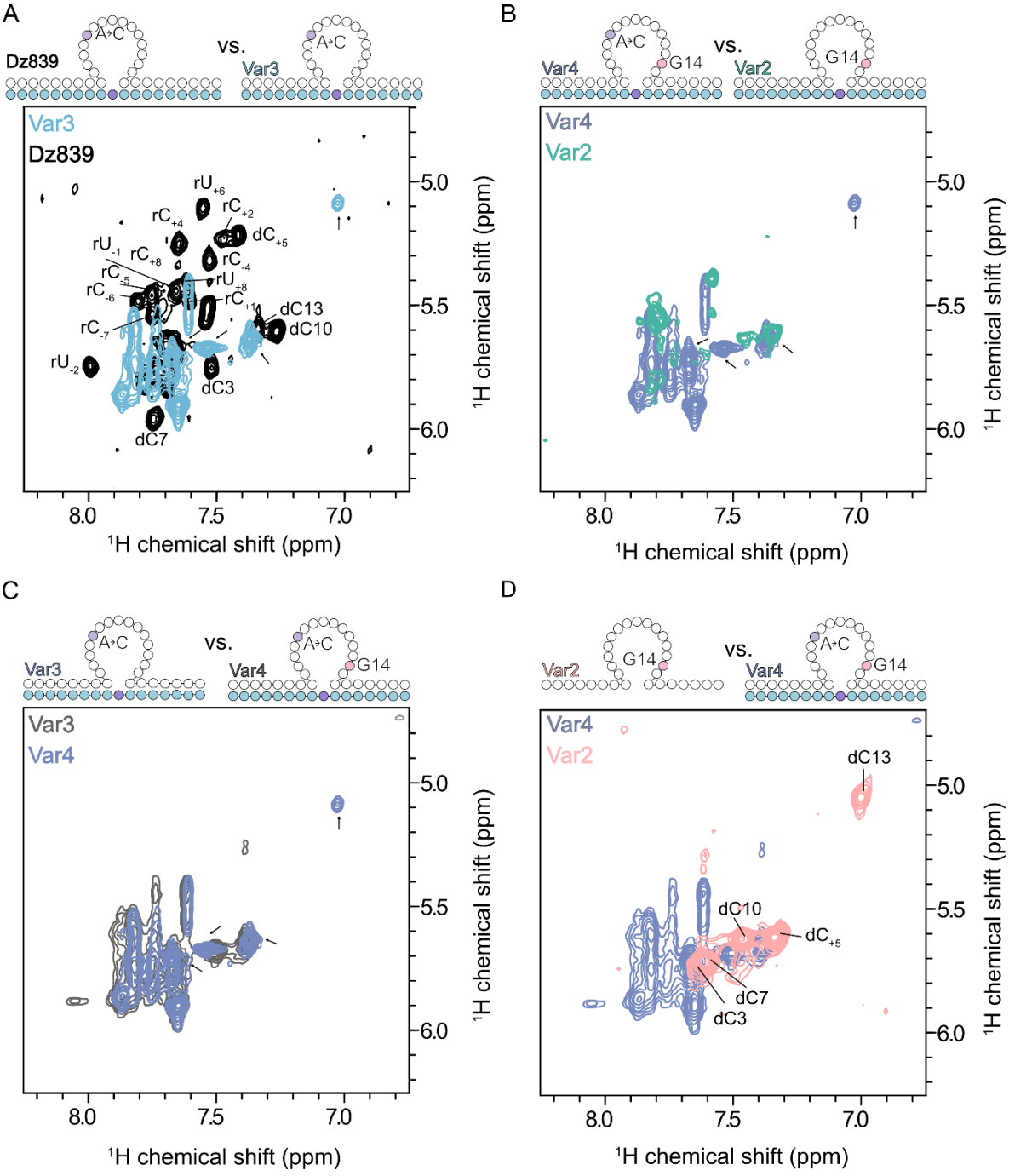

Figure 16: Shortened target recognition arms in combination with the A5C variant destabilise the RNA-DNAzyme complex. Black arrows indicate not base-paired DNAzyme peaks, and differences in nucleic acid modifications between the two constructs are shown in colour above the fingerprint spectrum. **A:** ^{1}H-^{1}H TOCSY fingerprint overlay of DNAzyme 839 (black, three additional nucleotides in the target recognition arms) and Var3 (blue) (37°C, 50 mM dTris, pH 7.5, 100 mM NaCl and 10% D_2O). **B:** ^{1}H-^{1}H TOCSY fingerprint overlay of Var4 (purple) and Var2 (green) (37°C, 50 mM dTris, pH 7.5, 100 mM NaCl and 10% D_2O). **C:** ^{1}H-^{1}H TOCSY fingerprint overlay of Var2 without target RNA (rose) and Var4 (purple) (37°C, 50 mM dTris, pH 7.5, 100 mM NaCl and 10% D_2O). **D:** ^{1}H-^{1}H TOCSY fingerprint overlay of Var4 (purple) and Var2 (green) (37°C, 50 mM dTris, pH 7.5, 100 mM NaCl and 10% D_2O).

3.1.1.4 Enhancing duplex stability by introducing 2′-O-methyl modifications to the binding arms

To stabilise the DNAzyme-RNA complex by increasing the melting temperature of the arms, six OMe modifications, three at the 5'end and three on the 3' end of the target recognition arms, were introduced. In combination with increased duplex stability through the introduction of OMe arm modifications, the measurement temperature was optimised to ensure proper duplex formation. The ^{1}H-^{1}H TOCSY fingerprint of Var6 at 25°C **(Figure 17A**, **Supplement Figure 44C and D)** displays narrower peaks, a strongly increased number of peaks, and an improved signal-to-noise ratio compared to Var2 measured at 37°C. This demonstrated that the duplex could be stabilised by inserting the modifications, thereby significantly improving the spectral resolution. In the ^{1}H-^{1}H NOESY **(Supplement Figure 44C and D)** of Var6, the base-pairing signals of RNA-DNAzyme complex reappear. Resonance peaks of the loop also improve slightly, though they remain broad and diffuse. Since the spectral resolution has now been significantly improved, the question arose whether Var6 could be assigned. Therefore, the ^{1}H-^{1}H TOCSY fingerprint region of Var6 was compared with the fingerprint region of DNAzyme 10-23 wt **(Figure 16B)**, and revealed only a few matching peaks. As a result, further assignment was still not feasible, mainly since the resonances of the loop remained insufficiently resolved to allow meaningful structural interpretation of how the G14 MOE modification affects the folding of the catalytic loop.

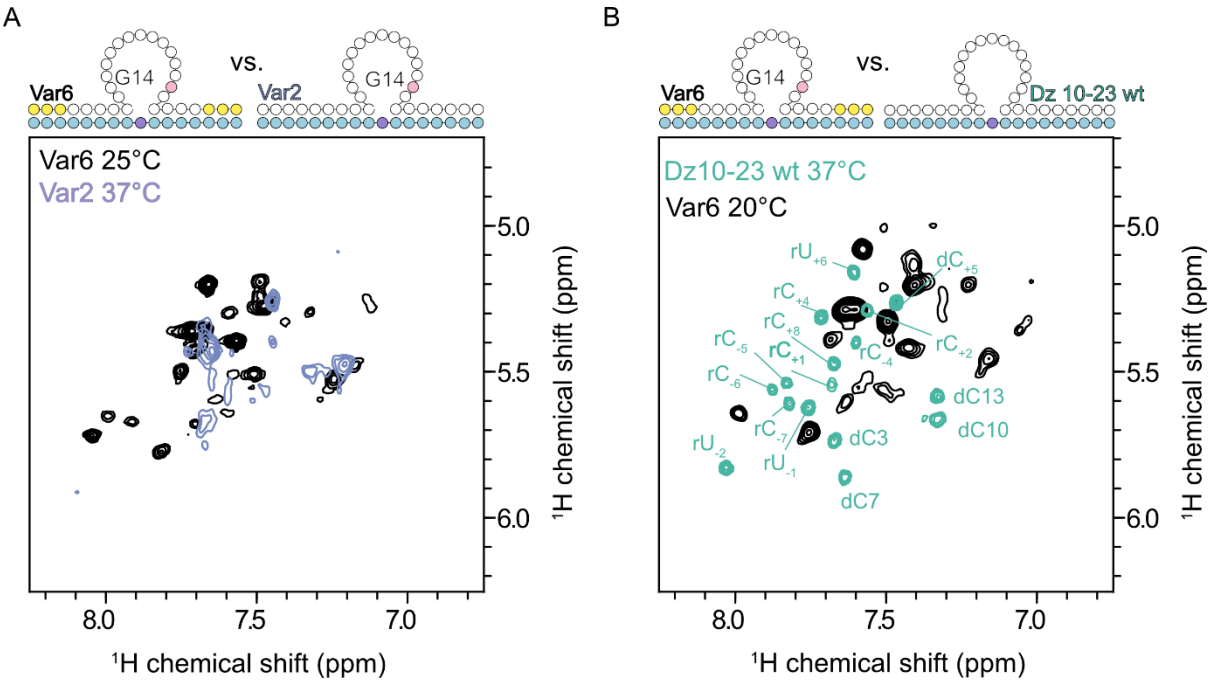

Figure 17: Enhancing the duplex stability by introducing 2'-O-methyl modifications to the binding arms of the DNAzyme. Differences in nucleic acid modifications between the two constructs are shown in colour above the fingerprint spectrum. **A:** ^{1}H-^{1}H TOCSY fingerprint overlay of Var6 at 25 °C (black) and Var2 at 37°C (purple) (50 mM dTris, pH 7.5, 100 mM NaCl and 10% D_2O). **B:** ^{1}H-^{1}H TOCSY fingerprint overlay of Var6 at 20 °C (black) and Dz 10-23 wt at 37°C (green) (50 mM dTris, pH 7.5, 100 mM NaCl and 10% D_2O).

3.1.1.5 Characterisation of dG14 MOE modification

As already described in the chapters above, which address the NMR spectroscopic characterisation of Dz46-like DNAzymes, we aimed to characterise the influence of the dG14 MOE modification in the catalytic loop of the RNA-DNAzyme complex. To characterise the influence of the dG14 MOE modification, the RNA-DNAzyme complex needs to be assigned. However, previous results and optimisation processes did not yield spectra with high spectral resolution. Therefore, the aim was still to identify the dG14 MOE modification; however, to simplify the assignment, only the DNAzyme without a target was used. The same approach, as previously described, was used to compare Var1 and Var2 in the absence of target RNA to identify the modified dG14 in the DNAzyme. Plevnik *et al.* identified the additional peaks arising from the MOE modification itself between 3.5 and 4.7 ppm, Bruker chemical shift tables predict for O-CH_2 groups a proton chemical shift between 3.5 and 4.5 ppm (^{13}C: 50 to 70 ppm), for O-CH_3 between 3.5 and 4ppm (^{13}C: 50-60 ppm) (Plevnik et al., 2013, Bruker BioSpin). Sequential assignment of Var2 was carried out as described in the introduction chapter using ^{1}H-^{1}H NOESY and TOCSY spectra at 37°C and 45°C. Although the complete assignment was not possible, 76.7% of the residues were successfully assigned, including the dG14 residue of the catalytic loop. For Var2, the ^{1}H-^{1}H NOESY spectrum displays 3 to 4 additional, “unusual” peaks for dG14 between 3 and 4 ppm, which are absent for Var1 **(Figure 18A, magnified region II, Supplement Figure 45)**. In comparison to the non-modified sample Var1, residual peaks for Var2, with special emphasis on dC13, dG14, dA15, dA_{+1}, and $dG_{+2,}$ are strongly shifted. All of the shifted peaks are in proximity to the G14 and linked to the catalytic loop or the cleavage site. These shifted residual peaks indicate, on the one hand, that sequential assignment of the residues is correct, as the introduction of the MOE modification is expected to change the chemical environment of adjacent residues. On the other hand, they indicate that the introduction of the MOE modification indeed alters the chemical environment and likely the structure of the DNAzyme as well **(Figure 18A, magnified regions I and II, Supplement Figure 45)**.

Additionally, ^{1}H-^{13}C HSQC of Var1 and Var2 were recorded to identify the ^{13}C carbon shifts of the additionally identified protons, to determine the effects of the MOE modifications to spatially close carbons, and to identify additional effects introduced by the modification. For the ^{1}H-^{13}C HSQC of Var2, four additional proton-carbon correlation peaks appear between 64 and 72 ppm and 3.2 and 4.0 ppm, compared to the ^{1}H-^{13}C HSQC of Var1 well **(Figure 18B, Supplement Figure 46).** These additional correlation peaks were assigned to the chemical shifts of dG14, as shown in magnified region I of **Figure 18A.**

In addition to the structural characterisation of the DNAzyme, the cleavage activity of the DNAzymes Var1 to Var6 was characterised using FRET at 37°C and Mg^{2+} as a cofactor with

a concentration between 1.0 and 2.0 mM **(Figure 18C)**. The cleavage activity of the chemical evolution constructs was also characterised in the Nguyen *et al.* study. However, the studied variants differ significantly from the variants investigated in this thesis, preventing direct comparison. At low $MgCl_2$ concentrations, Var6 has a slightly higher cleavage activity compared to Var2. With increasing $MgCl_2$, both k_{obs} values increase, but the activity of Var2 increases more pronouncedly as compared to Var6. A common understanding in literature is that the OMe modification in DNA is shifting the sugar pucker conformation into C3'endo conformation (Abou Assi et al., 2020, Lubini et al., 1994) and increases the base pairing stability (Lubini et al., 1994). Another factor associated with the increased base-pairing stability is that it might also slow the dissociation of the cleaved RNA from the DNAzyme, and therefore, the cleavage activity is supposedly slowed. In addition, cleavage efficiency depends on the rate-limiting step of the formation of a stable RNA-DNAzyme complex. At low Mg^{2+} concentrations, the duplex is not additionally stabilised by Mg^{2+}; therefore, the complex is not stable enough and may dissociate before the cleavage. As a result, at low Mg^{2+}, the additional stability and rigidity introduced through the OMe modifications could stabilise the complex and enhance the cleavage reaction compared to the non-modified variant. Whereas at higher Mg^{2+} concentrations, the magnesium stabilises the complex in both variants, but in Var6 the additionally stabilised OMe arms slow the dissociation of the target RNA, leading to slower cleavage efficiency compared to Var2. The k_{obs} values for both A5C variants with and without dG14 MOE modification (Var3 and Var4) display the lowest activity compared to the other variants, independent of the Mg^{2+} concentration. The lowered activity through the introduction of the A5C variant is also already well known and characterised (Zaborowska et al., 2002). Interestingly, although the G14 MOE modification increased cleavage efficiency strongly for all other introduced variants, it is not the case for the A5C variant. In the catalytic loop, the G14 and A5C were spatially very close to each other. The introduction of the G14 MOE modification increases the number of steric residues within a minimal space, and the A5C variant also alters the architecture and flexibility of the catalytic loop. As a result, the combination of modification and nucleotide exchange may alter the conformation and folding of the catalytic loop, thereby increasing its rigidity. This rigidity may lead to fewer conformational sampling, and therefore the DNAzyme is less likely to adopt a cleavage-competent conformation (Borggräfe et al., 2022; Nguyen et al., 2023).

The structural investigation of the A5C variant with and without G14 MOE modification thus does not appear to be a good model system to mimic the activity-increasing effects introduced by the G14 modification in the regular 5A DNAzyme. The measured activity data, in combination with the measured NMR data from the previous chapters, show that even low Mg^{2+} concentrations contribute significantly to the stabilisation of the RNA-DNAzyme complex, despite a marked shortening of the binding arms.

In summary, the Var2 (DNAzyme only) was successfully assigned using ^{1}H-^{1}H NOESY and TOCSY at 37°C. The dG14 MOE nucleotide was identified and assigned as such, and additional peaks introduced through the modifications were localised in the ^{1}H-^{1}H NOESY and ^{1}H-^{13}C HSQC. The chemical shift perturbation of the extra peaks of the MOE modification was in agreement with Bruker chemical shift tables and literature. The k_{obs} values of all used variants (Var1 to Var6) were determined for 1.0 to 2.0 mM $MgCl_2$ at 37°C and compared to each other, resulting in the conclusion that the addition of $MgCl_2$ is stabilising the RNA-DNAzyme complex better than the introduction of OMe modifications to the target recognition arms of the DNAzyme.

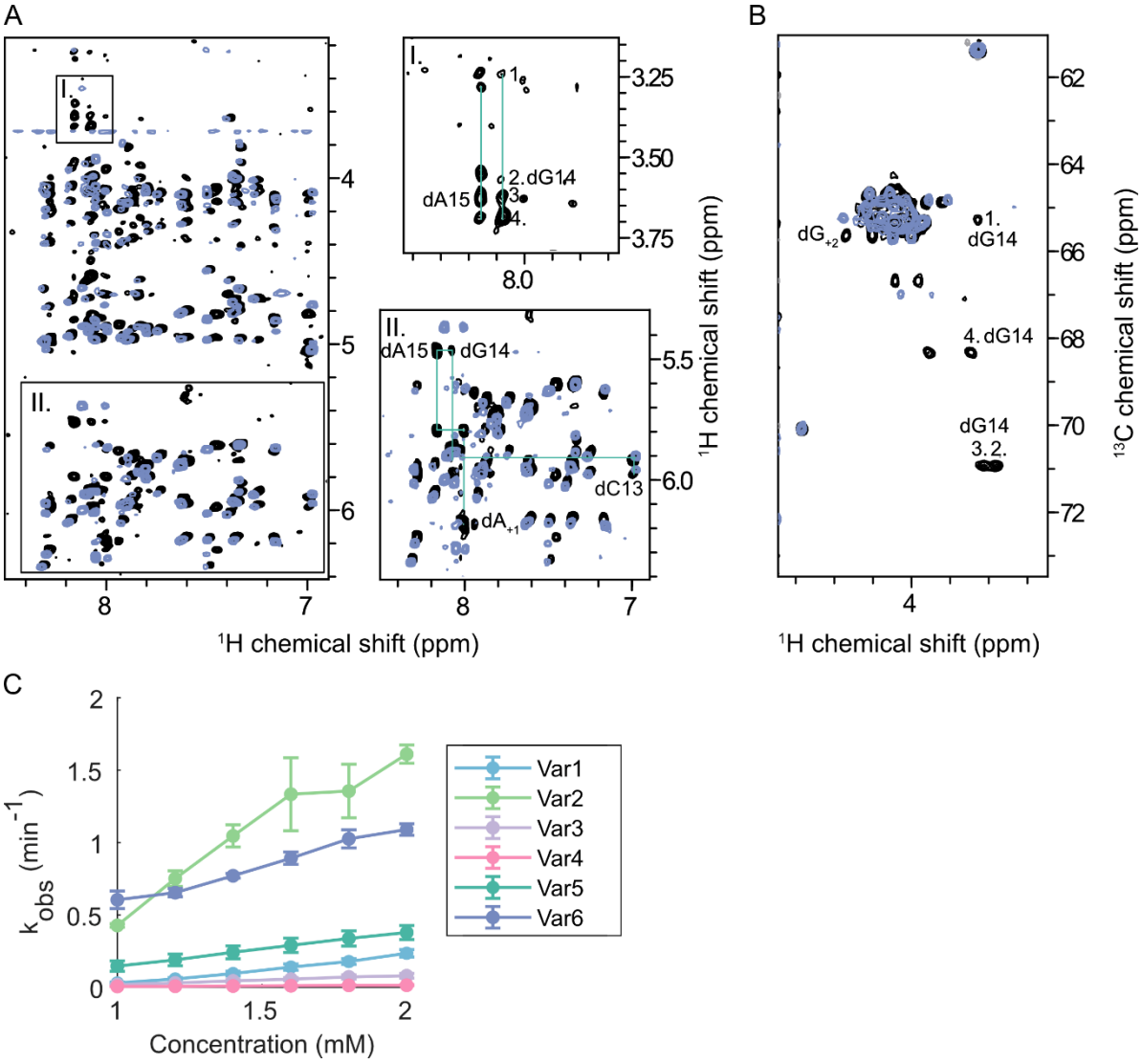

Figure 18: Characterisation of G14 MOE using NMR spectroscopy and FRET. A: 2D ^{1}H-^{1}H NOESY overlay of Var1 (purple) and Var2 at 37°C (50 mM dTris, pH 7.5, 100 mM NaCl and 10% D_2O). Characteristic regions are highlighted and magnified next to the overlay. Region I shows additional peaks for Var2 between 3 and 3.75 ppm. These extra peaks lie within the expected range of chemical shift perturbation for O-CH_2 and O-CH_3. Additional peaks are numbered from 1 to 4. Region II exemplifies the assigned residues for dA15, dG14, and dA_{+1}, as they are most affected by the modification compared to the unmodified Var1. Spin systems and their through-space connections are highlighted by green, straight lines. **B:** 2D ^{1}H-^{13}C HSQC overlay of Var1 (purple) and Var2 at 37°C (50 mM dTris, pH 7.5, 100 mM NaCl and 10% D_2O). The magnified overlay highlights additional, numbered peaks assigned to dG14 between 3 and 3.75 ppm and 64 and 71 ppm. **C:** kobs(min^{-1}) values of Var1 to Var6 with

increasing $MgCl_2$ concentration (mM) at 37°C (50 mM Tris-Base, pH 7.5, 10 mM NaCl, 140 mM KCl and 0.1 mM EDTA).

3.1.2 Summary and Outlook

In summary, nucleic acid modifications of Dz46 transferred to the Dz839 with the PrP sequence (Dz46-like DNAzyme), result in a destabilised base-pairing at the 3' and 5' ends of the duplex, indicated by missing peaks. The so-called frayed ends are accompanied by increased conformational plasticity in the catalytic loop, whereby the RNA target molecule remains largely unaffected. In conclusion, it is striking that modifications that have been used to increase the stability of the duplex cannot adequately compensate for the absence of three nucleic acids. As a result, the assignment could not be transferred. Alterations in the cleavage site pattern (from 5'-CGUU-3' to 5'-UGUU-3') appear to have a major influence on the overall structure of DNAzyme, resulting in altered dynamics and conformational exchange of the whole DNAzyme RNA complex. Modulated dynamics of the catalytic loop were reflected in significantly broader peaks and a poorer signal-to-noise ratio. These changes in dynamics may reflect a more rigid structure of the DNAzyme-RNA as predicted by Chaput and colleagues. However, a simple assignment transfer, as initially intended, is not possible because the peaks in the catalytic loop lack sufficient resolution.

The duplex stability of a DNAzyme RNA complex is affected by three factors: length of the target recognition arms, concentration of bivalent metal ions (e.g., Mg^{2+}) in solution and, according to our knowledge, whether a cytosine replaces the adenine in position 5 of the catalytic loop. Here, we report that the combination of the nucleotide exchange from adenine to cytosine (A5C) in the catalytic loop and the reduced arm length is mutually unfavourable by destabilising the complex.

The free DNAzyme Var2 with the dG14 MOE modification in the catalytic loop was successfully assigned, and additional peaks from the MOE modification were identified and further characterised using the ^{1}H-^{1}H NOESY and ^{1}H-^{13}C HSQC. The chemical shift perturbation of the identified extra peaks, assigned to the dG14 MOE modification, were in agreement with the Bruker chemical shift prediction tables and the literature. Residues in the catalytic loop and cleavage site of the DNAzyme were particularly affected by the G14 MOE modification, indicated by increased chemical shift perturbations. Additionally, the k_{obs} values of all in this thesis used variants (Var1 to Var6) were determined for 1.0 to 2.0 mM $MgCl_2$ at 37°C. Results showed that a DNAzyme with an OMe modification arm to counteract shortened binding arms by increasing the melting temperature, in combination with a G14 MOE modification, is particularly advantageous at low Mg^{2+} concentrations as it stabilises the DNAzyme RNA complex. In contrast, at higher Mg^{2+} concentrations, the OMe modification is rather

disadvantageous compared to the unmodified arms, as it is likely to slow down substrate dissociation. In addition, as previously reported, the introduction of the A5C variant impairs catalytic cleavage efficiency, and combining the G14 MOE modification with the A5C variant further impairs it. This additional negative influence can only be depicted from the catalytic data, and not from the measured spectra.

In summary, the DNAzyme 10-23 wt is a dynamic system, and by introducing nucleic acid modifications, particularly those that improve catalytic activity and efficiency, such as the G14 MOE modification, intermediate chemical exchange is promoted, which strongly complicates further evaluation. Taking this into consideration, it is reasonable that, although the G14 MOE modification with its resonances was identified in the free DNAzyme, these pronounced signals were not observed in any of the measured spectra, as the whole complex, but especially the catalytic loop, is also affected by the promoted intermediate chemical exchange. In this regard, using NMR spectroscopy as a tool to gain structural insights on an atomic level into cleavage efficiency-improving modifications localised in the catalytic loop of DNAzyme 10-23 may not be suitable.

3.2 Biophysical characterisation of the DNAzyme 8-17

DNAzyme 8-17 is an RNA-cleaving DNAzyme with a catalytic core consisting of 14–15 nucleotides in length, with a GT wobble base pair, a three-nucleotide-long Watson-Crick base-paired stem, AGC-loop and four to five unpaired residues (Hollenstein, 2015, Santoro and Joyce, 1997, Schlosser and Li, 2010). Throughout a variety of *in vitro* selections, approximately 150 8-17 variants were identified. These variants revealed that in the 8-17 catalytic core sequence, the four residues A6, G7, C13, and G14 are strictly conserved. The DNAzyme 8-17 was selected to cleave all-RNA targets. However, diverse studies characterising the structure and catalytic activity of DNAzyme 8-17 resorted to chimeric-target-constructs composed of RNA and DNA (Liu et al., 2017, Kim et al., 2007b, Mazumdar et al., 2009). Most of the constructs used were all-DNA constructs except for the cleavage site, which was an RNA nucleotide. The chimeric constructs were not chosen for their biological relevance, but for practical reasons. Reasons were explained as: RNA constructs are more costly, and cleavage is “naturally” limited to a specific cleavage site, ensuring cleavage after a certain type of dinucleotide (Schlosser and Li, 2010). The helical type of a double helix varies depending on whether both strands are DNA or one strand is RNA and one is DNA. A DNA-DNA double-strand forms a B-form DNA helix molecule, and an RNA-RNA double-strand forms an A-form double helix. A DNAzyme 8-17 variant demonstrated that the DNAzyme can cleave both RNA and the chimeric target constructs. However, the characterised cleavage activity differs between the two target constructs, with a fourfold higher activity against the chimeric substrate (Schlosser and Li, 2010, Li et al., 2000). Until now, no study has addressed the influence of an all-RNA versus a chimeric DNA construct on the structure and activity of DNAzyme 8-17.

FRET studies, again with all-DNA or chimeric targets, on DNAzyme 8-17, assessed metal ion-induced global folding after addition of Zn^{2+}, Mg^{2+} and Pb^{2+}. In the presence of Zn^{2+} and Mg^{2+}, folding into a compact structure is induced. In the presence of Pb^{2+}, no global folding was observed. It has been established that global folding is saturated at lower Zn^{2+} and Mg^{2+} concentrations than catalytic activity. In combination with metal ion affinity and metal-dependent activity, it was suggested that for Zn^{2+} and Mg^{2+}, global folding happens before cleavage activity; in the presence of $Pb^{2+,}$ global folding is not a necessity (Kim et al., 2007a). The follow-up paper underpinned, using single-molecule FRET, global folding in the presence of Zn^{2+} and Mg^{2+}, but not in the presence of Pb^{2+}, suggesting that DNAzyme 8-17s metal-binding differs according to the metal ion (Kim et al., 2007b).

In 2017, Liu and colleagues were the first to report three precatalytic crystal structures of the 8-17 DNAzyme. Crystallisation was facilitated with an all-DNA target, with a 2’-OMe-guanine (RNA) at the cleavage site, in the presence and absence of Pb^{2+}, and in the presence of the African swine fever virus DNA polymerase X. Three DNAzyme constructs were used, including

Dz36 (36 nucleotide (nt) long, based on the first reported sequence (Santoro and Joyce, 1997)), and two 23nt non-cleavable analogues as an all-DNA construct and one with 2'OMe-guanine at the cleavage site. The DNAzyme 8-17 forms a V-like shape with both arms oriented at a 70° angle. The two arms flanking the catalytic core form a dinucleotide kink at the cleavage site, whereas the catalytic core forms a DNA pseudoknot. The previously predicted canonical Watson-Crick base pairs between G2:C10, C3:G8, and C4:G8 were confirmed. The AGC-loop and four unpaired residues contain two base pairs, G6:C12 and A5:G13. Structural similarities of the metal ion binding site between the Pb^{2+}-bound and a construct without Pb^{2+} indicate that Pb^{2+} binding does not induce local and global conformational changes, which is in agreement with previous FRET results (Liu et al., 2017).

Since the discovery, DNAzyme 8-17 has always been of great interest due to its minimal size and its ability to catalyse, as one of two major DNAzymes, RNA cleavage. Numerous studies characterising structural and functional characteristics have been carried out to broaden potential purposes in usage (Schlosser and Li, 2010). Based on the already decoded structure of DNAzyme 10-23 (Borggräfe et al., 2022), we aimed to resolve the solution structure of DNAzyme 8-17 with RNA as a substrate and to characterise how the choice of a chimeric or full-RNA target affects the activity of the DNAzyme 8-17.

3.2.1 Results and Discussion

The DNAzyme 8-17 is one of the most studied and characterised RNA-cleaving DNAzymes besides the DNAzyme 10-23. Nevertheless, the DNAzymes differ significantly from one another in terms of their structure and metal ion affinity. The precatalytic structure of DNAzymes with an all-DNA target (not RNA) has already been deciphered using X-ray crystallography. Following the recent success from the solved solution-structure of DNAzyme 10-23, it was aimed to solve the solution-structure of DNAzyme 8-17 with an RNA substrate by making use of the structure of DNAzyme 10-23 (Borggräfe et al., 2022). To simplify the analysis, the same arm sequence of the assigned human prion protein DNAzyme 10-23 is transferred to DNAzyme 8-17. This enables the identification of differences and similarities between the RNA-cleaving DNAzymes more easily.

The kinetic assays were performed and measured by Kübra Arslan (Master Student, AG Etzkorn) under my supervision. Dr Jan Borggräfe measured the NMR data of the DNAzyme 10-23.

Only one previous paper shed light on how the choice of a target nucleic acid (DNA/RNA) affects the catalytic activity of the DNAzyme 8-17. The discussed DNAzyme is an 8-17 variant that is a Zn^{2+}-only DNAzyme. It has already been shown for the DNAzyme 8-17 variant that

the choice of target nucleic acids influences activity. In the case of chimeric DNA targets that only carry an RNA nucleotide at the cleavage site, approximately four times higher activity was observed compared to an RNA target. (Li et al., 2000). In our study, we investigated whether the activity of the DNAzyme 8-17 is affected by the choice of nucleic acids in the target, using a time-resolved *in vitro* activity assay. The chimeric target enhances the cleavage activity for both metal ions, $PbCl_2$ and $MgCl_2$ **(Figure 19A, B and C)**. The difference in cleavage activity for RNA and chimeric DNA is significantly greater using $MgCl_2$. The kinetic measurement data were also fitted to determine the k_{obs} values of the cleavage reaction. For 100 µM $PbCl_2$, the k_{obs}-values were fitted for RNA as 0.266 min^{-1} and for chimeric DNA as 0.734 min^{-1}. Whereas for 10 mM $MgCl_2$, the k_{obs}-values were determined for RNA as 0.00325 min^{-1} and for chimeric DNA as 0.0536 min^{-1} **(Figure 19A, B and C)**. Li and colleagues stated that the DNAzyme 8-17E is approximately fourfold faster in cleavage compared to the RNA target when Zn^{2+} is used as a cofactor (Li et al., 2000). For $MgCl_2$, the catalytic activity of DNAzyme 8-17 with chimeric DNA is 16.4-fold higher than with the RNA target and 2.7 times higher with $PbCl_2$. Several other publications found similar results (Schlosser and Li, 2010, Ota et al., 1998). The type of metal ion also influences the difference in catalytic activity between the targets. The measured results raised two questions. Firstly, why is the activity higher for chimeric DNA than for the full RNA target, even though the selection process selects for RNA and not chimeric DNA? Secondly, why is the difference particularly pronounced with $MgCl_2$?

Addressing the first question, several assumptions have already been made to explain the activity difference between the DNAzyme 8-17 and its RNA or chimeric DNA target. Ota and colleagues found the same catalytic reaction rate enhancement due to a chimeric DNA target for the DNAzyme 10-23, and discussed the form of the double helix as a possible reason. The differences in the structure of the duplexes of the DNAzyme and its target (either RNA or chimeric DNA) caused by changes in position, orientation of the bases or functional moieties in the catalytic loop, and changes in the positioning of the metal ion cofactor (Ota et al., 1998). For the DNAzyme 8-17E, the mechanism underlying the catalytic rate enhancement has been compared to that of the hammerhead ribozyme, for which similar observations have been reported. If chemical cleavage is the rate-limiting step, it is suggested that exchanges in the substrate binding region from RNA to DNA result in a ribozyme-substrate complex closer to the structure of the transition state (Li et al., 2000). It can be assumed that similar reasons exist here for the enhancement in the cleavage rate through a chimeric DNA target. These could be examined in more detail using NMR spectroscopy.

Addressing the second question, i.e., why is the difference particularly pronounced with $MgCl_2$? The findings of Wieruszewska et al. must be evaluated (Wieruszewska et al., 2024). The recent publication will be discussed more deeply in Chapter 3.2.2. Previous assumptions about the

structure of the DNAzyme 8-17 with incorporated metal ions suggested that there is an ion-specific folding. Wieruszewska et al. showed that the DNAzyme 8-17 has a very similar tertiary folding with different metal ions. On this basis, it was suggested that there is no ion-specific folding, but a single active structure which is populated with varying probability depending on the metal ion. Metal ions such as Pb^{2+} are catalytically more effective in the DNAzyme 8-17 and stabilise the active structure more strongly. It can be deduced that the reaction speed depends on the distribution of the DNAzymes, which are folded in an active conformation. Some metal ions induce active folding more quickly or more stably, while others may require higher concentrations or more time, thus influencing the reaction speed. In this case, the choice of metal ions and the two targets (RNA or chimeric DNA) effectively amplifies the effect. The cleavage speed when using $PbCl_2$ is so fast that the reaction speed masks the difference between RNA and chimeric DNA targets. It is to be expected that at lower $PbCl_2$ concentrations, the same speed difference between RNA and chimeric DNA targets will become apparent with the $MgCl_2$ used, due to the slower reaction speed.

Moreover, NMR spectroscopy was used to study how the choice of target nucleic acid affects the structure of DNAzyme 8-17. As already explained above, the same nucleic acid sequence of the PrP was used as for DNAzyme 10-23. First, DNAzyme 8-17 with 2'F RNA target was compared with the already assigned spectrum of DNAzyme 10-23 with 2'F RNA as a target **(Figure 19D, full ^{1}H-^{1}H-NOESY/TOCSY in the Supplement Figure 47)**. Interestingly, the ^{1}H-^{1}H TOCSY shows that the arm sequence of both DNAzymes and RNA targets appears to be very similar in structure. The catalytic loop differs between the two variants, which is to be expected, as the two catalytic loops vary in length and secondary and tertiary structure. Unexpectedly, the fingerprint region in ^{1}H-^{1}H TOCSY of the 8-17 DNAzyme with 2'F RNA target **(Figure 19E)** differs greatly from the chimeric DNA target, even though they carry the same sequence (thymine is replaced by uracil in RNA). There are no matching peaks in either the arm region or the loop region. These results suggest that the DNAzyme with RNA target has a different structural geometry and chemical environment compared to its chimeric DNA variant. RNA with 2'OH adopts an A-form helix, which forces the sugar into a C3'-endo conformation. In a B-form helix, which is usually built by DNA-DNA double strands, the sugar is forced into a C2'-endo conformation (Jaishree et al., 1993, Chou et al., 1991). The ideas described above by Ota and colleagues regarding the difference in activity between RNA and chimeric DNA targets also apply in relation to the structure (Ota et al., 1998). In DNAzyme 8-17 with a 2'F RNA target, the arms of the DNAzyme and the target are almost completely assigned, whereas DNAzyme 8-17 with the chimeric DNA target is not assigned at all. Partial assignment of the DNAzyme arms and the target could be used to determine the sugar conformation. However, analysis of DNAzyme 8-17 was not continued due to the recent publication by Wieruszewska and colleagues, who successfully solved the solution structure

of DNAzyme 8-17. Wieruszewska and colleagues discuss in detail the effects of various metal ions on the structure of DNAzyme 8-17 (Chapter 3.2.2).

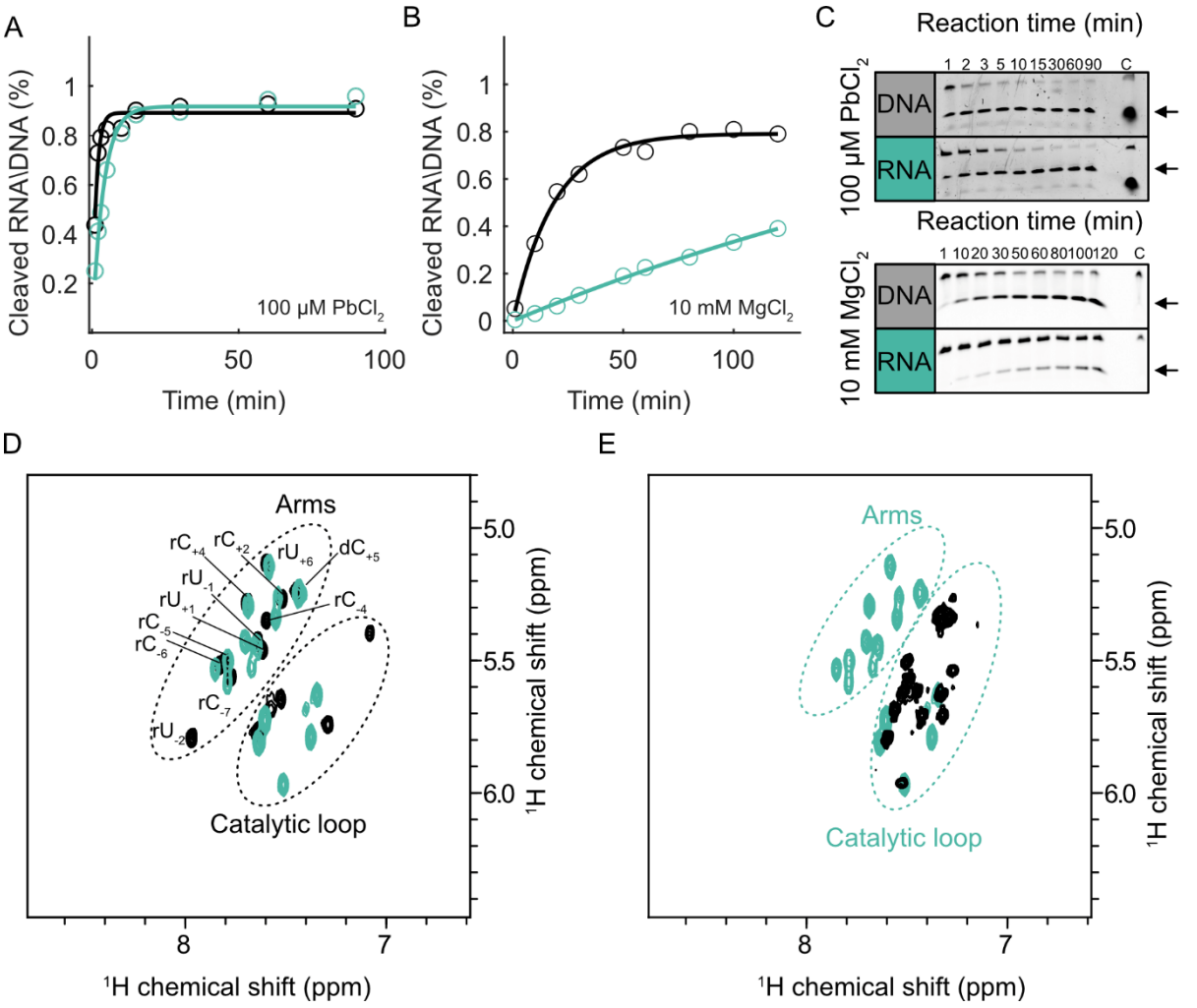

Figure 19: Influence of the target, all-RNA or a chimeric target, on the activity and the structure of DNAzyme 8 -17. A: Time-resolved (min) activity of DNAzyme 8-17 with an RNA (green) and a chimeric DNA (black) target at 37°C with 100 µM $PbCl_2$. Measured data were fitted for the k_{obs} value RNA: 0.266 min^{-1} (R^2 = 0.98) and chimeric DNA: 0.734 min^{-1} (R^2 = 0.94). **B:** Time-resolved (min) activity of the DNAzyme 8-17 with an RNA (green) and a chimeric DNA (black) target of DNAzyme at 37°C with 10 mM $MgCl_2$. Measured data were fitted for the k_{obs} value RNA: 0.00325 min^{-1} (R^2 = 0.99) and chimeric DNA: 0.0536 min-1 (R^2 = 0.99). **C:** Urea-Pages of the DNAzyme kinetics displayed in A and B. **D:** Overlay of two 2D ^{1}H-^{1}H TOCSY spectra. In green DNAzyme 8-17 with 2'F RNA target and in black DNAzyme 10-23 with 2'F RNA target. 2D ^{1}H-^{1}H TOCSY spectrum of DNAzyme 10-23 was measured by Jan Borggäfe. Dashed lines highlight binding arms and catalytic loop, and were extracted from (Borggräfe et al., 2022). **E:** Overlay of two 2D ^{1}H-^{1}H TOCSY spectra. In green DNAzyme 8-17 with 2'F RNA target and in black DNAzyme 8-17 with chimeric DNA target. Dashed lines highlight binding arms and the catalytic loop.

3.2.2 The dynamic world of the 8-17 DNAzyme—A commentary on Wieruszewska, Pawlowicz et al.

The content of this chapter 3.2.2 reflects the content of the following manuscript (published):

The dynamic world of the 8-17 DNAzyme

By

Jessica Felice Schmuck, Jan Borggräfe and Manuel Etzkorn

High-precision DNA-based biocatalysts, known as DNA enzymes or DNAzymes, are experiencing a revival in biotechnological, analytical, and therapeutical applications. Discovered in the 1990s, mechanistic insights in their mode-of-action have been sparse for decades, coinciding with inherent limitations associated with their desired cellular applications. It appears that the current emerging interest in the DNAzyme technology is primarily due to three technological advances: (i) general progress in related nucleic acid-based therapeutics overcoming limitations in DNAzyme delivery, (ii) the availability of chemically modified building blocks to increase bioactivity and stability, and (iii) developments in our mechanistic understanding of the system. The latter gained momentum by deciphering several molecular structures of DNAzymes, starting with the crystal structure of the RNA-ligating 9DB1 DNAzyme (Ponce-Salvatierra et al., 2016), followed by the crystal structure of the 8–17 DNAzyme (Liu et al., 2017), and the recent solution structure of the 10-23 DNAzyme (Borggräfe et al., 2022). The 8–17 and 10-23 DNAzymes are among the most prominent DNAzymes and are capable of target-selective RNA cleavage (Santoro and Joyce, 1997).

The work of Wieruszewska, Pawlowicz et al. now contributes to the solution structure of the 8–17 DNAzyme (Dz) (Wieruszewska et al., 2024). A remarkable feature of the structure (solved in the presence of Zn^{2+} and Na^{+}) is its high similarity to the corresponding crystal structure (solved in the presence of Pb^{2+}). This result reshapes the current understanding of the Dz mechanism, so far been suggested to use different structural arrangements associated with the coordination of different metal ions. To obtain the reported Dz solution structure, Wieruszewska, Pawlowicz et al. optimised the construct design to improve NMR-spectral features **(Figure 20A and B)**. Generating a single-sequence DNA construct with shortened arms **(Figure 20B)** yielded well-resolved data and enabled structure calculation of an NMR ensemble with low RMSD values **(Figure 20C and D)**.

A central aspect of DNAzyme activity is the role of metal ion cofactors, essential for Dz-mediated substrate cleavage. Previous studies have demonstrated that different divalent metal ions can serve as cofactors. The solution structure of Dz was determined in the presence of

Zn^{2+} and Na^{+} and is structurally similar to the crystal structures of Dz in the absence and presence of Pb^{2+} (Liu et al., 2017), this finding is surprising since previous FRET studies showed, that the Zn^{2+} and Mg^{2+} bound forms of Dz are more condensed than the metal ion-free state (Kim et al., 2007b, Kim et al., 2007a). In addition, a condensation step was also observed preceding the metal ion-induced substrate cleavage (Kim et al., 2007b). In contrast, this effect could not be observed for the catalytically more activating Pb^{2+}, which led to the long-standing hypothesis that Pb^{2+}-dependent catalysis follows a different mechanism dictated by a distinct fold (Kim et al., 2007b).

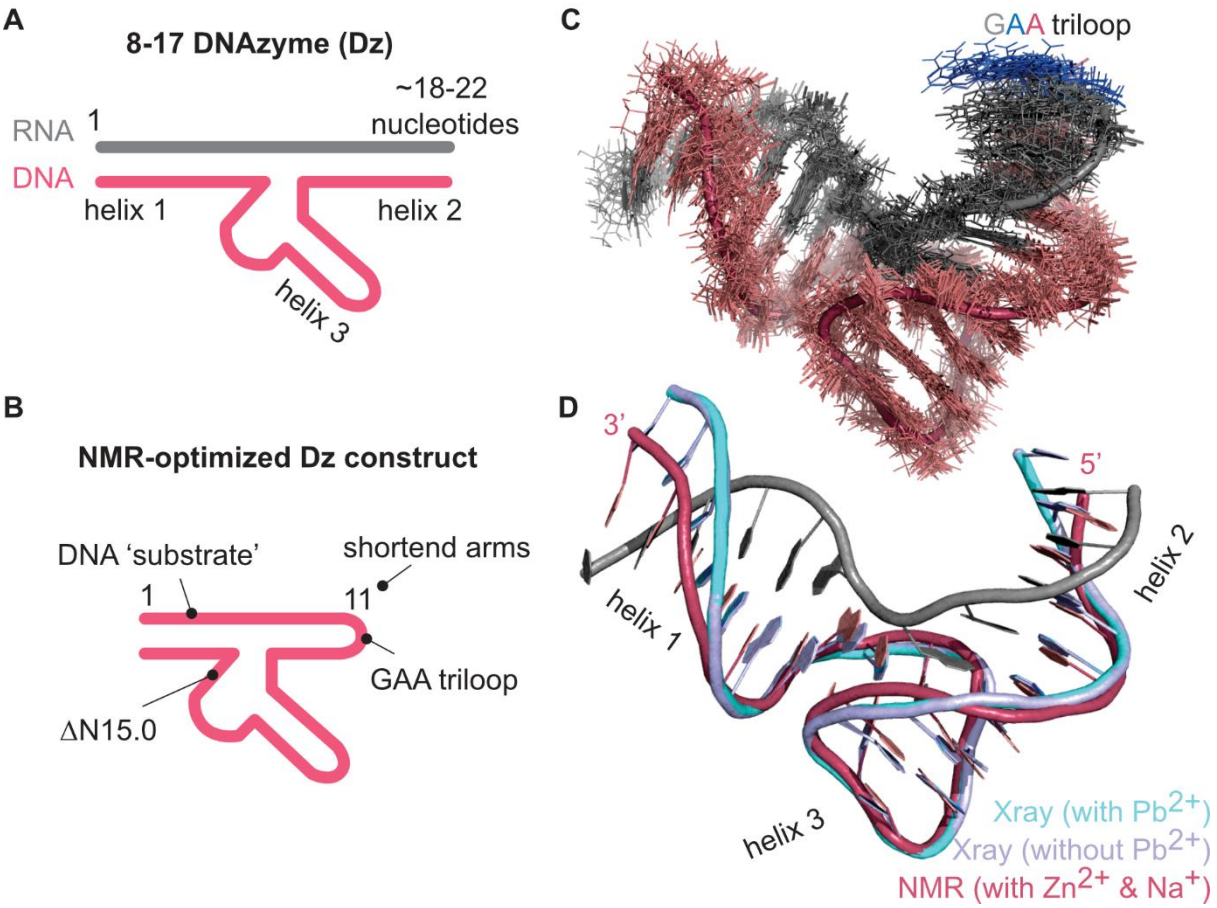

Figure 20:Overview of the 8–17 DNAzyme (Dz) system. Schematics of the general Dz design A: and the construct designed for NMR studies **B:** (b) NMR ensemble (20 structures) determined by Wieruszewska, Pwlowicz et al. (Wieruszewska et al., 2024) using the construct shown in (b). For simplicity, the substrate sequence of the all-DNA construct is shown in grey and the GAA-triloop in indicated colours. **D:** Comparison of recently reported solution structure (pink, pdb code: 8OR8) in the presence of Zn^{2+} and Na^{+}, with previous crystallographic data obtained in the presence (cyan) or absence of Pb^{2+} (purple) (Liu et al., 2017), pdb code: 5XM8 and 5XM9, respectively. For simplicity, the substrate strand is only shown for the NMR structure (grey), and the triloop is omitted.

To better understand and explain the potentially contradicting results, Wieruszewska, Pawlowicz et al. studied the Zn^{2+}, Mg^{2+}, Na^{+}, and Pb^{2+} induced folding by NMR and CD-spectroscopy (Wieruszewska et al., 2024). The respective titration experiments on non-cleavable (all-DNA) constructs revealed comparable structural effects induced by all tested metal ions. However, a substantial dissimilarity between Pb^{2+} and the other tested divalent ions

was detected when the titration was complemented with activity assays. Here, the observed rate constants of Mg^{2+} and Zn^{2+} induced substrate cleavage (k_{obs}) reached saturation in the mM range. This is about two orders of magnitude larger than the observed apparent dissociation constant (K_d) of the respective metal ions that are associated with the Mg^{2+}/Zn^{2+}-induced structural changes. This observation suggests the presence of at least two metal ion binding sites (MBS I and II), one that induces structural condensation (MBS I with high affinity for Mg^{2+} and Zn^{2+}) and a second binding site additionally required for substrate cleavage (MBS II with lower affinity for Mg^{2+} and Zn^{2+}). In strong contrast to Pb^{2+} titrations, k_{obs} is saturated at much lower Pb^{2+} concentrations, which are comparable to the respective K_d values for Pb^{2+} binding to MBS I.

Based on their observations, Wieruszekska, Pwlowicz et al. develop a unified model that can accommodate the previous and current data. According to this model, the interplay of dynamics and conformational plasticity and its modulation by the respective metal ions is the central element of Dz activity **(Figure 21)**. In this regard, the differential affinities of Mg^{2+}/Zn^{2+} to MBS I and II will promote the population of an activated precatalytic complex that is characterised by a structural condensation induced by occupancy of MBS I. Subsequent and less frequent occupation of MBS II will than lead to substrate cleavage. The presence of Pb^{2+}, however, does not lead to a strongly overpopulated condensed form, since comparable affinities to MBS I and II could promote cleavage before stabilising a condensed form over a longer time. Remaining differences in reported behaviours could then be attributed to blind spots in the respective detection techniques, variations in experimental conditions, or differential behaviour associated with different sequences. To further support their model, Wieruszekska, Pwlowicz et al. also pinpoint MBS I via chemical shift perturbations, showing that MBS I is not directly involved in catalysis, and demonstrating that scaffolding the Dz with high concentrations of Mg^{2+} assists cleavage in the presence of Pb^{2+} (Wieruszewska et al., 2024). In light of this model, it can be argued that the solution structure is in its activated condensed form, since all ion-dependent effects are saturated under the applied conditions (i.e., 3 mM Zn^{2+}, 200 mM NaCl). The high similarities to the previous crystal structures of the Dz's Pb^{2+}-bound form and in the absence of Pb^{2+} **(Figure 20D)** further suggest that the respective structures represent the same state and may have formed due to selection bias under the chosen crystallisation conditions.

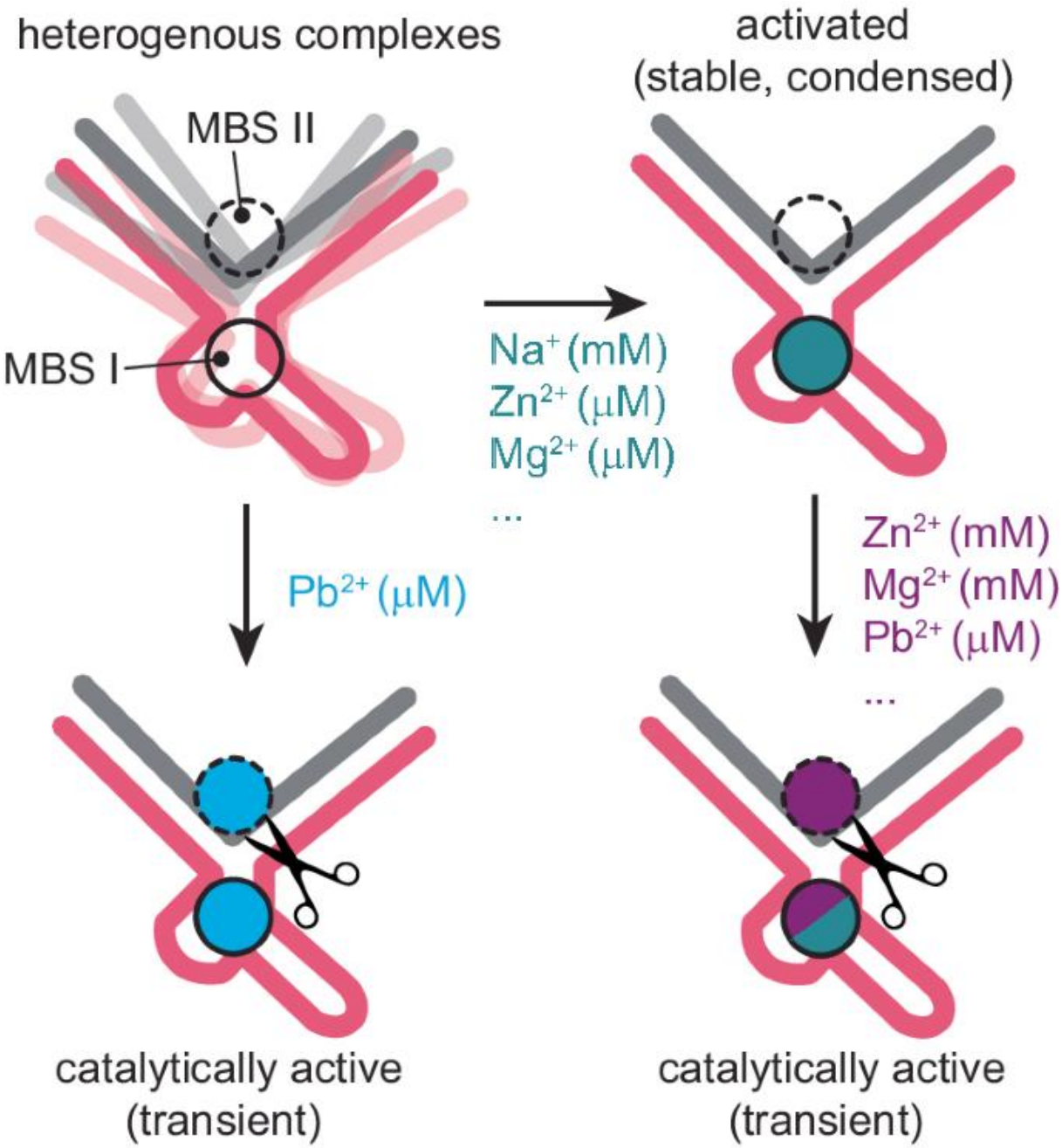

Figure 21: Unifying model proposed by Wieruszekska, Pwlowicz et al. to explain the effect of different metal ions on Dz's structure and activity. According to this model, the DNA's catalytic capability is associated with at least two metal ion binding sites (MBS I and II). Binding in MBS I will induce a condensed state. (Additional) binding in MBS II will promote the cleavage reaction itself. Different metal ions will have differential affinities to the two MBSs (indicated by molarity values in parentheses). Among the tested metal ions, Pb^{2+} has by far the highest affinity for MBS II. As a consequence, the presence of Pb^{2+} will directly promote cleavage without considerably increasing the population of the condensed (activated) state.

Concluding Remarks

In general, the structural data reported by Wieruszekska, Pwlowicz et al. confirm that NMR spectroscopy is a powerful tool to determine a well-defined molecular arrangement of DNAzymes in solution **(Figure 20C)**. Simultaneously, these data also identify the interplay of

multiple conformational, dynamic exchange processes, conformational plasticity, and its modulation by metal ions as central features responsible for the catalytic capability of the system. Excitingly, these features share high similarities with the 10-23 DNAzyme despite their strongly diverging structural architecture (Borggräfe et al., 2022, Borggräfe et al., 2023), suggesting that DNA catalysts are highly dynamic molecules that are exceptionally dependent on the applied measurement condition. In this respect, the strength of NMR spectroscopy is the ability to investigate the system in solution, under adequate buffer conditions and temperatures. However, determining the exact localisation of the central metal ion cofactors is still a bottleneck of the technique and may strongly benefit from complementary crystallographic and molecular dynamic simulations capturing the catalytically relevant state. The dynamic features of the system, as well as a quantitative analysis of the occurrence and population of different states, may be sensitive to construct engineering and crystallisation conditions. Therefore, these aspects must be carefully evaluated when linking the respective structural features with their mechanistic implications in the native system.

The structural and biophysical data reported by Wieruszekska, Pwlowicz et al. unravel key features of the system while highlighting a number of open questions that should be investigated in subsequent studies. These include the importance of buffer conditions to disentangle the effects of monovalent and divalent metal ions and potential cooperative effects between multiple binding sites in FRET studies, as well as possible effects of different arm sequences and artificial modifications.

In conclusion, it appears that a better understanding of the dynamic world of DNA catalysts is emerging as a central element in our view of these fascinating systems. In this picture, specific DNA sequences, which on their own predominantly sample catalytically inactive conformations, can be stabilised in an active conformation by the appropriate metal ions. While this scaffolding step may be required for activity, it may not be sufficient, advocating for the need for a second metal ion for catalysis. Consequently, metal ion-dependent affinities, occupation times in the different binding sites, and cooperative effects determine the population of activated (scaffolded) states as well as catalytic rates. For the 8–17 DNAzyme, the data suggest that Pb^{2+} is a particularly potent cofactor due to its favourable interactions in MBS II that are essential for catalysis.

3.2.3 Summary and Outlook

In summary, it was shown, in agreement with similar publications on other DNAzyme variants, that the choice of target RNA or chimeric DNA significantly influences both DNAzyme activity and structure. Essential aspects regarding the solution structure of DNAzyme 8-17 have already been solved and characterised. Nevertheless, some questions remain unanswered, including how the two targets differ structurally, whether the difference is actually a difference in sugar conformation, or whether other structural factors play a role. Additionally, it is of interest how the choice of nucleic acid affects the conformation of the actual cleavage site and its cleavage activity. To gather a first impression of the helical structure regarding the choice of target nucleic acid, a CD spectrum can be measured to characterise the helical structure. Moreover, NMR spectroscopy can be used to determine the sugar conformation of the duplex. Using DQF-COSY experiments, ^{13}C HSQC, and ^{1}H-^{1}H NOESY spectra, the sugar pucker of DNAzyme complex (RNA or chimeric-DNA) can be determined through measurements of distances between H1'-H2' of NOEs and through scalar couplings between ^{3}J(H1′–H2′) (Clay et al., 2017, Ebrahimi et al., 2001).

3.3 Materials and methods

3.3.1 Chemicals

Information about the used chemicals is listed in **Table 2**.

Table 2: Used chemicals.

Chemical nomenclature	Manufacturer	Chemical formula
Acrylamide:Bisacrylamide (19:1)	Carl Roth, Karlsruhe, Germany	
Ammonium persulfate (APS)	Carl Roth, Karlsruhe, Germany	$(NH_4)_2S_2O_8$
Lead (II) chloride	Merck KGaA, Darmstadt, Germany	$PbCl_2$
Boric acid	ChemSolute, Renningen, Germany	$B(OH)_3$
Bromophenol blue	Riedel-de Haan, Seelze, Germany	$C_{19}H_{10}Br_4O_5S$
Ethylenediaminetetraacetic acid (EDTA)	Acros Organics, Geel, Belgium	$C_{10}H_{16}N_2O_8$
Deuterated Water		^2D_2O
Formamide	Riedel-de Haan, Seelze, Germany	CH_3NO
GelRed	Biotium	$C_{60}H_{72}I_2N_8O_5$
Urea	Sigma-Aldrich, St. Louis, Missouri, USA	$CO(NH_2)_2$
Magnesium chloride	Carl Roth, Karlsruhe, Germany	$MgCl_2$
Sodium chloride	Merck KGaA, Darmstadt, Germany	NaCl
Tetramethylethylenediamine (TEMED)	Merck KGaA, Darmstadt, Germany	$C_6H_{16}N_2$
Tris(hydroxymethyl)aminomethane base (Tris-Base)	Sigma-Aldrich, St. Louis, Missouri, USA	$C_4H_{11}NO_3$
Tris(hydroxymethyl)aminomethane base (Tris-Base) deuterated	Sigma-Aldrich, St. Louis, Missouri, USA	$(DOCD_2)_3CND_2$
Xylene Cyanole FF	Serva, Heidelberg, Germany	$C_{25}H_{27}N_2NaO_6S_2$

3.3.2 Buffer solutions

Buffers and solutions were used as listed below **(Table 3)**. Unless otherwise stated, the quantities refer to 1 L of distilled water. Table 3: Used buffers and solutions.

Table 3: Used buffers and solutions.

Name	Contents	pH
10x TBE buffer	890 mM Tris-Base	8.2

	890 mM Boric acid	
	20 mM EDTA	
4x Kinetic reaction buffer	200 mM Tris-Base	7.5
	560 mM KCl	
	40 mM NaCl	
	0.4 mM EDTA	
Loading Dye	95% (v/v) Formamide	8.0
	0.5 M EDTA	
	Bromophenol blue	
	Xylene Cyanole FF	
GelRed staining solution	5 mL 1x TBE buffer	8.0
	5 µL GelRed	
	45 mL H_2O	

3.3.3 Constructs

Used DNAzymes are listed in **Table 4**.

Table 4: Used DNAzymes. DNA modifications are highlighted in the sequence by a specific colour.

DNAzyme	Sequence 5'-3'	Type	Modifications	Manufacturer
Dz46 (full modified)	tgg ggt aag gct agc uac aac gag gtg cat	10-23	LNA, OMe, 2O-MOE, PS	Chaput Lab (University of California, Irvine, CA, USA)
Dz46nmr2 (full modified)	tgg ggt aag gct agc uac acc gaa gtg cat	10-23	LNA, OMe, 2O-MOE, PS	Chaput Lab (University of California, Irvine, CA, USA)
Var1 wt	ttg ggt aag gct agc tac aac gaa gtg cat	10-23	none	Biomers (Ulm, Germany)
Var2 wt (G14 2O-MOE)	ttg ggt aag gct agc tac aac gaa gtg cat	10-23	2O-MOE	Biomers (Ulm, Germany)
Var3 A5C	tgg ggt aag gct cgc tac aac gga gtg cat	10-23	none	Biomers (Ulm, Germany)
Var4 A5C (G14 2O-MOE)	tgg ggt aag gct cgc tac aac gga gtg cat	10-23	2O-MOE	Biomers (Ulm, Germany)

Var5 wt (OMe arms)	ttg ggt aag gct agc tac aac gaa gtg cat	10-23	OMe	Biomers (Ulm, Germany)
Var6 wt (OMe arms, G14 2O-MOE)	ttg ggt aag gct agc tac aac gaa gtg cat	10-23	OMe, 2O-MOE	Biomers (Ulm, Germany)
Var7 A5G	ttg ggt aag gct ggc tac aac gaa gtg cat	10-23	none	Biomers (Ulm, Germany)
Dz839 wt	Ttg ggg taa ggc tag cta caa ca ggt gca tgt	10-23	none	Biospring (Frankfurt, Germany)
DNAzyme 839 P	ttg ggg tat ccg agc cgg acg agg tgc atg t'	8-17	none	Biospring (Frankfurt, Germany) NMR, Biomers (Ulm, Germany) activity assay.
DNAzyme 839 (A5C)	ttg ggg taa ggc tcg cta caa cga ggt gca tgt-	10-23	none	Biospring (Frankfurt, Germany

Suitable targets for the DNAzyme are listed in **Table 5**. Modifications in the RNA or DNA are highlighted in red.

Table 5: Used DNAzyme targets.

Target	**Sequence 5'-3'**	**Modifications (highlighted in red)**	**Manufacturer**
Dz46sub2	aug cac ugu uac ccc a	2'Fluorine-guanine	Biomers (Ulm, Germany
T839 wt	aca ugc acc guu acc caa a	2'Fluorine-guanine	Biomers (Ulm, Germany
T839 RNA	aca ugc acc agu acc cca a	none	Biomers (Ulm, Germany)
T839 DNA rA	aca tgc acc agt acc cca a	Ribonucleotide a	Biomers (Ulm, Germany)
T839 RNA	aca ugc acc agu acc cca a	2'Fluorine-guanine	Biospring (Frankfurt, Germany)

T839 DNA	aca tgc acc agt acc cca a	none	Biospring (Frankfurt, Germany)
T839	aca ugc acc guu acc cca a	2'Fluorine-guanine	Biospring (Frankfurt, Germany)

3.3.4 *In vitro* DNAzyme activity assays

For the sample, target RNA/DNA and DNAzyme were pipetted into a reaction tube; for the control, DNAzyme was replaced with water **(Table 6)**. Samples were heated to 73°C for 5 minutes and cooled for 10 minutes at room temperature. Samples were centrifuged for 10 seconds at 7000 x g at room temperature. H_2O and 4x Tris buffer were added to the samples and incubated for 30 minutes at 37°C in a heating block. The cleavage reaction was started by adding either $PbCl_2$ or $MgCl_2$ to the samples and the control. The reaction was carried out for a total of 2 h at 37°C. At distinct time points, 10 µL samples were taken, and the reaction was stopped by adding loading dye (ratio 1:1).

Table 6: Experimental approach for in vitro activity assay.

Component	Quantity (µL)	
Target RNA/DNA	1	Sample
DNA	4	
4x Kinetic buffer	10	
Water	20	
Target RNA/DNA	1	Control
DNA	0	
4x Kinetic buffer	10	
Water	24	
$PbCl_2$ (800 µM Stock)	5	Sample/Control
$MgCl_2$ (80 mM Stock)	5	

3.3.5 Denaturing Urea Polyacrylamide Gel Electrophoresis (Urea PAGE)

Urea Page is an electrophoresis-based separation technique for short nucleic acids, using 6–8 M Urea as a denaturation detergent to denature secondary structural elements of the nucleic acids. To pour a Urea gel **(Table 7)**, Urea, 10x TBE buffer, and acrylamide: bisacrylamide (19:1) are combined. Since being highly concentrated, Urea is usually not dissolved at room temperature, the mixture is heated up in the microwave for 5–10 seconds. The mixture is mixed using a magnet fish and a magnet stirrer. The mixture is filled with water up to 8 mL. After each of the following two steps, the sample is properly mixed by turning the sample a few times upside down. APS and, after that, TEMED are added. The mixture is then poured or pipetted

between the glass plates of an already prepared SDS PAGE gel cassette. Afterwards, a suitable comb is inserted into the gel.

Table 7: Components for a single 15% Urea gel.

Components	Quantity
Urea (6-8 M)	3.6 g
10x TBE buffer	800 µL
Acrylamide:Bisacrylamide (19:1)	3.6 mL
10% APS	80 µL
TEMED	8 µL

The Urea-Page is pre-run for approximately 30 minutes before sample injection to heat the gel in 1x TBE buffer at 40 mA. This is intended to prevent the formation of secondary structures in nucleic acids. If the pockets are dirty and blocked with gel remains and Urea, the pockets should be flushed. After the pre-run, 10 µL of the samples are pipetted into the gel pockets, and the Urea page is run for 30–60 minutes at 40 mA. If non-fluorescent samples were used, the gels are incubated in GelRed staining solution for 5 minutes, followed by a gentle wash in H_2O for 5 minutes. Gels are analysed with a gel documentation system (Gel Doc XR+ Gel Documentation System, BioRad, Hercules, California, USA). Gels were analysed using ImageJ (Wayne Rasband), MATLAB R2021a (MathWorks, Natick, USA) and Excel (Microsoft Office 2021, Redmond, USA). Data was fitted using Equation 1 (Rosenbach et al., 2020b).

Equation 1: Fit cleaved RNA ([$RNA_{cleaved}$]) over time (t). k_{obs} – observed first-order rate constant, t – time in (min).

$$[\mathrm{RNA_{cleaved}}]_t = [\mathrm{Dz{:}\,RNA}] \cdot (1 - e^{(k_{obs}\, t)})$$

3.3.6 FRET assay

Förster resonance energy transfer is a fluorescence method making use of energy transfer between two fluorophores in proximity or one fluorophore and one quencher. The energy is transferred from a donor-fluorophore to an acceptor-fluorophore through intermolecular long-range dipole–dipole coupling (Sekar and Periasamy, 2003). In our case, all used samples possess a 5'FAM fluorophore and 3' black hole quencher 1 (BHQ1). Using a quencher as an acceptor, fluorescence is quenched as long as both molecules are in proximity. Samples were prepared as described above in Chapter 3.3.4. However, the samples were not incubated in the heating block, but 20 µL per well were pipetted into a microtiter plate, sealed with sealing tape and incubated in the Tecan Spark 10M (Männedorf, Switzerland) for 30 minutes at 37°C. Before the incubation step, if necessary, prewarmed water is added with the injector. At the

start of the measurement, 30 cycles of fluorescence are measured to determine the baseline. Subsequently, the appropriate amount of $MgCl_2$ (final concentration between 1 and 2 mM MgCl2) is pipetted into the designated wells using an injector. Control experiments were performed using either the A5G variant (inactive DNAzyme) of the DNAzyme or in the absence of DNAzyme, but still in the presence of $MgCl_2$. Reaction was measured for at least 3 hours, up to 8 hours. Measurement parameters can be depicted from **Table 8**. Results were evaluated using Excel (Microsoft Office 2021, Redmond, USA) and MATLAB R2021a (MathWorks, Natick, USA). Data was fitted and plotted using a MATLAB script of Justin Darwin Böcker (can be found in his doctoral thesis).

Table 8: Used FRET assay measurement parameters.

Parameters	Value
Temperature	37°C
Plate	Corning 384 Flat Black [COS384fb]
Measurement	Fluorescence Top Reading
Excitation wavelength	485 nm
Excitation bandwidth	20 nm
Emission wavelength	535 nm
Emission wavelength	20 nm
Gain	45 (manual)
Number of flashes	20
Integration time	40 µs
Z-Position	19500 µM

3.3.7 NMR spectroscopy

DNA oligos were obtained from Biospring (Frankfurt, Germany) in the case of the DNAzyme 8-17 and for the DNAzyme 10-23 from Biomers (Ulm, Germany). DNA samples were resuspended in pure water. DNAzymes with target RNA were measured at a concentration of either 200 µM or 500 µM in 50 mM deuterated Tris pH 7.5, 100 mM NaCl, and 10% (v/v) D_2O. All NMR experiments were recorded with a 200 µl sample volume in a 3 mm NMR sample tube at 37°C. 1D ^{1}H, 2D ^{1}H-^{1}H NOESY/ TOCSY and ^{1}H-^{13}C HSQC experiments were measured at 20°C, 25°C, 37°C or 45°C using a Bruker spectrometer (Avance III HD+ or NEO), equipped with inverse detection triple-resonance z-gradient cryogenic probes, operating at a ^{1}H frequency of 700, 750, 900 MHz or 1.2 GHz. TOCSY experiments were recorded with 80 or 120 ms of mixing time. NMR data were processed using Topspin 3.6.5 or 4.4.0. Spectra were analysed and plotted using Cara 1.9.1.7, Topspin 3.6.5 or 4.4.0.

4 Biophysical characterisation of doxorubicin interaction with MDM2-119 Quadruplex

Cancer is one of the leading causes of death in Western countries. Well-differentiated liposarcoma (WDLPS) is associated with the MDM2 genomic region. MDM2 is an oncogene which serves as the master regulator of the tumour suppressor protein p53. P53 is a transcription factor that activates the expression of several genes and is critical for regulating the cell cycle, apoptosis and genomic stability (Wang et al., 2023). Overexpression of MDM2 enhances p53 degradation, leading to inhibited cell apoptosis and supporting tumour cell survival. A recent publication revealed that the MDM2 promoter folds a stable G-quadruplex (Lago et al., 2021).

Doxorubicin (DOX) **(Figure 22)** is one of the most effective cancer therapeutics used to treat a broad spectrum of cancers, e.g., breast cancer, carcinomas, sarcomas, and haematological malignancies (Carvalho et al., 2009, Kciuk et al., 2023). Doxorubicin is categorised as a topoisomerase II inhibitor, introducing DNA double-strand breaks and then hindering the action of topoisomerases (Bukowski et al., 2020, Kciuk et al., 2023). Topoisomerases are involved in DNA replication by unwinding or twisting the helix structure of the DNA double-strand. For now, the exact consequences of intercalation are not sufficiently understood, but several theories exist explaining that, e.g., intercalation changes the topology of DNA or destabilises nucleosomes. Doxorubicin is considered to intercalate with DNA through the formation of hydrogen bonds with guanines in adjacent GC base pairs (Kciuk et al., 2023).

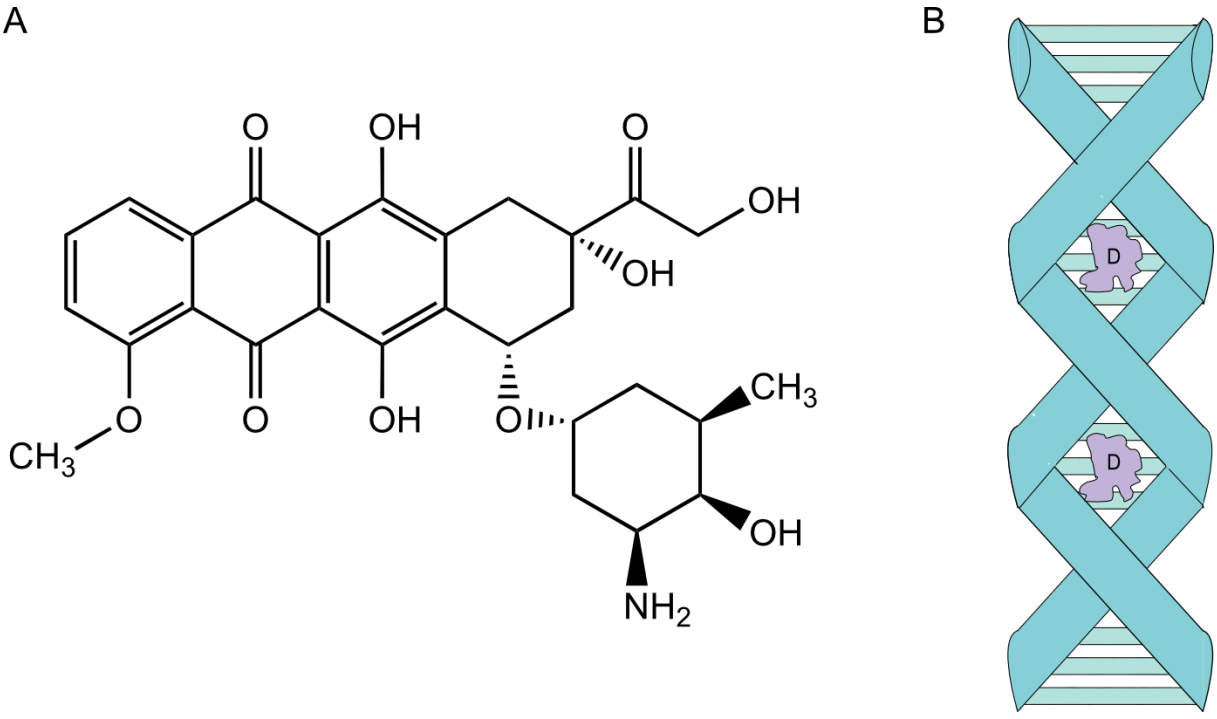

Figure 22: Chemical features of doxorubicin. A: Chemical structure of doxorubicin. **B:** Doxorubicin intercalates double-stranded DNA**.**

In 2016, Scaglioni and colleagues revealed the interaction of doxorubicin and nemorubicin, a doxorubicin derivative, and the G-quadruplex c-MYC. Both show a similar binding mode by intercalating between A3 and G4 of the c-MYC quadruplex $d(TTAGGT)_4$ and the formation of a cap-complex at the G6pT7 site. Adenine is essential for the interaction with doxorubicin, as adenine-exchanging experiments have revealed. Moreover, nemorubicin binds to Pu22 at the 3' and 5'-end. Nemorubicin and Pu22 form a stable complex, where both nemorubicin molecules form an additional plane to the tetrad by stacking over each other (Scaglioni et al., 2016).

Especially in human telomeres, ribosomal DNA and gene promoters, G-quadruplex structures are present and serve as a novel target for cancer treatment. Stabilising G-quadruplex structures by small molecules aims to inhibit enzyme activity. Cell treatment of the gene promoter MDM2 with G-quadruplex-ligands decreased the expression of MDM2 and p53 degradation, resulting in apoptosis (Lago et al., 2021). In cooperation with the Universitätsklinikum Düsseldorf (AG Myelodysplastic Syndrome, Prof. Dr. Gattermann, Dr Fatemeh Majidi), we aim to study the interaction between doxorubicin and the G-quadruplex-forming MDM2, using biophysical methods (NMR, CD and UV-Spectroscopy). These studies can help enhance the understanding of possible interactions between the quadruplex and doxorubicin and introduce doxorubicin as a potential new drug in the treatment of dedifferentiated liposarcoma (DDLPS).

4.1 Results and Discussion

MDM2 is an oncogene which serves as the master regulator of the tumour suppressor protein p53. Overexpression of MDM2 is associated with p53 degradation, leading to tumour cell survival. A recent publication revealed that the MDM2 inducible promoter G-rich region folds into stable G-quadruplexes both *in vitro* and *in vivo*. Different sequences of the MDM2 region appear to form different stable G-quadruplex structures (rated with a G-score). The G-score is a numerical value that quantifies the probability that DNA and RNA sequences will form a G-quadruplex structure and is usually predicted via an algorithm (Bedrat et al., 2016, Puig Lombardi and Londoño-Vallejo, 2020). MDM2-119 was rated with a G-score of 93 and possesses a hybrid G-quadruplex conformation. The cancer therapeutic doxorubicin can bind to G4-quadruplexes such as c-MYC (Lago et al., 2021, Scaglioni et al., 2016).

First, it was investigated whether MDM2-119 forms a stable, hybrid G-quadruplex structure in the presence of high potassium chloride concentrations. 1D ^{1}H NMR spectrum of MDM2-119 with potassium chloride showed proton resonance peaks between 10–12.5 ppm **(Supplement Figure 48E)**, which are characteristic of guanine imino protons (Hoogsteen base pairs) in G-quadruplexes (Adrian et al., 2012). The observed peak distribution in a ^{1}H-^{1}H TOCSY spectrum, along with a defined imino proton signal, supports the presence of a folded structure (**Figure 23A, black peaks, Supplement Figure 48D, black)**. A CD spectrum (200–350 nm) of MDM2-119 **(Figure 23B, black curve)** shows the characteristic curve progression of a hybrid G4-quadruplex topology. Hybrid G4-quadruplexes usually have their curve maximum at ~ 260 nm, and their curve minima at ~295 nm and ~240–245 nm (Małgowska et al., 2012, Del Villar-Guerra et al., 2018). The topology of G4-quadruplexes always depends on pH value, buffer, salt concentration and temperature, and therefore always deviates slightly from the topologies specified in the literature. The curve progression of the MDM2-119 CD spectrum was fitted using reference spectra of G4-quadruplexes with a characterised and stable topology, revealing 95.5% hybrid and 4.5% parallel topology **(Supplement Figure 48A, black bars)**. The presented data prove that in the presence of high potassium chloride concentrations, MDM2-119 folds into a stable, hybrid G4-quadruplex conformation. The hybrid G4-Quadrulex MDM2-119 is suitable for investigating interaction with the cancer therapeutic agent doxorubicin.

A previous study on the G4-quadruplex c-MYC, with doxorubicin and nemorubicin, a derivative of doxorubicin, showed interaction and stabilisation through binding between the G-quadruplex and the cancer therapeutic (Scaglioni et al., 2016). To investigate whether doxorubicin interacts with the MDM2-119 G4-quadruplex, diverse biophysical experiments were carried out. The hybrid topology of the CD spectrum of MDM2-119 with two equivalents of doxorubicin **(Figure 23B, blue curve)** changed slightly regarding the amplitude of the minima and maxima.

The fitted topology reveals 98.34% hybrid and 1.66% antiparallel topology **(Supplement Figure 48A, blue bars)**. A strong change in the peak distribution in a ^{1}H-^{1}H TOCSY **(Figure 23A, blue peaks)** can also be seen. However, the spectrum features broad, weak peaks and a poor signal-to-noise ratio. The poor resolution may be caused by the suboptimal pH value of 7.2 (Adrian et al., 2012). ^{1}H NMR spectrum of MDM2-119 **(Supplement Figure 48D, black)** showed narrow proton resonance peaks between 10 and 12.5 ppm. In the ^{1}H NMR spectrum of MDM2-119 with two equivalents of doxorubicin **(Supplement Figure 48D, blue)**, proton resonance peaks broadened and shifted between 10 and 13 ppm. As a result, some of the signals are no longer in the classic Hoogsteen imino base pair range but in the Watson-Crick base pair range. However, it is not clear whether the peaks have simply broadened or whether a type of base pairing has changed due to the addition of doxorubicin. As doxorubicin does not have peaks in the Watson-Crick base pair range, this may indicate that the additional peaks occur due to the interaction between the G-quadruplex and doxorubicin through hydrogen bonds. Line broadening of peaks usually indicates a change in the dynamics or heterogeneity of the system without destroying the quadruplex. Additional checks were carried out to determine whether the proton resonances of doxorubicin could be identified in the spectrum of MDM2-119 with doxorubicin **(Supplement Figure 48G)**, which was not the case. Moreover, it was tested whether potassium is still essential for quadruplex formation **(Supplement 13 Figure 48F)**, which was the case. In summary, all measured parameters hint at the binding of doxorubicin to the hybrid quadruplex MDM2-119.

After determining that doxorubicin is binding to MDM2-119, the most important question, whether the binding is stabilising or destabilising the G-quadruplex, needs to be answered. In the already mentioned study, nemorubicin and doxorubicin stabilised c-MYC. However, the interaction of nemorubicin with c-MYC was more specific than that of doxorubicin (Scaglioni et al., 2016). Using CD-spectroscopy, melting curves **(Figure 23C, D and Supplement Figure 48B and C, blue lines and black lines)** of the G4-quadruplex with and without two equivalents of the ligand were measured and fitted using the Boltzmann equation. Addition of doxorubicin to MDM2-119 increased the melting temperature by approximately 6°C from 67.8°C to 73.94°C. The fit **(Supplement Figure 48B)** also shows that the melting curve is less steep. The derivative plot of the melting data **(Supplement Figure 48C)** clearly indicates that the addition of doxorubicin results in a wide melting transition. The melting curves of MDM2-119 with and without doxorubicin were measured at different wavelengths due to a divergent signal shift between the sample with and without doxorubicin. To validate these results, FRET-based melting experiments were carried out. The MDM2-119 G4-quadruplex was equipped 5'-end with Atto 647N at the 3'-end and BBQ-650. Fluorophore and quencher were selected so that the emission of doxorubicin does not interfere with the detection of the signal. Doxorubicin absorbs around 500 nm and emits light usually between 560–600 nm (Shah et al., 2017). If

the MDM2-119 G4-quadruplex attached with quencher and fluorophore is melting, the fluorescence signal must arise proportionally to the melting of the structures. Both melting curves of MDM2-119 with and without doxorubicin **(Figure 23E)** do not reach a melting plateau. As a result, neither curve can be fitted, and no actual melting point can be determined. However, the melting curve of MDM2-119 with doxorubicin is less steep. The derivative of both melting curves **(Figure 23F)** indicates that for MDM2-119, small structures are melting between 50–80°C, and those features are missing in the MDM2-199 with doxorubicin sample. Usually, CD-spectroscopy is more sensitive to the melting of secondary structural elements, since the method directly detects changes in the secondary structure. This could explain why no melting point could be detected using FRET-based melting experiments. Overall, the FRET-based melting experiment results confirm that doxorubicin is stabilising the G-quadruplex MDM2-119.

Scaglioni and colleagues determined that doxorubicin intercalates between the A3 and G4 of c-MYC and forms a cap-complex at the G6pT7. Mutation experiments revealed that adenine is essential for the interaction, and only one doxorubicin molecule binds per quadruplex (Scaglioni et al., 2016). CD titration experiments **(Figure 23G)** with a stable MDM2-119 concentration and an increasing doxorubicin concentration were carried out. The data reveal that after approximately 1.5 equivalents of doxorubicin, the CD curves are saturated. The data also suggest that for MDM2-119, only one molecule binds per G4-quadruplex. MDM2-119 also possesses a single adenine in the oligonucleotide sequence, which is part of an outer turn and not directly involved in the quadruplex structure. These data suggest that a similar type of binding as with doxorubicin and c-MYC may exist. However, further experiments must be conducted to verify this hypothesis.

In summary, MDM2-119 forms a stable hybrid G-quadruplex and is suitable for interaction studies with doxorubicin. Doxorubicin binds to MDM2-119 and stabilises the structure. Doxorubicin may have a similar binding type to MDM2-119 compared to c-MYC.

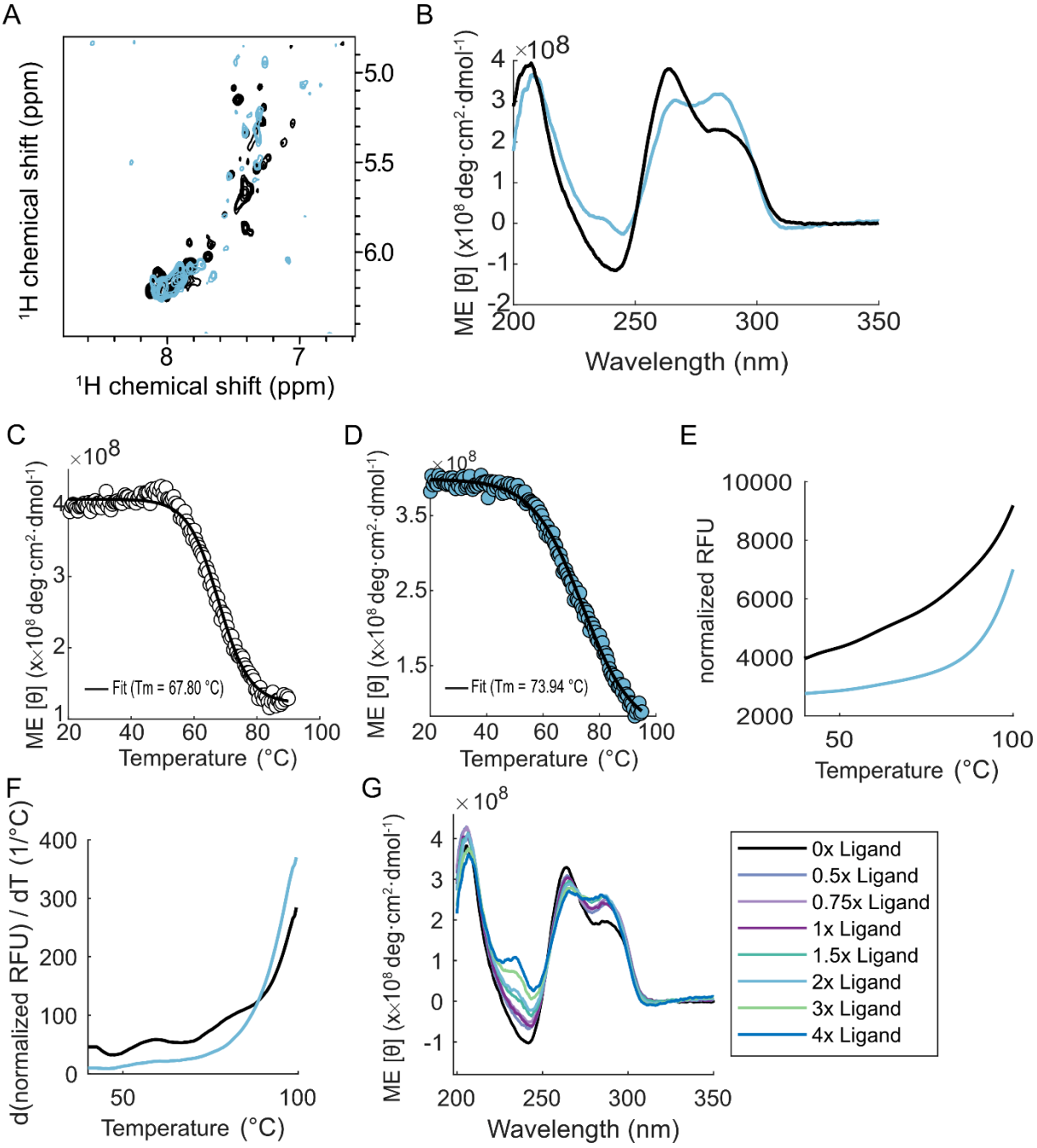

Figure 23: Characterisation of G-quadruplex MDM2-119 interaction with chemotherapeutic doxorubicin. Black lines and peaks are MDM2-119, and blue lines and peaks are MDM2-119 with two equivalents of doxorubicin. **A:** ^{1}H-^{1}H-TOCSY Fingerprint of MDM2-199 with and without doxorubicin in 20 mM potassium phosphate, pH 7.2, and 100 mM KCl at 37 °C. **B:** CD-spectrum of MDM2-119 with and without doxorubicin (two equivalents) in 20 mM potassium phosphate, pH 6.2, and 100 mM KCl at 25°C. Molar ellipticity (ME, deg cm^2 dmol^{-1}) plotted against measured wavelength in nm. **C:** Melting curve (20–90°C) of MDM2-119 in 20 mM potassium phosphate, pH 6.2, and 100 mM KCl measured at 285 nm. The melting point was fitted using the Boltzmann equation and determined as 67.80 °C. **D:** Melting curve (20–95°C) of MDM2-119 with doxorubicin (two equivalents) in 20 mM Potassium phosphate, pH 6.2, and 100 mM KCl measured at 266 nm. The melting point was fitted using the Boltzmann equation and determined as 73.94 °C. **E:** qPCR melting curve (40–100°C) measurement of MDM2-119 with and without doxorubicin (two equivalents), normalised RFU plotted against temperature (°C) in 20 mM potassium phosphate, pH 6.2, and 100 mM KCl. **F:** Derivation of normalised RFU (derived from E) plotted against the temperature (°C). **G:** CD titration experiments plotting ME against the wavelength (nm). Titration of diverse equivalents of doxorubicin (0x, 0.5x, 0.75x, 1x, 1.5x, 2x, 3x, and 4x) to a stable MDM2-119 concentration at 25°C in 20 mM potassium phosphate, pH 6.2, and 100 mM KCl.

Moreover, the question arose whether doxorubicin binds to any kind of G4-quadruplex, since it is known to intercalate with DNA, or does it only bind sequence-specifically to distinct types of G-quadruplexes? Three well-established quadruplex topologies were used to test the interaction with doxorubicin: a hybrid quadruplex belonging to telomere 26 (Ambrus et al., 2006), an antiparallel quadruplex belonging to the thrombin-binding aptamer (Boyle et al., 2022), and a parallel quadruplex HIV-integrase aptamer (Kelley et al., 2011). As a positive control, an antisense DNA duplex was used. The topology of the duplex DNA **(Figure 24 A, black)** usually has its curve maxima between ~260–280 nm and its minimum of ~245 nm (Chang et al., 2012). Melting curves **(Figure 24B, D, F and H)** for all three G4-quadruplexes and the DNA duplex with and without two equivalents of the ligand were measured and fitted using the Boltzmann equation. Melting curves of DNA duplex with and without doxorubicin prove that doxorubicin is binding to DNA duplexes through increased melting temperatures by approximately 6.6°C from 66.45°C to 73.07°C. The hybrid topology of the CD spectrum of telomere 26 with two equivalents of doxorubicin **(Figure 24C)** changed strongly regarding the increased amplitude of the minima and maxima. Melting curves of DNA hybrid quadruplex telomere 26 with and without doxorubicin indicate weaker interaction, suggesting that doxorubicin slightly destabilises the quadruplex through decreased melting temperatures by approximately 1.69°C from 63.69°C to 61.99°C. Interestingly, the telomere 26 sequence contains various adenines, but no dinucleotide with the sequence ‘AT’, only ‘TA’. The antiparallel topology of the CD spectrum of the thrombin-binding aptamer with two equivalents of doxorubicin **(Figure 24E)** is not changed. Melting of the quadruplex with and without doxorubicin **(Figure 24F)** is only slightly altered from 52.32°C to 51.89°C, suggesting no interaction of doxorubicin with the antiparallel quadruplex. The quadruplex sequence does not carry adenine residues. The parallel topology of the CD spectrum of the HIV-integrase aptamer with two equivalents of doxorubicin **(Figure 24G)** remains unchanged. Melting of the quadruplex with doxorubicin is slightly increased by approximately 2°C from 79.82°C to 81.79°C, indicating a slight binding of doxorubicin to the quadruplex. The nucleotide sequence of the parallel quadruplex does not carry an adenine.

In summary, it is unclear whether structural features or the sequence of a G-quadruplex promote the binding of doxorubicin. However, it can be observed that doxorubicin does not bind to every quadruplex. Comparing the data on the different quadruplex melting point shifts caused by doxorubicin with that of the melting point shift of duplex DNA and the quadruplex MDM2-119, it is noticeable that the shifts are significantly greater (at least 6°C). This difference points towards a specific binding of doxorubicin to the quadruplex MDM2-119.

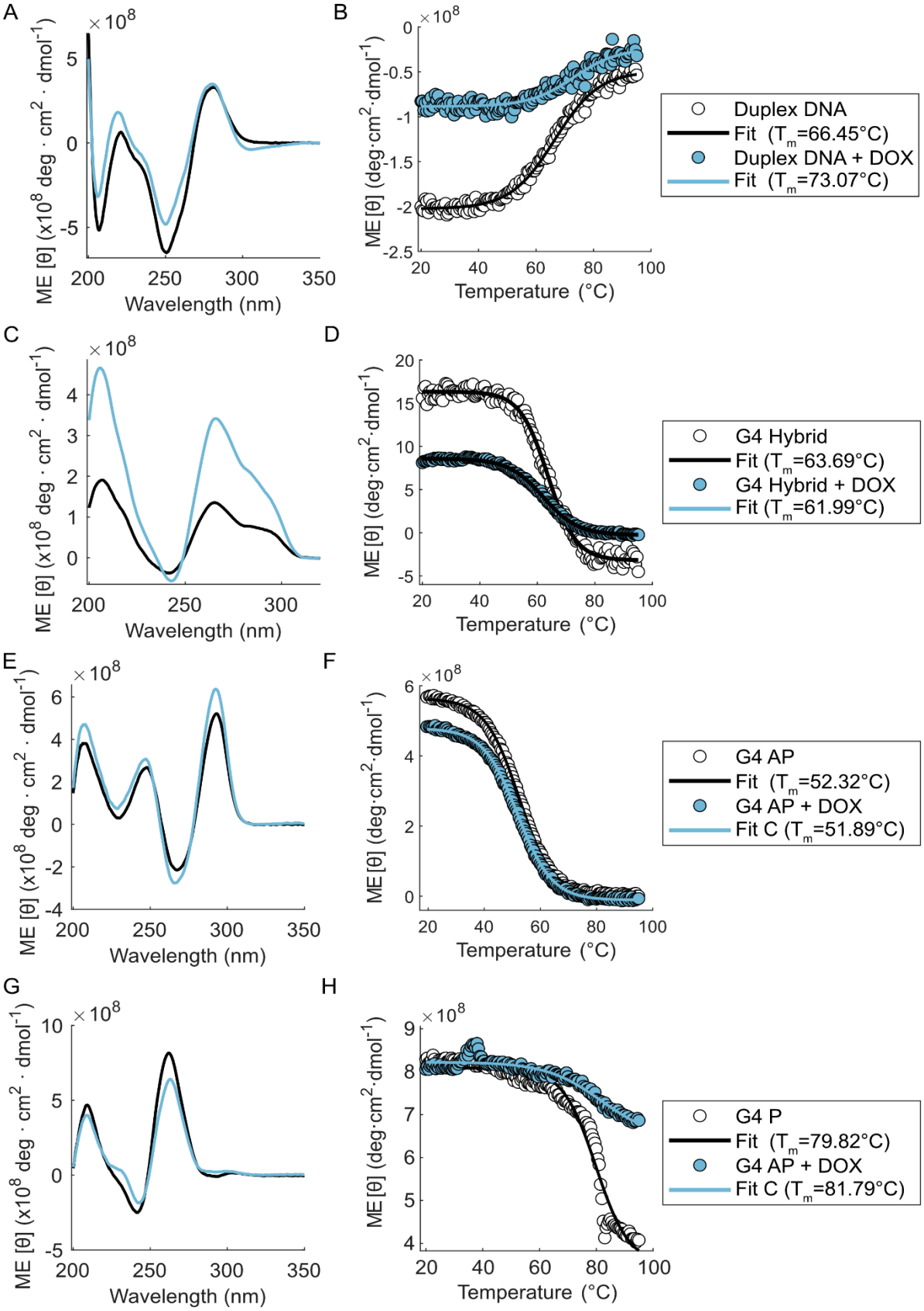

Figure 24: Characterisation of doxorubicin interaction with DNA duplex, AP, Parallel and Hybrid quadruplexes using CD-spectroscopy. All samples were measured in 20 mM potassium phosphate, pH 6.2, and 100 mM KCl. Black lines are MDM2-119, and blue lines are MDM2-119 with two equivalents of doxorubicin. The melting point was fitted using the Boltzmann equation. **A:** Full CD spectrum of duplex DNA with and without doxorubicin at 25°C. **B**: Melting curve (20–95°C) of duplex DNA with (66.46°C) and without doxorubicin (73.07°C) measured at 206 nm. **C:** Full CD spectrum of hybrid DNA G4-quadruplex with and without doxorubicin at 25°C. **D:**

Melting curve (20**–**95°C) of hybrid DNA G4-quadruplex with (63.69°C) and without doxorubicin (61.99°C) measured at 295 nm. **E:** Full CD spectrum of antiparallel (AP) DNA G4-quadruplex with and without doxorubicin at 25°C. **F:** Melting curve (20–95°C) of AP DNA G4-quadruplex with (52.32°C) and without doxorubicin (51.89°C) measured at 294 nm. **G:** Full CD spectrum of parallel DNA G4-quadruplex with and without doxorubicin at 25°C. H: Melting curve (20–95°C) of parallel DNA G4-quadruplex with (81.79°C) and without doxorubicin (79.82°C) measured at 262 nm.

4.2 Conclusion and Outlook

MDM2-119 forms a stable, hybrid G-quadruplex structure under high potassium chloride concentrations. MDM2-119 is a suitable model to study the interaction of doxorubicin with the MDM2 gene (diverse sequences linked to form G-quadruplexes). The results strongly hint that doxorubicin binds to the hybrid quadruplex MDM2-119. Via CD spectroscopy, the melting temperatures of MDM2-119 and MDM2-119 with doxorubicin were investigated, revealing an increased melting temperature of approximately 6°C from 67.8°C to 73.94°C after the addition of doxorubicin to MDM2-119. Measurements thus reveal that doxorubicin is stabilising MDM2-119. Furthermore, the data suggest that a similar type of binding as with doxorubicin and c-MYC may exist. However, further experiments must be conducted to verify this hypothesis.

Out of the above-mentioned results, the question of whether doxorubicin binds to all types of G-quadruplexes arose. The results show that doxorubicin does not bind to every G-quadruplex and thus has a certain specificity towards its potentially new target. However, it is not yet clear whether binding criteria are structural or sequential in nature and when binding has a stabilising or destabilising effect.

The group of Myelodysplastic Syndrome at Universitätsklinik Düsseldorf (Prof. Dr Gattermann, Dr Fatemeh Majidi) already showed that cell treatment of the gene promoter MDM2 could decrease the expression of MDM2 and p53 degradation, which is in agreement with the stabilisation of the G-quadruplex MDM2-199 through treatment with doxorubicin. The sum of results introduces doxorubicin as a potential new drug in the treatment of DDLPS.

In further NMR titration experiments, it would be interesting to determine the binding site of doxorubicin on MDM2-119 with atomic resolution. The deletion of adenine from the sequence (either replacing it with another base or omitting it entirely) could also provide information on whether the CAT sequence represents the potential binding site of doxorubicin. This could also lead to further experiments investigating the conditions under which MDM2-119 binds to G-quadruplexes and stabilises or destabilises them. Since nemorubicin, a doxorubicin derivative, is suggested to have a more stable binding to the c-MYC G-quadruplex, CD-melting curve experiments with nemorubicin to MDM2-119 would also be of interest (Scaglioni et al., 2016).

4.3 Materials and Methods

All oligonucleotide samples **(Table 9)** were measured in 100 mM KCl (Sigma-Aldrich, St. Louis, USA) and 20 to 25 mM potassium phosphate buffer (Sigma-Aldrich, St. Louis, USA) with a pH of either 6.2 or 7. 2.

Table 9: Used G-quadruplex oligonucleotide sequences.

Oligomer	Sequence
Antiparallel GQ_	GGTAGGTGTGGTTGG
Antisense DNA Duplex	CGCGAATTCGCG
Hybrid GQ tel26	AAAGGGTTAGGGTTAGGGTTAGGGAA
MDM2-119	GGGGCGCGGGGCGCGGGGCATGGGG
Parallel GQ HIV-int.apt.	GGGTGGGTGGGTGGG
Sense DNA Duplex	GCGCTTAAGCGC

4.3.1 NMR measurements

DNA oligos were obtained from Merck KGaA (HPLC-purified, Darmstadt, Germany) or Biomers (Ulm, Germany). DNA samples were resuspended in pure water. Samples were measured at DNA concentrations of 200 µM in 20 mM potassium phosphate buffer (Sigma-Aldrich, St. Louis, USA), pH 7.4, 100 mM KCl (Sigma-Aldrich, St. Louis, USA), and 10% (v/v) D_2O (Sigma-Aldrich, St. Louis, Missouri, USA). Doxorubicin (MP Biomedicals, Irvine, California, USA) ligand concentration was, when applied, 400 µM. All NMR experiments were recorded with a 200 µl sample volume in a 3 mm NMR sample tube. 1D experiments were carried out using diverse temperatures between 10–64 °C (2°C temperature steps) and the Topspin Makro “multi_zgvt”. TOCSY experiments were measured at 37°C using a Bruker spectrometer (Avance III HD+ or NEO), equipped with inverse detection triple-resonance z-gradient cryogenic probes, operating at a ^1H frequency of 750 MHz. TOCSY experiments were recorded with an 80 ms mixing time. NMR data were processed using Topspin 3.6.5 or 4.4.0. Spectra were analysed and plotted using Cara 1.9.1.7, Topspin 3.6.5 or 4.4.0.

4.3.2 Circular dichroism (CD) spectroscopy

Circular dichroism spectroscopy is a sensitive tool for characterising the secondary structure of proteins and nucleic acids. Changes in secondary structures resulting from folding, ligand binding and environmental perturbations (e.g., pH or temperature) can be monitored. DNA secondary structures like A-, B-, and C-form, duplex-DNA or quadruplexes display characteristic CD spectra (Del Villar-Guerra et al., 2018). All CD spectra were measured using the JASCO J-815 (Easton, MD, USA) and evaluated with JASCO's own software.

Whole-spectrum measurements and titration experiments

To measure the secondary structure of diverse G-quadruplexes and a DNA Duplex (Used constructs: **Table 9**), a whole CD spectrum at 25 °C was measured. For the measurements, 250 µL of 20 mM KPi (Sigma-Aldrich, St. Louis, USA), pH 6.2, and 100 mM KCl (Sigma-Aldrich, St. Louis, USA) were used as the buffer. Samples were measured with a DNA concentration of 30 µM. To characterise ligand binding to the DNA, 60 µM of doxorubicin, a cytotoxic anthracycline used as a cancer therapeutic, was added to each DNA sample. The CD spectra were acquired with a wavelength range of 320/350 to 200 nm. A quartz cuvette with a path length of 3 mm was used for the measurement. Whole measurement parameters can be extracted from **Table 10**. For evaluation, the data were first normalised to the buffer. This was either done manually or automatically with the CD spectrometer. For evaluation, the data were transformed **(Equation 2)** from millidegrees (mdeg) to Molar Ellipticity (ME).

Equation 2: Transformation of mdeg to ME (deg·cm²·dmol⁻¹); c – concentration (mol/L), l pathlength cuvette (cm), θ_{obs}= Observed absorption (mdeg).

$$\theta = \frac{\theta_{obs}\,(mdeg) \times 100}{c\,\left(\frac{mol}{L}\right) * l\,(cm)}$$

Titration experiments with MDM2-119 and doxorubicin were carried out using CD spectroscopy. For this purpose, 11 different samples were prepared in which the ligand concentration of doxorubicin was gradually increased (0, 0.5x, 0.75x, 1x, 2x, 3x and 4x Ligand equivalents). As described above, the quadruplex remained constant at a concentration of 30 µM. The same measurement conditions and evaluation were applied, as described above. Titration data evaluation and fitting were performed using MATLAB R2021a (MathWorks, Natick, USA and Excel (Microsoft Office 2021, Redmond, USA).

Table 10: CD spectroscopy parameters for whole spectra CD measurements.

Parameters	Value/mode
Data interval	0.1 nm
Start	350/ 320 nm
End	200 nm
Temperature	25°C
Instrument	J-815
Accessory	PTC-4235
Photometric mode	CD. HT. Abs.

Sensitivity	Standard
Bandwidth	2.00 nm
Scanning mode	Continuous
Scanning speed	50 nm/min
CD Detector	PMT
Accumulations	15

Melting Curve measurements

To understand how ligand binding affects the secondary structure of the DNA constructs, melting curves from 20 to 95 °C were measured. Ligands can either stabilise, destabilise or not interact with the sample. Stabilisation of ligands would result in increased, destabilisation decreased, and missing binding would not change the melting temperature of the DNA construct. The same sample **(Table 9)** conditions were applied, as described above. No entire spectra were recorded (only individual wavelengths), listed in **Table 12**. The wavelengths were determined based on the high, low, and turning points of the whole spectrum data and used as the initial wavelength for measuring the melting curves. Whole measurement parameters can be extracted from **Table 11**. The data were first normalised to the buffer and then, as described above, transformed from mdeg to Molar Ellipticity. Melting curves were evaluated and fitted using MATLAB. Melting temperatures were calculated with a sigmoidal fit using the Boltzmann equation (Equation 3).

Equation 3 Sigmoidal fit (Boltzmann equation). T – temperature (°C), A1 – Absorption 1st plateau (θ), A2 – Absorption second plateau (θ), Tm – melting temperature (°C), k – slope (°C).

$$y(T) = \frac{A1 - A2}{1 - e^{\frac{T - Tm}{k}}} + A2$$

Table 11: CD spectroscopy parameters for melting curve measurements.

Parameters	Value/mode
Data interval	0.1 nm
Wavelength	diverse
Temperature	20–95°C
Instrument	J-815
Accessory	PTC-4235
Photometric mode	CD. HT. Abs.
Sensitivity	Standard
Bandwidth	1.00 nm

CD Detector	PMT
Number of cycles	1
Data points	151
D.I.T.	2 sec

Table 12: CD spectroscopy melting curve measured wavelength for each DNA construct.

Construct	Measured wavelength [nm]
Hybrid G-quadruplex	206, 219, 240, 242, 243, 265, 291, 295
Duplex-DNA	206, 220, 250, 281
Antiparallel G-quadruplex	229, 248, 267, 280, 294
Parallel G-quadruplex	208, 230, 240, 241, 242, 262
MDM2-119	204, 236, 238, 245, 266, 285, 289, 293

4.2.3. FRET-based melting experiments

Quantitative PCR (BioRad, CFX Opus 96, Real-Time PCR System) was used to study the melting temperature of the MDM2-119. Therefore, MDM2-119 was equipped on the 5'-end with Atto 647N, on the 3'-end with BBQ-650. MDM2-119 samples were measured as triplicates in 20 mM KPi, pH 6.2 and 100 mM KCl with 10 µM DNA, and 20 µM of doxorubicin. Measurement parameters can be depicted from **Table 13**. The relative fluorescence units (RFU) of samples were normalised to the buffer. The derivative of the normalised RFU was used to determine the melting point.

Table 13: FRET-based melting experiments parameters for melting curve measurement.

Parameters	Values
Sample volume per well	10 µL
Temperature range	40–100 °C
Fluorophore channel	Cy5
Lid temperature	105 °C
Temperature step size	0.1 °C

5 General Conclusion

A uniform aim of this thesis was to understand structure, folding and dynamics to further improve or apply nucleic acids, whether in the form of oligonucleotides (DNAzymes, biosensors) or at the cellular level (G-quadruplex). The applications and functions of nucleic acids, specifically DNA, have long since ceased to be merely carriers of genetic information, and the areas of application and understanding of nucleic acids have diversified. Still, this diversity is not reflected in the building blocks provided by nature; it is essential to understand how sequences, metal ions, biophysical factors (e.g., temperature or pH value), cellular, cellular-like or synthetic environments (e.g., in vitro selection conditions, structural/ chemical evolution) determine function and application. The general research question of this thesis can be categorised into two sub-questions: On the one hand, this thesis aims to characterise catalytically active nucleic acid systems, and, on the other hand, to investigate and characterise the possible interactions of a medically relevant ligand with a G-quadruplex. In detail, we aimed to address the questions of (1) how a completely new and innovative self-cleaving DNAzyme system is functionally, structurally and mechanistically characterised (including structure, folding, dynamics, metal-ion dependency, mode-of-action etc.), (2) how the structure and folding of an RNA-cleaving DNAzyme are influenced by nucleic acid modifications, as the introduction of nucleic acid modifications can enhance activity and function, (3) how the choice of target nucleic acids (either DNA or a chimeric RNA) for an RNA-cleaving DNAzyme influences the structure and catalytic activity, and (4) how and if a chemotherapeutic is interacting with an cancer-driving G-quadruplex. The methodological framework is dominated by NMR spectroscopy, but also includes other biophysical methods such as CD and UV/Vis spectroscopy.

Chapter 2 demonstrated, using NMR spectroscopy among other methods, a shift in paradigm in the understanding of DNA catalysis, as the pin system does not rely on a stable structural framework to catalyse its cleavage reaction. Our research demonstrated that pin acts in a dynamic interplay between conformational plasticity and the cadmium cofactor. Structural evolution as a tool, combined with rational selection, leads to optimised constructs.

Chapter 3 contains two subchapters, 3.1 and 3.2, which address two different types of RNA-cleaving DNAzymes. Chapter 3.1 demonstrated that the introduction of modified nucleic acids (Dz46-like DNAzyme) increased the dynamics in the catalytic loop but left the RNA target mostly unaffected. The alteration of the cleavage site appears to influence the global folding and dynamics of the DNAzyme. A strategic and stepwise assignment process was complicated as extensive spectral optimisations and addition of a nucleic acid modification were necessary to generate results that, in their resolution, made further evaluation possible. Chapter 3.2 evidenced that the choice of a target nucleic acid (DNA or chimeric-RMA) strongly influences

the activity and structure of the DNAzyme 8-17. Wieruszewska, Pawlowicz *et al.* revealed through comprehensive NMR spectroscopic studies of the DNAzyme 8-17, the up to this point missing solution structure, which we also aimed for. However, some questions remained unanswered, especially regarding whether the proposal of the sugar conformation of C3'-endo or C2'-endo is the cause for the structural difference and how the choice of a nucleic acid as a target can actually influence the activity of a DNAzyme.

Chapter 4 exhibits, using mostly biophysical approaches such as CD-spectroscopy, MDM2-119 as a suitable G-quadruplex variant of the MDM2 gene to study the interaction with the chemotherapeutic doxorubicin. Results strongly indicate that doxorubicin binds specifically to MDM2. The results support the in vivo studies of Myelodysplastic Syndrome at Universitätsklinik Düsseldorf (Prof. Dr Gattermann, Dr Fatemeh Majidi) fiercely. However, some questions, which arose during the studies, remained unanswered, addressing whether the binding mode is influenced either by the structure or the sequence of the G-quadruplex. This makes further studies necessary.

All chapters are connected through the diverse nature of nucleic acids: DNAzymes, which fall into the category of therapeutics or biosensors, and quadruplexes, which represent a structural variation of DNA as part of the genetic information and thus fall into the category of therapeutic targets. Although each chapter focused on different types of nucleic acids and their respective related systems, all addressed questions contribute to the understanding of molecular structures in the context of conformation and dynamics. This clearly shows that synthetically developed nucleic acid systems, such as DNAzymes, do indeed overlap with natural nucleic acid systems and that a single methodological framework, such as NMR spectroscopy, can be adapted to address diverse questions and nucleic acid systems. NMR spectroscopy, as a diverse tool, was used for (1) structural characterisation (mostly proton NMR spectroscopy) of Dz46-like DNAzyme, the self-cleaving DNAzyme pin, DNAzyme 8-17, and G-quadruplex MDM2-119, (2) interaction studies (ligands and metal ions) of the Q-quadruplex MDM2-119 and pin, (3) temperature studies for pin and Dz46-like DNAzyme (spectral optimisation). Complementary biophysical approaches, such as FRET or CD-spectroscopy, offer opportunities to complement, validate or overcome limitations of NMR spectroscopy (e.g., sensitivity, chemical exchange, spectral resolution) to generate a broader, comprehensive picture.

The comparative perspective gained from this thesis provides a broader understanding of the structure-function relationships of DNAzymes and the G-quadruplex MDM2-119 with doxorubicin. The combination of structure, function, and mechanism opens up possibilities for optimisation on the one hand and enables targeted use, e.g., in therapeutics or biosensors, on the other. On the structural level, this thesis reveals that sequence, type of nucleic acid,

cofactors and temperatures influence conformations of nucleic acids, therefore suspending or diversifying the chemical limitations of the five building blocks. However, this thesis not only answers questions, but the results also raise new questions that address the structural-functional level or, more generally, how the characterised structure is affecting the function (DNAzyme 8-17 and quadruplex MDM2-119).

At present, 2D homonuclear proton experiments and measurements are size-limited for unlabelled nucleic acids, with an upper limit around 30–50 residues (depending on the conformation and dynamics). New perspectives on cost-effective isotope labelling strategies and synthesis methods for nucleic acids, like segmental labelling of large complexes, will push size limits to higher boundaries. Measurements under physiological conditions, like in In-cell NMR, will continue to be at the forefront as they directly connect conformation and dynamics to physiological conditions. New NMR spectroscopic experimental approaches, like SELOPE, will further improve spectral resolution and complement experiments for isotope labelled samples with experiments for unlabelled, native samples.

Also, the implementation of modified nucleic acids, e.g., therapeutics, biosensors or delivery systems will increase strongly, as chemical diversity and additional attributes are essential for improving functionality and stability. Therefore, the rational design of new chemically modified nucleic acids as building blocks is crucial. Further studies on conformational effects of modified nucleic acids using NMR spectroscopy will implement a fundamental understanding of the modification-effect relation and improve, simplify, time-saving and cost-effective research approaches.

Meta-studies addressing the connection between sequence, metal ions, biophysical factors (e.g., temperature or pH), cellular, cellular-like, or synthetic environments (e.g., in vitro selection conditions, structural/chemical evolution), and the structure-function relation will further improve our understanding. This knowledge will improve rational design, the development of targeted therapies, the evolution of completely new nucleic acid systems with a wide variety of functions, and the understanding of *in vivo*-related nucleic acids.

Here, NMR spectroscopy is showing its potential as a versatile tool in the scientific and comprehensive analysis of an increasing diversity of nucleic acids.

6 Supplement

6.1 Supplementary Figures

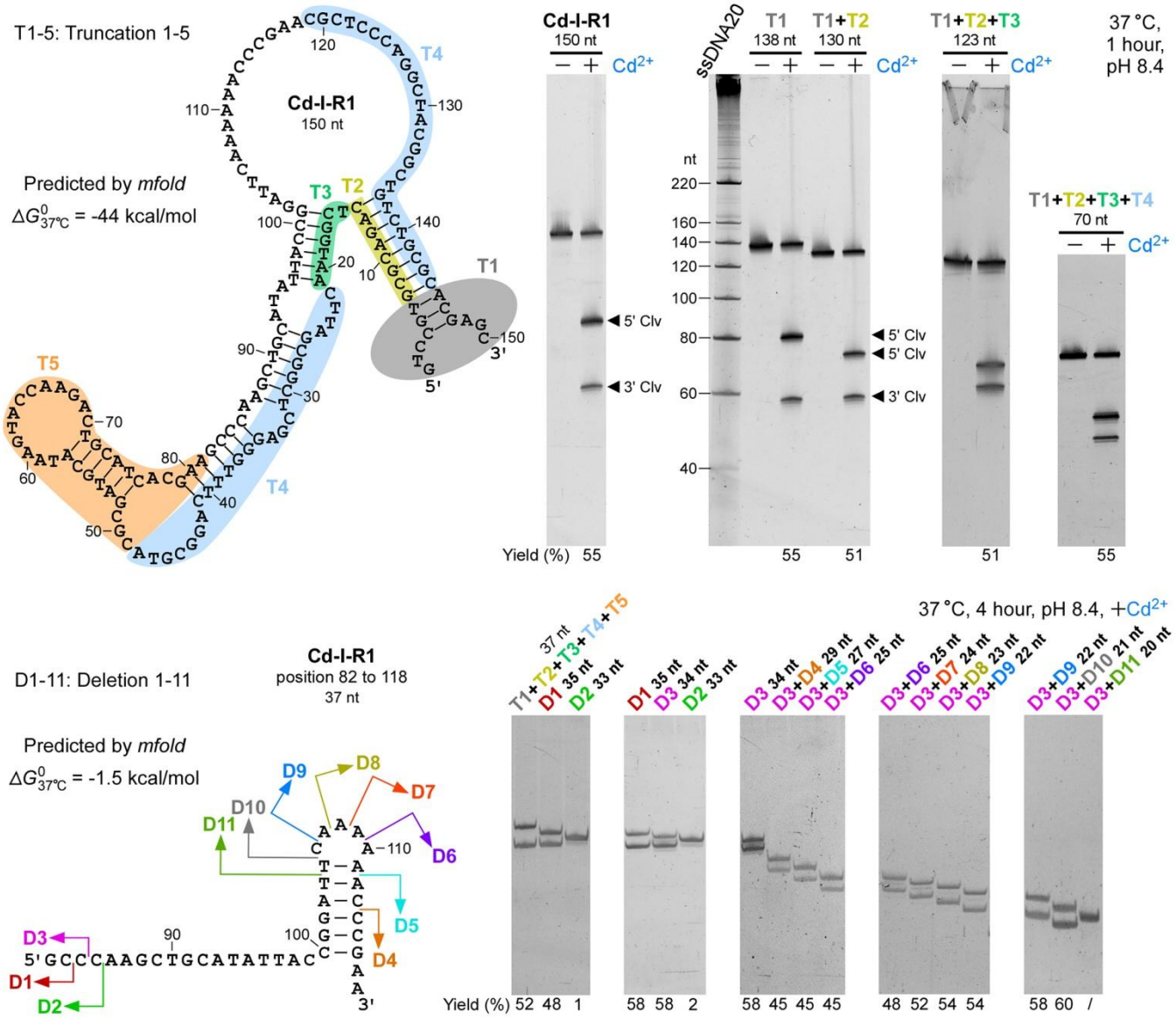

Figure 25: Truncation of a major class of Cd^{2+}-dependent (Cd-I) autohydrolytic DNA. Shown on the left is the mfold-predicted secondary structure models of the full- and partial-length of representative 1 (R1) DNA of Cd-I. A series of nucleotide truncations (T1–5) and deletions (D1–11) were conducted on these models. Cleavage activity of the truncated Cd-I-R1 DNAs was analysed by dPAGE and shown on the right. The gels were stained with nucleic acid staining for band quantification. ssDNA20: a single-stranded DNA ladder. For certain truncations, the 5' and 3' cleavage products were pointed out by arrowheads. Cleavage yield for each truncated DNA was calculated and listed at the bottom of the gels. By comparing the cleavage yields, it was concluded that the minimum deoxyribozyme of Cd-I seemed to be a 21 nt fragment, corresponding to positions 85 to 105, of the full-length (150 nt) Cd-I-R1 DNA.

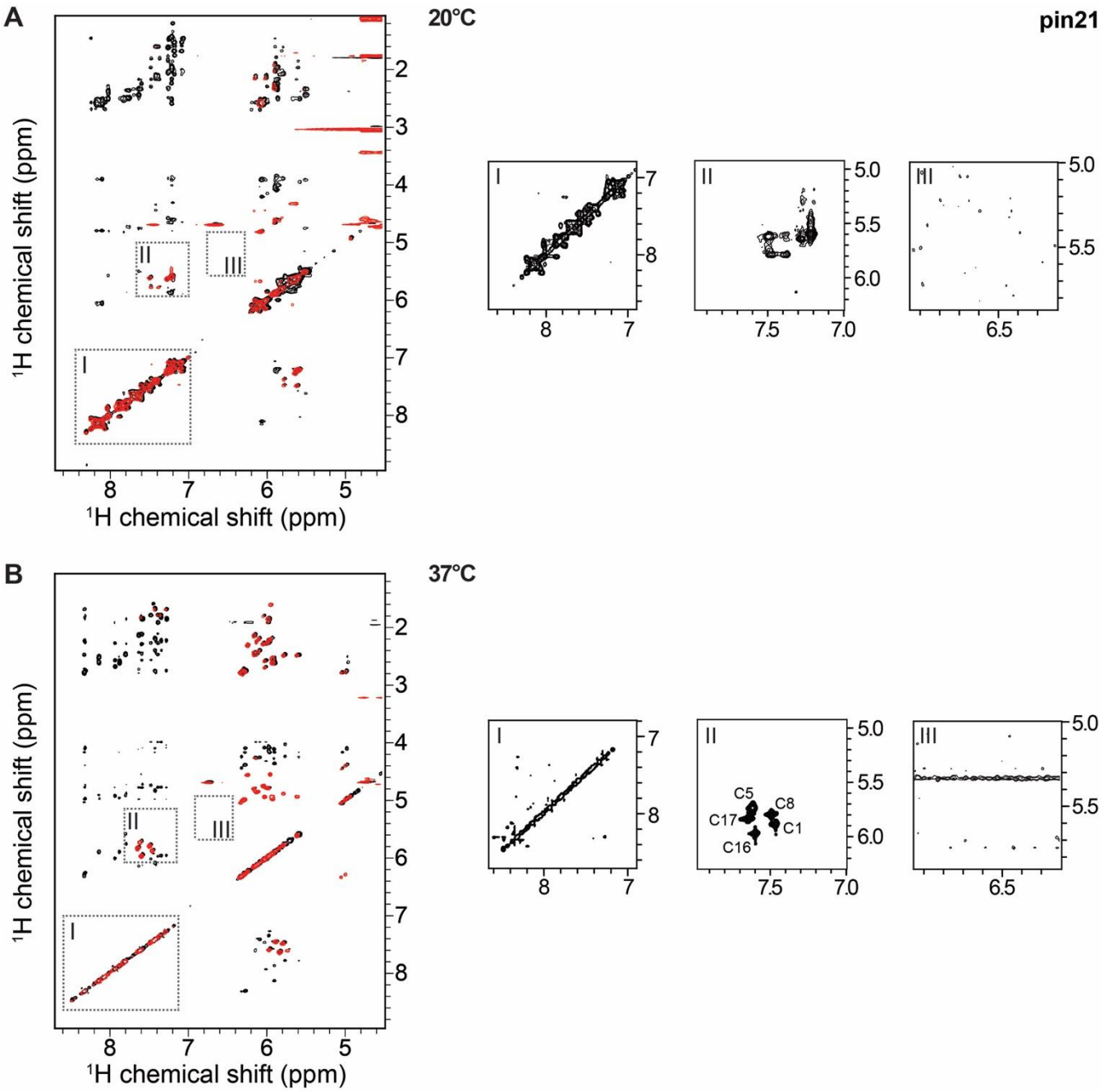

Figure 26: NMR characterisation of pin21. A, B: Overlay of 2D(^{1}H,^{1}H)-TOCSY (red) and 2D(^{1}H,^{1}H)-NOESY (black) spectra. Characteristic regions are highlighted and magnified on individual panels with the respective number. Data was recorded at 20°C (A) and 37°C (B). Characteristic regions report on different features. Cross peaks in region I (NOESY data) report on sequential connectivities, such as Pi-Pi stacking or conformational exchange of heterogeneous states. The number and shape of peaks in region II (TOCSY data) report on possible conformational heterogeneity. Appearance of peaks in region III (NOESY data) reports on hydrogen bonds found in classical Watson-Crick base-pairing. The data on pin21 show heterogeneous, exchanging conformations without a defined stable Watson-Crick pairing at 20°C. At 37°C, defined structural features remain low, but the signal gets more homogenous (fewer conformations) or averaged out (faster exchange of conformations).

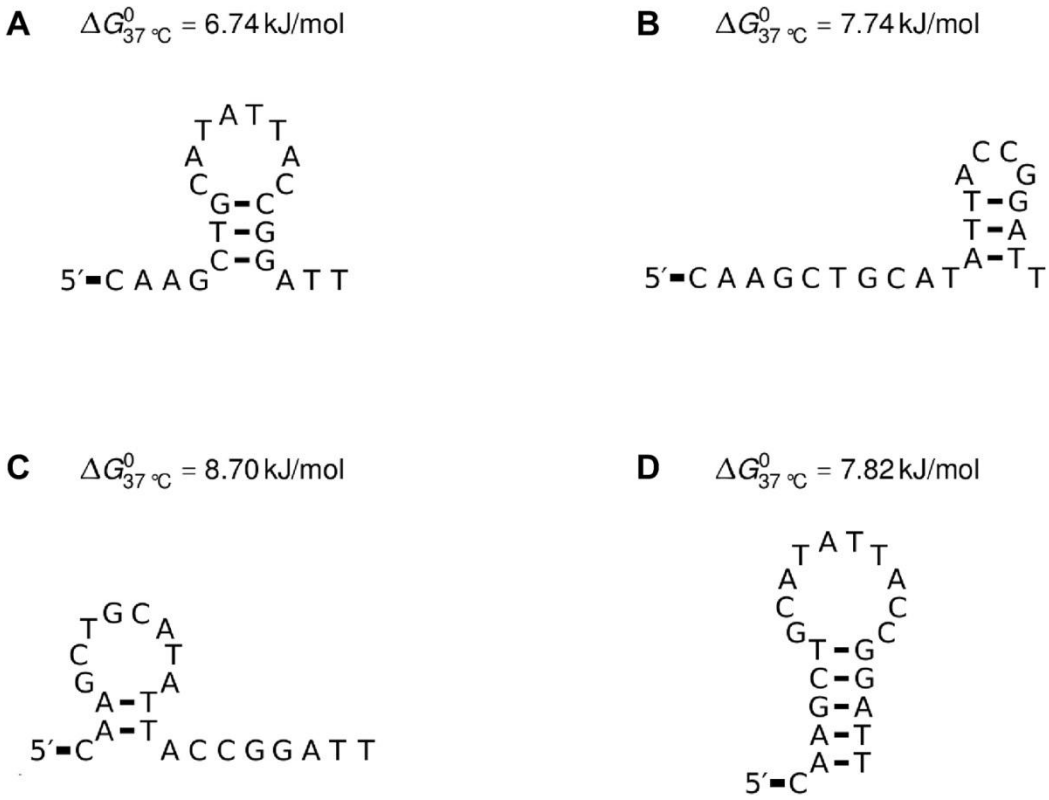

Figure 27: Predicted secondary structures of pin21 by mfold. Four representatives of the predicted structures were chosen for presentation. Based on their respective predicted ΔGº values at 37°C (in 100 mM NaCl and 7 mM $MgCl_2$), none of these conformations is expected to be thermodynamically stable.

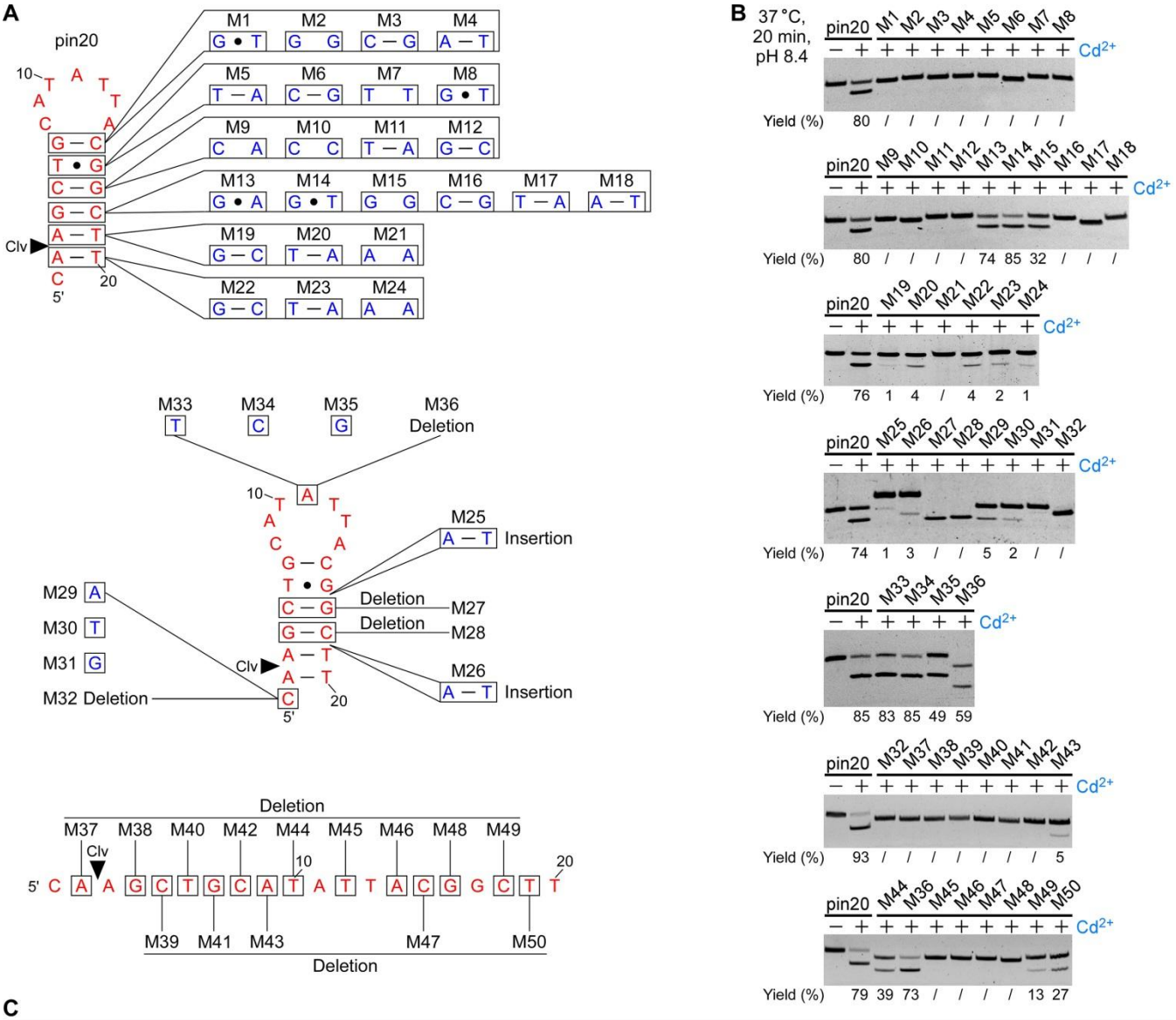

Figure 28: Analysis of the nucleotide conservation in pin20 self-cleaving DNA. A: Mutant constructs (M1–50) examined in this study. Arrowheads point to the cleavage (Clv) site. **B:** Analysis of the cleavage activity of the mutant constructs by dPAGE. Each mutant DNA construct was incubated at 37°C in the selection buffer for 20 min and then separated by dPAGE. The gels were stained with nucleic acid staining for band quantification. Cleavage yield for each mutant DNA was calculated and listed at the bottom of the gels. '/' means no detectable cleavage signal. **C:** Summary of the effect of the mutations on deoxyribozyme activity. The results were concluded on the basis of the dPAGE analysis in B.

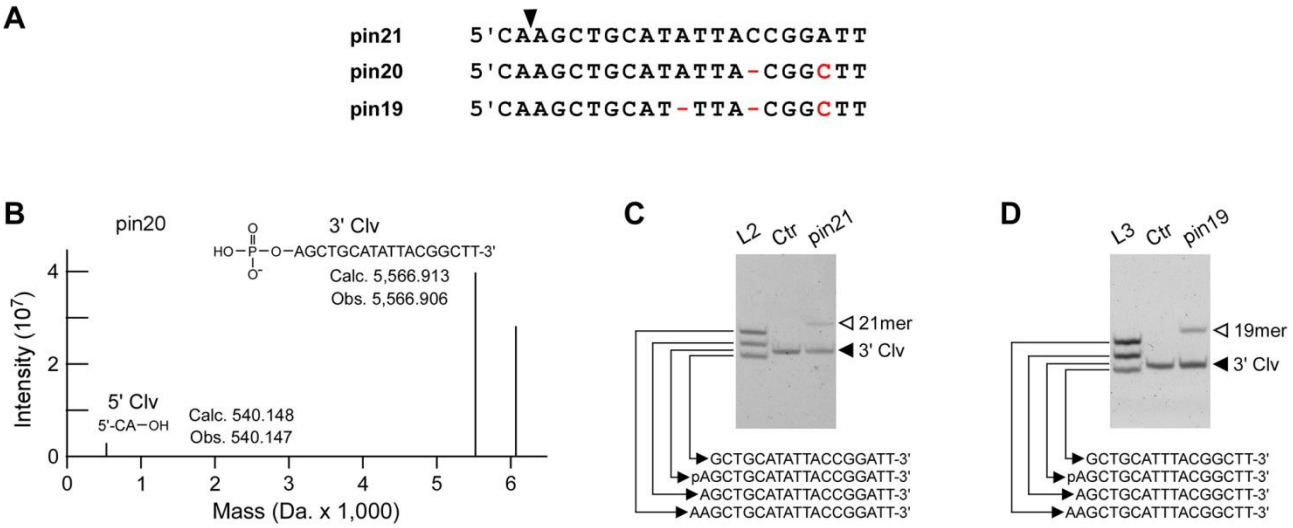

Figure 29: Mapping the cleavage site of pin21, pin20, and pin19. A: Sequences of pin21, pin20, and pin19. Arrowhead points to the cleavage site deduced from data in B-D. **B:** Exact mass spectroscopic determination of pin20 cleavage products. The proposed hydrolysis product peaks were annotated with the calculated (Calc.) and observed (Obs.) mass for hydrolysis of the 3' phosphoester bond. **C:** PAGE analysis of the cleavage site of pin21. L2: an 18–20mer DNA ladder. Ctr: a 19mer DNA with 5' phosphate (p) modification. **D:** PAGE analysis of the cleavage site of pin19. L3: a 16–18mer DNA ladder. Ctr: a 17mer DNA with 5' phosphate (p) modification. Hollow and filled arrowheads point to the full length and 3' cleavage products, respectively.

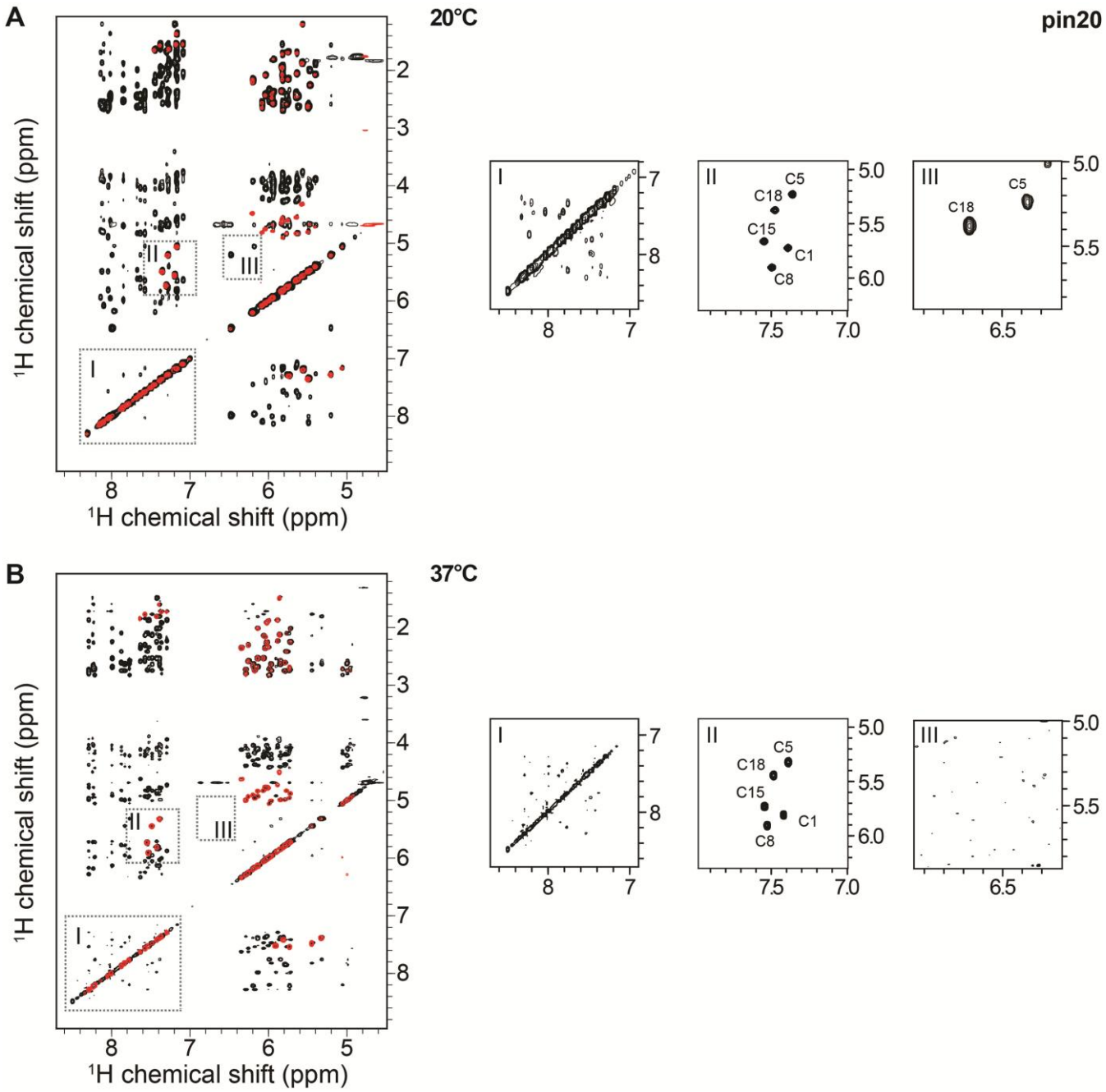

Figure 30: NMR characterisation of pin20. A, B: Overlay of 2D(^{1}H,^{1}H)-TOCSY (red) and 2D(^{1}H,^{1}H)-NOESY (black) spectra. Characteristic regions are highlighted and magnified on individual panels with respective numbers. Data was recorded at 20°C (A) and 37°C (B). Characteristic regions report on different features. Cross peaks in region I (NOESY data) report on sequential connectivities, such as Pi-Pi stacking or conformational exchange of heterogeneous states. Number and shape of peaks in region II (TOCSY data), report on possible conformational heterogeneity. Appearance of peaks in region III (NOESY data) reports on hydrogen bonds found in classical Watson-Crick base-pairing. The data on pin20 shows a homogeneous conformation with defined stacking interactions and stable Watson-Crick pairing at 20°C. At 37°C, most stacking interactions remain present while stable base-pairing is not detected anymore.

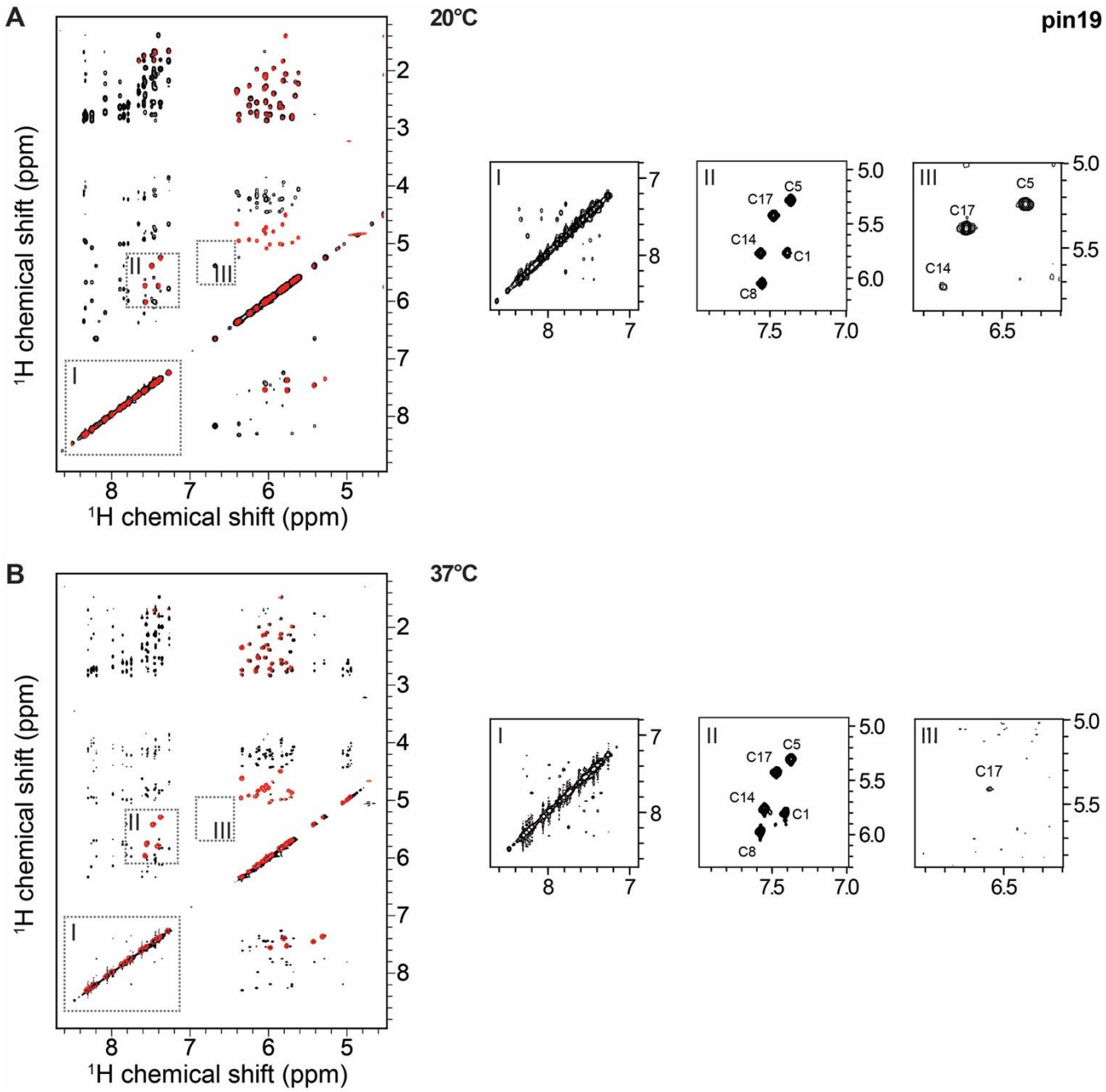

Figure 31: NMR characterisation of pin19. A, B: Overlay of 2D(^{1}H,^{1}H)-TOCSY (red) and 2D(^{1}H,^{1}H)-NOESY (black) spectra. Characteristic regions are highlighted and magnified on individual panels with respective numbers. Data was recorded at 20°C (A) and 37°C (B). Characteristic regions report on different features. Cross peaks in region I (NOESY data) report on sequential connectivities, such as Pi-Pi stacking or conformational exchange of heterogeneous states. Number and shape of peaks in region II (TOCSY data), report on possible conformational heterogeneity. Appearance of peaks in region III (NOESY data) reports on hydrogen bonds found in classical Watson-Crick base-pairing. The data on pin19 shows a homogeneous conformation with defined stacking interactions and stable Watson-Crick pairing at 20°C. At 37°C, most stacking interactions remain present while stable base-pairing is barely detected. The residual NOESY cross signal in region III indicates that the hairpin conformation of pin19 is slightly more stable than that of pin20.

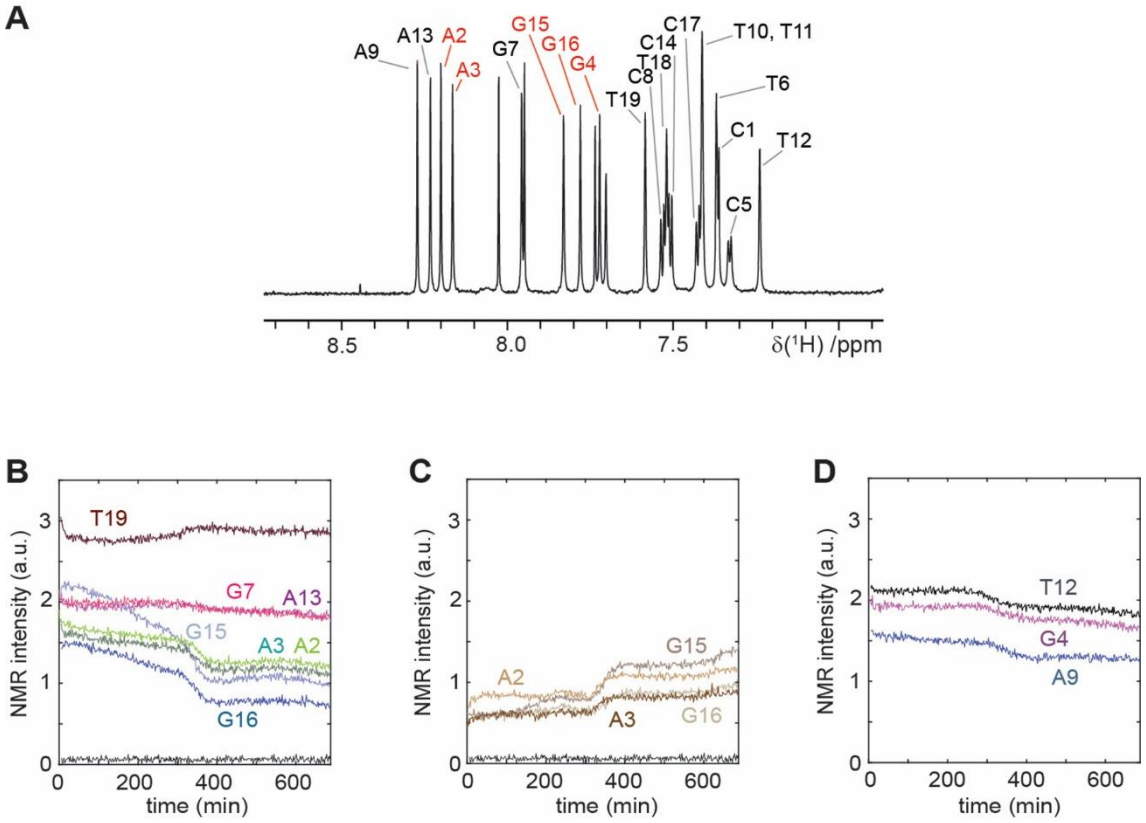

Figure 32: Real-time NMR data of pin19. A: 1D ^{1}H spectrum of pin19 reflecting the general level of spectral resolution and accessible nucleotide-specific information of the experimental setup. (B-D) Time traces of peak-specific signal intensities (raw data). **B:** Peaks of the educt state that are either strongly affected (A2, A3, G15, G16) or not/weakly affected (G7, A13, T19). **C:** Build-up of signal associated with the product states of the respective strongly affected nucleotides. **D:** Time-traces of moderately affected nucleotides (G4, A9, T12; educt state).

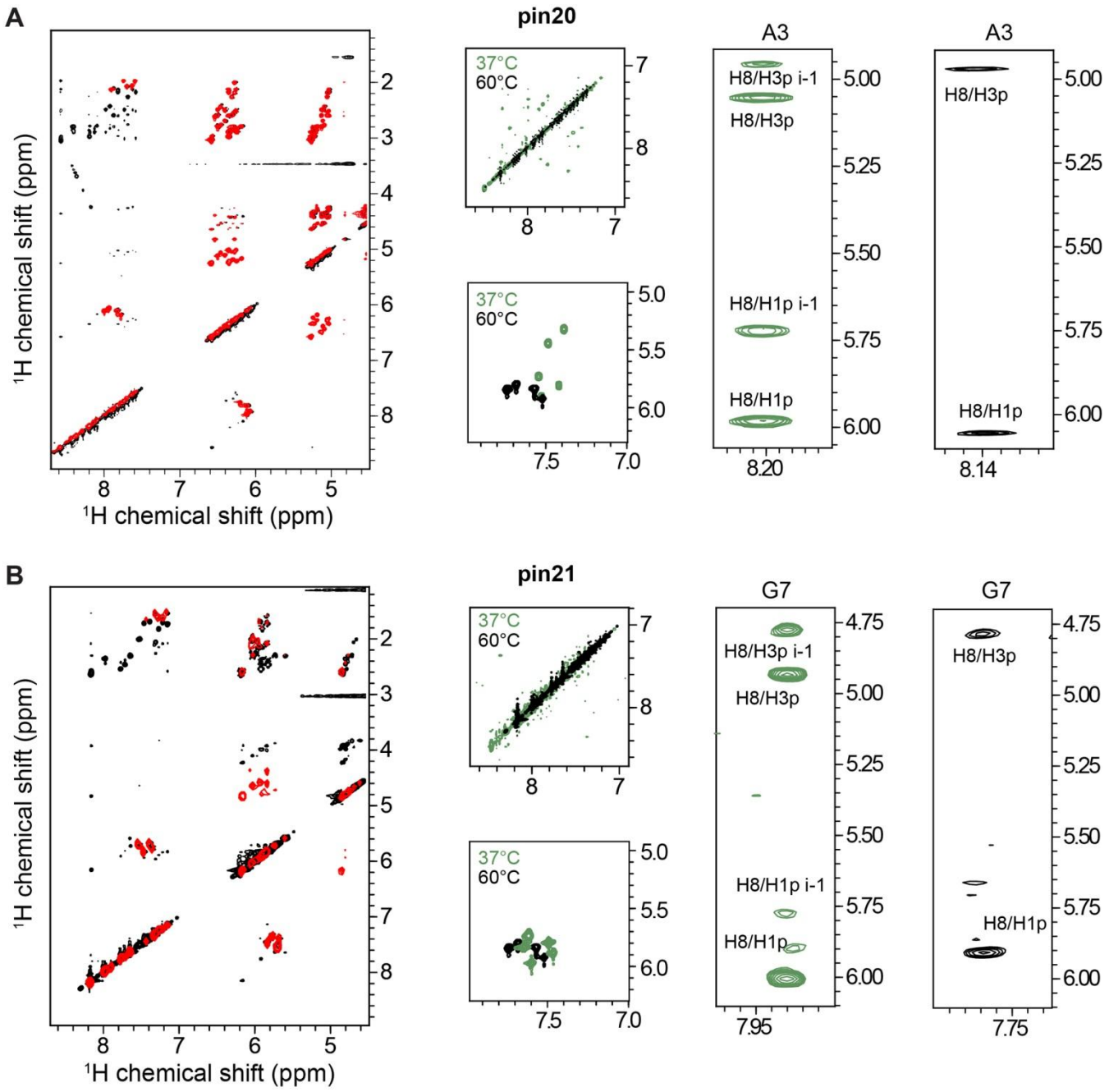

Figure 33: Pin20 and pin21 do not have detectable structural features at 60°C. NMR characterisation of pin20 (A) and pin21 (B). Spectral overlay of 2D TOCSY data (red) and 2D NOESY data (black), as well as characteristic spectral extracts comparing features at 60°C (black) to the data at 37°C (green), are shown. The data reveal no structural features in both samples at 60°C, including the full absence of sequential connectivities.

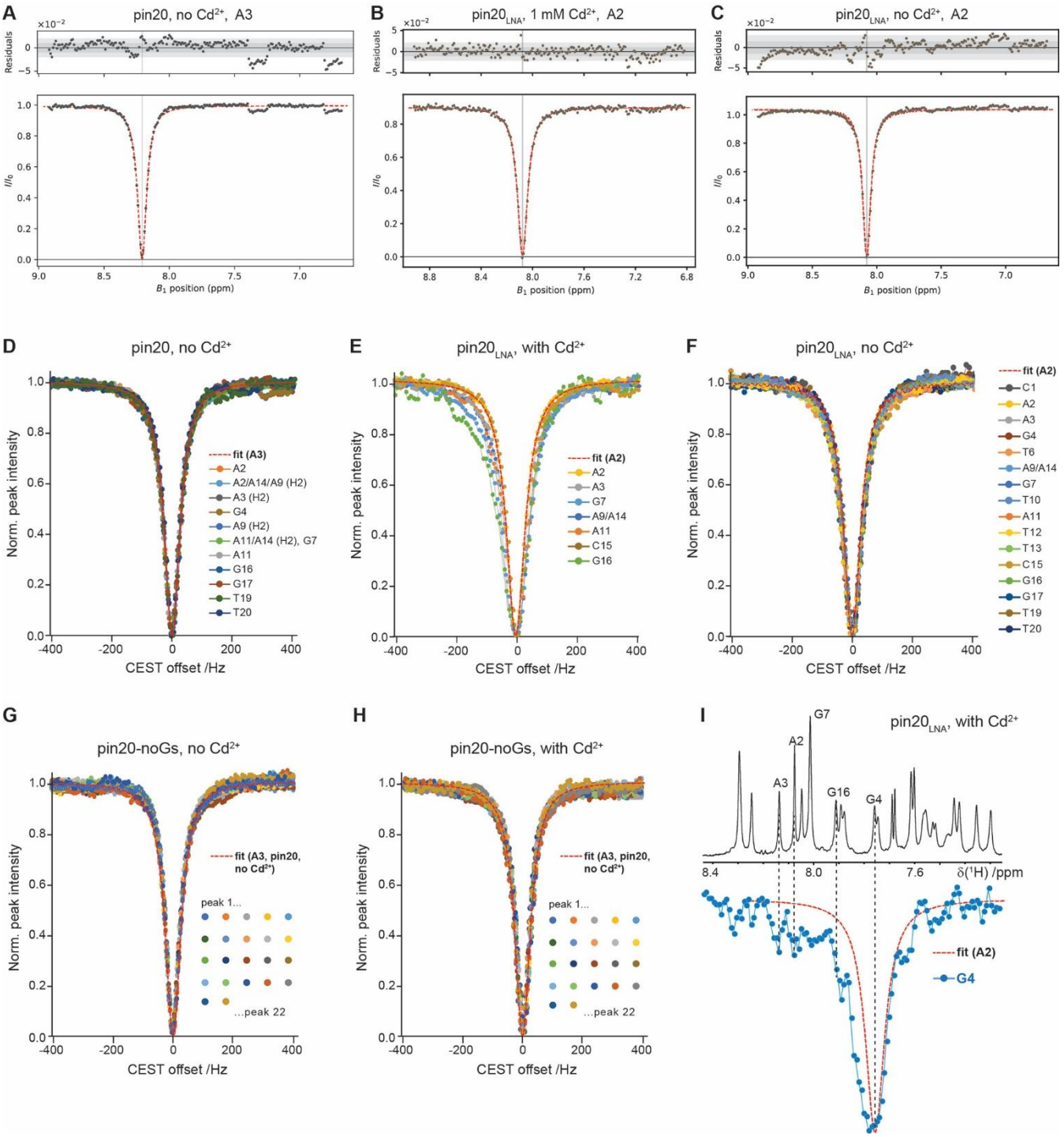

Figure 34: CEST NMR analysis of different pin20 variants and conditions. A: 1H-SELOPE-CEST profile associated with A3 (^{1}H8) of pin20, recorded in the absence of Cd^{2+}. Data was fitted with ChemEx using a standard 2-state exchange model. A fit with no exchange contributions of a second conformation provided the best fit (red) to the experimental data (black dots). However, the data shows considerable intensity 'dips' (around 7.4 ppm), which are present at exactly the same ^{1}H frequencies for ^{1}H spins associated with a number of, but not all, other nucleotides. Due to the good S/N and well-separated ^{1}H frequencies, these signal dips can be classified as significant and can be associated with the frequencies of T10 (^{1}H6) and T13 (^{1}H6). **B:** ^{1}H-SELOPE-CEST profile associated with A2 (^{1}H8) of pin20LNA, recorded in the presence of 1 mM Cd^{2+}. Note that the signal of A2 was chosen as a representative of non-affected nucleotides, since it fully matches the profile shown in (A), unlike the signal of A3 in the same sample (see panel E for more details). **C:** ^{1}H-SELOPE-CEST profile associated with A2 (^{1}H8) of pin20LNA, recorded in the absence of 1 mM Cd^{2+}, fully matching the respective data in the absence of Cd^{2+} (B). **D, E, F:** Overlay of CEST profiles associated with all resolved signals for the respective samples and conditions. Note that in the absence of Cd^{2+}, the profiles of all peaks are merely identical for pin20 (D) and pin20LNA (F). However, several peaks show clearly deviating profiles for pin20LNA in the presence of Cd^{2+} (E). While, in general, these deviations could be associated with exchange contributions, their appearance and shape (ppm values and

asymmetry) point to NOE contributions from specific spins as the cause of the perturbed CEST profiles (such as shown in **Figure 11J**). **G, H:** ^{1}H-SELOPE-CEST profiles of a control sample in which all four guanines are mutated to adenines. Data was recorded in the absence (G) and the presence (H) of 1 mM Cd^{2+}. The CEST profiles of all resolved peaks are plotted and overlaid to the fit obtained in (A), showing no detectable deviation. **I:** ^{1}H-SELOPE-CEST profiles associated with G4 (^{1}H8) of pin20LNA, recorded in the presence of 1 mM Cd^{2+}. While this position was not included in the analysis shown in (E) due to its reduced signal-to-noise ratio, the obtained data is also well consistent with NOE contributions perturbing the profile at the indicated frequencies.

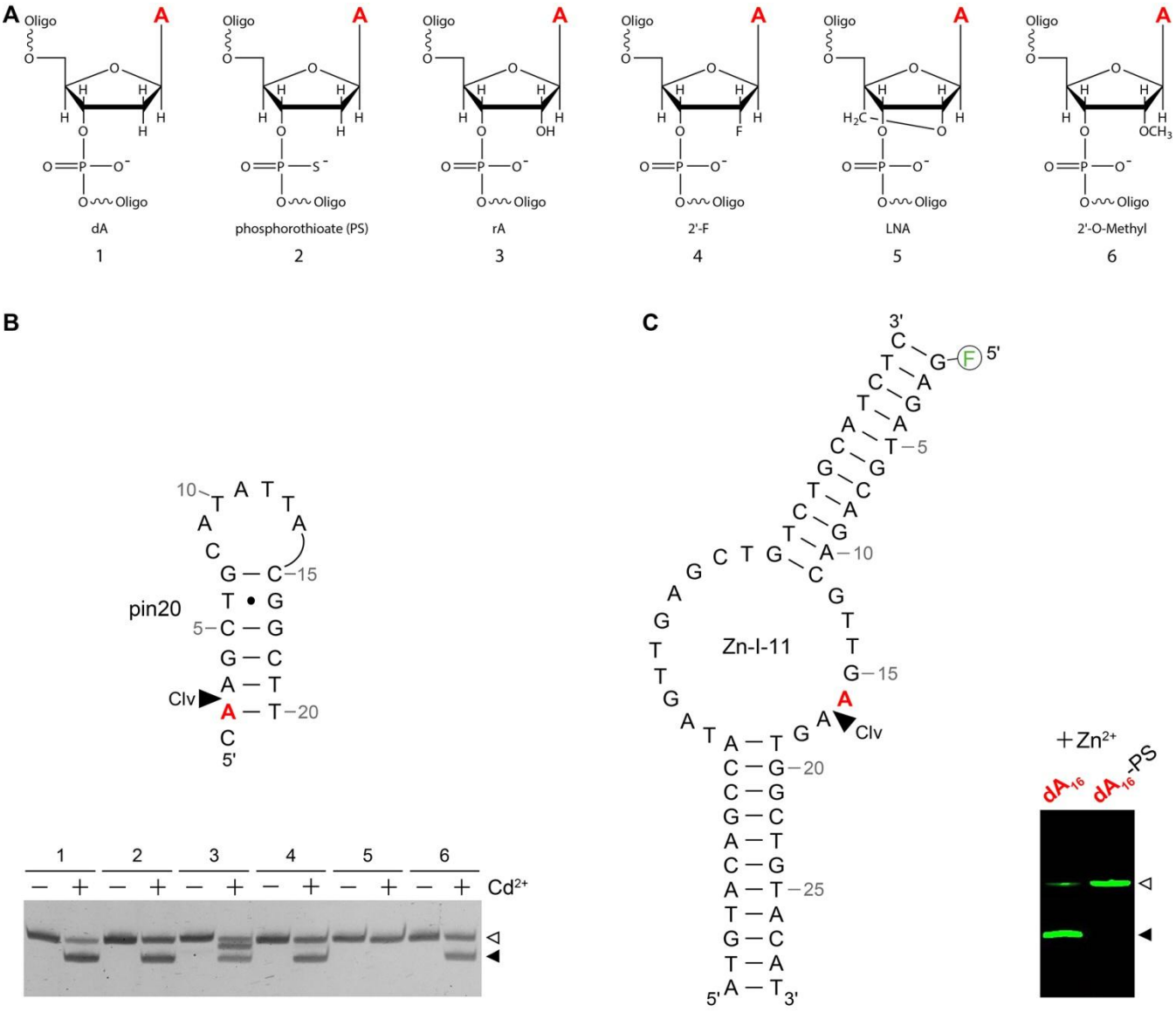

Figure 35: Screening of chemical modifications to prevent deoxyribozyme cleavage. A: Chemical modifications tested on the deoxyribonucleotide at the cleavage site. For the pin20 deoxyribozyme, these included a phosphorothioate (PS) linkage between A2 and A3 (2), 2′-OH on A2 (3), 2′-F on A2 (4), LNA on A2 (5), and 2′-O-methyl on A2 (6). **B:** Among these, only the LNA modification at A2 protected pin20 from cleavage. Samples were incubated in selection buffer at 37 °C for 1 h and analysed by dPAGE. Hollow and filled arrowheads indicate the full-length and 3′ cleavage products of pin20 DNA, respectively. **C:** For comparison, phosphorothioate modification completely prevented cleavage of a previously identified Zn^{2+}-dependent deoxyribozyme, Zn-I-11. Intact and PS-modified Zn-I-11 DNAs were incubated under standard Zn-I conditions (pH 7.0, 2 mM $ZnCl_2$) at 37°C for 1 h. A fluorophore label was attached to the substrate DNA for tracking. Products were then separated by dPAGE. Hollow and filled arrowheads indicate the full-length and 5′ cleavage products of the Zn-I-11 substrate DNA, respectively.

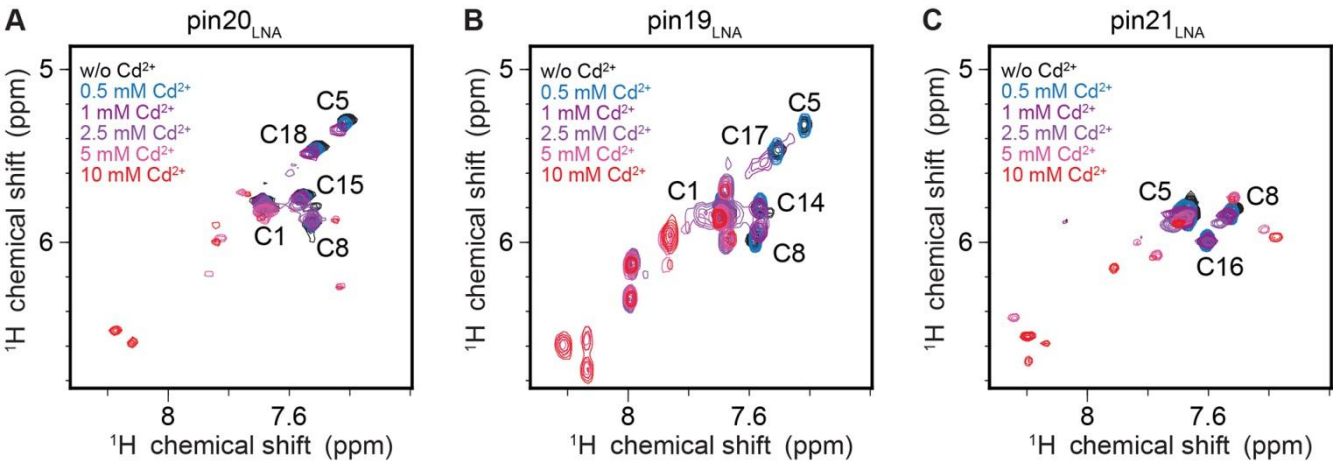

Figure 36: Cd^{2+} NMR titration experiments show similar characteristics for LNA-stabilised variants of pin20, pin19, and pin21. A, B, C: Effects of increasing Cd^{2+} concentrations as observed by 2D (^{1}H, ^{1}H)-TOCSY NMR spectra (fingerprinting region) recorded for pin20LNA **(A; same data as Figure 11C**), pin19LNA (B), and pin21LNA (C) at 37°C and the indicated Cd^{2+} concentrations. All variants exhibit characteristic peak shifts at high Cd^{2+} concentrations (5–10 mM), along with an increased number of peaks and an initial decrease in peak intensities at low to medium Cd^{2+} concentrations (< 5 mM).

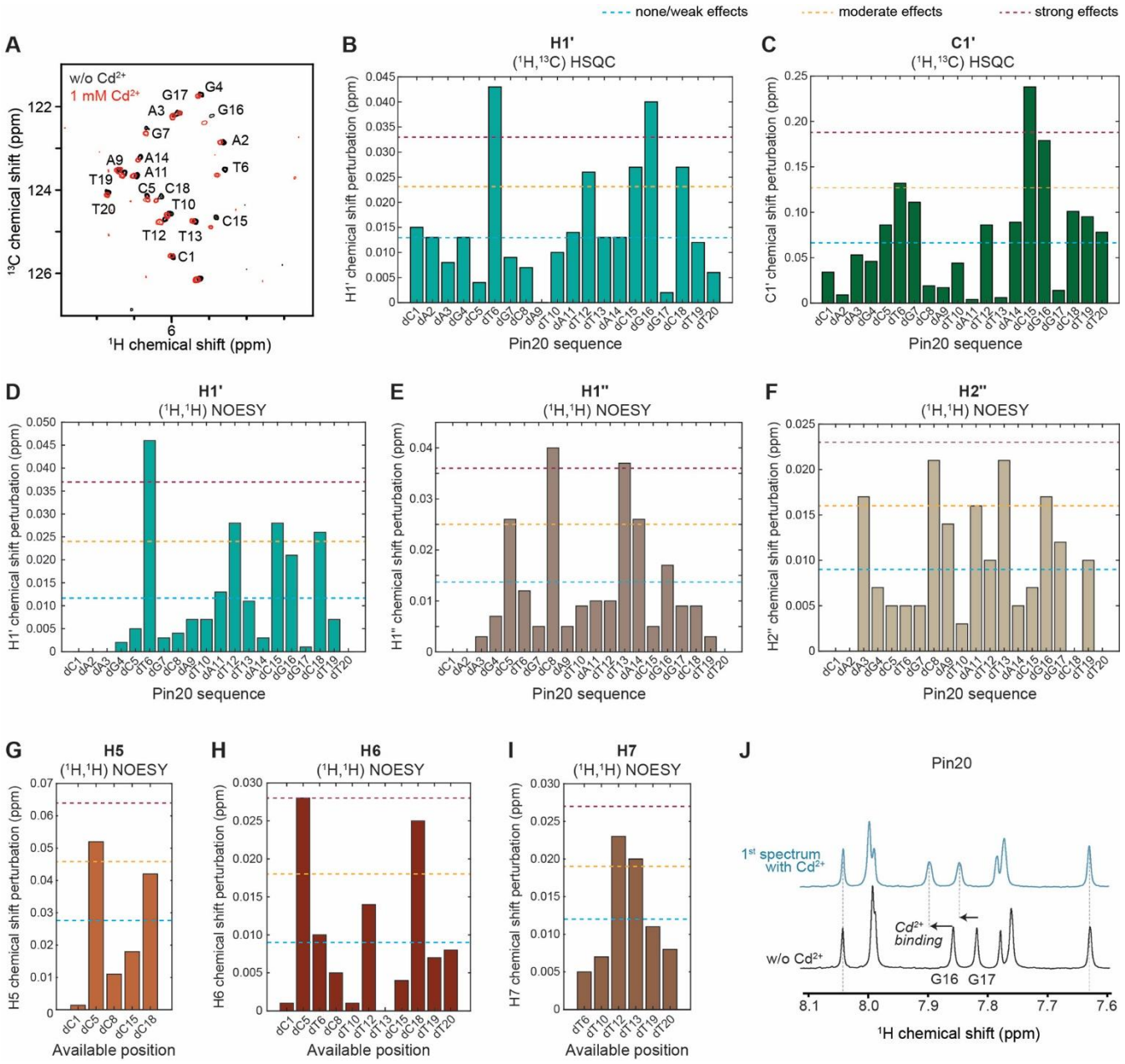

Figure 37: NMR-observed effects induced by cadmium interactions with pin20. A: Overlay of spectral extract (H1', C1' region) of 2D ($^{1}H,^{13}C$)-HSQC spectra recorded on pin20 in the absence (black) and presence (red) of 1 mM Cd^{2+} at 37°C. **B, C:** CSP induced on the indicated spins as seen in 2D HSQC data (A). **D, E, F, G, H, I:** CSPs induced on the indicated spins as seen in 2D NOESY data. Blue/orange/red lines in (B-I) indicate variations of $1\sigma/2\sigma/3\sigma$ to the mean, respectively. **J:** Real-time NMR observation of pin20 before and after the addition of Cd^{2+}. The spectra follow a very similar pattern to that of pin19 **(Figure 10A)**, confirming comparable Cd^{2+} interactions in both systems. The data in (B-J) were combined to generate the most consistent picture of Cd^{2+}-induced effects in pin20 **(Figure 11F).**

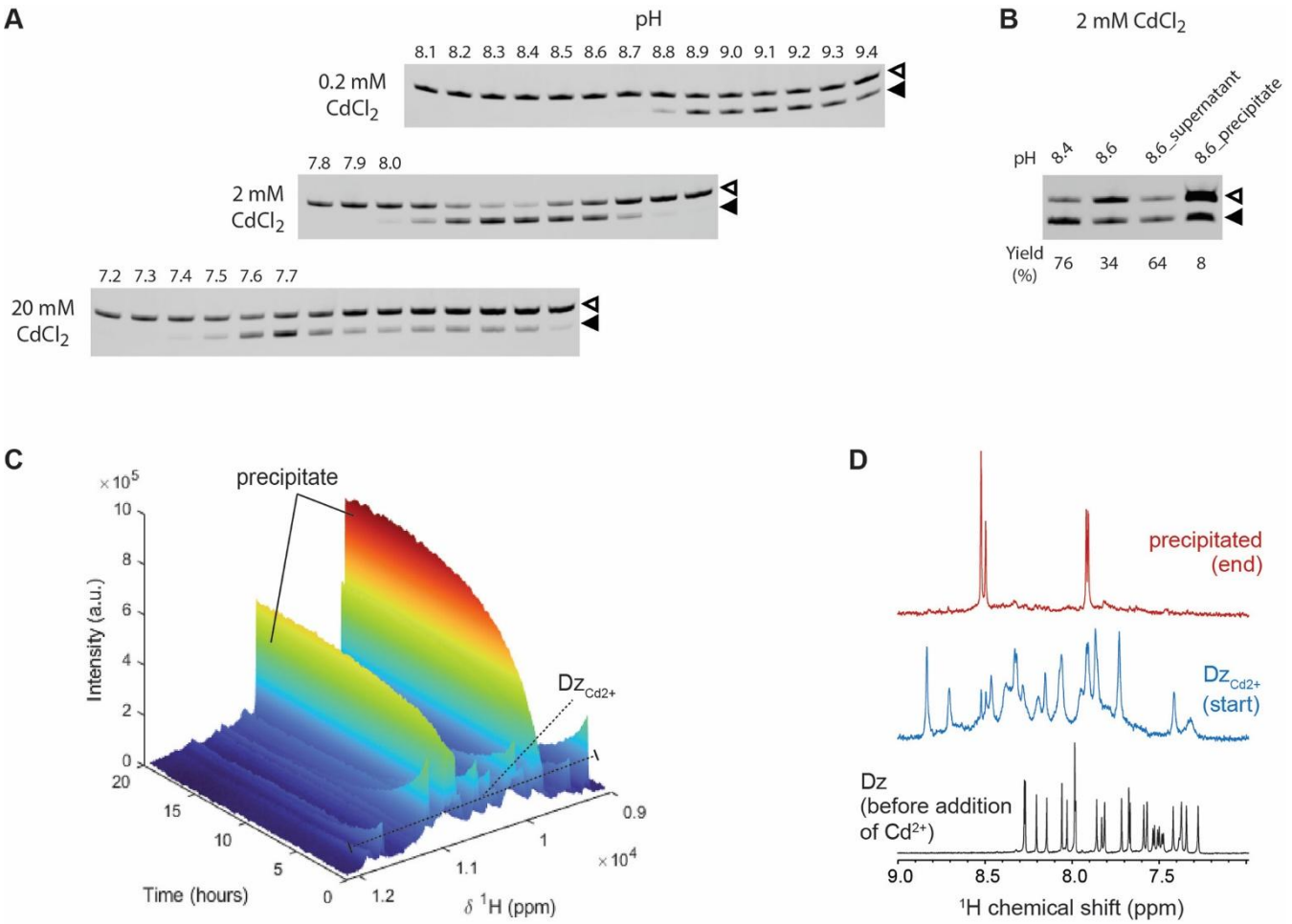

Figure 38: The pH dependency of the pin system is influenced by $CdCl_2$ concentration. A: Pin20 activity was assessed across a broad pH range at three $CdCl_2$ concentrations: 0.2, 2, and 20 mM. Pin20 deoxyribozyme was first incubated in Cd^{2+}-free buffers of varying pH, followed by the direct addition of 0.2, 2, or 20 mM Cd^{2+} to initiate the reaction (37 °C, 20 min). Reaction products were analysed by dPAGE. Cleaved products (indicated by hollow arrowheads) and uncleaved DNAs (solid arrowheads) revealed that pin20 activity peaked at an intermediate pH and dropped sharply at higher pH values, particularly above the typical $Cd(OH)_2$ precipitation threshold (e.g., pH ≥ 8.5 at 2 mM Cd^{2+}). **B:** $Cd(OH)_2$ precipitation suppresses pin20 activity. At 2 mM $CdCl_2$ and pH 8.6, the reaction mixture was centrifuged to rapidly separate the supernatant and precipitate fractions, which were then analysed by dPAGE. The results suggest that freshly formed $Cd(OH)_2$ precipitates adsorb DNA, thereby reducing the apparent activity of the deoxyribozyme. **C:** Surface plot of 1D-^{1}H real-time NMR data recorded on pin20LNA after addition of 10 mM $CdCl_2$. While the first spectrum is in line with the features observed for $DzCd^{2+}$, a strong transition of peak intensities and positions is observed over a time course of ca. 15 h. **D:** 1D-^{1}H NMR spectra of pin20LNA before addition of $CdCl_2$ (black), directly after addition of 10 mM $CdCl_2$ (blue) and 20 h later (red). The product state is dominated by a small number of peaks that do not resemble classical features of the DNA system. In line with (visually) observed precipitation and previous literature reports, the data are consistent with the formation of larger molecular aggregates that are not detectable in solution NMR due to their unfavourable relaxation properties. In this picture, an insoluble $Cd(OH)_2$ particle with a positive surface charge will form, which in turn will attract the negatively charged DNA molecules, leading to co-precipitation of the DNA. The remaining NMR peaks could either originate from still flexible parts of the (co-precipitated) DNA, or system-specific “unusual” ^{1}H spins, e.g., originating from trapped and/or coordinated H_2O or OH moieties.

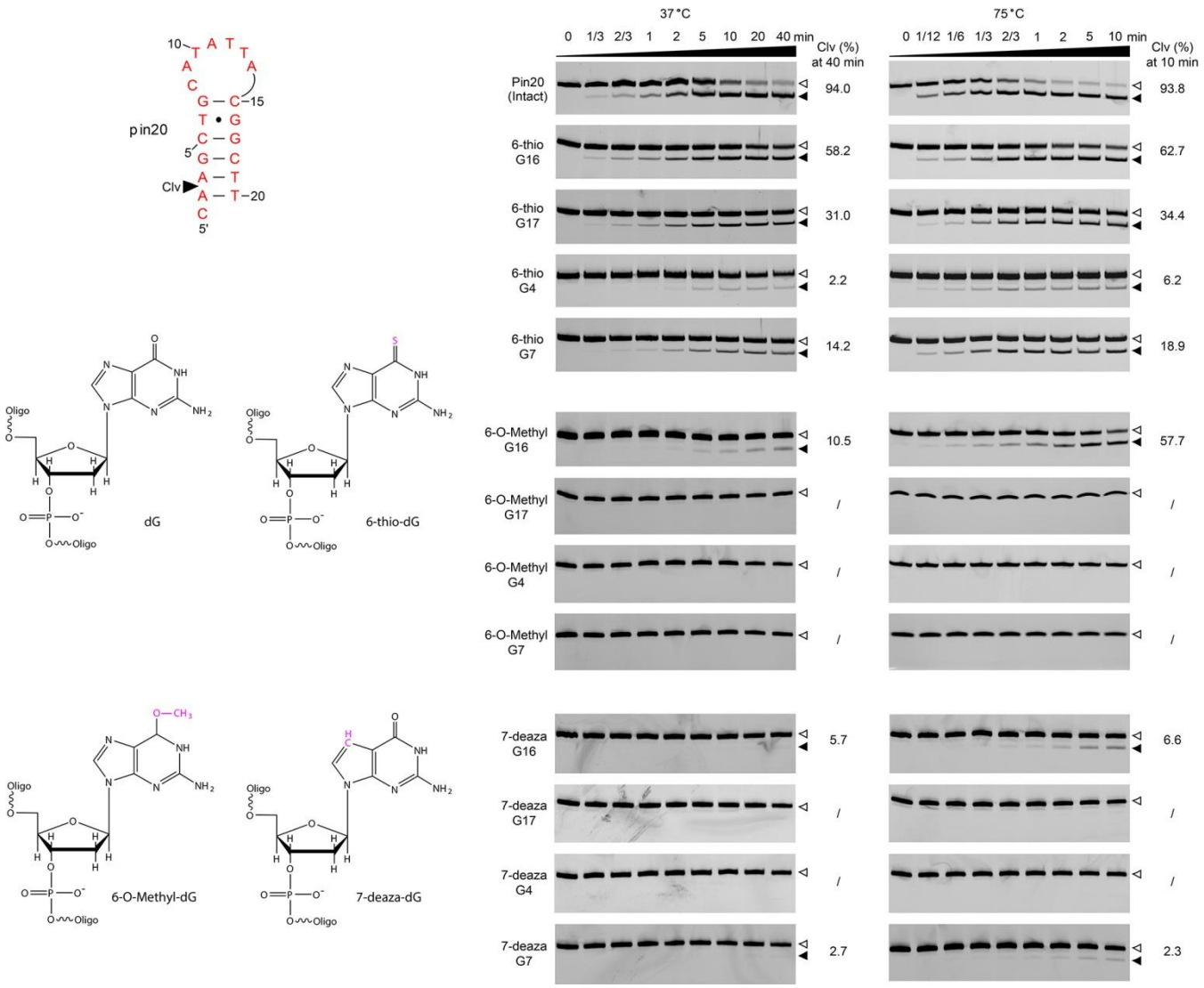

Figure 39: Modifications on each of the four guanines (Gs) have strong effects on pin20 activity, suggesting that all four Gs are essential for catalysis. The tested modifications include 6-thiol-dG, 6-O-Methyl-dG, and 7-deaza-dG. Trace amounts of the 3' FAM-labelled pin20 DNAs carrying a modification on any of the four Gs were incubated in the selection buffer at 37 °C or 75°C for the times indicated and separated by dPAGE. Hollow and filled arrowheads point to the full length and 3' cleavage product of the modified pin20 DNA, respectively. The cleavage (Clv) signals for 40 min (at 37°C) and 10 min (at 75°C) were calculated, listed next to the gels, and used to plot Fig. 3O.

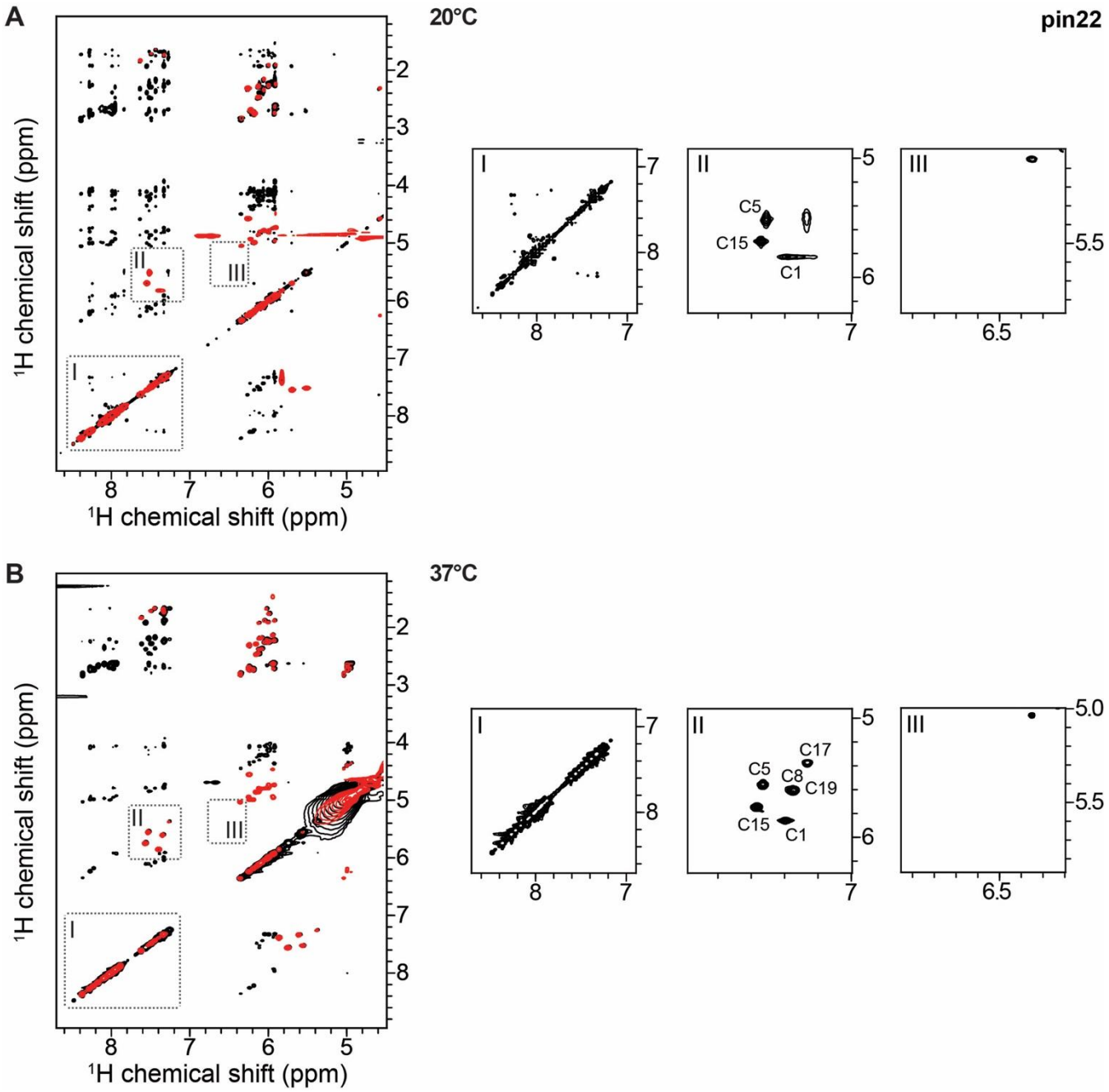

Figure 40: NMR characterisation of pin22. A, B: Overlay of 2D (^{1}H, ^{1}H)-TOCSY (red) and 2D (^{1}H, ^{1}H)-NOESY (black) spectra. Characteristic regions are highlighted and magnified on individual panels with respective numbers. Data was recorded at 20°C (A) and 37°C (B). Characteristic regions report on different features. Cross-peaks in region I (NOESY data) report on sequential connectivities, such as Pi-Pi stacking or conformational exchange of heterogeneous states. The number and shape of peaks in region II (TOCSY data) report on possible conformational heterogeneity. Appearance of peaks in region III (NOESY data) reports on hydrogen bonds found in classical Watson-Crick base-pairing. The data on pin22 show a largely homogenous conformation with defined stacking interactions but no stable Watson-Crick pairing at 20°C (note that the peak in region III (in A and B) is assigned and is not indicative of hydrogen bond formation). At 37°C, no structural features are detected. The data is consistent with the picture that pin22 is less heterogeneous than pin21, but also does not form a stable hairpin conformation as compared to pin20 and pin19. Thus, the data indicate that (i) structural evolution from the pin21 parent and (ii) rational devolution of the unproductive hairpin conformation were successful.

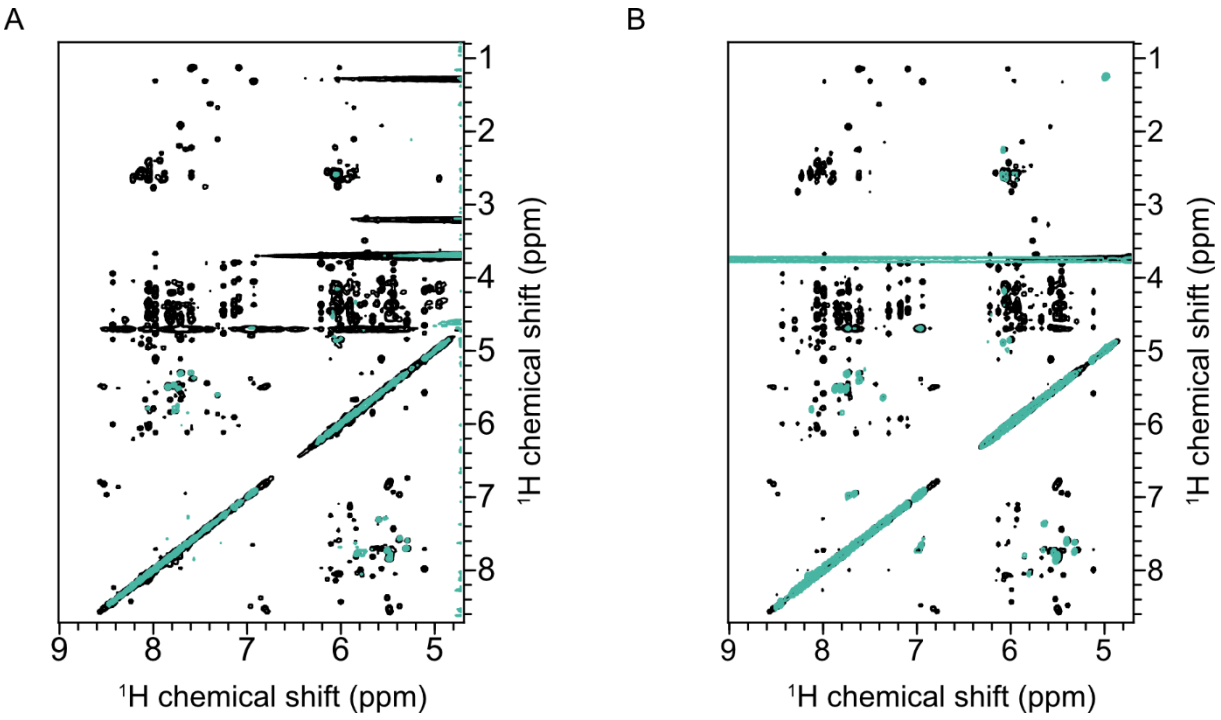

Figure 41: Spectral section overlay of 2D ^{1}H-^{1}H NOESY in black and 2D ^{1}H-^{1}H TOCSY in green (37°C, 50 mM dTris, pH 7.5, 100 mM NaCl and 10% D_2O). A: Spectral section overlay of 2D ^{1}H-^{1}H NOESY in black and 2D ^{1}H-^{1}H TOCSY in green of Dz46-like DNAzyme. **B:** Spectral section overlay of 2D ^{1}H-^{1}H NOESY in black and 2D ^{1}H-^{1}H TOCSY in green of Dz46nmr2-like DNAzyme.

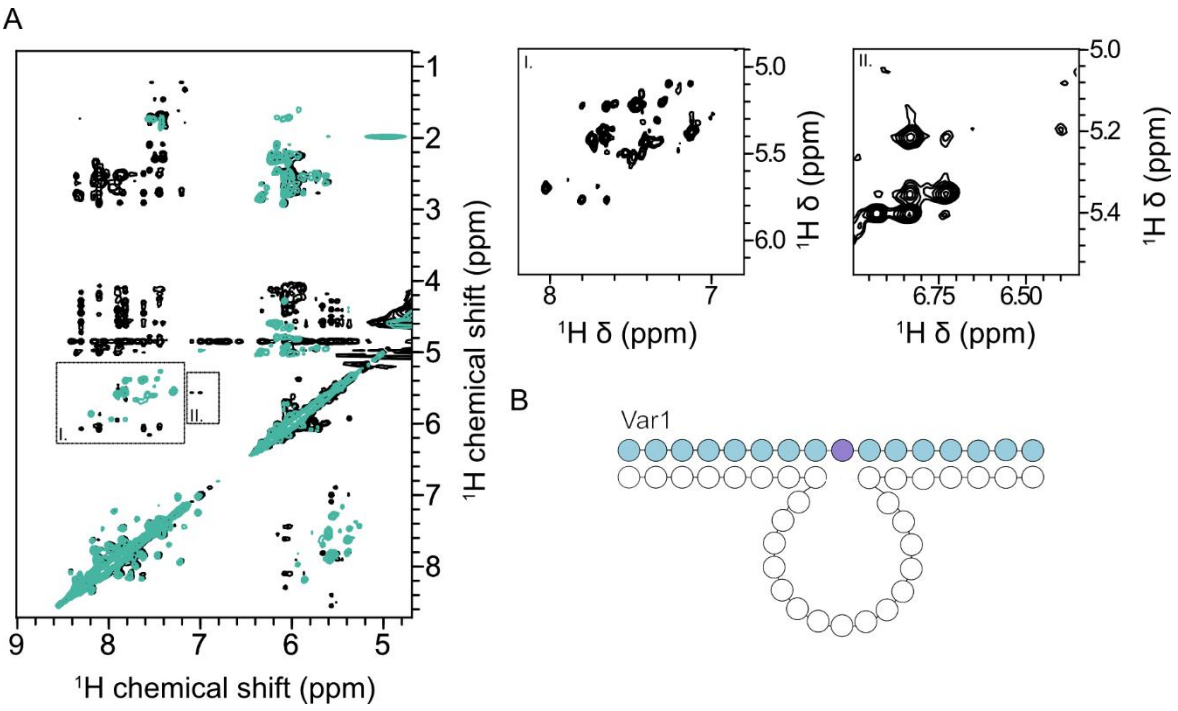

Figure 42: NMR spectroscopic characterisation of Var1. A: Overlay of 2D ^{1}H-^{1}H NOESY in black and 2D ^{1}H-^{1}H TOCSY in green (37°C, 50 mM dTris, pH 7.5, 100 mM NaCl, 1 mM $MgCl_2$ and 10% D_2O). Characteristic regions are highlighted and magnified next to the overlay. Region I (^{1}H-^{1}H TOCSY) show the fingerprint region of Var1, and region II (^{1}H-^{1}H NOESY) highlights the appearance of classical hydrogen bonds found in Watson-Crick base pairing. **B:** Schematic figures of modifications featured in Var1.

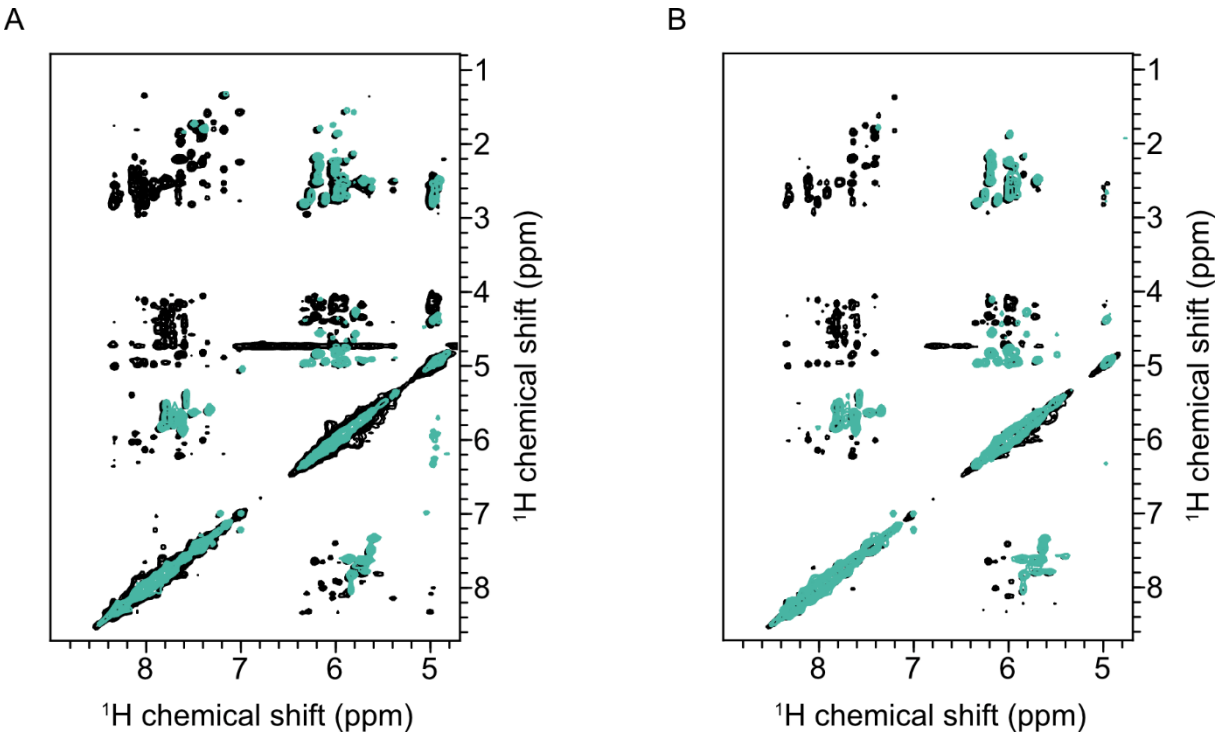

Figure 43: Introduction of the A5C variant to improve the stability of the catalytic loop of Var1 and Var2. A: Overlay of 2D ^{1}H-^{1}H NOESY in black and 2D ^{1}H-^{1}H TOCSY in green for Var3 (37°C, 50 mM dTris, pH 7.5, 100 mM NaCl, 1 mM $MgCl_2$ and 10% D_2O). **B:** Overlay of 2D ^{1}H-^{1}H NOESY in black and 2D ^{1}H-^{1}H TOCSY in green for Var4 (37°C, 50 mM dTris, pH 7.5, 100 mM NaCl, 1 mM $MgCl_2$ and 10% D_2O).

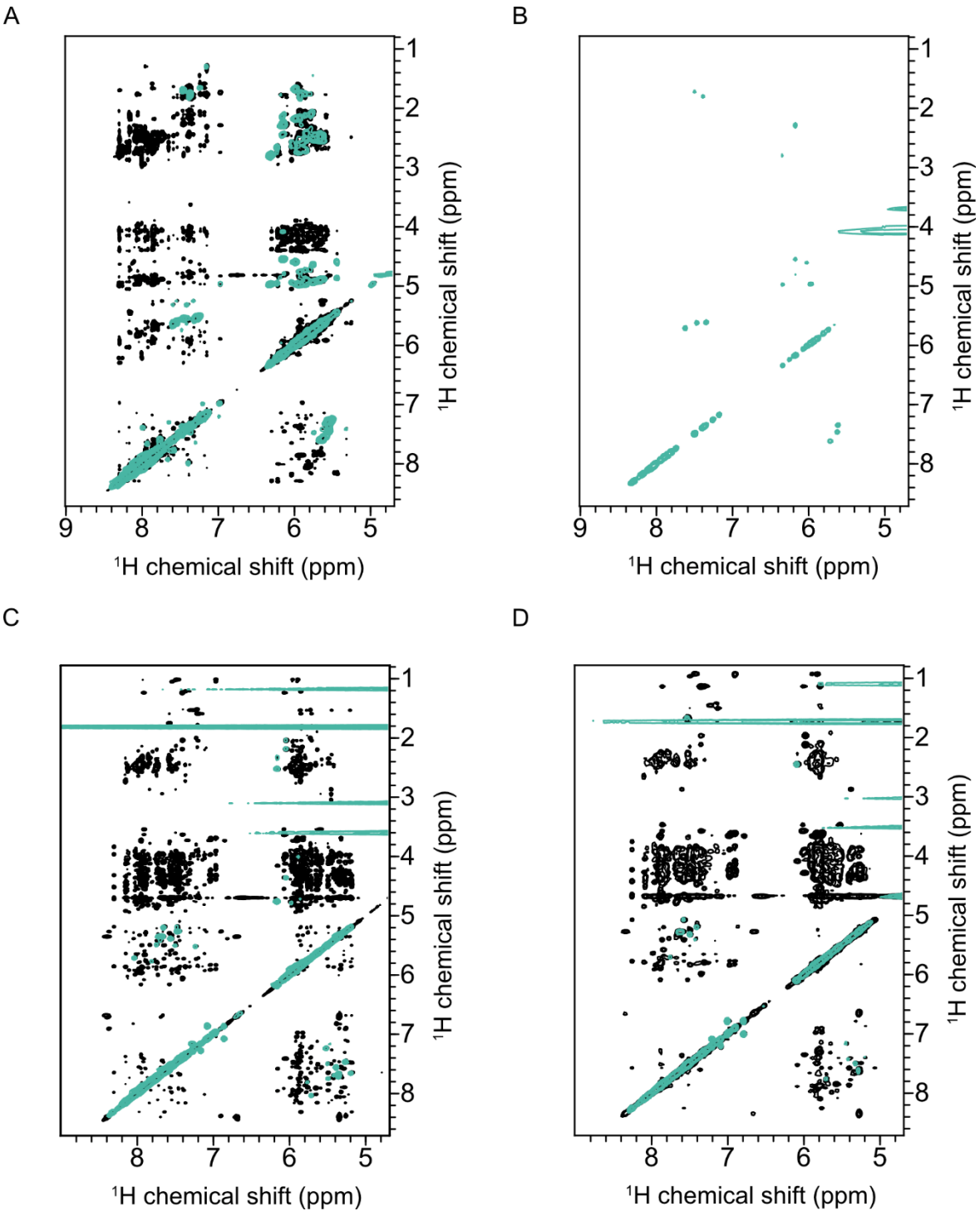

Figure 44: Overlay of ^{1}H-^{1}H NOESY (black) with ^{1}H-^{1}H TOCSY (green). A: Overlay of ^{1}H-^{1}H NOESY (black) with ^{1}H-^{1}H TOCSY (green) of a single DNAzyme without target RNA Var2 at 25°C. **B:** ^{1}H-^{1}H TOCSY (green) of single DNAzyme without target RNA Var2 at 37 °C. **C:** Overlay of ^{1}H-^{1}H NOESY (black) with ^{1}H-^{1}H TOCSY (green) of Var6 at 25°C. **D:** Overlay of ^{1}H-^{1}H NOESY (black) with ^{1}H-^{1}H TOCSY (green) of Var6 at 20 °C.

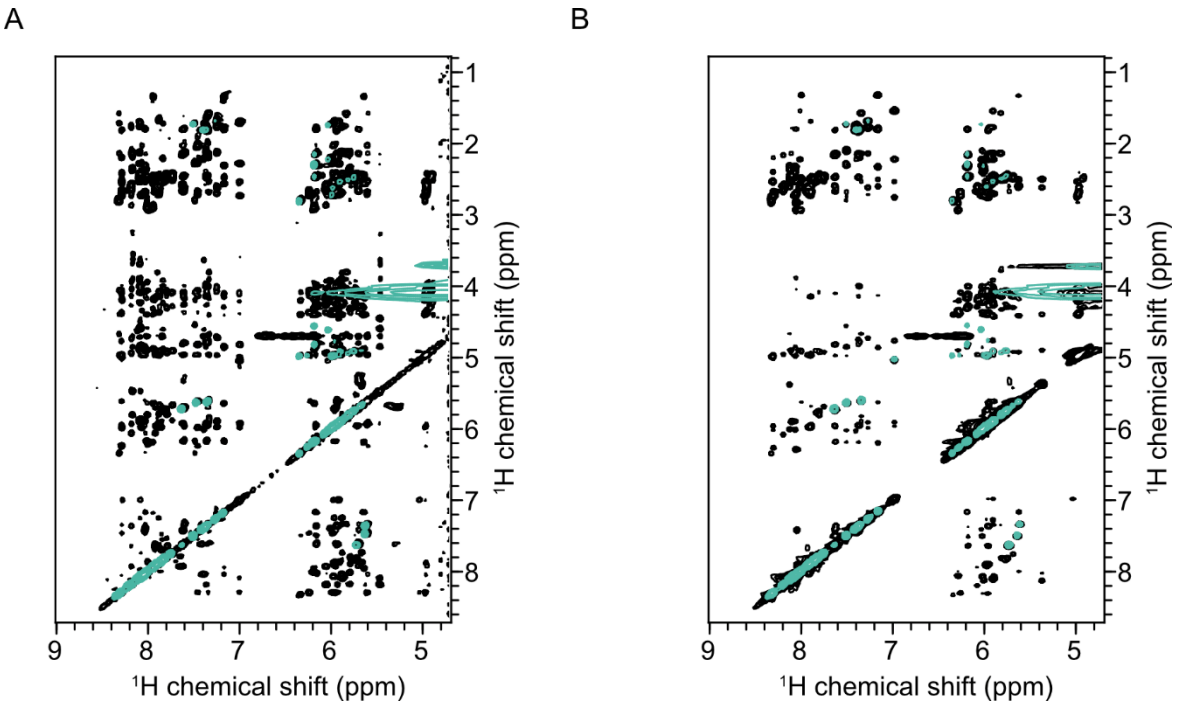

Figure 45 A: Overlay of ^{1}H-^{1}H NOESY (black) with ^{1}H-^{1}H TOCSY (green) of Var2 without target RNA. **B:** Overlay of ^{1}H-^{1}H NOESY (black) with ^{1}H-^{1}H TOCSY (green) of Var1 without target RNA.

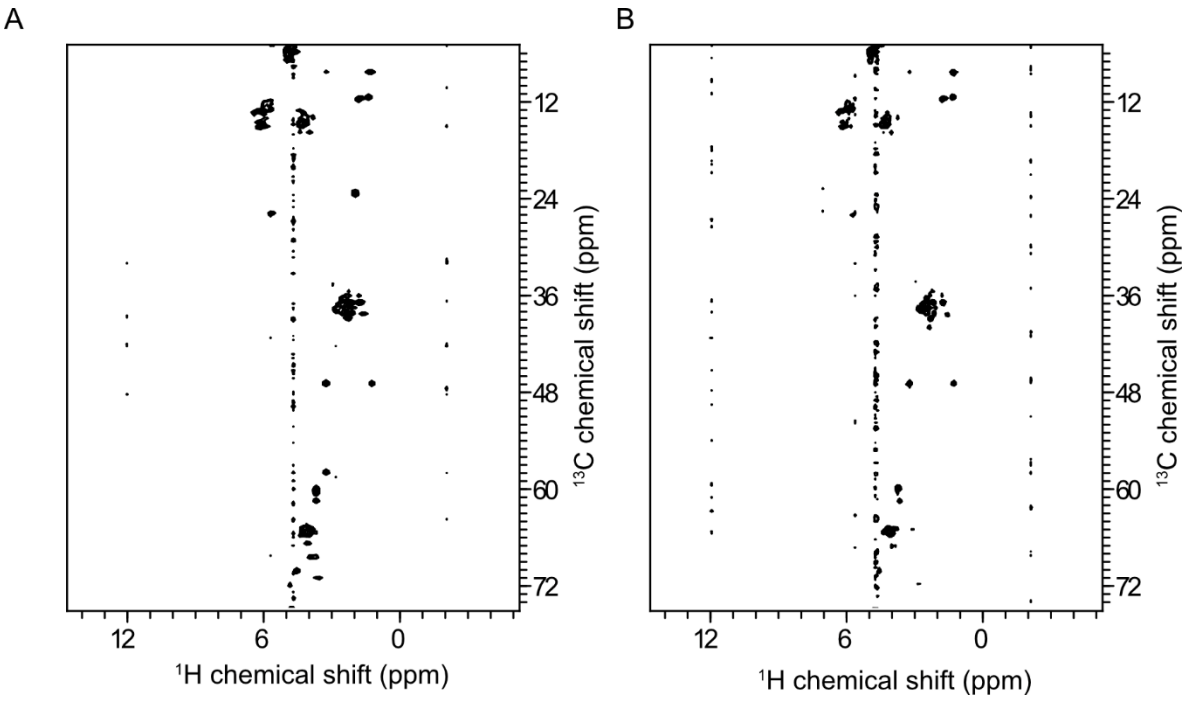

Figure 46: A: ^{1}H-^{13}C HSQC Var2 without target RNA. **B:** ^{1}H-^{13}C HSQC of Var1 without target RNA.

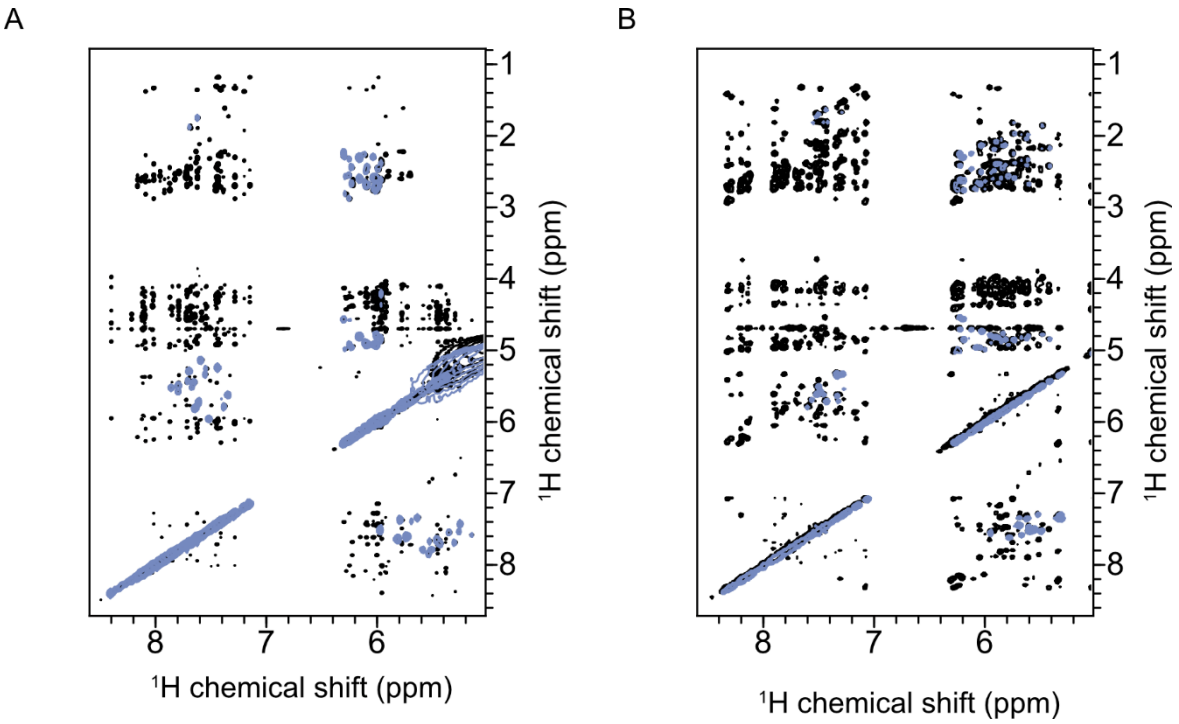

Figure 47 A: Overlay of ^{1}H-^{1}H NOESY (black) with ^{1}H-^{1}H TOCSY (purple) of DNAzyme 8-17 with 2'F-RNA target. **B:** Overlay of ^{1}H-^{1}H NOESY (black) with ^{1}H-^{1}H TOCSY (purple) of DNAzyme 8-17 with a chimeric-DNA target.

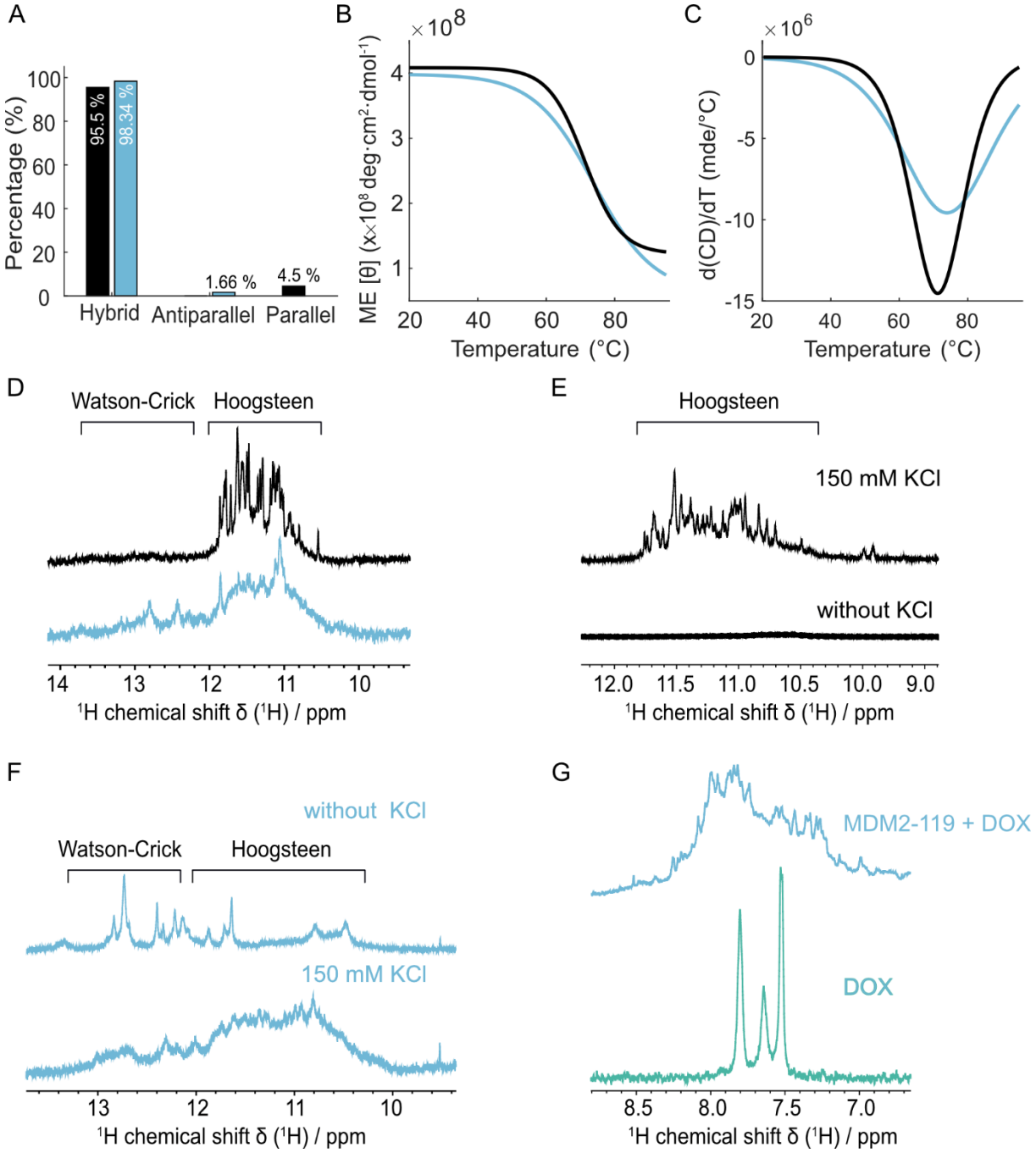

Figure 48: CD and NMR spectroscopic characterisation of MDM2-119 interacting with doxorubicin. Black lines are MDM2-119, and blue lines are MDM2-119 with two equivalents of doxorubicin. All CD samples were measured in 20 mM potassium phosphate, pH 6.2, and 100 mM KCl. **A:** Bar graph of MDM2-119 fitted G4 quadruplex conformation with and without doxorubicin measured at 25°C. **B:** Both fitted melting curves (20–95°C) of MDM2-119 and MDM2-119 with doxorubicin in one plot. **C:** Derivation of fitted melting curves of MDM2-119 and MDM2-119 with doxorubicin. **D:** Imino-area 1D ^{1}H NMR spectrum of MDM2-119 and MDM2-119 with two equivalents of doxorubicin without (20 mM potassium phosphate, pH 7.4, 100 mM KCl) measured at 20°C.**E:** Imino-area 1D ^{1}H NMR spectrum of MDM2-119 without and with 150 mM KCl (25 mM lithium acetate, pH 6.2) measured at 20 °C. **F:** Imino-area 1D ^{1}H NMR spectrum of MDM2-119 with two equivalents of doxorubicin without and with 150 mM KCl (25 mM lithium acetate, pH 6.2) measured at 20°C. **G:** 1D ^{1}H NMR spectrum of doxorubicin (400 µM, 20 mM potassium phosphate, pH 7.4, 100 mM KCl) in light green and MDM2-119 + DOX (200 µM MDM2-119, 400 µM, 20 mM potassium phosphate, pH 7.4, 100 mM KCl) measured at 30°C.

6.2 Supplementary additional Material and Methods

6.2.1 Biochemical characterisation of pin deoxyribozymes

According to the sequencing data on the reselected G4 population, pin deoxyribozymes own a high level of nucleotide conservation throughout the construct **(Figure 9G).** Mutation assays confirmed that for most positions, including those in the stem of pin20, nucleotide changes are deleterious to hydrolysis activity, and compensatory mutations that restore base pairing in the stem cannot restore activity **(Supplement Figure 29, M1-50)**, suggesting that nucleotide identity, rather than base pairing, in the stem is important for robust catalysis. Certain mutation tolerance was observed on two nucleotides, one at position 11, where single point mutations of A11T (M33) and A11C (M34) retain full DNA cleavage activity whereas that of A11G (A35) and deletion of A11 (M36) cause partial loss of activity, the other at position 18, where single point mutations of C18A (M13) and C18T (M14) have no effect on activity while that of C18G (M15) and deletion of C18 (M49) reduce activity. These findings are consistent with the consensus sequence model of pin deoxyribozymes **(Figure 9G)**.

Besides A11 and C18, single point deletions of A9 (M43), T10 (M44), and T19 (M50) are also tolerable by pin20, though that weakens its activity. On any of the five resulting 19-nt variants, further single-point deletions completely inactivated the deoxyribozyme (data not shown), suggesting a minimum size of 19 nt for pin. Of the 19-nt variants of pin20, the one with deletion of A11 was the least affected in activity and was named pin19 **(Figure 9A)**. In the selection buffer at 37°C, pin19 hydrolysed 1.9-fold slower than pin20 **(Figure 9I)**.

6.2.2 Metal-ion dependence of self-hydrolysing DNAs

To identify the metal ion dependence of the self-hydrolysing deoxyribozymes, a series of buffers (50 mM HEPES (pH 8.4 at 23°C), 100 mM LiCl) containing different types of divalent metal ions (2 mM Cu^{2+}, Ca^{2+}, Zn^{2+}, Mn^{2+}, Co^{2+}, Mg^{2+}, or Ni^{2+}) or different combinations of divalent metal ions were prepared. To identify the dependence of Cd^{2+} concentration for the self-hydrolysing deoxyribozymes, a series of buffers (50 mM HEPES (pH 8.4 at 23°C), 100 mM LiCl, 5 mM $MgCl_2$) containing various concentrations of Cd^{2+} (from 0.1 mM to 20 mM) were prepared. About 5 pmol of the DNA sample was then incubated at 37°C in 40 µl of each reaction buffer for either 20 min or 2 h. To identify the dependence of the self-hydrolysing deoxyribozymes on monovalent metal ions, the DNA samples were incubated at 37°C in the reaction buffers (50 mM HEPES (pH 8.4 at 23°C), 5 mM $MgCl_2$, 2 mM $CdCl_2$) containing different monovalent metal ions (100 mM Li^+, Na^+, or K^+) for 0 min, 5 min or 20 min. All reaction systems were stopped by adding an equal volume of the loading buffer (90% formamide, 30 mM EDTA, 0.025% bromophenol blue, 0.025% xylene cyanol); ~15 µl of each product was loaded onto 20% dPAGE gels for band separation and further analysis.

6.2.3 pH dependence of self-hydrolysing DNAs

A series of buffers (50 mM HEPES or Tris, 100 mM LiCl, 5 mM $MgCl_2$ and 2 mM $CdCl_2$) was prepared with different pH values (HEPES: from 7.60 to 8.70, Tris: from 8.00 to 9.10, at 23°C). To identify the pH dependence, 5 pmol of DNA samples were incubated at 37°C in 40 µl volume of each of these buffers for either 20 min or 2 h. All reaction systems were stopped by adding equal volume of the loading buffer (90% formamide, 30 mM EDTA, 0.025% bromophenol blue, 0.025% xylene cyanol) and analysed by 20% dPAGE.

Interpretation of the pH dependency of the pin system in relation to $CdCl_2$ concentration

The pH dependency of the catalytic activity in the pin system is strongly influenced by the concentration of $CdCl_2$ **(Figure 11G, Supplement Figure 27A)**, supporting the hypothesis that a soluble, polynuclear $Cd_n(OH)_m$ cluster functions as the true catalytic cofactor. In this scenario, the formation and availability of the catalytically active Cd-cluster are governed by the equilibrium:

$$n \cdot Cd^{2+} + m \cdot OH \rightleftharpoons Cd_n(OH)_m$$

with an associated dissociation constant

$$K_b = \frac{[Cd^{2+}]^n \cdot [OH]^m}{[Cd_n(OH)_m]}$$

As a result, the effective concentration of the catalytically active Cd-cluster is governed by the interplay between free Cd^{2+} concentration and pH. At low pH, limited hydroxide availability suppresses cluster formation; however, this can be compensated for by increasing the Cd^{2+} concentration. Conversely, at higher pH, cluster formation is promoted, but excessive hydroxide may lead to precipitation—an effect that can be mitigated by reducing the Cd^{2+} concentration to maintain the system within an optimal range **(Figure 11G, Supplement Figure 27A).** This balance explains the observed pH-dependent catalytic profile as a function of Cd^{2+} concentration.

Impact of buffer handling on the observed pH dependency of pin activity

To investigate the pH dependence of pin deoxyribozyme activity, we conducted experiments across a series of buffer solutions spanning a wide pH range, including values above the theoretical precipitation point of $Cd(OH)_2$ (~pH 8.5 for 2 mM Cd^{2+}). Interestingly, when the Cd^{2+} concentration was fixed at 2 mM, different buffer preparation protocols led to distinct activity profiles. In one approach, buffers containing 2 mM Cd^{2+} were pre-prepared at various pH values and allowed to rest for 1–2 days. Any resulting $Cd(OH)_2$ precipitates were settled, and

only the supernatants were used for subsequent reactions. Under these conditions, pin activity reached and maintained a high plateau with increasing pH **(Figure 9O)**. In contrast, when Cd^{2+}-free buffers at various pH values were freshly mixed with pin deoxyribozymes, and Cd^{2+} was added directly to initiate the reaction, a spike-like activity profile was observed: activity peaked at an intermediate pH and then declined sharply at higher pH values **(Figure 11G, Supplement Figure 27A).**

We attribute this discrepancy to the potential adsorption of DNA onto freshly formed $Cd(OH)_2$ precipitates, which suppresses deoxyribozyme activity. In the first (rested) condition, precipitates were removed by settling to minimise interference. In the second (fresh) condition, $Cd(OH)_2$ formed in situ remained in the reaction mixture, thereby impacting activity **(Supplement Figure 27B)**.

Table 14: Assignment of Pin20 at 37°C. Chemical shifts are listed in ppm.

Nucleotide	H1'	H2'	H2''	H3'	C1'	C3'	H6/H8	H5	H7
dC1	5.801				126.1099	115.7099	7.364	5.762	
dA2	5.676	2.652	2.691	4.91	122.8459	116.7709	8.184		
dA3	5.935	2.68	2.784	5.011	122.1879	116.4389	8.153		
dG4	5.794	2.531	2.589	4.94	121.7049	116.7139	7.717		
dC5	6.082	1.768	2.49	4.79	124.1339	115.3519	7.333	5.27	
dT6	5.662	1.979	2.205	4.828	123.5019	115.6099	7.372		1.77
dG7	6.078	2.496	2.642	4.874	122.5329	116.2339	7.941		
dC8	5.944	1.84	2.296	4.731	125.5849	115.9929	7.473	5.854	
dA9	6.231	1.686	2.764	4.945	123.5139	115.7579	8.232		
dT10	5.964	1.875	2.215	4.683	124.5639	115.4169	7.308		1.689
dA11	6.139	1.558	2.603	4.855	123.6529	115.6199	8.17		
dT12	5.986	2.113	2.312	4.722	124.6779		7.338		1.557
dT13	5.824	1.828	2.187	4.683	124.7449	115.7979	7.244		1.684
dA14	6.118	2.69	2.704	4.915	123.1989	116.2199	8.236		
dC15	5.714	2.058	2.374	4.781	124.6399	114.6959	7.491	5.678	
dG16	5.735	2.567	2.712	4.934	122.2089		7.817		

Table 15: Assignment of Pin19 at 37°C. Chemical shifts are listed in ppm.

Nucleotide	H1'	H2'	H2''	H3'	H6/H8	H5	H7
dC1	5.7987	1.4467	2.0867		7.3667	5.7547	
dA2	5.6727	2.6767	2.7157	4.9227	8.1997		
dA3	5.9477	2.6887	2.8067	5.0217	8.1637		
dG4	5.7967	2.5417	2.6087	4.9547	7.7197		
dC5	6.0907	1.9737	2.5027	4.8017	7.3267	5.2617	
dT6	5.6497	1.9607	2.1927	4.8437	7.3647		1.7787
dG7	6.1067	2.4777	2.6587	4.8687	7.9547		
dC8	5.9427	2.3597	1.9307	4.7547	7.5307	5.9457	
dA9	6.3057	2.7157	2.7997	4.9327	8.2697		
dT10	6.0317	2.1367	2.3237	4.7567	7.4117		1.6777
dT11	5.9817	2.0627	2.2767	4.6977	7.4087		1.6787
dT12	5.8097	1.8197	2.1617	4.6527	7.2367		1.6497
dA13	6.1247	2.6897	2.7387	4.9147	8.2317		
dC14	5.6877	2.1057	2.3977	4.7987	7.5067	5.7237	
dG15	5.7387	2.5927	2.7457	4.9537	7.8287		
dG16	5.9167	2.6027	2.7217	4.9677	7.7777		
dC17	6.0037	2.0957	2.4957	4.7887	7.4237	5.3837	
dT18	6.2077	2.2647	2.5557	4.8917	7.5177		1.7327
dT19	6.3017	2.2667	2.3247	4.5957	7.5837		1.8067

Table 16: Assignment of Pin21 at 37°C. Chemical shifts are listed in ppm.

Nucleotide	H1'	H2'	H2''	H3'	H6/H8	H5	H7
dC1	5.895	1.566	1.566	4.496	7.406	5.829	
dA2	5.872	2.5	2.583	4.888	8.099		
dA3	5.862	2.483	2.584	4.941	8.089		
dG4	5.873	2.54	2.54	4.93	7.839		
dC5	6.104	2.445	2.091		7.55	5.669	
dT6	5.943	1.892	2.251		7.349		1.749
dG7	5.973	2.543	2.652	4.901	7.892		
dC8	5.986	1.765	2.244		7.433	5.74	
dA9	6.228	2.729	2.729		8.265		
dT10	5.928	1.829	2.205	4.748	7.241		1.656
dA11	6.227	2.719	2.719	4.951	8.277		
dT12	5.931	1.805	2.21	4.742	7.305		1.756
dT13	6.051	2.16	2.375	4.801	7.387		1.638
dA14	6.236	2.695		4.936	8.267		
dC15	6.111	2.107	2.402	4.748	7.591	5.783	
dC16	5.978	1.828	2.258	4.694	7.543	5.915	
dG17	5.73	2.443	2.443	4.845	7.748		
dG18	5.556	2.453	2.453	4.895	7.76		
dA19	6.284	2.753	2.753	5.002	8.284		
dT20	6.085	2.201	2.423	4.807	7.374		1.667
dT21	6.195	2.267	2.267	4.521	7.559		1.795

Table 17: Assignment of Pin23 at 37°C. Chemical shifts are listed in ppm.

Nucleotide	H1'	H2'	H2''	H3'	H6/H8	H5	H7
dC1	5.9094	1.5734	2.1774	4.5074	7.4064	5.8354	
dA2	5.8774	2.5104	2.5794	4.8924	8.1064		
dA3	5.9214	2.4884	2.5984	4.9484	8.0704		
dG4	5.8604			4.9174	7.7964		
dC5	6.1164			4.7694	7.5874	5.7344	
dT6	5.9634	1.9084	2.2534	4.7314	7.3544		1.7474
dG7	5.9734	2.5554	2.6654	4.9094	7.8804		
dC8	6.0004	1.7984	2.2664	4.7164	7.4434	5.7324	
dA9	6.3314	1.6444	2.7594	4.9614	8.2934		
dT10	6.1144	2.1804	2.3834	4.8054	7.3934		1.6464
dC11	6.1414	2.1974	2.4844	4.7894	7.7174	5.9484	
dT12	6.1134	2.2014	2.4174	4.8114	7.5264		1.7884
dT13	5.9764	1.8824	2.2504	4.7594	7.3404		7.3404
dA14	6.2914	2.7734	2812.975	4.9754	8.3274		
dT15	6.0604	2.1284	2.3454	4.7814	7.3494		1.6444
dC16	6.0244	1.7964	2.2574	4.7784	7.5064	5.8994	
dG17	5.8384	2.4944	2.5064	4.8804	7.7834		
dG18	6.0274	2.6414	2.6994	4.9784	7.8754		
dT19	6.1354	2.1864	2.3954	4.8654	7.4174		1.6894
dC20	6.1604	2.1244	2.4164	4.7604	7.6764	5.9584	
dC21	6.0344	2.2654	2.2814	4.7244	7.5354	5.9504	
dA22	6.3474	2.7944	2.8274	4.9754	8.3394		
dT23	6.1584	2.2574	2.2724	4.5374	7.4694		1.7144

Table 18: Assignment of Pin22 at 20°C. Chemical shifts are listed in ppm.

Nucleotide	H1'	H2'	H2''	H3'	H6/H8	H5	H7
dC1							
dC2							
dA3							
dG4							
dC5				4.879	7.489	5.493	
dT6							
dG7							
dC8							
dA9							
dT10	5.974			4.777	7.301		1.66
dA11	6.201			4.903	8.246		
dT12	7.406	2.14	2.332	4.766	7.406		1.625
dT13	5.885			4.71	7.301		1.725
dA14	6.152	2.737		4.974	8.213		
dC15	6.085	1.91	2.362	4.78	7.52	5.675	
dG16	5.897			4.946	7.96		
dC17					-0.03		
dG18	5.802			5.007	7.808		
dC19	5.913			4.749	7.246	5.458	
dA20	6.319	2.96	2.849	5.025	8.356		
dT21	6.107	2.27	2.461	4.837	7.463		1.702
dT22	6.235			4.558	7.605		1.824

Table 19: Assignment of free Var2 (without target RNA) at 37°C. Chemical shifts are listed in ppm. Asterisks indicate unassigned residues, and subscripted numbers represent residues located in the target recognition arms.

Nucleotide	H1'	H2'	H2''	H3'	H6/H8	H5	H7
dT_{+1}	6.008	1.734	2.217	4.61	7.379		6.008
dG_{+2}	5.736	2.475	2.522	4.888	7.828		
dG_{+3}*							
dG_{+4}*							
dG_{+5}	5.965			4.966	7.877		
dT_{+6}	5.886	1.768	2.134	4.721	7.246		1.681
dA_{+7}*							
dA_{+8}*							
dG1*							
dG2*							
dC3*	6.163	2.149	2.46	4.799	7.612	5.699	
dT4	5.934	2.095	2.392	4.736	7.354		1.77
dA5	6.054	2.587	2.6653	4.939	8.173		
dG6	5.955			4.95	7.913		
dC7	6.151	2.14	2.46	4.795	7.595	5.698	
dT8	5.942	1.821	2.199	4.77	7.34		1.787
dA9	6.237	2.672	2.726	4.962	8.279		
dC10	5.977	2.034	2.275	4.821	7.452	5.609	
dA11*							
dA12	5.977	2.543	2.741	4.985	8.276		
dC13	5.92	1.711	2.292	4.818	6.992	5.035	
dG14	5.466			4.851	8.074		
dA15	5.796	2.146	2.361	4.698	8.159		
dA_{-1}	6.185	2.869	2.917	4.892	8.002		
dG_{-2}	5.641				7.937		
dT_{-3}	6.166	1.804	2.316	4.843	7.164		1.351
dG_{-4}	5.882	2.534	2.695	4.965	8.025		
dC_{-5}	5.832	1.592	2.141	4.667	7.329	5.6	
dA_{-6}	6.328	2.784	2.814	4.972	8.309		
dT_{-7}	6.164	2.279		4.549	7.483		1.73

7 Publication list

Zhang, C.*, **Schmuck, J.F.***, Wang, M.*, Hesse, R., Gertzen, C., Zhou, M., Fan, C., Steger, G., Gohlke, H., Etzkorn, M., & Gu, H. Structural (d)evolution of a minimalistic DNA enzyme. – submitted

Hesse, R., Gertzen, C. G. W., **Schmuck, J. F**., Böcker, J. D., Pandey, P., Behn, T., Ruth, C., Riesner, D., Kath-Schorr, S., Lang, P. A., Gohlke, H., & Etzkorn, M. (2025). The coming of age of DNA-based catalysts for therapeutic applications. *Clinical and translational medicine*, 15(7), e70408. https://doi.org/10.1002/ctm2.70408

Schmuck, J. F., Borggräfe, J., & Etzkorn, M. (2024). The dynamic world of the 8-17 DNAzyme. *Nature communications*, 15(1), 5145. https://doi.org/10.1038/s41467-024-49500-w

8 List of oral presentations, poster flash talks, conference posters and further worked on projects

In the following chapter, oral presentations, poster flash talks, conference posters, and further work on projects (mostly cooperation projects) during the PhD will be listed and shortly explained.

8.1 Oral presentations

Schmuck, J.F., Zhang, C., Gu, H., Etzkorn, M., *NMR spectroscopy of self-hydrolysing DNA,* 9th Murnau Conference 4D Structural Biology, Murnau 2024

Schmuck, J.F., Zhang, C., Gu, H., Etzkorn, M., *NMR spectroscopy of self-hydrolysing DNA,* Annual Meeting bio-N^{3}MR Netzwerk NRW, Essen 2024

Schmuck, J.F., Borggräfe, J, Etzkorn, M., NMR insights into DNA catalysts*,* Annual Meeting bio-N^{3}MR Netzwerk NRW, Dortmund 2023

8.2 Poster Flash Talks

Schmuck, J.F., Zhang, C., Gu, H., Etzkorn, M., *NMR spectroscopy of self-hydrolysing DNA,* XIVth International Conference, NMR: a tool for biology, Paris 2025

Schmuck, J.F., Borggräfe, J, Etzkorn, M., NMR insights into DNA catalysts*,* XI. Nucleinsäuretreffen, Würzburg 2023

8.3 Poster

Schmuck, J.F., Zhang, C., Gu, H., Etzkorn, M., *NMR spectroscopy of self-hydrolysing DNA,* XIVth International Conference, NMR: a tool for biology, Paris 2025

Schmuck, J.F., Zhang, C., Gu, H., Etzkorn, M., *NMR spectroscopy of self-hydrolysing DNA,* Euromar 2024, Bilbao 2024

Schmuck, J.F., Borggräfe, J, Etzkorn, M., NMR insights into DNA catalysts*,* XI. Nucleinsäuretreffen, Würzburg 2023

8.4 Projects

This chapter provides a brief overview of the results from additional projects.

NMR and CD spectroscopic characterisation of Sense/Antisense DNA Duplexes with and without Overhang (Cooperation with Christine Wübben, Universität Bonn)

NMR spectroscopic characterisation of a sense/antisense oligonucleotide with and without overhang and with and without an attached cholesterol, regarding diverse buffer conditions, and their effects on the structure.

G4-quadruplex (Cooperation with Barbara Kirchner, Oldamur Holloóczki, Universität Bonn)

NMR spectroscopic characterisation of three multimeric G-quadruplexes, varying in their sequence and abundance of guanines, regarding their thermal stability and resulting structural differences.

NMR-spectroscopic characterisation of the G14 6-thioguanine DNAzyme-variant:

NMR spectroscopic characterisation of introduced 6-thio-guanine at the G14 positions of the catalytic loop of the DNAzyme-variant 839 wt and effects on the catalytic loop. The results are presented in Justin Darvin Böcker's doctoral thesis.

NMR spectroscopic supervision in Master project (Kübra Arslan)

Aptamers (Nuckey), developed by Justin Darvin Böcker, are attached to either the 5' or 3'-end of a DNAzyme. The master's thesis aimed to investigate the aptamer without attached DNAzyme and with the two 3' and 5' variants using NMR spectroscopy. Samples were either measured by me or under my supervision, and I supervised further evaluation (e.g., resonance assignment). The results can be found in Justin Darvin Böcker's doctoral thesis and Kübra Arslan's master's thesis.

NMR-spectroscopic characterisation of FANAzyme DNAzyme (Cooperation with Phillip Holliger from Cambridge University)

2D ^{1}H-^{1}H NOESY and TOCSY spectra were measured for further characterisation. A short attempt was made at resonance assignment. However, the spectra suffered from poor spectral quality (spectral resolution, background noise and broad peaks). As a result, the project was not pursued further.

DNAzymes for novel cancer therapies targeting the KRAS signalling pathway (Manchot Project)

DNAzymes are short, single-stranded oligonucleotides capable of catalysing a variety of chemical reactions, among others, the sequence-specific cleavage of RNA. Therefore, DNAzymes have a growing therapeutic potential in diseases associated with elevated protein levels or long non-coding RNA. Different types of DNAzymes are already well-known and characterised. For RNA-cleaving DNAzymes, these include the DNAzyme types 8-17 and 10-23 (more detailed review in Chapter 1.2.1), which differ by their catalytic loop sequence and structural conformation. The catalytic loop is flanked by two target recognition arms, which can be freely designed in a sequence-specific manner. Sequence-specific cleavage carried out by a DNAzyme results in fast degradation of the target mRNA. Thus, leading to a decreased expression of cancerogenic proteins (Thomas et al., 2021).

KRAS (Kirsten rat sarcoma) **(Figure 49)** is a proto-oncogene and has the highest point mutation rate among all cancers, including colorectal cancer, pancreatic cancer, and many more. RAS is a GTPase working as a molecular switch in the signal transduction responsible for cell division. Point mutations in the mRNA of the KRAS gene lead to permanent activation of the KRAS-controlled signal transduction, resulting in permanent, uncontrolled cell division (Huang et al., 2021, Liu et al., 2019). Long non-coding RNAs (lncRNAs) bind to microRNAs (miRNAs) and inactivate them through binding. However, microRNAs are of great importance since they can suppress tumour growth. High concentrations of specific lncRNAs are associated with diverse cancers (Mattick et al., 2023)

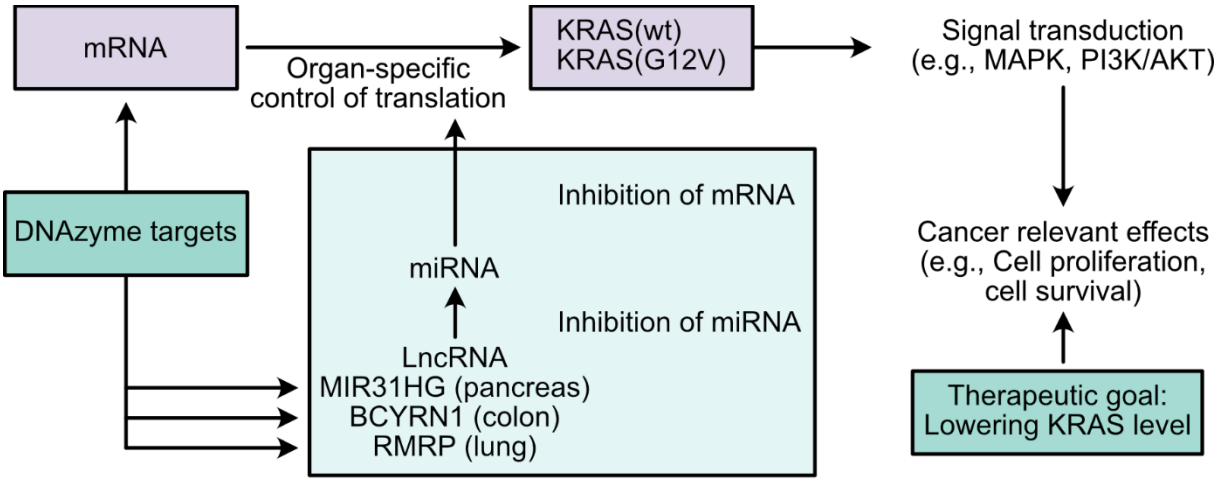

Figure 49: Schematic Overview of KRAS-involved signal transductions.

This project aimed to study the DNAzyme-mediated direct reduction of KRAS mRNA in cells and the indirect reduction of KRAS mRNA through targeting organ-specific long non-coding RNAs **(Figure 49)**.

The project application aimed to develop new DNAzyme variants that target the mRNA of the KRAS G12V mutation to lower KRAS levels. The development algorithm of the institute was used to design the best DNAzyme in terms of cleavage site, spatial accessibility and optimal thermodynamic sequence/structure. The development algorithm revealed that the mRNA of the G12V mutation has a predicted, limited spatial accessibility for DNAzymes. As a result, a mutation was sought that is clinically relevant and spatially more accessible to DNAzymes. The choice fell on a mutation upstream of codon 12, which was named in the following paragraphs as KRAS mutant (mt).

Development of KRAS mt targeting DNAzymes

Four different DNAzyme constructs were designed **(Table 20)** targeting the KRAS mt. The DNAzymes differ in their cleavage site and DNAzyme type.

Table 20: Overview of designed DNAzymes targeting the KRAS mt mutation using 8-17 and 10-23 DNAzyme types and different cleavage sites.

Name	DNAzyme-typ	Cleavage site
DNAzyme mt1	10-23	GU
DNAzyme mt2	10-23	GC
DNAzyme mt3	8-17	AG
DNAzyme mt4	8-17	AG

Characterisation of the catalytic activity of newly designed KRAS-targeting DNAzymes

To gain a first impression of the catalytic activity of the previously designed DNAzymes, minimal-length RNA targets with 5'-FAM-fluorophore were designed. Activity was tested *in vitro* for 1 h with 10 mM $MgCl_2$ at 37°C (50 mM Tris-Base, pH 7.5, 10 mM NaCl, 140 mM KCl, and 0.1 mM EDTA). Urea-denaturing PAGE was used to denature DNA constructs for electrophoretic separation by size. All of the designed DNAzymes possess catalytic activity **(Figure 50A)**. However, after 1 h of reaction time, only DNAzyme mt1 fully cleaved the RNA. Therefore, DNAzyme mt1 of the designed DNAzymes was the most potent and was further characterised.

Furthermore, the specificity of the DNAzyme mt1 targeting oncogenic point mutations was studied by the development of three additional DNAzyme variants **(Figure 50B)**. One DNAzyme targeting the wildtype RNA and two DNAzymes specific for a single mutation of the double mutant RNA. The RNA target remained unaltered. FRET assays were used to study the catalytic activity of all four constructs, using 5'-FAM as a fluorophore and BHQ1 (Blackhole quencher 1) as a FRET-construct. FRET assays were carried out for six hours at 37°C with 1

mM $MgCl_2$ (50 mM Tris-Base, pH 7.5, 10 mM NaCl, 140 mM KCl and 0.1 mM EDTA). All designed DNAzymes are active **(Figure 50C and D)**. DNAzyme 189 mt1 (k_{obs}/ min^{-1} 0.00079 ± 0.00008) has the strongest activity compared to the DNAzymes with single point mutations (k_{obs}/ min^{-1} TA 0.0002 ± 0.00003 and GT 0.00019 ± 0.00001) and wildtype (k_{obs}/ min^{-1} 0.00019 ± 0.00004). In summary, designing a DNAzyme targeting the KRAS mt mutation was successful. Since off-target effects in therapeutics are one of the undesirable side effects, it is important to investigate and characterise them. These off-target cleavage effects are characterised as RNA getting cleaved, although differences in the target sequence of the DNAzyme are present in at least one or two bases. The DNAzyme recognises different RNA sequences and cleaves them with comparable or much slower activity than the actual target RNA. Our data therefore indicated that the newly developed DNAzyme can increasingly reduce the oncogene variant, an effect that has been impossible to achieve with existing treatment options. In 2023, a KRAS G12V mutation-targeting and fully modified DNAzyme was published. The publication proves that it is possible to design a DNAzyme targeting the KRAS G12V mutation in an allele specific manner with a smart target mechanism. The Dz46 utilises the point mutation occurring in the G12V mutation, generating a cleavage site for the DNAzyme that would not be present without the point mutation. Therefore, the DNAzyme is highly selective and allele-specific. Moreover, the publication could show that the DNAzyme is highly active in lung cancer cells (Nguyen et al., 2023). Corresponding NMR spectroscopic characterisation of the Dz46 G14 MOE modification is further discussed in chapter 3.1.

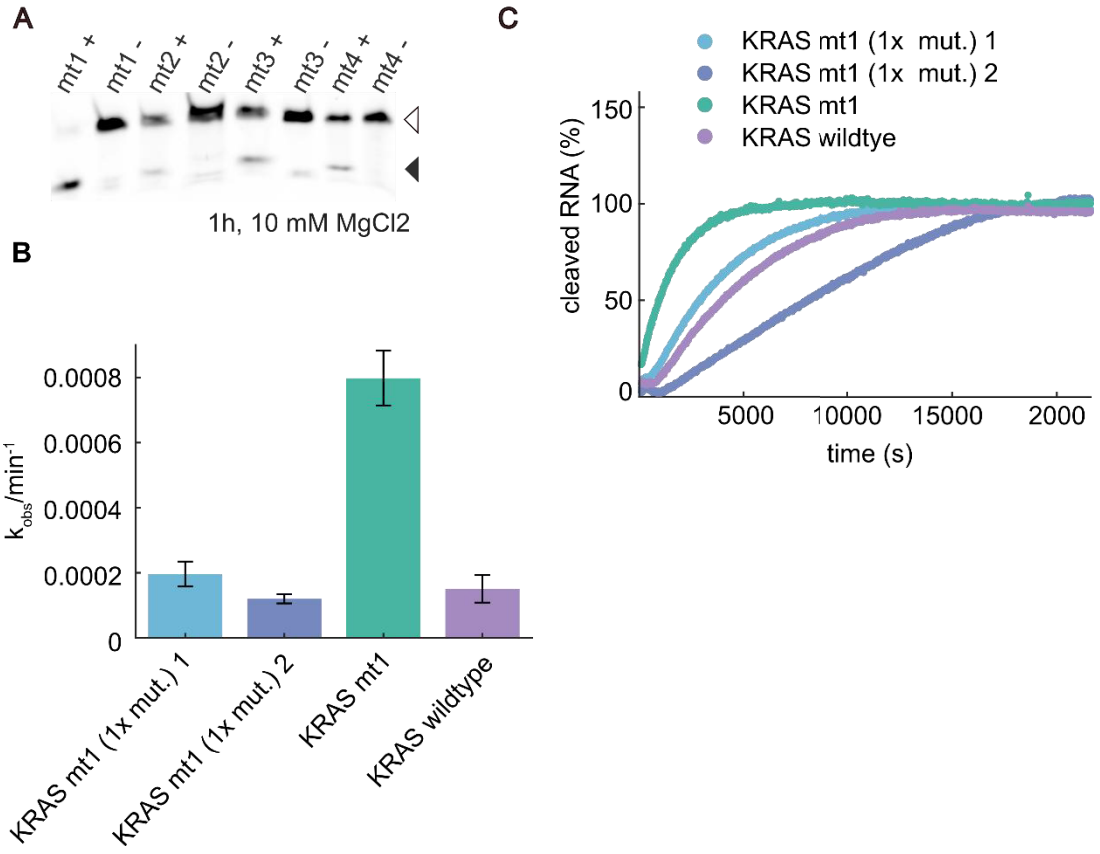

Figure 50: Characterisation of DNAzyme catalytic activity using denaturating Urea-PAGE and FRET assay. **A:** Urea-PAGE of DNAzymes mt1, mt2, mt3 and mt4. '+' indicates samples containing both DNAzyme and RNA. The negative control is represented with '-'. The filled arrow points to the height of the cut product. **B**: Shows DNAzyme mt1 of type 10-23 and the mutation constructs used for the selectivity study. **C:** k_{obs} values of the four different DNAzymes tested. **D:** Shows the corresponding measured activity curves of the different DNAzymes over time.

Characterisation of DNAzyme 8-17 using NMR spectroscopy

Recently, the high-resolution structure of the DNAzyme 10-23 was deciphered by this research group (Borggräfe et al., 2022). Based on these results, interest in the NMR structure for DNAzyme type 8-17 is also growing. DNAzyme 8-17 is equally active in the presence of Ca^{2+} and Mg^{2+} (Brown et al., 2003) and thus has an intracellular advantage over DNAzyme 10-23, which can only access Mg^{2+} intracellularly, in that it can use a larger repertoire of metal ions for catalytic activity. Although the crystal structure of the DNAzyme was deciphered several years ago (Liu et al., 2017), not all questions have yet been answered. Therefore, new DNAzymes with different targets were designed, both of the type 8-17. On the one hand, both newly designed DNAzymes share the same DNAzyme type; on the other hand, the DNAzymes differ in the form of target, either RNA or DNA. Results and further insights into this work can be depicted in Chapter 3.2.

Development of long non-coding DNAzymes and characterisation of their catalytic activity

As before, DNAzymes based on the lncRNA of MIR31HG, RMRP and BCYRN1 were designed using prediction algorithms. For each long non-coding RNA, a DNAzyme was selected that was assigned the highest spatial accessibility. The activity of the DNAzymes was again examined using a FRET assay. For this purpose, a 6-FAM fluorophore was added to the 5' end of the RNA and BHQ to the 3'-end. The FRET assay was measured at 37°C with 0.6–5 mM $MgCl_2$ for three hours (50 mM Tris, pH 7.5, 10 mM NaCl, 140 mM KCl and 0.1 mM EDTA). All three DNAzymes are active under the measured conditions **(Figure 51A, B, C, and D)**. Compared to the other two DNAzymes, the DNAzyme BCYRN1 is the most active.

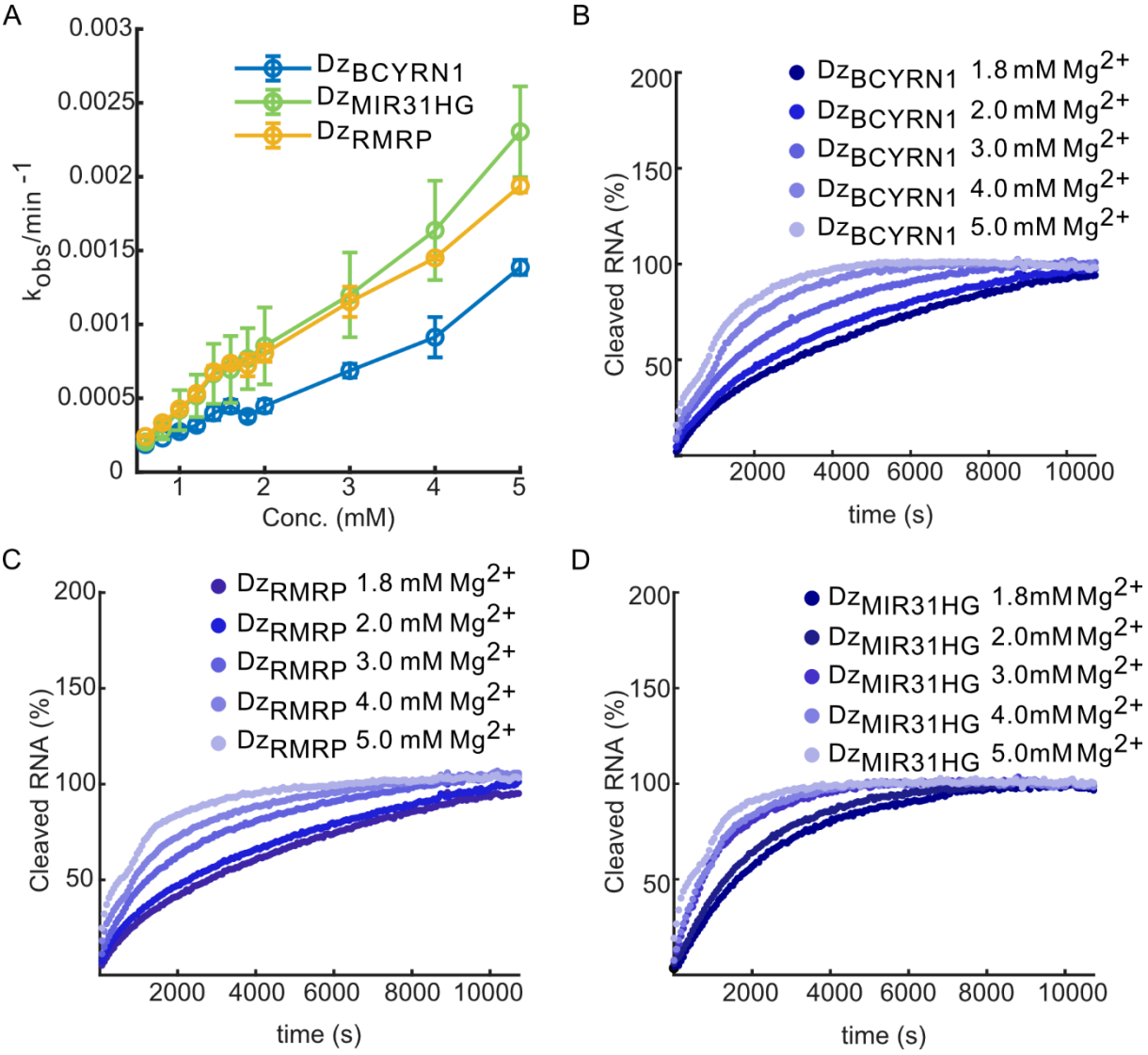

Figure 51: ***In vitro*** **characterisation of the catalytic activity of the DNAzyme RMRP, BCYRN11 and MIR31HG. A:** k_{obs} values for the DNAzymes BCYRN1, MIR31HG, and RMRP as a function of Mg^{2+} concentration (from 0.6 to 5 mM $MgCl_2$). **B-D:** Example reaction of the DNAzymes MIR31HG (B), RMRP (C) and BCYRN1 (D). The figure shows the percentage of cleaved RNA over time (s) at different Mg^{2+} concentrations ranging from 1.8 mM to 5 mM.

Transfer from *in vitro* activity tests to *in vivo* activity tests using SW80 colon cells

Since DNAzymes targeting long non-coding RNAs were successfully designed and *in vitro* catalytic activity was proven using FRET assays, a transfer from *in vitro* to *in vivo* (cell culture) testing of DNAzymes was implemented. The following cell culture experiments were all conducted by Andrea Janosch (Institute for Physical Biology, BTA). Since long non-coding RNAs are always specific to a certain cell type, the DNAzyme targeting the long non-coding RNA BCYRN1 in combination with SW480 colon cells was tested. Cells were plated and allowed to grow for 24 hours. Afterwards, the cells were transfected with either 0.5 or 1 µg of DNAzyme targeting the long non-coding RNA BCYRN1 using the transfection reagent JetPRIME (Sartorius AG, Göttingen, Germany). As controls, the A5G variant of the DNAzyme was used, which has no catalytic activity, a transfection reagent only and cells without any treatment. After 24 hours, cells were harvested, and RNA was isolated. Cellular mRNA levels of BCYRN1 were quantified using qPCR.

In SW480, the DNAzyme targeting BCYRN1 should lower the cellular level of mRNA compared to the catalytically inactive A5G, the transfection reagent only and the cells without any transfection. Repeatedly, the experiment revealed no change **(Figure 52A)** in the Cq values between all tested samples and controls, so no change in the mRNA level of the cells after treatment with the DNAzyme. These results indicate that the conducted experiments are either not working out at all or the DNAzymes have no *in vivo* activity. Based on the results, it is more likely that the experiment did not work out. This is evident from the fact that the DNAzyme variant A5G functions in the same way as an unmodified ASO. An ASO forms an RNA: DNA complex, which then recruits ribonuclease H. This enzyme then breaks down the complex. In theory, there should be a difference in Cq levels between the only cells and the DNAzymes.

Various optimisations and tests were performed to gain an understanding of the problem at hand. For example, different transfection reagents were used, or the RNA was purified with different kits for qPCR. Another idea was to test a different DNAzyme system in cells. For this purpose, DNAzymes targeting the RNA of the yellow fluorescent protein (EYFP) were used. During transfection, a plasmid carrying the RNA sequence for the EYFP protein was co-transfected, because the protein is not naturally occurring in SW480 cells. The advantage of this experimental strategy is that, in addition to qPCR, detection can also be performed using fluorescence microscopy. This change in strategy also has the advantage that the protein is overexpressed compared to cellular proteins. It acts as a kind of effect amplifier, helping to make smaller changes in mRNA levels caused by DNAzymes more clearly visible. Literature searches revealed that other groups working with long non-coding RNA and SW480 cells, and similar experimental strategies to detect mRNA levels, waited at least 24 hours, most likely 48

to 72 hours after transfection, for detection of mRNA levels. Following the approach of incubating the cells longer, we observed measurable changes in the Cq values **(Figure 52B)**.

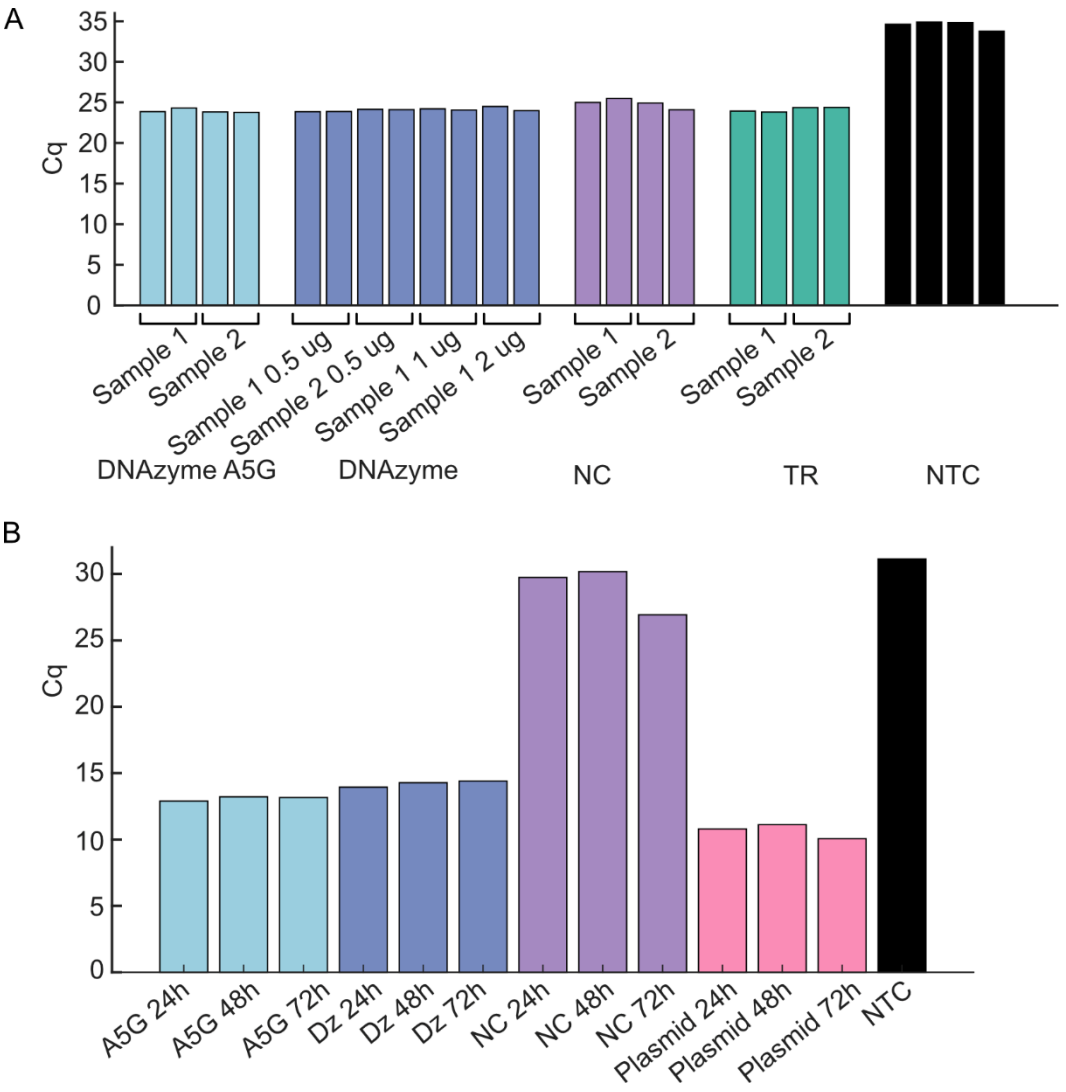

Figure 52: qPCR data in SW480 colon cells. A: qPCR data of in vivo assay using a DNAzyme targeting the long non-coding RNA BCYRN1. Each sample was plated twice. For the DNAzyme, two transfection concentrations were used: 0.5 and 1 µg. As a negative control, non-treated cells (NC) and cells only treated with the transfection reagent (TR) were used. In the qPCR, a no-template control (NTC), containing only water and primer, was used as a negative control. **B:** qPCR data of in vivo assay using a DNAzyme targeting EYFP with SW480 cells. DNAzyme was cotransfected with a plasmid carrying. Time-resolved mRNA levels of EYFP in SW480 cells after 24, 48 and 72 hours of transfection. As a negative control, non-treated cells (NC) and cells only transfected with the plasmid were used. In the qPCR, a no-template control (NTC), containing only water and primer, was used as a negative control.

Summary and Outlook

DNAzymes were successfully designed to function in vitro and to target KRAS directly or indirectly via long non-coding RNA. The KRAS DNAzyme was not pursued further because other solutions were published. Transition from *in vitro* assays to *in vivo* assays in SW480 cells was achieved. Problems were encountered and solved using a different DNAzyme system in the SW480 cell line; a lower mRNA level due to DNAzymes was detected. The next step is to

establish a time-resolved assay in SW480 using DNAzymes that target the long non-coding RNA BCYRN1.

9 Acknowledgement

I would like to express my sincere thanks to the Jürgen Manchot Foundation for my three-year doctoral scholarship and the provided material resources. Without this support, my doctoral thesis would not have been possible. Hereby, I would like to thank Prof. Dr Dieter Willbold for the opportunity to join the Institute of Physical Biology at Heinrich-Heine University and for access to the Biomolecular NMR centre at Forschungszentrum Jülich. I want to thank Dr Manuel Etzkorn for the opportunity to do my PhD in his group and for his constant constructive support throughout my thesis. I am thankful to Prof. Dr Henrike Heise, who supported my work as a mentor.

I would like to thank Dr Hongzhou Gu from Fudan University in Shanghai, China, for the opportunity to work together on the pin project. Thanks to Prof. Dr John Chaput from the University of California, Irvine, for the chance to work on the Dz46 project.

I give my honest credit to Tobias Stief, Dr Nils Lakomek, Kevin Bochinsky and Dr Matthias Stoldt for helpful and lasting support at the NMR spectrometer. I would like to thank the members of the AG Etzkorn—especially Lora Denson, Christopher Ruth and Justin Böcker. Moreover, I would like to thank all members of the Institute of Physical Biology—I would like to emphasise in particular Melinda Jaspert, Sophia Werner, Andrea Janosch and Mirko Kraus.

I would like to thank Dr Christine Beuck, who, although she did not actively contribute to this work, supported me during my master's thesis in a way that made it possible for me to pursue a doctorate. You showed me what teaching should look like and sparked my endless enthusiasm for NMR spectroscopy.

I would like to thank my parents for their financial support throughout my studies— I know that this is not a given. I am grateful to you for always supporting and believing in me. Dear Tobias, thank you for being not only my partner in crime, but also my best friend. I couldn't be more grateful that you were and are part of this journey. Dear Opa Walter, unfortunately, you can no longer read this. I would have loved to share this moment with you. Thank you for the time we spent together. I am grateful to Jara, Nadia, Nina and Lena. Thank you for everlasting friendship, support and trust.

10 Bibliography

2002. Safety of intravitreous fomivirsen for treatment of cytomegalovirus retinitis in patients with AIDS11InternetAdvance publication at ajo.com Feb 8, 2002.Financial disclosures and conflict of interest statements are listed at the end of the article.Correspondence to Stephen L. Hutcherson, MBA, Cyclix Ltd. LLC, 11851 Rexmoor Drive, Richmond, VA 23236; fax: (804) 897-9544; e-mail: cyclix@comcast.netReprint requests to René Lanz, PHD, Novartis Ophthalmics AG, Grenzstrasse 10, CH-8180 Bülach, Switzerland; fax: (41) 1-862-0762; e-mail: rene.lanz@pharma.novartis.com. *American Journal of Ophthalmology,* 133**,** 484-498.

ABOU ASSI, H., RANGADURAI, A. K., SHI, H., LIU, B., CLAY, M. C., ERHARTER, K., KREUTZ, C., HOLLEY, C. L. & AL-HASHIMI, HASHIM M. 2020. 2′-O-Methylation can increase the abundance and lifetime of alternative RNA conformational states. *Nucleic Acids Research,* 48**,** 12365-12379.

ADRIAN, M., HEDDI, B. & PHAN, A. T. 2012. NMR spectroscopy of G-quadruplexes. *Methods,* 57**,** 11-24.

AFONIN, K. A., DOBROVOLSKAIA, M. A., KE, W., GRODZINSKI, P. & BATHE, M. 2022. Critical review of nucleic acid nanotechnology to identify gaps and inform a strategy for accelerated clinical translation. *Adv Drug Deliv Rev,* 181**,** 114081.

AL-HASHIMI, H. M. 2013. NMR studies of nucleic acid dynamics. *Journal of Magnetic Resonance,* 237**,** 191-204.

ALVES FERREIRA-BRAVO, I., COZENS, C., HOLLIGER, P. & DESTEFANO, J. J. 2015. Selection of 2'-deoxy-2'-fluoroarabinonucleotide (FANA) aptamers that bind HIV-1 reverse transcriptase with picomolar affinity. *Nucleic Acids Res,* 43**,** 9587-99.

AMBRUS, A., CHEN, D., DAI, J., BIALIS, T., JONES, R. A. & YANG, D. 2006. Human telomeric sequence forms a hybrid-type intramolecular G-quadruplex structure with mixed parallel/antiparallel strands in potassium solution. *Nucleic Acids Research,* 34**,** 2723-2735.

ANDREATTA, D., SEN, S., PÉREZ LUSTRES, J. L., KOVALENKO, S. A., ERNSTING, N. P., MURPHY, C. J., COLEMAN, R. S. & BERG, M. A. 2006. Ultrafast dynamics in DNA: "fraying" at the end of the helix. *J Am Chem Soc,* 128**,** 6885-92.

BECETTE, O., OLENGINSKI, L. T. & DAYIE, T. K. 2019. Solid-Phase Chemical Synthesis of Stable Isotope-Labeled RNA to Aid Structure and Dynamics Studies by NMR Spectroscopy. *Molecules,* 24.

BEDRAT, A., LACROIX, L. & MERGNY, J. L. 2016. Re-evaluation of G-quadruplex propensity with G4Hunter. *Nucleic Acids Res,* 44**,** 1746-59.

BENSON, M. D., WADDINGTON-CRUZ, M., BERK, J. L., POLYDEFKIS, M., DYCK, P. J., WANG, A. K., PLANTÉ-BORDENEUVE, V., BARROSO, F. A., MERLINI, G., OBICI, L., SCHEINBERG, M., BRANNAGAN, T. H., 3RD, LITCHY, W. J., WHELAN, C., DRACHMAN, B. M., ADAMS, D., HEITNER, S. B., CONCEIÇÃO, I., SCHMIDT, H. H., VITA, G., CAMPISTOL, J. M., GAMEZ, J., GOREVIC, P. D., GANE, E., SHAH, A. M., SOLOMON, S. D., MONIA, B. P., HUGHES, S. G., KWOH, T. J., MCEVOY, B. W., JUNG, S. W., BAKER, B. F., ACKERMANN, E. J., GERTZ, M. A. & COELHO, T. 2018. Inotersen Treatment for Patients with Hereditary Transthyretin Amyloidosis. *N Engl J Med,* 379**,** 22-31.

BIAN, X., ZHOU, L., LUO, Z., LIU, G., HANG, Z., LI, H., LI, F. & WEN, Y. 2025. Emerging Delivery Systems for Enabling Precision Nucleic Acid Therapeutics. *ACS Nano,* 19**,** 4039-4083.

BIBOW, S. 2019. Opportunities and Challenges of Backbone, Sidechain, and RDC Experiments to Study Membrane Protein Dynamics in a Detergent-Free Lipid Environment Using Solution State NMR. *Front Mol Biosci,* 6**,** 103.

BINAS, O. 2020. *Structural and functional investigation of nucleic acids with NMR spectroscopy.* Doctoral Thesis, Goethe-Universität.

BOMBARD, S., KOZELKA, J., FAVRE, A. & CHOTTARD, J. C. 1998. Probing the mechanism of an Mn2+-dependent ribozyme by means of platinum complexes. *Eur J Biochem,* 252**,** 25-35.
BORGGRÄFE, J. & ETZKORN, M. 2022. Solution NMR Spectroscopy as a Tool to Study DNAzyme Structure and Function. *Methods Mol Biol,* 2439**,** 131-151.
BORGGRÄFE, J., GERTZEN, C. G. W., VIEGAS, A., GOHLKE, H. & ETZKORN, M. 2023. The architecture of the 10-23 DNAzyme and its implications for DNA-mediated catalysis. *Febs j,* 290**,** 2011-2021.
BORGGRÄFE, J., VICTOR, J., ROSENBACH, H., VIEGAS, A., GERTZEN, C. G. W., WUEBBEN, C., KOVACS, H., GOPALSWAMY, M., RIESNER, D., STEGER, G., SCHIEMANN, O., GOHLKE, H., SPAN, I. & ETZKORN, M. 2022. Time-resolved structural analysis of an RNA-cleaving DNA catalyst. *Nature,* 601**,** 144-149.
BOTHE, J. R., NIKOLOVA, E. N., EICHHORN, C. D., CHUGH, J., HANSEN, A. L. & AL-HASHIMI, H. M. 2011. Characterizing RNA dynamics at atomic resolution using solution-state NMR spectroscopy. *Nature Methods,* 8**,** 919-931.
BOYLE, E. P., LOMIDZE, L., MUSIER-FORSYTH, K. & KANKIA, B. 2022. A Chimeric DNA/RNA Antiparallel Quadruplex with Improved Stability. *ChemistryOpen,* 11**,** e202100276.
BREAKER, R. R. & JOYCE, G. F. 1994. A DNA enzyme that cleaves RNA. *Chemistry & Biology,* 1**,** 223-229.
BROWN, A. K., LI, J., PAVOT, C. M. B. & LU, Y. 2003. A Lead-Dependent DNAzyme with a Two-Step Mechanism. *Biochemistry,* 42**,** 7152-7161.
BRUKER BIOSPIN Chemical Shifts Reference Table. Rheinstetten, Germany: Bruker BioSpin GmbH.
BUKO, T., TUCZKO, N. & ISHIKAWA, T. 2023. DNA Data Storage. *BioTech (Basel),* 12.
BUKOWSKI, K., KCIUK, M. & KONTEK, R. 2020. Mechanisms of Multidrug Resistance in Cancer Chemotherapy. *Int J Mol Sci,* 21.
CARMI, N., BALKHI, S. R. & BREAKER, R. R. 1998. Cleaving DNA with DNA. *Proceedings of the National Academy of Sciences,* 95**,** 2233-2237.
CARMI, N., SHULTZ, L. A. & BREAKER, R. R. 1996. In vitro selection of self-cleaving DNAs. *Chemistry & Biology,* 3**,** 1039-1046.
CARVALHO, C., SANTOS, R. X., CARDOSO, S., CORREIA, S., OLIVEIRA, P. J., SANTOS, M. S. & MOREIRA, P. I. 2009. Doxorubicin: the good, the bad and the ugly effect. *Curr Med Chem,* 16**,** 3267-85.
CHANDRA, M., SACHDEVA, A. & SILVERMAN, S. K. 2009. DNA-catalyzed sequence-specific hydrolysis of DNA. *Nature Chemical Biology,* 5**,** 718-720.
CHANG, Y.-M., CHEN, C. K. M. & HOU, M.-H. 2012. Conformational Changes in DNA upon Ligand Binding Monitored by Circular Dichroism. *International Journal of Molecular Sciences* [Online], 13.
CHEN, Y., QI, F., GAO, F., CAO, H., XU, D., SALEHI-ASHTIANI, K. & KAPRANOV, P. 2021. Hovlinc is a recently evolved class of ribozyme found in human lncRNA. *Nature Chemical Biology,* 17**,** 601-607.
CHEN, Y. & YANG, D. 2012. Sequence, stability, and structure of G-quadruplexes and their interactions with drugs. *Curr Protoc Nucleic Acid Chem,* Chapter 17**,** Unit17.5.
CHOU, S. H., FLYNN, P., WANG, A. & REID, B. 1991. High-resolution NMR studies of chimeric DNA-RNA-DNA duplexes, heteronomous base pairing, and continuous base stacking at junctions. *Biochemistry,* 30**,** 5248-57.
CLAY, M. C., GANSER, L. R., MERRIMAN, D. K. & AL-HASHIMI, H. M. 2017. Resolving sugar puckers in RNA excited states exposes slow modes of repuckering dynamics. *Nucleic Acids Res,* 45**,** e134.
DANTU, S. C., KHALIL, M., BRIA, M., SAINT-PIERRE, C., ORIO, M., GASPARUTTO, D. & SICOLI, G. 2024. Cleaving DNA with DNA: Cooperative Tuning of Structure and Reactivity Driven by Copper Ions. *Adv Sci (Weinh),* 11**,** e2306710.
DAVIS, J. T. 2004. G-quartets 40 years later: from 5'-GMP to molecular biology and supramolecular chemistry. *Angew Chem Int Ed Engl,* 43**,** 668-98.

DEL VILLAR-GUERRA, R., TRENT, J. O. & CHAIRES, J. B. 2018. G-Quadruplex Secondary Structure Obtained from Circular Dichroism Spectroscopy. *Angew Chem Int Ed Engl,* 57**,** 7171-7175.

DHARA, D., MULARD, L. A. & HOLLENSTEIN, M. 2025. Natural, modified and conjugated carbohydrates in nucleic acids. *Chem Soc Rev,* 54**,** 2948-2983.

DOKUKIN, V. & SILVERMAN, S. K. 2012. Lanthanide ions as required cofactors for DNA catalysts. *Chemical Science,* 3**,** 1707-1714.

DOWLER, T., BERGERON, D., TEDESCHI, A. L., PAQUET, L., FERRARI, N. & DAMHA, M. J. 2006. Improvements in siRNA properties mediated by 2'-deoxy-2'-fluoro-beta-D-arabinonucleic acid (FANA). *Nucleic Acids Res,* 34**,** 1669-75.

DU, Y. & DONG, S. 2017. Nucleic Acid Biosensors: Recent Advances and Perspectives. *Analytical Chemistry,* 89**,** 189-215.

DUFFY, K., ARANGUNDY-FRANKLIN, S. & HOLLIGER, P. 2020. Modified nucleic acids: replication, evolution, and next-generation therapeutics. *BMC Biology,* 18**,** 112.

EBRAHIMI, M., ROSSI, P., ROGERS, C. & HARBISON, G. S. 2001. Dependence of 13C NMR Chemical Shifts on Conformations of RNA Nucleosides and Nucleotides. *Journal of Magnetic Resonance,* 150**,** 1-9.

ETHERIDGE, W., BROSSARD, F., ZHENG, S., MOENCH, S., PAVAGADA, S., OWENS, R. M. & FRUK, L. 2023. Activity-enhanced DNAzyme for design of label-free copper(ii) biosensor. *Nanoscale,* 15**,** 10776-10782.

FEDOR, M. J. 2009. Comparative enzymology and structural biology of RNA self-cleavage. *Annu Rev Biophys,* 38**,** 271-99.

FÜRTIG, B., RICHTER, C., WÖHNERT, J. & SCHWALBE, H. 2003. NMR spectroscopy of RNA. *Chembiochem,* 4**,** 936-62.

GRÜNWELLER, A. & HARTMANN, R. K. 2007. Locked nucleic acid oligonucleotides: the next generation of antisense agents? *BioDrugs,* 21**,** 235-43.

GU, H., FURUKAWA, K., WEINBERG, Z., BERENSON, D. F. & BREAKER, R. R. 2013. Small, Highly Active DNAs That Hydrolyze DNA. *Journal of the American Chemical Society,* 135**,** 9121-9129.

GUISET MISERACHS, H., DONGHI, D., BÖRNER, R., JOHANNSEN, S. & SIGEL, R. K. O. 2016. Distinct differences in metal ion specificity of RNA and DNA G-quadruplexes. *JBIC Journal of Biological Inorganic Chemistry,* 21**,** 975-986.

HÄNSEL-HERTSCH, R., DI ANTONIO, M. & BALASUBRAMANIAN, S. 2017. DNA G-quadruplexes in the human genome: detection, functions and therapeutic potential. *Nature Reviews Molecular Cell Biology,* 18**,** 279-284.

HE, Q. C., ZHOU, J. M., ZHOU, D. M., NAKAMATSU, Y., BABA, T. & TAIRA, K. 2002. Comparison of metal-ion-dependent cleavages of RNA by a DNA enzyme and a hammerhead ribozyme. *Biomacromolecules,* 3**,** 69-83.

HERKT, M. & THUM, T. 2021. Pharmacokinetics and Proceedings in Clinical Application of Nucleic Acid Therapeutics. *Molecular Therapy,* 29**,** 521-539.

HESSE, R., GERTZEN, C. G. W., SCHMUCK, J. F., BÖCKER, J. D., PANDEY, P., BEHN, T., RUTH, C., RIESNER, D., KATH-SCHORR, S., LANG, P. A., GOHLKE, H. & ETZKORN, M. 2025. The coming of age of DNA-based catalysts for therapeutic applications. *Clin Transl Med,* 15**,** e70408.

HILBER, S., ATTIONU, S. K., DAYIE, T. K. & KREUTZ, C. 2025. Advances in Isotope Labeling for Solution Nucleic Acid Nuclear Magnetic Resonance Spectroscopy. *Chempluschem,* 90**,** e202400752.

HOLLENSTEIN, M. 2015. DNA Catalysis: The Chemical Repertoire of DNAzymes. *Molecules,* 20**,** 20777-20804.

HUANG, L., GUO, Z., WANG, F. & FU, L. 2021. KRAS mutation: from undruggable to druggable in cancer. *Signal Transduction and Targeted Therapy,* 6**,** 386.

JAISHREE, T. N., VAN DER MAREL, G. A., VAN BOOM, J. H. & WANG, A. H. 1993. Structural influence of RNA incorporation in DNA: quantitative nuclear magnetic resonance refinement of d(CG)r(CG)d(CG) and d(CG)r(C)d(TAGCG). *Biochemistry,* 32**,** 4903-11.

JAROSZEWSKI, J. W., CLAUSEN, V., COHEN, J. S. & DAHL, O. 1996. NMR Investigations of Duplex Stability of Phosphorothioate and Phosphorodithioate DNA Analogues Modified in Both Strands. *Nucleic Acids Research,* 24**,** 829-834.

JIA, Y., CHEN, L., LIU, J., LI, W. & GU, H. 2021. DNA-catalyzed efficient production of single-stranded DNA nanostructures. *Chem,* 7**,** 959-981.

JINEK, M., CHYLINSKI, K., FONFARA, I., HAUER, M., DOUDNA, J. A. & CHARPENTIER, E. 2012. A Programmable Dual-RNA–Guided DNA Endonuclease in Adaptive Bacterial Immunity. *Science,* 337**,** 816-821.

KAWALE, A. A. & BURMANN, B. M. 2021. Characterization of backbone dynamics using solution NMR spectroscopy to discern the functional plasticity of structurally analogous proteins. *STAR Protoc,* 2**,** 100919.

KAZAKOV, S. & ALTMAN, S. 1992. A trinucleotide can promote metal ion-dependent specific cleavage of RNA. *Proceedings of the National Academy of Sciences,* 89**,** 7939-7943.

KAZAKOV, S. A., ASTASHKINA, T. G., MAMAEV, S. V. & VLASSOV, V. V. 1988. Site-specific cleavage of single-stranded DNAs at unique sites by a copper-dependent redox reaction. *Nature,* 335**,** 186-188.

KCIUK, M., GIELECIŃSKA, A., MUJWAR, S., KOŁAT, D., KAŁUZIŃSKA-KOŁAT, Ż., CELIK, I. & KONTEK, R. 2023. Doxorubicin-An Agent with Multiple Mechanisms of Anticancer Activity. *Cells,* 12.

KELLEY, S., BORODA, S., MUSIER-FORSYTH, K. & KANKIA, B. I. 2011. HIV-integrase aptamer folds into a parallel quadruplex: A thermodynamic study. *Biophysical Chemistry,* 155**,** 82-88.

KENSKI, D. M., BUTORA, G., WILLINGHAM, A. T., COOPER, A. J., FU, W., QI, N., SORIANO, F., DAVIES, I. W. & FLANAGAN, W. M. 2012. siRNA-optimized Modifications for Enhanced In Vivo Activity. *Mol Ther Nucleic Acids,* 1**,** e5.

KIM, H.-K., LIU, J., LI, J., NAGRAJ, N., LI, M., PAVOT, C. M. B. & LU, Y. 2007a. Metal-Dependent Global Folding and Activity of the 8-17 DNAzyme Studied by Fluorescence Resonance Energy Transfer. *Journal of the American Chemical Society,* 129**,** 6896-6902.

KIM, H.-K., RASNIK, I., LIU, J., HA, T. & LU, Y. 2007b. Dissecting metal ion–dependent folding and catalysis of a single DNAzyme. *Nature Chemical Biology,* 3**,** 763-768.

KLEIBL, K. 2002. Molecular mechanisms of adaptive response to alkylating agents in Escherichia coli and some remarks on O6-methylguanine DNA-methyltransferase in other organisms. *Mutation Research/Reviews in Mutation Research,* 512**,** 67-84.

KOWAL, E. A., GANGULY, M., PALLAN, P. S., MARKY, L. A., GOLD, B., EGLI, M. & STONE, M. P. 2011. Altering the Electrostatic Potential in the Major Groove: Thermodynamic and Structural Characterization of 7-Deaza-2′-deoxyadenosine:dT Base Pairing in DNA. *The Journal of Physical Chemistry B,* 115**,** 13925-13934.

KULKARNI, J. A., WITZIGMANN, D., THOMSON, S. B., CHEN, S., LEAVITT, B. R., CULLIS, P. R. & VAN DER MEEL, R. 2021. The current landscape of nucleic acid therapeutics. *Nature Nanotechnology,* 16**,** 630-643.

KUO, T.-C. & HERRIN, D. L. 2000. Quantitative studies of Mn2+-promoted specific and non-specific cleavages of a large RNA: Mn2+-GAAA ribozymes and the evolution of small ribozymes. *Nucleic Acids Research,* 28**,** 4197-4206.

LAGO, S., NADAI, M., RUGGIERO, E., TASSINARI, M., MARUŠIČ, M., TOSONI, B., FRASSON, I., CERNILOGAR, F. M., PIROTA, V., DORIA, F., PLAVEC, J., SCHOTTA, G. & RICHTER, S. N. 2021. The MDM2 inducible promoter folds into four-tetrad antiparallel G-quadruplexes targetable to fight malignant liposarcoma. *Nucleic Acids Res,* 49**,** 847-863.

LARCHER, L. M., PITOUT, I. L., KEEGAN, N. P., VEEDU, R. N. & FLETCHER, S. 2023. DNAzymes: Expanding the Potential of Nucleic Acid Therapeutics. *Nucleic Acid Ther,* 33**,** 178-192.

LESNIK, E. A. & FREIER, S. M. 1995. Relative Thermodynamic Stability of DNA, RNA, and DNA:RNA Hybrid Duplexes: Relationship with Base Composition and Structure. *Biochemistry,* 34**,** 10807-10815.

LI, J., LIU, X., WANG, J., JIANG, Q., CHEN, M., ZHANG, W., CHEN, Y., PU, Y. & HUANG, J. 2023. Self-Assembled DNA Nanospheres: Design and Applications. *Chemistry,* 5**,** 1882-1910.

LI, J., ZHENG, W., KWON, A. H. & LU, Y. 2000. In vitro selection and characterization of a highly efficient Zn(II)-dependent RNA-cleaving deoxyribozyme. *Nucleic Acids Res,* 28**,** 481-8.

LI, Q., TONG, Z., CAO, Y. & GU, H. 2021. DNAs catalyzing DNA nanoconstruction. *Chem,* 7**,** 2556-2568.

LI, Y. & BREAKER, R. R. 1999. Kinetics of RNA Degradation by Specific Base Catalysis of Transesterification Involving the 2‘-Hydroxyl Group. *Journal of the American Chemical Society,* 121**,** 5364-5372.

LIANG, X.-H., SUN, H., NICHOLS, J. G. & CROOKE, S. T. 2017. RNase H1-Dependent Antisense Oligonucleotides Are Robustly Active in Directing RNA Cleavage in Both the Cytoplasm and the Nucleus. *Molecular Therapy,* 25**,** 2075-2092.

LIU, B., SHI, H. & AL-HASHIMI, H. M. 2021. Developments in solution-state NMR yield broader and deeper views of the dynamic ensembles of nucleic acids. *Current Opinion in Structural Biology,* 70**,** 16-25.

LIU, H., YU, X., CHEN, Y., ZHANG, J., WU, B., ZHENG, L., HARUEHANROENGRA, P., WANG, R., LI, S., LIN, J., LI, J., SHENG, J., HUANG, Z., MA, J. & GAN, J. 2017. Crystal structure of an RNA-cleaving DNAzyme. *Nature Communications,* 8**,** 2006.

LIU, J. & GU, H. 2021. Biotechnological production of ssDNA with DNA-hydrolyzing deoxyribozymes. *STAR Protocols,* 2**,** 100531.

LIU, P., WANG, Y. & LI, X. 2019. Targeting the untargetable KRAS in cancer therapy. *Acta Pharm Sin B,* 9**,** 871-879.

LIU, Z.-X., ZHANG, S., ZHU, H.-Z., CHEN, Z.-H., YANG, Y., LI, L.-Q., LEI, Y., LIU, Y., LI, D.-Y., SUN, A., LI, C.-P., TAN, S.-Q., WANG, G.-L., SHEN, J.-Y., JIN, S., GAO, C. & LIU, J.-J. G. 2024. Hydrolytic endonucleolytic ribozyme (HYER) is programmable for sequence-specific DNA cleavage. *Science,* 383**,** eadh4859.

LOUIS, J. M., MARTIN, R. G., CLORE, G. M. & GRONENBORN, A. M. 1998. Preparation of uniformly isotope-labeled DNA oligonucleotides for NMR spectroscopy. *J Biol Chem,* 273**,** 2374-8.

LU, K., MIYAZAKI, Y. & SUMMERS, M. F. 2010. Isotope labeling strategies for NMR studies of RNA. *J Biomol NMR,* 46**,** 113-25.

LUBINI, P., ZÜRCHER, W. & EGLI, M. 1994. Stabilizing effects of the RNA 2'-substituent: crystal structure of an oligodeoxynucleotide duplex containing 2'-O-methylated adenosines. *Chem Biol,* 1**,** 39-45.

MA, L., LIU, B., HUANG, P.-J. J., ZHANG, X. & LIU, J. 2016. DNA Adsorption by ZnO Nanoparticles near Its Solubility Limit: Implications for DNA Fluorescence Quenching and DNAzyme Activity Assays. *Langmuir,* 32**,** 5672-5680.

MAIZELS, N. 2015. G4-associated human diseases. *EMBO reports,* 16**,** 910-922-922.

MALEK-ADAMIAN, E., FAKHOURY, J., ARNOLD, A. E., MARTÍNEZ-MONTERO, S., SHOICHET, M. S. & DAMHA, M. J. 2019. Effect of Sugar 2',4'-Modifications on Gene Silencing Activity of siRNA Duplexes. *Nucleic Acid Ther,* 29**,** 187-194.

MAŁGOWSKA, M., GUDANIS, D., TEUBERT, A., DOMINIAK, G. & GDANIEC, Z. 2012. REVIEW PAPER
How to study G-quadruplex structures. *BioTechnologia,* 93**,** 381-390.

MANGHRANI, A., RANGADURAI, A. K., SZEKELY, O., LIU, B., GUSEVA, S. & AL-HASHIMI, H. M. 2024. Quantitative and systematic NMR measurements of sequence-dependent A-T Hoogsteen dynamics uncovers unique conformational specificity in the DNA double helix. *bioRxiv*.

MARKHAM, N. R. & ZUKER, M. 2005. DINAMelt web server for nucleic acid melting prediction. *Nucleic Acids Research,* 33**,** W577-W581.

MARUŠIČ, M., SCHLAGNITWEIT, J. & PETZOLD, K. 2019. RNA Dynamics by NMR Spectroscopy. *Chembiochem,* 20**,** 2685-2710.

MATTICK, J. S., AMARAL, P. P., CARNINCI, P., CARPENTER, S., CHANG, H. Y., CHEN, L.-L., CHEN, R., DEAN, C., DINGER, M. E., FITZGERALD, K. A., GINGERAS, T. R.,

GUTTMAN, M., HIROSE, T., HUARTE, M., JOHNSON, R., KANDURI, C., KAPRANOV, P., LAWRENCE, J. B., LEE, J. T., MENDELL, J. T., MERCER, T. R., MOORE, K. J., NAKAGAWA, S., RINN, J. L., SPECTOR, D. L., ULITSKY, I., WAN, Y., WILUSZ, J. E. & WU, M. 2023. Long non-coding RNAs: definitions, functions, challenges and recommendations. *Nature Reviews Molecular Cell Biology,* 24**,** 430-447.

MAZUMDAR, D., NAGRAJ, N., KIM, H.-K., MENG, X., BROWN, A. K., SUN, Q., LI, W. & LU, Y. 2009. Activity, Folding and Z-DNA Formation of the 8-17 DNAzyme in the Presence of Monovalent Ions. *Journal of the American Chemical Society,* 131**,** 5506-5515.

MEIER-STEPHENSON, V. 2022. G4-quadruplex-binding proteins: review and insights into selectivity. *Biophysical Reviews,* 14**,** 635-654.

MINCHIN, S. & LODGE, J. 2019. Understanding biochemistry: structure and function of nucleic acids. *Essays Biochem,* 63**,** 433-456.

MOCCIA, M., PASCUCCI, B., SAVIANO, M., CERASA, M. T., TERZIDIS, M. A., CHATGILIALOGLU, C. & MASI, A. 2024. Advances in Nucleic Acid Research: Exploring the Potential of Oligonucleotides for Therapeutic Applications and Biological Studies. *International Journal of Molecular Sciences* [Online], 25.

MOE, J. G., REDDY, G. R., MARNETT, L. J. & STONE, M. P. 1994. 1H NMR characterization of a duplex oligodeoxynucleotide containing propanodeoxyguanosine opposite a two-base deletion in the (CpG)3 frameshift hotspot of Salmonella typhimurium hisD3052. *Chem Res Toxicol,* 7**,** 319-28.

MOON, W. J., YANG, Y. & LIU, J. 2021. Zn2+-Dependent DNAzymes: From Solution Chemistry to Analytical, Materials and Therapeutic Applications. *ChemBioChem,* 22**,** 779-789.

NGUYEN, K., MALIK, T. N. & CHAPUT, J. C. 2023. Chemical evolution of an autonomous DNAzyme with allele-specific gene silencing activity. *Nature Communications,* 14**,** 2413.

NIELSEN, K. E., RASMUSSEN, J., KUMAR, R., WENGEL, J., JACOBSEN, J. P. & PETERSEN, M. 2004. NMR Studies of Fully Modified Locked Nucleic Acid (LNA) Hybrids: Solution Structure of an LNA:RNA Hybrid and Characterization of an LNA:DNA Hybrid. *Bioconjugate Chemistry,* 15**,** 449-457.

OTA, N., WARASHINA, M., HIRANO, K. I., HATANAKA, K. & TAIRA, K. 1998. Effects of helical structures formed by the binding arms of DNAzymes and their substrates on catalytic activity. *Nucleic Acids Research,* 26**,** 3385-3391.

PERACCHI, A. 1999. Origins of the temperature dependence of hammerhead ribozyme catalysis. *Nucleic Acids Research,* 27**,** 2875-2882.

PINE, A. C., BROOKE, G. N. & MARCO, A. 2023. A computational approach to identify efficient RNA cleaving 10–23 DNAzymes. *NAR Genomics and Bioinformatics,* 5**,** lqac098.

PLAVEC, J. 2023. NMR Study on Nucleic Acids. *In:* SUGIMOTO, N. (ed.) *Handbook of Chemical Biology of Nucleic Acids.* Singapore: Springer Nature Singapore.

PLEVNIK, M., CEVEC, M. & PLAVEC, J. 2013. NMR structure of 2′-O-(2-methoxyethyl) modified and C5-methylated RNA dodecamer duplex. *Biochimie,* 95**,** 2385-2391.

PONCE-SALVATIERRA, A., WAWRZYNIAK-TUREK, K., STEUERWALD, U., HÖBARTNER, C. & PENA, V. 2016. Crystal structure of a DNA catalyst. *Nature,* 529**,** 231-234.

PRADEEP, S. P., MALIK, S., SLACK, F. J. & BAHAL, R. 2023. Unlocking the potential of chemically modified peptide nucleic acids for RNA-based therapeutics. *Rna,* 29**,** 434-445.

PRAETORIUS, F., KICK, B., BEHLER, K. L., HONEMANN, M. N., WEUSTER-BOTZ, D. & DIETZ, H. 2017. Biotechnological mass production of DNA origami. *Nature,* 552**,** 84-87.

PUIG LOMBARDI, E. & LONDOÑO-VALLEJO, A. 2020. A guide to computational methods for G-quadruplex prediction. *Nucleic Acids Res,* 48**,** 1-15.

RANGADURAI, A., SZYMASKI, E. S., KIMSEY, I. J., SHI, H. & AL-HASHIMI, H. M. 2019. Characterizing micro-to-millisecond chemical exchange in nucleic acids using off-

resonance R(1ρ) relaxation dispersion. *Prog Nucl Magn Reson Spectrosc,* 112-113**,** 55-102.
ROBERTSON, D. L. & JOYCE, G. F. 1990. Selection in vitro of an RNA enzyme that specifically cleaves single-stranded DNA. *Nature,* 344**,** 467-468.
ROSENBACH, H., BORGGRÄFE, J., VICTOR, J., WUEBBEN, C., SCHIEMANN, O., HOYER, W., STEGER, G., ETZKORN, M. & SPAN, I. 2020a. Influence of monovalent metal ions on metal binding and catalytic activity of the 10-23 DNAzyme. *Biol Chem,* 402**,** 99-111.
ROSENBACH, H., VICTOR, J., ETZKORN, M., STEGER, G., RIESNER, D. & SPAN, I. 2020b. Molecular Features and Metal Ions That Influence 10-23 DNAzyme Activity. *Molecules* [Online], 25.
ROTH, A., WEINBERG, Z., CHEN, A. G. Y., KIM, P. B., AMES, T. D. & BREAKER, R. R. 2014. A widespread self-cleaving ribozyme class is revealed by bioinformatics. *Nature Chemical Biology,* 10**,** 56-60.
SANDOVAL-MOJICA, A. F., HUNTER, W. B., AISHWARYA, V., BONILLA, S. & PELZ-STELINSKI, K. S. 2021. Antibacterial FANA oligonucleotides as a novel approach for managing the Huanglongbing pathosystem. *Scientific Reports,* 11**,** 2760.
SANTORO, S. W. & JOYCE, G. F. 1997. A general purpose RNA-cleaving DNA enzyme. *Proceedings of the National Academy of Sciences,* 94**,** 4262-4266.
SCAGLIONI, L., MONDELLI, R., ARTALI, R., SIRTORI, F. R. & MAZZINI, S. 2016. Nemorubicin and doxorubicin bind the G-quadruplex sequences of the human telomeres and of the c-MYC promoter element Pu22. *Biochim Biophys Acta,* 1860**,** 1129-38.
SCHLAGNITWEIT, J., STEINER, E., KARLSSON, H. & PETZOLD, K. 2018a. Efficient Detection of Structure and Dynamics in Unlabeled RNAs: The SELOPE Approach. *Chemistry – A European Journal,* 24**,** 6067-6070.
SCHLAGNITWEIT, J., STEINER, E., KARLSSON, H. & PETZOLD, K. 2018b. Efficient Detection of Structure and Dynamics in Unlabeled RNAs: The SELOPE Approach. *Chemistry,* 24**,** 6067-6070.
SCHLOSSER, K. & LI, Y. 2010. A versatile endoribonuclease mimic made of DNA: characteristics and applications of the 8-17 RNA-cleaving DNAzyme. *Chembiochem,* 11**,** 866-79.
SCHNIEDERS, R., KNEZIC, B., ZETZSCHE, H., SUDAKOV, A., MATZEL, T., RICHTER, C., HENGESBACH, M., SCHWALBE, H. & FÜRTIG, B. 2020. NMR Spectroscopy of Large Functional RNAs: From Sample Preparation to Low-Gamma Detection. *Curr Protoc Nucleic Acid Chem,* 82**,** e116.
SEKAR, R. B. & PERIASAMY, A. 2003. Fluorescence resonance energy transfer (FRET) microscopy imaging of live cell protein localizations. *J Cell Biol,* 160**,** 629-33.
SHAH, S., CHANDRA, A., KAUR, A., SABNIS, N., LACKO, A., GRYCZYNSKI, Z., FUDALA, R. & GRYCZYNSKI, I. 2017. Fluorescence properties of doxorubicin in PBS buffer and PVA films. *J Photochem Photobiol B,* 170**,** 65-69.
SHERRY, A. D. & WOODS, M. 2008. Chemical exchange saturation transfer contrast agents for magnetic resonance imaging. *Annu Rev Biomed Eng,* 10**,** 391-411.
SMITH, M. J., MARSHALL, C. B., THEILLET, F.-X., BINOLFI, A., SELENKO, P. & IKURA, M. 2015. Real-time NMR monitoring of biological activities in complex physiological environments. *Current Opinion in Structural Biology,* 32**,** 39-47.
STEFFEN, F. D., CUNHA, R. A., SIGEL, R. K. O. & BÖRNER, R. 2024. FRET-guided modeling of nucleic acids. *Nucleic Acids Res,* 52**,** e59.
SUGIMOTO, N., OKUMOTO, Y. & OHMICHI, T. 1999. Effect of metal ions and sequence of deoxyribozymes on their RNA cleavage activity. *Journal of the Chemical Society, Perkin Transactions 2***,** 1381-1386.
SUN, X., SETRERRAHMANE, S., LI, C., HU, J. & XU, H. 2024. Nucleic acid drugs: recent progress and future perspectives. *Signal Transduction and Targeted Therapy,* 9**,** 316.
TAYLOR, A. I., WAN, C. J. K., DONDE, M. J., PEAK-CHEW, S. Y. & HOLLIGER, P. 2022. A modular XNAzyme cleaves long, structured RNAs under physiological conditions and enables allele-specific gene silencing. *Nat Chem,* 14**,** 1295-1305.

THOMAS, I. B. K., GAMINDA, K. A. P., JAYASINGHE, C. D., ABEYSINGHE, D. T. & SENTHILNITHY, R. 2021. DNAzymes, Novel Therapeutic Agents in Cancer Therapy: A Review of Concepts to Applications. *J Nucleic Acids,* 2021**,** 9365081.

THOMPSON, R. D., BAISDEN, J. T. & ZHANG, Q. 2019. NMR characterization of RNA small molecule interactions. *Methods,* 167**,** 66-77.

VELEZ, T. E., SINGH, J., XIAO, Y., ALLEN, E. C., WONG, O. Y., CHANDRA, M., KWON, S. C. & SILVERMAN, S. K. 2012. Systematic Evaluation of the Dependence of Deoxyribozyme Catalysis on Random Region Length. *ACS Combinatorial Science,* 14**,** 680-687.

VICTOR, J., STEGER, G. & RIESNER, D. 2018. Inability of DNAzymes to cleave RNA in vivo is due to limited Mg$$^{2+}$$concentration in cells. *European Biophysics Journal,* 47**,** 333-343.

VORLÍČKOVÁ, M., KEJNOVSKÁ, I., BEDNÁŘOVÁ, K., RENČIUK, D. & KYPR, J. 2012. Circular dichroism spectroscopy of DNA: from duplexes to quadruplexes. *Chirality,* 24**,** 691-8.

WANG, H., GUO, M., WEI, H. & CHEN, Y. 2023. Targeting p53 pathways: mechanisms, structures and advances in therapy. *Signal Transduction and Targeted Therapy,* 8**,** 92.

WANG, J., WANG, H., WANG, H., HE, S., LI, R., DENG, Z., LIU, X. & WANG, F. 2019. Nonviolent Self-Catabolic DNAzyme Nanosponges for Smart Anticancer Drug Delivery. *ACS Nano,* 13**,** 5852-5863.

WANG, P., CHATTERJEE, G., YAN, H., LABEAN, T. H., TURBERFIELD, A. J., CASTRO, C. E., SEELIG, G. & KE, Y. 2017. Practical aspects of structural and dynamic DNA nanotechnology. *MRS Bulletin,* 42**,** 889-896.

WANG, Y., NGUYEN, K., SPITALE, R. C. & CHAPUT, J. C. 2021. A biologically stable DNAzyme that efficiently silences gene expression in cells. *Nature Chemistry,* 13**,** 319-326.

WATTS, J. K., KATOLIK, A., VILADOMS, J. & DAMHA, M. J. 2009. Studies on the hydrolytic stability of 2′-fluoroarabinonucleic acid (2′F-ANA). *Organic & Biomolecular Chemistry,* 7**,** 1904-1910.

WEINBERG, Z., KIM, P. B., CHEN, T. H., LI, S., HARRIS, K. A., LÜNSE, C. E. & BREAKER, R. R. 2015. New classes of self-cleaving ribozymes revealed by comparative genomics analysis. *Nature Chemical Biology,* 11**,** 606-610.

WIERUSZEWSKA, J., PAWŁOWICZ, A., POŁOMSKA, E., PASTERNAK, K., GDANIEC, Z. & ANDRAŁOJĆ, W. 2024. The 8-17 DNAzyme can operate in a single active structure regardless of metal ion cofactor. *Nature Communications,* 15**,** 4218.

WIJMENGA, S. S. & VAN BUUREN, B. N. M. 1998. The use of NMR methods for conformational studies of nucleic acids. *Progress in Nuclear Magnetic Resonance Spectroscopy,* 32**,** 287-387.

WOLFENDEN, R. & SNIDER, M. J. 2001. The Depth of Chemical Time and the Power of Enzymes as Catalysts. *Accounts of Chemical Research,* 34**,** 938-945.

XIAO, Y., ALLEN, E. C. & SILVERMAN, S. K. 2011a. Merely two mutations switch a DNA-hydrolyzing deoxyribozyme from heterobimetallic (Zn2+/Mn2+) to monometallic (Zn2+-only) behavior. *Chem Commun (Camb),* 47**,** 1749-51.

XIAO, Y., ALLEN, E. C. & SILVERMAN, S. K. 2011b. Merely two mutations switch a DNA-hydrolyzing deoxyribozyme from heterobimetallic (Zn2+/Mn2+) to monometallic (Zn2+-only) behavior. *Chemical Communications,* 47**,** 1749-1751.

XIAO, Y., CHANDRA, M. & SILVERMAN, S. K. 2010. Functional Compromises among pH Tolerance, Site Specificity, and Sequence Tolerance for a DNA-Hydrolyzing Deoxyribozyme. *Biochemistry,* 49**,** 9630-9637.

XIAO, Y., WEHRMANN, R. J., IBRAHIM, N. A. & SILVERMAN, S. K. 2011c. Establishing broad generality of DNA catalysts for site-specific hydrolysis of single-stranded DNA. *Nucleic Acids Research,* 40**,** 1778-1786.

XIAO, Y., WEHRMANN, R. J., IBRAHIM, N. A. & SILVERMAN, S. K. 2012. Establishing broad generality of DNA catalysts for site-specific hydrolysis of single-stranded DNA. *Nucleic Acids Research,* 40**,** 1778-1786.

XU, J., HUANG, H. & ZHOU, X. 2021. G-Quadruplexes in Neurobiology and Virology: Functional Roles and Potential Therapeutic Approaches. *JACS Au,* 1**,** 2146-2161.
YAN, J., RAN, M., SHEN, X. & ZHANG, H. 2023. Therapeutic DNAzymes: From Structure Design to Clinical Applications. *Advanced Materials,* 35**,** 2300374.
YANG, D. 2019. G-Quadruplex DNA and RNA. *Methods Mol Biol,* 2035**,** 1-24.
YOSHIDA, T., HAGIHARA, T., UCHIDA, Y., HORIUCHI, Y., SASAKI, K., YAMAMOTO, T., YAMASHITA, T., GODA, Y., SAITO, Y., YAMAGUCHI, T., OBIKA, S., YAMAMOTO, S. & INOUE, T. 2024. Introduction of sugar-modified nucleotides into CpG-containing antisense oligonucleotides inhibits TLR9 activation. *Scientific Reports,* 14**,** 11540.
ZABOROWSKA, Z. A., FÜRSTE, J. P., ERDMANN, V. A. & KURRECK, J. 2002. Sequence Requirements in the Catalytic Core of the “10-23” DNA Enzyme*. *Journal of Biological Chemistry,* 277**,** 40617-40622.
ZEEB, M. & BALBACH, J. 2004. Protein folding studied by real-time NMR spectroscopy. *Methods,* 34**,** 65-74.
ZHANG, C., LI, Q., XU, T., LI, W., HE, Y. & GU, H. 2021. New DNA-hydrolyzing DNAs isolated from an ssDNA library carrying a terminal hybridization stem. *Nucleic Acids Research,* 49**,** 6364-6374.
ZHANG, Z., HONG, X., XIONG, P., WANG, J., ZHOU, Y. & ZHAN, J. 2024. Minimal twister sister-like self-cleaving ribozymes in the human genome revealed by deep mutational scanning. *eLife,* 12**,** RP90254.
ZHAO, B., BAISDEN, J. T. & ZHANG, Q. 2020. Probing excited conformational states of nucleic acids by nitrogen CEST NMR spectroscopy. *Journal of Magnetic Resonance,* 310**,** 106642.
ZUKER, M. 2003. Mfold web server for nucleic acid folding and hybridization prediction. *Nucleic Acids Res,* 31**,** 3406-15.